27 March 2009 | $10

Science

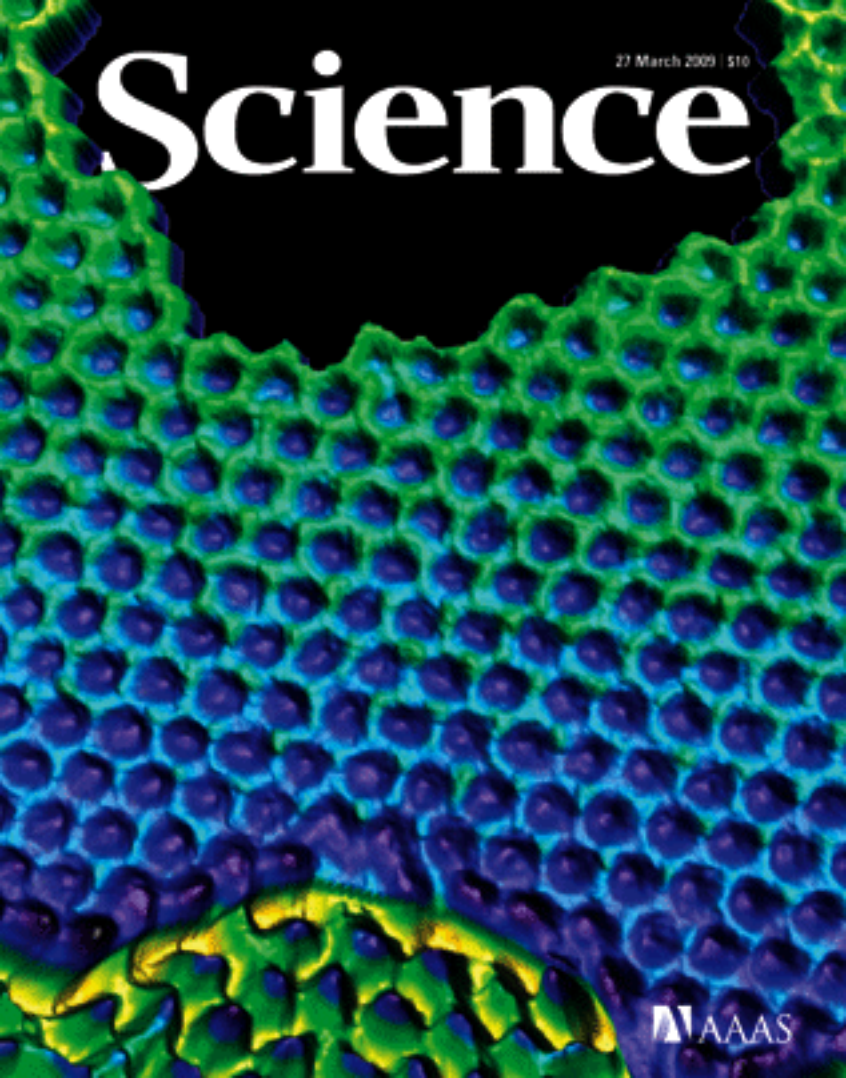

AAAS

EDITORIAL

NEWS OF THE WEEK

NEWS FOCUS

LETTERS

BOOKS *ET AL.*

EDUCATION FORUM

PERSPECTIVES

page 1662

page 1674

BREVIA

CONTENTS continued >>

COVER

False-color, aberration-corrected transmission electron microscope image of a suspended single atomic layer of graphene. When an electron beam induces ejection of an atom from the edge of an intentionally made ~3-nm hole (black), the hole enlarges; the remaining edge carbon atoms rearrange from perfect hexagons into predicted metastable configurations. See page 1705.

Image: Zettl Research Group and National Center for Electron Microscopy, Lawrence Berkeley National Laboratory; 3D visualization via WSxM software

DEPARTMENTS

Published by AAAS

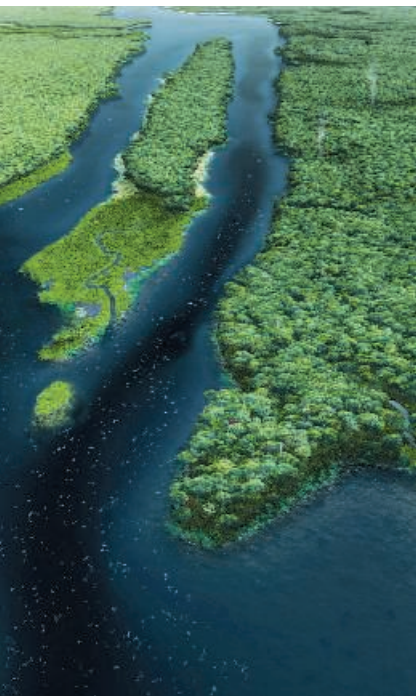

page 1675

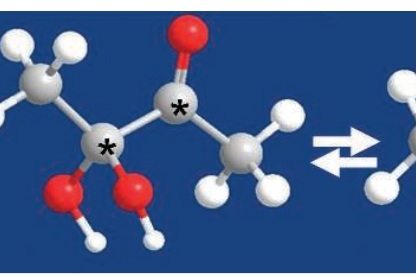

page 1711

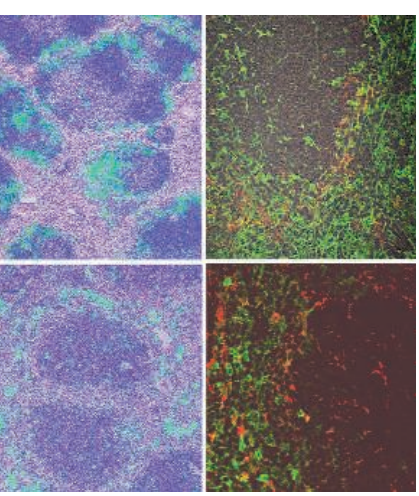

page 1726

RESEARCH ARTICLES

REPORTS

Published by AAAS

SCIENCEONLINE

SCIENCEXPRESS
www.sciencexpress.org

Human Induced Pluripotent Stem Cells Free of Vector and Transgene Sequences
J. Yu et al.

Human induced pluripotent stem cells can be generated without integration of exogenous DNA into their genomes.
10.1126/science.1172482

Sequential Regulation of DOCK2 Dynamics by Two Phospholipids During Neutrophil Chemotaxis
A. Nishikimi et al.

The signaling lipid phosphatidic acid links chemoattractant signals to directional movement of neutrophils.
10.1126/science.1170179

A Frazzled/DCC-Dependent Transcriptional Switch Regulates Midline Axon Guidance
L. Yang et al.

A single receptor in *Drosophila* is involved in two molecular strategies that coordinate axon guidance.
10.1126/science.1171320

The Role of Aerosols in the Evolution of Tropical North Atlantic Ocean Temperature Anomalies
A. T. Evan et al.

Changes in tropical North Atlantic sea surface temperatures are caused by variability in atmospheric aerosol abundances.
10.1126/science.1167404

Asymmetric Autocatalysis Triggered by Carbon Isotope ($^{13}C/^{12}C$) Chirality
T. Kawasaki et al.

The origin of chirality in asymmetric autocatalysis is due to carbon isotope substitution.
10.1126/science.1170322

SCIENCENOW
www.sciencenow.org
Highlights From Our Daily News Coverage

When Frying the Hard Drive Is a Good Thing
Laser-assisted magnetic recording could greatly increase storage capacity.

Corn: It's Not for Cocktails
Scientists find earliest traces of maize—and discount a leading hypothesis about what it was used for.

Feel-Good Music Feels Good Around the World
African tribal people can tell whether a Western song is happy or sad.

SCIENCESIGNALING
www.sciencesignaling.org
The Signal Transduction Knowledge Environment

RESEARCH ARTICLE: An Intramolecular Switch Regulates Phosphoindependent FHA Domain Interactions in *Mycobacterium tuberculosis*
T. J. Nott et al.

Binding of Rv1827 to target proteins through its forkhead-associated (FHA) domain does not require their prior phosphorylation at threonine residues.

RESEARCH ARTICLE: Dynamic Signaling in the Hog1 MAPK Pathway Relies on High Basal Signal Transduction
J. Macia et al.

High intrinsic basal signaling in mitogen-activated protein kinase pathways ensures proper dynamic responses to environmental stimuli.

PERSPECTIVE: Challenges and Opportunities in Defining the Essential Cancer Kinome
B. D. Manning

RNAi screens for essential kinases reveal that the potential therapeutic kinase universe is larger than expected.

PERSPECTIVE: Amyloid Goes Global
I. Bezprozvanny

Amyloid plaques have farther-reaching effects on astrocytes than previously suspected.

MEETING REPORT: Signal Transduction—Receptors, Mediators, and Genes
F. Entschladen et al.

Cell signaling researchers gathered in Weimar, Germany for the annual meeting of the Signal Transduction Society.

PRESENTATION: Early Events of B Cell Activation by Antigen
D. Depoil et al.

B cells undergo membrane spreading and contraction during activation in response to antigen-presenting cells.

PODCAST
S. J. Smerdon and A. M. VanHook

The activity of a bacterial FHA domain–containing protein is regulated intramolecularly.

SCIENCECAREERS
www.sciencecareers.org/career_magazine
Free Career Resources for Scientists

Special Feature: Not What You Thought You'd Be Doing
E. Pain

A visual artist, a cartoonist, and a winemaker—all trained as scientists—are pursuing unexpected careers.

The Itinerant Artist
E. Pain

Angelo Vermeulen eventually reconciled his talent for the arts with his scientific curiosity.

In Vino Oportunitas
A. Levine

Jeff Mangahas left scientific work to become an award-winning winemaker at Hartford Vineyards.
>> News story p. 1668

SCIENCEPODCAST
www.sciencemag.org/multimedia/podcast
Free Weekly Show

Download the 27 March *Science* Podcast to hear about genetic influences on cognition, visualizing HIV infection, professional science master's programs, and more.

SCIENCENOW
Corn's rock-hard history.

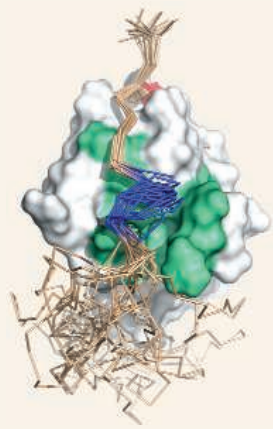

SCIENCESIGNALING
Rv1827 and its FHA domain.

ORIGINSBLOG
blogs.sciencemag.org/origins
A History of Beginnings

SCIENCEINSIDER
blogs.sciencemag.org/scienceinsider
Science Policy News and Analysis

SCIENCE (ISSN 0036-8075) is published weekly on Friday, except the last week in December, by the American Association for the Advancement of Science, 1200 New York Avenue, NW, Washington, DC 20005. Periodicals Mail postage (publication No. 484460) paid at Washington, DC, and additional mailing offices. The title SCIENCE is a registered trademark of the AAAS. Domestic individual membership and subscription (51 issues): $146 ($74 allocated to subscription). Domestic institutional subscription (51 issues): $835; Foreign postage extra: Mexico, Caribbean (surface mail) $55; other countries (air assist delivery) $85. First class, airmail, student, and emeritus rates on request. Canadian rates with GST available upon request, GST #1254 88122. Publications Mail Agreement Number 1069624. **Printed in the U.S.A.**

Change of address: Allow 4 weeks, giving old and new addresses and 8-digit account number. **Postmaster:** Send change of address to AAAS, P.O. Box 96178, Washington, DC 20090–6178. **Single-copy sales:** $10.00 current issue, $15.00 back issue prepaid includes surface postage; bulk rates on request. **Authorization to photocopy** material for internal or personal use under circumstances not falling within the fair use provisions of the Copyright Act is granted by AAAS to libraries and other users registered with the Copyright Clearance Center (CCC) Transactional Reporting Service, provided that $20.00 per article is paid directly to CCC, 222 Rosewood Drive, Danvers, MA 01923. The identification code for *Science* is 0036-8075. *Science* is indexed in the *Reader's Guide to Periodical Literature* and in several specialized indexes.

AAAS
ADVANCING SCIENCE, SERVING SOCIETY

EDITED BY STELLA HURTLEY

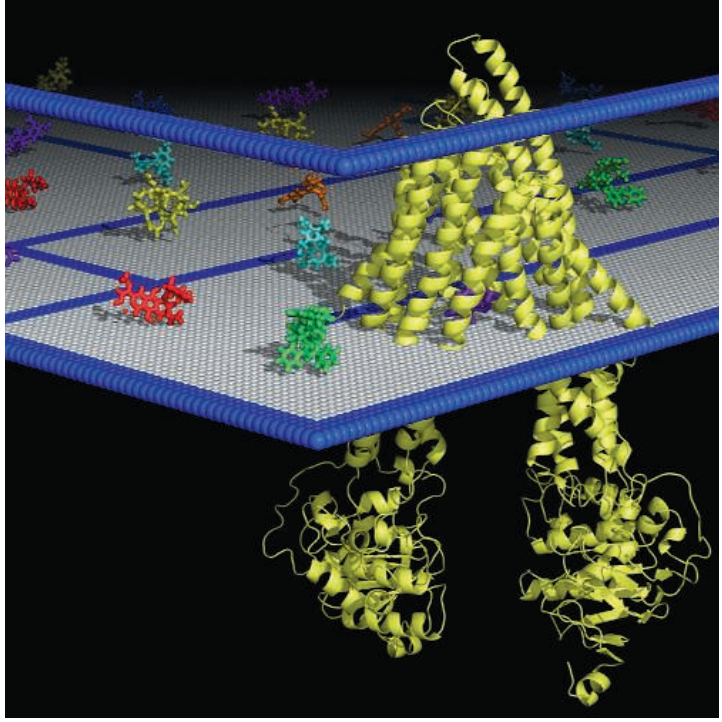

Dissecting Drug Expulsion Portal >>

P-glycoprotein (P-gp) is a transmembrane transporter protein with broad specificity for hydrophobic drugs found at the surface of many mammalian cells. P-gp detoxifies cells and, because of its ability to pump drugs out of the cell, has been implicated in multidrug resistance in cancer treatment. **Aller *et al.*** (p. 1718; see the Perspective by **Sheps**) now report crystal structures of mouse Pgp with and without cyclic peptide inhibitors bound in a large internal cavity. The inward-facing structures have two portals that allow entry of hydrophobic molecules directly from the inner leaflet of the lipid bilayer. Understanding in molecular detail how P-gp promotes cancer drug efflux will be key to preventing and reversing multidrug resistance in the future.

Graphene at the Edge

Although graphene is thought of as a uniform, two-dimensional material, the properties of a graphene specimen will depend on the structures and defects at its edges. **Jia *et al.*** (p. 1701) use Joule (resistive) heating to heal defects through the vaporization of carbon atoms. Tracking the process using electron microscopy revealed the main mechanisms by which sharp edges and step-edge arrays are stabilized into armchair and zigzag configurations. **Girit *et al.*** (p. 1705; see the cover) present a high-resolution transmission electron microscopy study of the structure and dynamics of graphene at the edge of a hole in a suspended, single atomic layer of graphene. The injection of electrons causes ejection of carbon atoms, leading to rearrangement of the bonds at the edges into a zigzag configuration, which represents the most stable form.

Folding Forum

The endoplasmic reticulum (ER) establishes and maintains a specialized environment capable of supporting the folding of secreted proteins. Reductionist approaches have focused on understanding the mechanism and biological role of a specific chaperone or degradation system in isolation. **Jonikas *et al.*** (p. 1693) present a complementary strategy using the cell's endogenous sensor of misfolding in the ER (the Ire1/Hac1 system) as a reporter to identify all the genes that contribute to ER folding. A remarkable array of different factors and processes were seen to contribute to ER folding. Measuring induction of the unfolded-protein response pathway in double mutants allowed the equivalent of hundreds of secondary screens in parallel and the systematic functional dissection of previously characterized and uncharacterized processes needed for proper ER function.

Very Extreme Light Source

The collapse of very massive stars can produce violent explosions accompanied by strong bursts of gamma-ray light. Typical gamma-ray bursts emit photons with energies between 10 kiloelectron volts (keV) and about 1 megaelectron volt (MeV). Rarely, photons with energies above 100 MeV have been observed, but the distances to their sources have been unclear. Now, **Abdo *et al.*** (p. 1688, published online 19 February) report that the Fermi Gamma-ray Space Telescope has detected photons with energies between 8 keV and 13 GeV, arriving from the gamma-ray burst 080916C, whose distance is known. These broad energy data, together with the distance to the burst, provide important constraints on the poorly understood gamma-ray burst emission mechanism.

Fighting Friction

If you rub two metal blocks against each other they will slide with a certain amount of resistance. If you push them together at the same time, the sliding motion will slow down and then suddenly cease due to a sudden jump in the friction between the two surfaces. To reduce friction, lubricants like oil are added. The coefficient of friction (COF) reflects this resistance to motion, and examples of materials with low COF can be found in the human body, such as in knee and hip joints, even at elevated pressures. While low friction synthetic materials have been fabricated, the low COF values are not retained at elevated pressures. **Chen *et al.*** (p. 1698) constructed phosphorylcholine group-containing polymeric brushes that showed extremely low COF values, even at high pressures. The polymer brushes retain a very large hydration shell, which enables easy sliding between two brush surfaces.

A Wider Warmth

The early Pliocene epoch from 5.3 to about 3 million years ago was much warmer than today. Despite this difference, the early Pliocene climate was very much like the preindustrial present in many important ways—including the amount of solar radiation Earth received, the concentration of atmospheric CO_2, and a nearly identical geographic environment. However, there was no permanent ice sheet in the Northern Hemisphere, and global sea level was 25 meters higher. Why then was the world so different? **Brierly *et al.*** (p. 1714, published online 26 February) analyze new and published data about sea surface temperatures 4 million years ago that show that the meridional temperature gradient between the equator and the subtropics was much shallower than it is today, implying that the ocean tropical warm pool was much larger. An atmospheric general circulation model shows what major atmospheric circulation

CREDITS (TOP TO BOTTOM): ANDREW WARD; JIA *ET AL.*

Published by AAAS

changes such a sea surface temperature field implies, with relevance for how climate warming may affect the future.

A Stealthy Exit

The mycobacterial pathogens that cause tuberculosis are difficult to work with because they grow very slowly, can require special laboratory containment facilities, and frequently cannot be grown independently of a host cell. Consequently, **Hagedorn *et al.*** (p. 1729; see the Perspective by **Carlsson and Brown**) have adopted a convenient model organism, the social amoeba *Dictyostelium discoideum,* which can be infected by certain mycobacteria and offers an analog for vertebrate macrophages—the preferred niche for tubercular mycobacteria. During their escape from *Dictyostelium* cells, mycobacteria use a so-called ejectosome. The ejectosome consists of a dense ring of actin surrounding a mycobacterium that is rupturing through the plasma membrane. The ejectosome is generated by mycobacteria that have escaped from phagosomes into the cytoplasm and requires the mycobacterial virulence locus RD1. The same type of structure could provide a route for mycobacterial spread between densely aggregated cells found in tubercular granulomatous disease.

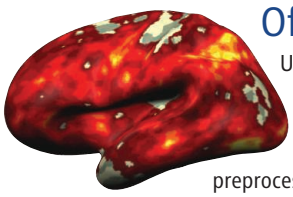

Of Twins and Brains

Until now, brain imaging studies in twins have used an approach that is well suited for group studies, which minimize individual differences in the brain imaging response. However, genetic imaging studies are concerned with the detection of individual differences that require preprocessing and brain alignment techniques. Now **Koten *et al.*** (p. 1737) have examined differences in the patterns of brain activity among identical and fraternal twins during the performance of arithmetic verification and working-memory tasks. A multivariate pattern analysis allowed the identification of regions of activity that were activated either consistently or inconsistently across subjects, which could then be assessed for the effects of heritability. Genetic effects were mainly found in brain regions that were not consistently activated in all individuals, particularly during more complex or demanding tasks. Thus, individual differences in patterns of brain activity may result from genetic factors.

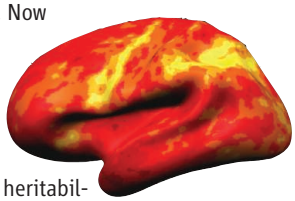

CREDIT: KOTEN *ET AL.*

Not Too Cold

Ambient temperature affects the physiology, behavior, and evolution of organisms. Genetic variants that confer heat- or cold-resistance on organisms can be selected during a period of extreme climate change, later allowing populations to spread to geographic regions beyond the boundaries of the ancestral population. **Takeuchi *et al.*** (p. 1740), in a screen for flies with abnormal temperature preferences, isolated the gene encoding the *Drosophila* ortholog of dystroglycan (DmDG) (a glycosylated peripheral membrane, abnormalities of which can cause muscular dystrophy). When given a choice of moving within a gradient of temperatures, the mutant flies lacking DmDG preferred a temperature a few degrees cooler than did wild-type flies. This behavior was associated with an increased rate of mitochondrial oxidative metabolism in the animals, and flies engineered with a second mutation that caused decreased activity of the mitochondrial enzyme pyruvate dehydrogenase reversed the effect of loss of DmDG. The dystroglycan mutant flies were also resistant to cold, with about half of the flies able to survive near-freezing temperatures that killed almost all of the wild-type flies.

Real-Time Visualization of HIV Entry

The ability to visualize fluorescently labeled viruses in real time as they infect target cells will generate new understanding and potentially suggest novel targets for disease intervention. During infection, human immunodeficiency virus (HIV) is able to spread between immune cells without seeming to be exposed to neutralizing immune responses. **Hübner *et al.*** (p. 1743) captured high-resolution images of the formation of infectious structures called virological synapses during HIV infection of T cells. Dynamic membrane trafficking and an endocytic pathway for HIV transfer between cells appeared to be triggered by cell-cell contact. Continuous long-duration imaging suggests that this pathway can promote infectious HIV spread between T cells.

Alice P. Gast is president of Lehigh University in Bethlehem, PA.

Shovel-Ready Science?

IT IS GRATIFYING TO SEE THE FUNDING FOR SCIENTIFIC RESEARCH IN THE U.S. ECONOMIC stimulus package, a critical short-term investment which must be spent over 2 years. Yet at the risk of sounding ungrateful and skeptical, it is worth sounding a note of caution. Transformative change requires long-term investment in the nation's intellectual infrastructure. "Shovel-ready" makes sense for getting people to work on deferred infrastructure needs, but how does it relate to the scientific research and education programs needed to address the many challenges looming before us?

Long-term research and education provide innovative, creative discoveries that spur transformative change. The United States needs to start making the down payment on this exploration, knowing that the needed breakthroughs cannot be generated within the next 2 years. As science funding agencies begin awarding their one-time money, they must be mindful of the sustainability of their programs. The recent signing of the fiscal year 2009 omnibus bill with its 4.7% increase for agencies funding science and technology R&D is a welcome sign. Maintaining that momentum in the coming years will be essential.

The urgency to stimulate the economy is understandable, but there are risks in not effectively using the funds that have suddenly become available. Here it is useful to consider the U.S. commitment to supporting scientific research and education, which arguably began after Vannevar Bush's persuasive work *Science: The Endless Frontier*. In a letter to President Roosevelt in 1945, Bush wrote: "Science offers a largely unexplored hinterland for the pioneer who has the tools for his task. The rewards of such exploration both for the Nation and the individual are great. Scientific progress is one essential key to our security as a nation, to our better health, to more jobs, to a higher standard of living, and to our cultural progress." We are still benefiting from this foresight. As noted in the U.S. National Academies 2007 report *Rising Above the Gathering Storm*, as much as 85% of the nation's economic growth has arisen from advances in science and technology. A pioneering spirit and progressive investments such as those in the current stimulus plan are as essential today as they were in 1945.

Reaping the benefits of investments in research takes time (see the *Beyond Discovery* series by the U.S. National Academies). Frequently, research fails to take the expected path or create the obvious solution, and the most critical results may not become evident for years. Witness the development of medical technologies such as laser surgery, computer-aided tomography, and magnetic resonance imaging, which resulted from decades of fundamental research on stimulated emission, accelerator physics, and nuclear magnetic resonance. These transformative medical technologies emerged as unexpected benefits of fundamental physics, chemistry, and molecular structure research. Thus, one cannot expect shovel-ready science to solve today's problems; long-term fundamental research develops the understanding and discoveries that will help us confront tomorrow's challenges.

One risk of haste is that short-term investments are neither sustainable nor sufficient to achieve the desired goals. The superconducting supercollider, Star Wars, and crash programs such as the "war on cancer" fell short of their audacious goals. Yet a nation's goals should be daring, because the world faces many urgent challenges, such as those highlighted last year by the U.S. National Academy of Engineering (www.engineeringchallenges.org). Its 14 "Grand Challenges" range from developing new medicines, to providing clean water around the world, to developing new energy sources. We must address each of these challenges with a long-term view, a pioneering spirit, and sustainable support for the bold innovative research that will be needed for ultimate success.

Now is the time to renew the U.S. commitment to research. The scientific community and funding agencies must ensure that our political leaders and the public understand how shovel-ready programs of rebuilding differ from the long-term research that drives innovation. Let's take the time needed to make sure we get this right.

– Alice P. Gast

10.1126/science.1173327

Published by AAAS

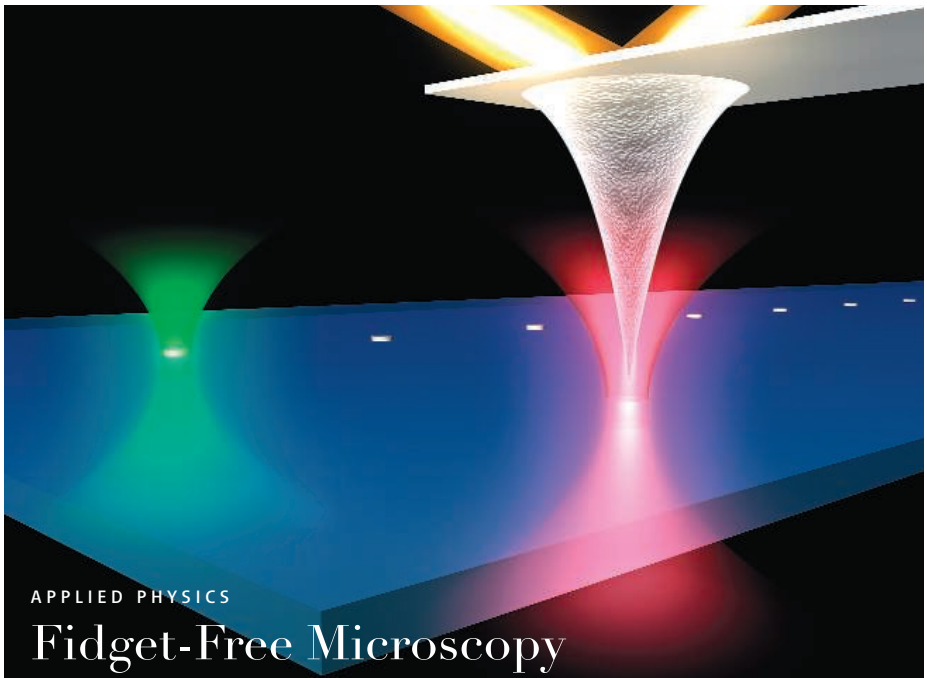

APPLIED PHYSICS

Fidget-Free Microscopy

Many people find it hard to sit still for extended periods without fidgeting and shifting about. A similar problem plagues the widely used technique of atomic force microscopy: Though the probing tip can resolve individual atoms, it is fundamentally a mechanical device and so inevitably drifts in space over time. As a result, the period available for signal-averaging to improve data quality is limited; moreover, it is often impossible to deliberately shift the tip to a different portion of the sample and then return to precisely the same starting position during the course of an imaging session (for example, to monitor slow rearrangements in two or more distinct domains of a protein). King *et al.* address this shortcoming using a laser-based feedback scheme for tip stabilization. Specifically, they detect backscattered laser light from the tip as well as a reference marker (a silicon disk) on the sample. The tip is then adjusted to remain in a fixed position relative to the marker. Studies of gold nanospheres in room-temperature air demonstrate a lateral drift rate limited to just 5 pm/min over the course of more than an hour. The method is optimized for transparent substrates, due to the backscattering detection geometry, but could potentially be extended by incorporating the reference marker into the instrument's cantilever assembly. — JSY

Nano Lett. **9**, 10.1021/nl803298q (2009).

BIOMEDICINE

Precipitating an Invasion

Anti-angiogenic drugs for cancer have commanded tremendous interest, especially over the past decade as they entered long-awaited clinical trials. This class of compounds inhibits the growth of tumors by cutting off their blood supply, usually by disabling cellular signaling pathways that are essential for blood vessel growth, such as the vascular endothelial growth factor (VEGF) pathway. Despite an abundance of promising preclinical data, most cancer patients have shown only a transient improvement in response to VEGF-targeting drugs, which is then followed by a progression to metastatic disease.

Two groups show that VEGF-targeting drugs have unanticipated—and undesirable—effects on tumor behavior that might explain their limited clinical efficacy. Working with four distinct mouse models, Pàez-Ribes *et al*. and Ebos *et al*. find that although the drugs initially inhibit primary tumor growth, they also appear to stimulate tumor cells to develop a more invasive and metastatic phenotype. This might occur because the drugs cause hypoxia (oxygen deficiency), which in turn selects for more malignant cells, or because the drugs increase the leakiness of blood vessels, thereby facilitating the entry of tumor cells into the circulation. — PAK

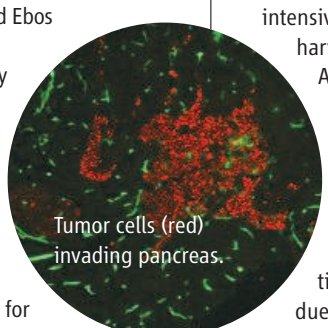

Tumor cells (red) invading pancreas.

Cancer Cell **15**, 220; 232 (2009).

GEOPHYSICS

Tossing Minerals into the Mix

Numerical models of flow in Earth's mantle have helped to constrain structural hypotheses about Earth's interior derived from seismic observations, mineral physics data on phase transitions, and geochemical data on the presence of possible distinct reservoirs. Typically, however, the models have required many simplifying assumptions—most, for example, have not explicitly used the wealth of mineral physics data. Nakagawa *et al.* have now developed a model framework that includes the phase relations, and corresponding thermodynamic properties, across five major components that dominate the major element chemistry of the mantle: the oxides of calcium, magnesium, iron, silicon, and aluminum. Models were run for the equivalent of 4.5 billion years of Earth's history, though it is still difficult to simulate the full convective vigor of Earth. The more realistic inclusion of mantle phases doesn't drastically affect many of the results as compared with prior simulations: subducting slabs, for example, are still predicted to penetrate the major phase boundary at 660 km and accumulate near the base of the mantle. The new models do show a reduced pattern of heterogeneity that is more in line with seismic data, but some of the richness of the seismic data is not as well reproduced, particularly in the complex upper mantle. — BH

Geochem. Geophys. Geosyst. **10**, 10.1029/2008GC002280 (2009).

EVOLUTION

Recovering from Stress

The evolutionary consequences of the overfishing of fish populations are generally not known, although there is evidence suggesting that fish are becoming smaller, especially in the most intensively targeted fisheries. Conover *et al.* harvested large fish from a captive Atlantic silverside population for five generations, followed by five generations without harvesting. They found that the population rebounded once culling had stopped, but that full recovery was estimated to take at least 12 generations. Hence, evolutionary changes due to selection on genetically determined traits, such as body size, are potentially reversible if the selective pressure is removed. — LMZ

Proc. R. Soc. London Ser. B **276**, 10.1098/rspb.2009.0003 (2009).

CREDITS (TOP TO BOTTOM): GREG KUEBLER/JILA; ELIZABETH ALLEN AND DOUGLAS HANAHAN

Published by AAAS

www.sciencemag.org

Science

1200 New York Avenue, NW
Washington, DC 20005
Editorial: 202-326-6550, FAX 202-289-7562
News: 202-326-6581, FAX 202-371-9227
Bateman House, 82-88 Hills Road
Cambridge, UK CB2 1LQ
+44 (0) 1223 326500, FAX +44 (0) 1223 326501

Subscription Services For change of address, missing issues, new orders and renewals, and payment questions: 866-434-AAAS (2227) or 202-326-6417, FAX 202-842-1065. Mailing addresses: AAAS, P.O. Box 96178, Washington, DC 20090-6178 or AAAS Member Services, 1200 New York Avenue, NW, Washington, DC 20005

Institutional Site Licenses please call 202-326-6755 for any questions or information

Reprints: Author Inquiries 800-635-7181
Commercial Inquiries 803-359-4578

Permissions 202-326-7074, FAX 202-682-0816

Member Benefits AAAS/Barnes&Noble.com bookstore www.aaas.org/bn; AAAS Online Store www.apisource.com/aaas/ code MKB6; AAAS Travels: Betchart Expeditions 800-252-4910; Apple Store www.apple/eppstore/aaas; Bank of America MasterCard 1-800-833-6262 priority code FAA3YU; Cold Spring Harbor Laboratory Press Publications www.cshlpress.com/affiliates/aaas.htm; GEICO Auto Insurance www.geico.com/landingpage/go51.htm?logo=17624; Hertz 800-654-2200 CDP#343457; Office Depot https://bsd.officedepot.com/portalLogin.do; Seabury & Smith Life Insurance 800-424-9883; Subaru VIP Program 202-326-6417; VIP Moving Services www.vipmayflower.com/domestic/index.html; Other Benefits: AAAS Member Services 202-326-6417 or www.aaasmember.org.

science_editors@aaas.org	(for general editorial queries)
science_letters@aaas.org	(for queries about letters)
science_reviews@aaas.org	(for returning manuscript reviews)
science_bookrevs@aaas.org	(for book review queries)

Published by the American Association for the Advancement of Science (AAAS), *Science* serves its readers as a forum for the presentation and discussion of important issues related to the advancement of science, including the presentation of minority or conflicting points of view, rather than by publishing only material on which a consensus has been reached. Accordingly, all articles published in *Science*—including editorials, news and comment, and book reviews—are signed and reflect the individual views of the authors and not official points of view adopted by AAAS or the institutions with which the authors are affiliated.

AAAS was founded in 1848 and incorporated in 1874. Its mission is to advance science, engineering, and innovation throughout the world for the benefit of all people. The goals of the association are to: enhance communication among scientists, engineers, and the public; promote and defend the integrity of science and its use; strengthen support for the science and technology enterprise; provide a voice for science on societal issues; promote the responsible use of science in public policy; strengthen and diversify the science and technology workforce; foster education in science and technology for everyone; increase public engagement with science and technology; and advance international cooperation in science.

Information for Authors
See pages 807 and 808 of the 6 February 2009 issue or access www.sciencemag.org/about/authors

Neolithic Site Ravaged

One of the most important prehistoric sites in Spain has been severely damaged by the landowner, archaeologists say.

The Cueva de Chaves de Bastaras in northeastern Spain shelters a 4000-square-meter Neolithic site discovered in 1974. It's protected under local heritage laws but is on land belonging to Fimbas S.A., a company that runs a game preserve.

Archaeologist Vicente Baldellou, director of the Museum of Huesca and chief of the excavation, says he found a "catastrophic" situation at the cave earlier this month. Earthmoving machines had hauled away blocks of stone that had fallen from the ceiling of the cave and scraped away 3 meters of soil. A drinking trough for game animals had been installed. "They've taken away the entire deposit of the Neolithic," says Baldellou. He complained to local authorities, who are investigating. Fimbas S.A. declined to comment.

Researchers have excavated only 10% of the site but have already found a man's grave, ceramics, and painted pebbles dating back to 5000 B.C.E., Baldellou says. "Chaves is exceptional for its unique stratigraphic sequence," says Mauro S. Hernández Pérez, a Neolithic researcher at the University of Alicante in Spain, who calls the cave "the best referent for knowledge of the Early Neolithic in the interior of the [Iberian] peninsula." Baldellou still hopes to retrieve some artifacts. "But without context, they lose 90% of their interest. This is irretrievable," he says.

Oldest Human Hair Found?

Human hairs in 200,000-year-old hyena feces could help settle a long-running dispute about ancient remains—if the hairs are indeed human.

Researchers have found fossils of early humans and their evolutionary forebears in many South African caves. Some think the hominins either died or were buried there, but others think it more likely that wild animals dragged their bones or bodies into the caves.

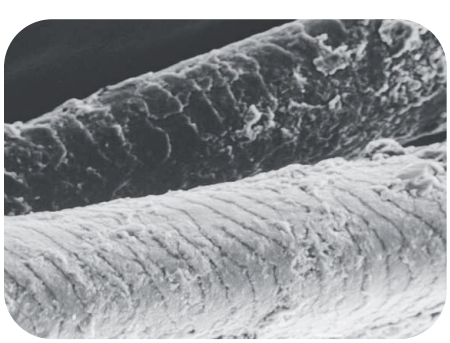

The fossilized hyena feces, or coprolites, come from Gladysvale Cave north of Johannesburg, where australopithecine teeth and a hominin hand bone were found in the 1990s. A team led by Lucinda Backwell, a paleontologist at the University of the Witwatersrand in Johannesburg, tweezed 40 hairs from a coprolite and examined half of them with a scanning electron microscope. Comparing their microscopic structure with that of other animal hairs, Backwell found that five of the hairs appeared to be human. If they are, the team says in a paper slated for the June issue of the *Journal of Archaeological Science*, they would be the oldest known—20 times as old as the previous record holder, hair from a 9000-year-old mummy found in Chile.

Some researchers say the team's conclusions are premature. Noel Boaz, a paleoanthropologist at Ross University School of Medicine in the West Indies, says the hairs might be from monkeys. And Robert Blumenschine, an anthropologist at Rutgers University, New Brunswick, says the hairs don't prove that hyenas carried hominin bones into their caves, just that "a hyena ate at least part of a hominin."

Antibiotics Bad for Vultures

Eating carcasses of livestock treated with antibiotics is wrecking the immune systems of Spanish vultures, according to a new study.

Spain is the European stronghold of vultures, who have long lived off dead livestock dumped by farmers at sites called *muladares*. Because research suggests that overuse of antibiotics can suppress the immune system, ecologists Jesús Lemus and Guillermo Blanco of the National Museum of Natural Sciences in Madrid have worried that the drugs, used widely in cattle and pigs, might hurt vultures.

Last year, they reported that high antibiotic levels in the birds were associated with severe bacterial and fungal diseases. In the latest study, Lemus and Blanco climbed trees to reach vulture nests in central Spain and took blood samples from 71 nestlings of three species. They then compared parameters related to immune function with blood samples from vultures in southern and western Spain, where fewer antibiotics are used and birds feed mainly on wild prey.

Both the cellular and the humoral immune systems of the central Spain vultures were suppressed, they reported online last week in the *Proceedings of the Royal Society B: Biological Sciences*. Pending further studies, they say *muladares* should be "rejected as a management tool in conservation programs."

The study shows that scientists need to be much more aware of unexpected effects of antibiotic use high up the food chain, says environmental chemist Alistair Boxall of the University of York, U.K. He notes that an anti-inflammatory drug has been linked to vulture deaths in India and Pakistan.

CREDITS (TOP TO BOTTOM): MUSEUM OF HUESCA; JAROSLAV PAP/AP; LUCINDA BACKWELL

Published by AAAS

EDITED BY YUDHIJIT BHATTACHARJEE

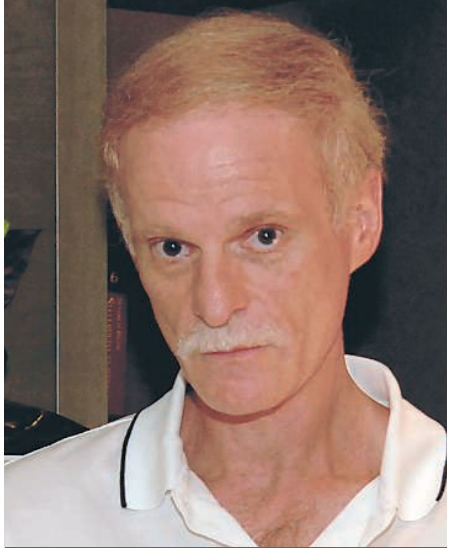

Three Q's >>

After 26 years at the Federal Bureau of Investigation (FBI), forensic microbiologist **Bruce Budowle** has joined academia. This month, he became executive director of the new Institute of Investigative Genetics at the University of North Texas (UNT) in Denton. Budowle is widely recognized for advancing the science of DNA fingerprinting and elevating its importance in criminal investigations.

Q: How did you get started in forensics?
I was a postdoc doing cancer and diabetes research at the University of Alabama in Birmingham when I developed a method for extracting proteins from hair. That led to a relationship with local law enforcement officials. When I saw an FBI job ad in the back of *Science*, I thought it was a good opportunity to help society directly rather than doing research for the sake of research.

Q: How has science's role in investigations evolved?
It used to be limited to matching the evidence to suspects. Now, science is routinely used to point the investigation in a specific direction. For example, if you find a bloodstain at a crime scene and typing it against a DNA database gives you no identification of the potential suspect, you can still use the phenotypic markers to recreate a physical description of an individual.

Q: What will the new institute do?
One goal is to strengthen a program at UNT on identifying human remains, a critically underfunded area nationally. Another is to develop a program on biosafety and biosecurity.

Got a tip for this page? E-mail people@aaas.org

CREDITS (TOP TO BOTTOM): SOURCE: BRUCE BUDOWLE; LLNL; PHOTOS.COM; JOANNE CACCIATORE; SUSAN LEO

INSIDE GOVERNMENT

FRACTION FACTION. "It doesn't seem like we should be wasting our time celebrating Pi Day in the midst of the current financial crisis." So says Representative Jason Chaffetz (R–UT), who, along with nine other House Republicans, voted this month against a bill designating 14 March (3.14) as Pi Day.

The lighthearted measure (H.Res. 224) notes the dismal performance of U.S. school students on international tests and suggests that "learning about Pi can be an engaging way to teach children about geometry." It also praises the National Science Foundation (NSF) for its efforts to improve math and science education. The resolution passed by a vote of 391 to 10. The opponents included Representative Randy Neugebauer (R–TX), a member of the House science committee that oversees NSF and whose chair, Representative Bart Gordon (D–TN), introduced the bill.

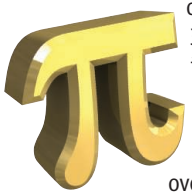

Chaffetz, who says "I don't believe that the federal government should be involved in education because it's a state responsibility," is not completely averse to celebrating numerical oddities, however. Two minutes after being told about another momentous mathematical event on the calendar, Chaffetz tweeted about Square Root Day (3.3.09). "This only happens eight [sic] times per century....awesome."

MOVERS

A CATCH FOR HARVARD. Cherry Murray, the incoming dean of Harvard University's School of Engineering and Applied Sciences, hopes to increase the size of the faculty despite a shrinking endowment. Colleagues say if anyone can do it, she can.

A soft condensed matter physicist, Murray spent most of her career as a scientist and then as a manager at Bell Laboratories before moving to the Department of Energy's Lawrence Livermore National Laboratory in 2004. Marc Kastner, dean of the School of Sciences at the Massachusetts Institute of Technology in Cambridge, calls her hire "a coup" for Harvard. She replaces Frans Spaepen, who has been interim dean since Venkatesh Narayanamurti stepped down in September.

Harvard had planned to house dozens of new faculty members in its future Allston campus (*Science*, 11 July 2008, p. 190), but the recession has slowed construction, and Murray says that hiring will also be affected. She plans to work on increasing gender and racial diversity as well. "I am absolutely committed to having the student body of Harvard, as well as the faculty, … look like the U.S. population in general," she says.

IN PRINT

(OVER)DUE DILIGENCE. The *Journal of the American Medical Association* (*JAMA*) this month admitted to having overlooked an author's conflict of interest days after a tense exchange between a journal editor and two academics who had publicized the matter.

The paper in question, by psychiatrist Robert Robinson of the University of Iowa and his colleagues, reported that the antidepressant Lexapro could prevent depression in stroke patients if given soon after a stroke. The paper was published in May 2008, and last fall Jonathan Leo (bottom) of Lincoln Memorial University in Harrogate, Tennessee, and Jeffrey Lacasse (top) of Arizona State University, West, say they "just stumbled on a disclosure" in a previous paper in which Robinson reported that he had been a paid speaker for Forest Pharmaceuticals, which makes the drug. Leo notified *JAMA* in October, and editors told him they "would look into it." On 5 March, after no further word from *JAMA*, Leo and Lacasse criticized the paper—and the nondisclosure—in a letter in the *British Medical Journal*.

Publicizing the case ticked off *JAMA*'s top brass. As first reported in the *Wall Street Journal*'s Health blog, Leo says *JAMA* Executive Deputy Editor Phil Fontanarosa called him and said, "You are banned from *JAMA* for life." *JAMA* Editor-in-Chief Catherine DeAngelis acknowledges that Fontanarosa called Leo to say that "what he was doing was quite unprofessional." But DeAngelis says Fontanarosa actually told Leo that "we certainly don't expect to receive anything from you to be published." On 11 March, *JAMA* published a letter from Robinson and his co-authors acknowledging the conflict.

Published by AAAS

Obama's science adviser confirmed
1656

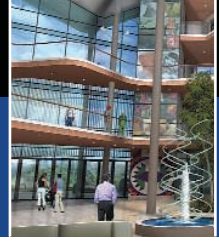

A new HIV/TB research center
1659

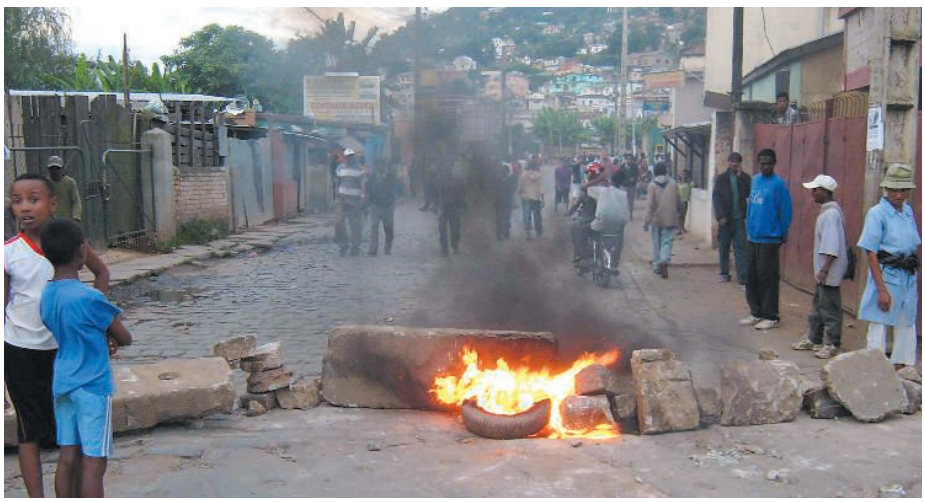

Blocked. Scientists returning from the field faced burning barricades in the capital.

AFRICA

Madagascar's Coup Endangers Science and Scientists

The government of Madagascar was toppled last week in a bloody military coup that is playing havoc with the research efforts, and lives, of the many scientists studying the island's rich biodiversity. As the violence subsided, several researchers told *Science* about the harrowing events and their fears for the future of the African nation's unique natural resources. "I had to jump over 12 manned barricades of burning tires and then sneak through the public zoo to get to my house to pack," says Brian Fisher, an entomologist at the California Academy of Sciences and director of the Madagascar Biodiversity Center in Antananarivo, the nation's capital.

Until this year, Madagascar had been enjoying an unusual period of peace and stability. After being democratically elected in 2001, now-ousted president Marc Ravalomanana had championed science and conservation. During its 160 million years of isolation in the Indian Ocean, a strange menagerie of life evolved on the California-sized landmass, from unique noncactus prickly plants to the only populations of our primate relatives, the lemurs. But since arriving 2000 years ago, human colonizers have cut down more than 90% of the island's forests, threatening the flora and fauna with extinction.

The Ravalomanana government was credited with opening the doors wide to ecotourism. The lure of lemurs brought in hundreds of millions of dollars annually to one of the world's poorest nations. Madagascar's system of protected areas and national parks was expanded with the help of international support. In parallel, education and research have flourished, says Steven Goodman, a biologist at The Field Museum in Chicago, Illinois, who has lived and worked in Madagascar for more than 3 decades (*Science*, 26 September 2003, p. 1835). Goodman and his Malagasy collaborators have identified a string of vertebrate species new to science, including, just 2 years ago, "one of the most marvelous bats in the world" that climbs surfaces with suction-cup elbows.

The trouble started in January as the global economic downturn hit Madagascar, says Goodman. "There were a lot of people with little to no means to feed their families, tourism was close to zero, and organized crime had notably grown," he says. Some of Ravalomanana's decisions came under harsh criticism, such as his leasing of half of Madagascar's arable land to a Korean company for corn and palm oil production. Ravalomanana tried to quell criticism by partially shutting down television and radio stations, but protesters took to the streets of Antananarivo, and dozens were killed in clashes with the police. After the city's mayor, Andry Rajoelina, called on the president to resign, Ravalomanana sacked him. Madagascar quickly descended into chaos.

"The situation has gone from bad to worse," wrote Goodman in an e-mail to *Science* on 17 March, the day the president resigned. "Gun fire around the house, raging fires in the neighborhood, and wide-scale looting and pillaging. … Several students have been killed." Fisher and other scientists were stranded in the turmoil after returning from fieldwork. On the way to the airport to flee the country, Fisher had "a close call" with a rock-throwing mob but escaped on a motorcycle. Nearly 200 deaths have been confirmed, but the true number is "far more than reported in the local and Western press," says Goodman, who remains in the capital.

When the country's military leaders declared support for the opposition last week, Ravalomanana resigned. Rajoelina, who had become the public face of the opposition, was installed as president and then dissolved Parliament. Supporters of Ravalomanana have held protest rallies, but little violence has been reported. On 21 March, Madagascar's highest court declared Rajoelina's leadership legal, although the 34-year-old former disc jockey is too young to hold office according to Madagascar's constitution. As *Science* went to press, the former president remained in hiding.

Biological riches. Steven Goodman holds newly discovered bat species of Madagascar.

Fisher says the coup derailed plans for donors to visit the island, placing his center in financial risk. "The big fear now is that this year's tourism revenue for Madagascar will be completely wiped out," adds Christopher Raxworthy of the American Museum of Natural History in New York City, who studies the island's unique reptiles and amphibians. "Sadly, any decrease in income from tourism may increase human

CREDITS (TOP TO BOTTOM): TANTELY NIRINA RANRIAMBOLOLONA; J. BOHANNON/*SCIENCE*

Published by AAAS


Re-evaluating state stem cell initiatives
1660

Science by the numbers
1662

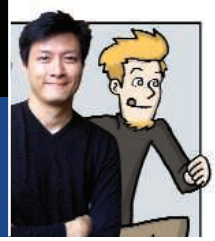
Seeing the humor in grad school
1668

pressures on the local natural resources."

A more immediate threat to the environment comes from "people taking advantage of a power vacuum," says An Bollen, a biologist who coordinates an international conservation organization based in Toamasina in eastern Madagascar called the Madagascar Fauna Group. Marojejy National Park has been shut down due to "looting and destruction," according to its Web site. It reports that "gangs of armed men (led primarily by foreign profiteers in conjunction with the rich local mafia) are plundering the rainforests. … Most worrisome is the well-being of the highly endangered Silky Sifaka," a lemur that exists only in the park's forests and the surrounding area.

Madagascar's new government is being greeted with international condemnation, and most nonhumanitarian aid to the nation has been frozen. In terms of conservation, "it is unclear what the new government will bring," says Bollen, noting that the new environment minister is a former employee of a major nickel-cobalt mining company. **–JOHN BOHANNON**

GLOBAL WARMING

Arctic Summer Sea Ice Could Vanish Soon But Not Suddenly

Global warming is causing trouble for polar bears, no doubt about that, but how long the bears will have floating ice for summer seal hunting has remained unclear. Just a few years ago, it looked as if summer ice would still be around at the end of the century, but when ice melting took a sharp turn for the worse in 2007, some scientists started talking about catastrophic "tipping points" and a possible imminent demise of summertime ice.

After paring their suite of 23 climate models down to the best half-dozen, two researchers now say with new confidence that summer ice will most likely disappear around 2037. But none of the select models predicts a tipping point—a sudden jump to an ice-free summer Arctic. "They've identified the most credible models," says polar researcher John Walsh of the University of Alaska, Fairbanks, and "the most realistic models are the most sensitive to future [greenhouse] changes." All in all, it's bad news for the bears.

The new model study recognizes that not all climate models are created equal. For the 2007 Intergovernmental Panel on Climate Change (IPCC) assessment, modelers around the world ran 23 different climate models with and without rising greenhouse gases. The fate they predicted for arctic ice ranged from complete loss in the summer by 2020 to only slight losses by 2100, and almost everywhere in between. Modeler Julienne Stroeve of the National Snow and Ice Data Center (NSIDC) at the University of Colorado, Boulder, and her colleagues shrank the IPCC list to the 13 models that did a reasonable job of reproducing the observed slow decline of the extent of summer sea ice, but that still left them with a considerable range of losses by 2100.

To further narrow the possible outcomes, arctic researchers Muyin Wang of the University of Washington, Seattle, and James Overland of the Pacific Marine Environmental Laboratory in Seattle added another constraint: Usable models must reasonably reproduce the ups and downs of sea ice area from summer to winter and back. As they report in a paper in press at *Geophysical Research Letters*, that shortened the list to six models. "That's a very important improvement," says Wang, because those models should have the most realistic response to the rising heating by the strengthening greenhouse.

Wang and Overland then examined each simulation to see how many years it took summer sea ice to dwindle from its current 4.6 million square kilometers to an essentially ice-free summer Arctic Ocean. The "expected time frame" for ice-free summers is about 30 years. Ice-free conditions aren't likely before the late 2020s, according to these models. And none of them go ice-free in a single, abrupt jump; there are no tipping points.

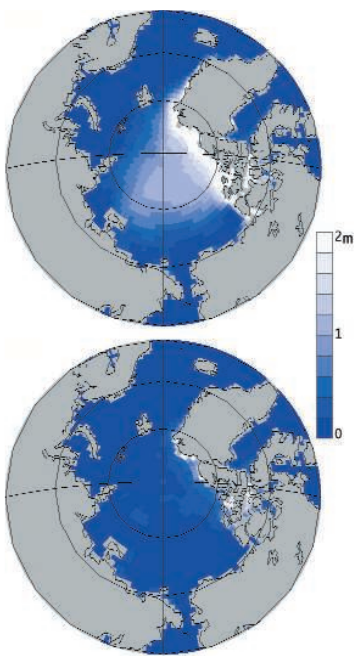

Won't be long. The six best climate models available show global warming clearing the Arctic Ocean of summer ice (*top*) within about 30 years (*bottom*).

Researchers have long worried that the models don't have ice tipping points because they simulate some key physical process poorly. In the real ocean, for example, a decline in ice coverage decreases the amount of solar energy that ice reflects back to space while increasing the amount of heat absorbed by the darker open water. This ice-albedo feedback, if unopposed, could drive the system past a tipping point, but ice physicists Ian Eisenman of the California Institute of Technology in Pasadena and John Wettlaufer of Yale University believe they have discovered what tends to counteract it.

In the 6 January issue of the *Proceedings of the National Academy of Sciences*, Eisenman and Wettlaufer report an underappreciated ice-thickness feedback that strongly opposes the ice-albedo feedback. When added summer heat thins the ice, the ice can grow back in winter all the faster because the ocean can lose heat faster through thinned ice. "The harder you kick the ice, the harder it tries to get back to where it was," says Eisenman. "The models do agree with our claim" that the competition between the two feedbacks that will hold off a tipping point, he says.

The loss of summer sea ice in 25 or 30 years "is probably the best estimate that models can come up with at the moment," says sea ice specialist Josefino Comiso of NASA's Goddard Space Flight Center in Greenbelt, Maryland. It coincides with the central tendency of expert opinion, adds Walsh. "We're resigned to losing the ice," says sea ice specialist Mark Serreze of NSIDC. And it looks as if that will happen sooner rather than later.

–RICHARD A. KERR

CREDIT: AGU/GRL

U.S. SCIENCE

OSTP, NOAA Chiefs Finally Get a Chance to Lead

Two major players on the Obama Administration's science team donned their uniforms last week, 3 months after being nominated for their prospective positions.

Physicist John Holdren and marine biologist Jane Lubchenco were confirmed by the Senate on 19 March and immediately took up their respective posts as director of the Office of Science and Technology Policy (OSTP) and as administrator of the National Oceanic and Atmospheric Administration (NOAA). Their confirmations had been held up by an anonymous senator or senators. The matter was resolved as part of congressional approval of the 2009 federal budget, and both scientists were approved without a recorded vote.

On the job. John Holdren and Jane Lubchenco are now official.

Lubchenco says she's moving "on fast forward" to get a handle on the $4 billion agency she'll be steering. Speaking this week with reporters, Lubchenco said she had yet to be briefed on some of the thorniest issues facing the agency, including fixing NOAA's ailing satellite program, tackling overfishing along the nation's coasts, and reviewing a budget she called insufficient for the task at hand. She also pledged support for the agency's extramural research efforts, although she said she had yet to calculate the ideal ratio of support for that enterprise. "NOAA has a strong track record on science," she says. "We are going to build on that track record."

Although the confirmation delay had prevented her from taking office, she says she has advised the White House on a number of issues, including working with Holdren on a 9 March presidential request to OSTP to review scientific integrity practices across the government (*Science*, 13 March, p. 1412).

Holdren's staff did not respond to an interview request. In a short video message released after he was confirmed, however, the former Harvard University physicist said he was eager to provide the president "all the clear and objective advice he needs about the scientific and technological aspects of all the issues on his plate." As examples, he cited the president's three priorities in his proposed 2010 budget: the economy, health care, and education.

With these two jobs now filled, the major remaining vacancies among science agencies are the heads of NASA, the National Institutes of Health, and the National Institute of Standards and Technology. **–ELI KINTISCH**

ENERGY RESEARCH

Koonin Tapped at DOE, Which Lays Out New Spending

A top theoretical physicist turned energy guru has been chosen as undersecretary of science at the Department of Energy (DOE), which this week announced how it would distribute $1.2 billion among its 10 national labs and to universities around the country.

On Friday, the president nominated physicist Steven Koonin, former provost of the California Institute of Technology and currently chief scientist at oil giant BP. If confirmed by the Senate, Koonin would replace Raymond Orbach as head of DOE's $4.8 billion Office of Science. Chu and Koonin are no strangers: In addition to their long California résumés, the two physicists teamed up on a BP-funded $500 million research program on biofuels and other new energy sources at DOE's Lawrence Berkeley National Laboratory (LBNL), which Chu led before coming to Washington.

The two Steves. Chu (*left*) hopes Koonin will join him at DOE.

Congress made Koonin's job a bit easier last month when it passed the $787 billion American Recovery and Reinvestment Act, otherwise known as the stimulus bill. The package gives DOE's Office of Science $1.6 billion to address a backlog of construction and research projects, and almost every lab comes away with something (www.tinyurl.com/cf9klp).

The biggest single chunk of cash—$150 million—will go to Brookhaven National Laboratory to speed up construction of its National Synchrotron Light Source II. The Pacific Northwest National Laboratory gets $124 million to equip an environmental molecular sciences lab and a climate research facility. LBNL gets $115 million for two facilities to support users of its Advanced Light Source, and Oak Ridge National Laboratory gets $71 million for a multipurpose facility to house its chemical and advanced materials research programs. SLAC National Accelerator Laboratory will receive $68 million for equipment and modernization, and the Thomas Jefferson National Accelerator Laboratory gets $65 million to complete an upgrade of its Continuous Electron Beam Accelerator Facility. Some $69 million will help to triple the speed of a 10-gigabit-per-second data network serving all the national labs. The eventual goal is a 100-gigabit network also connecting major universities. The NOvA neutrino experiment managed by Fermi National Accelerator Laboratory in collaboration with the University of Minnesota will get a $50 million boost.

The stimulus funding also provides $277 million to establish roughly a dozen Energy Frontier Research Centers. DOE has already reviewed 260 applications for the new program, which focuses on using basic science to tackle challenges such as solar power or hydrogen energy. Each center, a collaboration between universities and national labs, is expected to receive from $2 million to $5 million for up to 5 years. In addition, DOE's high-energy physics and fusion research programs will get $90 million on top of their regular budgets for competitive grants. **–DAN CHARLES, ELI KINTISCH, AND JEFFREY MERVIS**

CREDITS (TOP TO BOTTOM): SAM KITTNER/KITTNER.COM; STEVE MCCONNELL/UC BERKELEY

Published by AAAS

RESEARCH FUNDING

U.K. Funder Accused of 'Blacklisting' Repeatedly Unsuccessful Applicants

Do scientists have a fundamental right to apply for government money, even if their grant proposals are regularly rejected? That's one of the issues at the heart of a fiery debate now taking place in the United Kingdom, where a major funding agency has just announced it will ignore submissions from "repeatedly unsuccessful applicants," a policy that could exclude 5% of its previous grant applicants. The U.K.'s Engineering and Physical Sciences Research Council (EPSRC) says the move is designed to ease the burden on volunteer peer-reviewers, but outraged researchers have called the change "blacklisting" and "scientific McCarthyism."

"We don't think there's any precedent elsewhere," says organic chemist Joe Sweeney of the University of Reading, who started an online petition to repeal the EPSRC policy. More than 1200 scientists—including several fellows of the Royal Society, Britain's academy of science—had signed on by early this week. In a move that could thwart EPSRC's aims, organic chemist Philip Page of the University of East Anglia in Norwich says he and other scientists will strike: "A number of people will not referee proposals while this policy is in place," says Page.

EPSRC is the largest U.K. funder of engineers and physical scientists, handing out grants totaling more than £475 million in 2007–08 to more than 3200 researchers. It receives the most grant proposals among the seven research councils, and the number has grown dramatically in recent years, says David Reid, EPSRC's head of communications.

After rejecting options such as charging for proposal submissions or placing quotas on institutions, on 12 March the council announced a new policy to ban from any EPSRC funding consideration, for a year or even longer, any principal investigators who have "Three or more proposals within a 2-year period ranked in the bottom half of a funding prioritisation list or rejected before panel [without review]; AND An overall personal success rate of less than 25%." EPSRC notes that this policy should exclude about 200 to 250 people and is retroactive: Letters to those excluded go out on 1 April, and their proposals won't be considered after 1 June.

Reid says the idea is to weed out the small number of scientists who submit multiple, poor applications; the estimated 5% excluded submit 10% of applications, says EPSRC. "They're operating a scattergun approach" and placing a "huge burden" on the peer-review process, Reid says. He adds that EPSRC consulted with university officials who expressed a desire to know which researchers need mentoring to help them obtain funding.

Yet some U.K. scientists argue that any such exclusion policy is fundamentally unfair and that far more than 5% of EPSRC applicants will be affected by what could be a career-ending decision. Page says that whether a typical proposal ends up in the "bottom half" of the rankings is "rather a lottery." A more defensible criterion, he says, would be to use the quality cutoff line many panels already employ to indicate weak proposals that are not deserving of a funding ranking. Even that would disturb Peter Lawrence, a Royal Society fellow at the University of Cambridge who signed the online petition. Excluding people based on past proposal failures "doesn't support the unpredictability of original research," he says.

For the moment, EPSRC is vigorously defending its new policy and arguing that the online petition and many critics misstate its new measures. Reid adds that the council will review the impact of the changes after a year or so. This is part of an "evolving program to reduce the [peer-review] burden," he says.

–JOHN TRAVIS

CREDIT: (TOP) MICHELLE PADDACK

New and improved? Many U.K. scientists don't agree that EPSRC's new funding policies will help them.

ScienceNOW.org

From *Science*'s Online Daily News Site

Super hard drives coming soon? For those whose computer hard drives can never hold too much data, here's some good news. In *Nature Photonics*, researchers report finding a way to potentially boost disk capacity to 10 times the current theoretical limit—and without a correspondingly astronomical increase in cost.

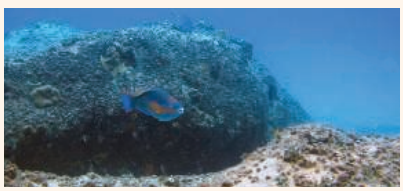

Bad for coral, bad for fish. Populations of Caribbean reef fish have plummeted between 32% and 72% over the past decade in response to widespread disappearance of coral, according to a new study published in *Current Biology*. If the trend continues, it could worsen the already unprecedented deterioration of reef habitats and disrupt Caribbean countries that rely on the fish as a source of food and income.

Happy music has worldwide appeal. Feeling a little blue? Why not kick back and put on Bobby McFerrin's "Don't Worry, Be Happy" or Queen's "We Are the Champions"? Chances are you'll feel more cheerful in no time. But what about people who have never been exposed to Western music? A new study, published in *Current Biology*, concludes that even they can tell the difference between a happy and a sad tune.

Earliest corn discovered. Pity the first corn eaters. The ancestor of the plant that gives us its succulent yellow kernels is an unappetizing grain known as teosinte, whose ears harbor only five to 12 rock-hard grains. Reporting in the *Proceedings of the National Academy of Sciences*, researchers say they have now found the earliest known traces of corn—or maize—at a site in central Mexico dated to nearly 9000 years ago. Although this ancient plant was probably tough on the teeth, the find suggests that early farmers did indeed eat it—rather than turn it into alcoholic beverages, as some researchers have suggested.

Read the full postings, comments, and more on **sciencenow.sciencemag.org**.

Published by AAAS

COGNITIVE SCIENCE

Twins May Think Alike Too, MRI Brain Study Suggests

Research on cognitive abilities has generally been split into two noncommunicating camps: cognitive scientists who look for strategies or brain regions that all humans employ for particular tasks, and intelligence researchers who are interested in individual differences.

On page 1737, a European team uses brain imaging with twins to achieve a rare fusion of the two approaches. The researchers show that different people may use different strategies to accomplish the same mental task, and that genes influence the type of strategy used.

A team led by Jan Willem Koten Jr. of RWTH Aachen University in Germany tested 10 sets of siblings, each consisting of a pair of male identical twins and a nontwin brother. While their brains were being scanned in a functional magnetic resonance imager (fMRI), they were asked to memorize a short span of digits. They were then given a "distraction" task to befuddle that memory: either a simple arithmetic problem (2 + 4 = 7, yes or no?) or instructions to categorize a picture of an object. They were then shown a number and asked if it was among the numbers in the memory task. All these chores took at most 7.5 seconds.

The team found that, when distracted by the photo-categorization task, many men used brain areas associated with language for the digit-memory task. When the distracter is the numerical problem, which also employs language areas, says Koten, "then the verbal loop gets interrupted," causing the original memory to rapidly decay. The point at which the subject has to judge whether he's seen a digit before is where "the genetic influences on brain activity starts to come out," says Koten. Subjects who used language areas when encoding the numbers took longer to come up with the answer than did those who resorted to a "visual-spatial memory system"—akin to counting on fingers—that the arithmetic task doesn't interfere with.

The scientists compared twins, who are 100% genetically alike, with each other and with their brothers, who share on average 50% of their genes. Twins used the same strategy more often than brothers did in the roughly 50 trials, suggesting that "there are qualitative differences in how individuals think, and these differences have a substantial genetic component," Koten says. He says the team was able to reliably estimate heritability even in this small sample by doing two identical scanning sessions with each of the 30 subjects. Estimated heritabilities ranged from 60% to 90% in the three phases of the task. Koten says such "highly individualized" responses "are of key importance for a proper understanding of the biological basis of individuality."

In sync. Identical twins tended to use the same strategies when faced with memory tasks.

CREDIT: COURTESY OF JAN WILLEM KOTEN

Behavioral geneticist Nick Martin of the Queensland Institute of Medical Research in Brisbane, Australia, says "I think this will prove to be a real watershed in how we think about brain activity. There is obviously a high degree of individuality in how the brain responds to external stimuli, and this is strongly genetically influenced." He adds that "studies focusing only on regions identified by averaging fMRI across individuals will miss the activity in regions which are even more important to particular genotypes."

Working memory of the type measured in this study is already known to have high heritability, notes brain imager Richard Haier of the University of California, Irvine, School of Medicine. Now, he says, the group has shown that the accompanying brain activation is heritable, too. "This combination of neuroimaging and genetic analysis," he says, "marks the beginning of new efforts to explain, rather than explain away, individual differences in cognition and intelligence."

–CONSTANCE HOLDEN

PHYSICS

Oddly, Too Much Weirdness Slows a Quantum Computer Down

Physicists dream of creating quantum computers that can swiftly solve problems that overwhelm the best conventional computers. Schemes for making the devices rely on a mysterious quantum connection called "entanglement," through which a measurement made on one particle can instantly affect the state of others. But too much entanglement is bad for a quantum computer and makes it run only marginally faster than a conventional one, a new analysis shows. "A lot of people, including myself, were surprised by this," says Richard Jozsa, a mathematical physicist at the University of Bristol in the United Kingdom "It's a thought-provoking result."

If a quantum computer could be built, it would outpace a conventional one by crunching many numbers at once. The trick is to replace a computer's bits, which can be set to either 0 or 1 to spell out binary numbers, with "qubits" that can be set to 0 and 1 at the same time. A qubit could be an ion or other particle that can spin in either of two directions, up or down, or, thanks to quantum weirdness, both ways at once. It's because qubits can express both values at once that a quantum computer could process many numbers simultaneously.

To achieve maximum efficiency, however, the qubits would have to be entangled. Suppose each of 100 ions is put in a both-ways state. If one ion is measured, then its state will instantly and randomly "collapse" so that it is found to be spinning either up or down. But the 100 ions can be entangled so that their undetermined directions are correlated. For example, they can be linked so that if one ion is measured and collapses into the down state, all the others will instantly collapse into the down state, as well.

The correlations can be more complicated than all the spins pointing in the same direction. They are also probabilistic and can be less than 100%, so, unlike pregnancy, entan-

Published by AAAS

BIOMEDICAL RESEARCH

Hughes Backs Institute at Epicenter of HIV and Resistant TB

When HIV/AIDS researcher Bruce D. Walker and tuberculosis investigator William R. Jacobs made their pitch for a new research center in South Africa 2 years ago to the Howard Hughes Medical Institute (HHMI), the concept was foreign in more ways than one. HHMI had never built an institute outside the United States, and no other research center anywhere had focused its work entirely on the two diseases. But, says HHMI President Thomas Cech, "their logic was compelling." The two researchers and their South African collaborators argued that medical science would benefit from a direct engagement with the epidemics of HIV/AIDS and drug-resistant TB in a region that has been devastated by them. HHMI bought the idea.

Last week, Cech joined Walker, Jacobs, and South African researchers in announcing the KwaZulu-Natal Research Institute for Tuberculosis and HIV (K-RITH), a $60 million project on the campus of the Nelson R. Mandela School of Medicine at the University of KwaZulu-Natal (UKZN) in Durban. The medical school—the only one in South Africa where blacks were allowed to study during the apartheid years—already has a modern HIV/AIDS research wing funded by the Doris Duke Charitable Foundation.

"There is no better place on Earth to investigate the confluence of HIV/AIDS and drug-resistant TB," says molecular immunologist Malegapuru Makgoba, vice chancellor of UKZN. KwaZulu-Natal province is the epicenter of both epidemics in South Africa, which has the most HIV/AIDS cases (5.4 million) and one of the world's highest per capita rates of TB. What Walker calls a "cataclysmic convergence" of the two epidemics has been further complicated by the emergence in 2005 of extensively drug-resistant TB (XDR-TB) in the province's town of Tugela Ferry; it has since spread through much of the country (*Science*, 15 February 2008, p. 894). This week, the World Health Organization reported that one out of four TB deaths is HIV-related—twice as many as previously recognized.

The six-story K-RITH center will house two floors of biosafety level 3 labs equipped for TB research. "We have a unique opportunity here to study the capacity of the TB bacterium to become more resistant and more virulent," says acting director A. Willem Sturm, who has led South Africa's genetic analysis of XDR-TB. "But first we need rapid diagnostic tests" to determine drug resistance.

That's where Jacobs and his lab at the Albert Einstein College of Medicine in New York City come in. Using tests that employ engineered bacteriophages—viruses that infect bacteria—Jacobs believes his group will be able to reduce the time it takes to diagnose resistant TB from 4 weeks to a matter of days.

The HIV/AIDS team will pursue parallel objectives. Walker, based at Massachusetts General Hospital in Boston and Harvard University, also directs the HIV Pathogenesis Program in Durban. His research group will focus on the immune response to TB in HIV-infected people. "Understanding how the immune system responds to TB will be essential" in developing vaccines for TB and HIV, he says. Another research team, led by UKZN epidemiologist Salim Abdool Karim, will study patterns of TB latency and reinfection.

African venture. Outgoing HHMI President Cech (*left*) backed institute in South Africa, shown above in an artist's rendering.

Cech says the institute has made a 10-year commitment to K-RITH. It will take more than a year to build the new center, starting in September. In the meantime, HHMI has awarded seed grants totaling $1.1 million to scientists who will be involved in K-RITH to jump-start research, as well as $3 million in grants to build temporary labs.

–ROBERT KOENIG

CREDITS: GARTH DYER/FGG ARCHITECTS; (INSET) BRUCE WELLER FOR HHMI

glement admits of degrees. Physicists know that entanglement is essential to enabling a quantum computer to take far fewer steps than an ordinary one to handle certain daunting calculations—such as factoring a huge number. They had assumed that more entanglement would yield greater efficiency.

Not so, say David Gross, a theorist at the Technical University of Braunschweig in Germany, and colleagues. To make that case, they considered a newer variant called "measurement-based quantum computing." Instead of using a computer with quantum circuits, this theoretical scheme combines an ordinary computer and an external string of qubits in a specially chosen entangled state, such as one known as a "cluster state." To perform a computation, a user makes successive measurements on the qubits and feeds each result back through the computer to determine how the next measurement should be made. Theorists have shown that, given the right arcane algorithm, the measurement-based scheme can do anything quantum circuits can.

But if the user sets the qubits to an even more entangled state, Gross and colleagues show, the correlations among them become so convoluted that the measurements yield an essentially random string of 0s and 1s. So in principle, a user could get the answer almost as easily by scrapping the qubits and tossing a coin instead, the researchers report in a paper in press at the journal *Physical Review Letters*.

Unlike the measurements, the coin flips aren't guaranteed to yield the right answer. But the results can be checked very quickly—it's much easier to check that $53 \times 61 = 3233$ than it is to factor the original number—and the process could be repeated until it works. The randomness of the qubits ensures that it won't take many iterations to hit on the solution. The quantum scheme would still be faster, but not exponentially so. That's key, as producing such a large advantage is the whole point of quantum computing.

Physicists have only a poor understanding of how entanglement and computational efficiency are connected, so it's valuable to know that more entanglement doesn't imply greater speed, says Norbert Schuch of the Max Planck Institute for Quantum Optics in Garching, Germany. "It certainly tells us how they're not related," he says, "which, given the difficulty of the question, is worth quite a lot." **–ADRIAN CHO**

Published by AAAS

STATE STEM CELL INITIATIVES

CIRM Close-Hauled, Seeks Bonds to Sustain Headway

With dramatic shifts in both the economic and political landscape for stem cell research, the California Institute for Regenerative Medicine (CIRM)—a state initiative set up to avoid restrictions on federal research laid down in 2001 by President George W. Bush—is scaling back, rethinking its priorities, and looking at how to mesh its activities with those that will soon be funded by the National Institutes of Health (NIH). The latter is somewhat tricky, as exactly what types of research NIH will support now that President Barack Obama has rescinded the Bush restrictions with his executive order (*Science*, 20 March, p. 1552)—and how much of the $8.2 billion in NIH's stimulus package will go into stem cell research—remain unclear.

The Center for Genetics and Society, a public interest group in Oakland, California, has hinted that the state may find better ways to spend its money now that the economy is tanking and NIH is no longer inhibited by the Bush policy. But scientists point out that as long as NIH has to comply with the Dickey-Wicker Amendment prohibiting research with human embryos, federally funded researchers will have to look to private or state-supported sources like CIRM for new ES cell lines. They also argue that in California, as elsewhere, a strong local establishment makes scientists more competitive when it comes to getting federal grants.

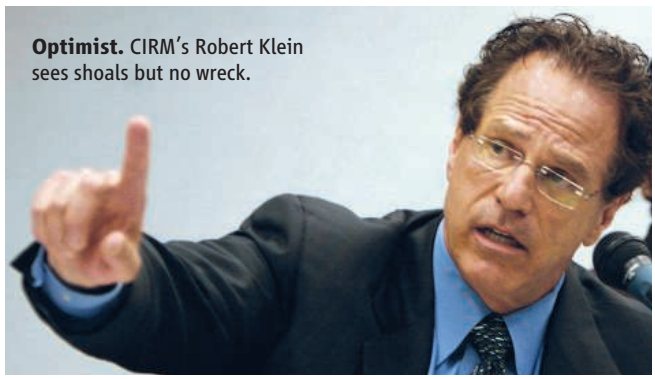

Optimist. CIRM's Robert Klein sees shoals but no wreck.

Even so, CIRM is simultaneously scrambling to replace a shrinking pot of money from state bond sales and shifting its emphasis from basic research toward bringing stem cell therapies to the clinic. Board chair Robert Klein says he sees the shift as particularly timely to complement NIH's expanded focus on basic stem cell research.

Until recently, things had been looking rosy for CIRM. After being delayed by lawsuits, the agency roared into action in the spring of 2006 with the promise of $3 billion over 10 years from the sale of state bonds ($250 million worth have been sold to date; CIRM got another $250 million as an advance loan on sales). So far, the agency has spent or promised $690 million, according to Vice President for Operations John Robson. That includes $271 million in grants awarded last spring for construction of new facilities at universities, $95 million for grants to train undergraduates, grad students, and postdocs, and close to $115 million in salaries and research awards for new faculty members. One hundred twenty million dollars has been committed to basic research.

Now, says Robson, CIRM has a cash-flow problem. State bond sales have been frozen, and CIRM "would still need another $112 million" to fulfill existing obligations up to the end of 2010. Before the crash, CIRM had anticipated committing $375 million between now and December 2010, says Robson; now, with some belt-tightening, $220 million seems more realistic. At its 12 March board meeting,

Most State Stem Cell Efforts Staying Afloat

In addition to California, several states have made serious attempts to encourage stem cell research. Although some are tightening their belts, these programs generally seem to be holding their own in this uncertain environment—at least for now.

An exception is **New Jersey**. In 2005, it became the first state to finance stem cell research, with a $10-million-a-year grants program. But the state's ambitions have hit some serious snags.

In November 2007, voters delivered a surprise rejection of a $450 million bond referendum to finance research and lab construction. Now, construction of a $150 million research facility for the Stem Cell Institute of New Jersey—for which ground was broken a month before the referendum—has had its budget cut and is on hold indefinitely. Then last month, Governor Jon Corzine zeroed out the annual $10 million for the grant program. Martin Grumet, director of the Rutgers Stem Cell Research Center, says there's still some hope: The governor plans to propose restoring grant money in his next budget.

In **Connecticut**, legislators voted in 2005 to invest $100 million in stem cell research over 10 years, starting in fiscal year 2007. So far, the state has given out $30 million in grants and shows no sign of stopping, says David Goldhamer, associate director of the University of Connecticut Stem Cell Institute. The current assumption is that a full $10 million will be available for the next grant cycle, to be announced at the end of March.

Maryland is committed to becoming "the biotech state," say Karen Rothenberg, dean of the University of Maryland law school, so the state is unlikely to back off its stem cell commitments. The Maryland Stem Cell Research Commission, set up in 2006, has overseen the funding of $36 million in grants so far. But overall funding may drop for a few years: Governor Martin O'Malley has proposed $18 million for stem cell research this year—compared with $23 million last year.

Massachusetts Governor Deval Patrick signed the Massachusetts Life Sciences Initiative last spring, which directs $1 billion in state funds toward biotechnology, including stem cell research, over a decade. Total investments to date amount to $33 million; $11 million of that has been stem cell–related, primarily to support a stem cell registry and bank at the University of Massachusetts Medical School. With the state facing a budget shortfall of $1.4 billion, the Life Sciences Initiative is slated to get a maximum of $20 million instead of the planned $25 million in fiscal 2010.

New York appears to be doing well despite the dour budget climate. Two years ago, the legislature created the Empire State Stem Cell Trust to dispense some $600 million to stem cell research over 10 years. The first grants, $14.4 million for research and training at 25 institutions, were awarded in January 2008. Governor David Paterson has proposed that New York State Stem Cell Science, the granting body, give out $50 million as planned in the next fiscal year. Scientists

Published by AAAS

CIRM decided to pull back on some plans—most notably, $40.6 million slated for training grants for undergraduates and graduate students will now shrink to $7 million in this period. Agency officials hope to restore that funding when the economy revives.

Until then, Klein has a bold plan to save the day. He recently obtained permission from the state treasurer to sell $400 million in bonds to private investors over the next 12 months. (Although state bonds are moving again, CIRM's would have low priority.) The perennially optimistic Klein thinks he'll find plenty of takers. "We're structuring it not as a donation but [as] an investment," and the guaranteed 5% interest rate should attract groups that fund biomedical research, he says. Robson adds that other CIRM officials "are not as optimistic as Bob" about finding buyers, but they should be able to carry through their modified plans if sales bring in at least $200 million. Even then, he says, grants for basic research will have to be reduced, from $60 million to $20 million, until at least the end of 2010.

CIRM's shift in focus from basic to translational research began last year, when Alan Trounson took the helm, and is now accelerating. The agency plans to throw major resources into the "valley of death"—the limbo in which promising research often languishes because of a lack of resources to bring it to the point at which it can be tested in clinical trials. A $210 million, 4-year program of "disease team grants," to be awarded this year, is the centerpiece of this thrust. The program will entail perhaps 10 large grants to teams combining academic and industrial researchers working on a specific stem cell product for, say, Parkinson's disease. The goal is to speed work to the point at which the team can apply to the U.S. Food and Drug Administration for a New Drug Application within 4 years. Under this program, biotech companies will receive loans, not grants, to ensure that companies will retain intellectual property. Klein wants to get those loans guaranteed by the federal government under the stimulus package.

Some scientists worry that the emphasis on applications is coming too soon. "I am concerned that some of this rush to the clinic is premature," says Arnold Kriegstein of the University of California, San Francisco. "My concern is … they're taking risks with potentially very little gain."

Officials appear confident that they can hang on until the economy picks up. "I don't think state initiatives will wither" despite the economy, says James Kovach, head of the Buck Institute for Age Research in Novato, California, where construction of a new building has been delayed. He predicts the new presidential stem cell policy will have a "big effect" on the morale of scientists, especially young ones just choosing their careers, who will no longer have to wonder if it's safe to invest their futures in stem cell research. **–CONSTANCE HOLDEN**

in New York have also gotten a boost from the privately supported New York Stem Cell Foundation, which supports a lab on the campus of Columbia University.

Wisconsin, where it all began with James Thomson's successful cultivation of human ES cells, is aiming to have a major presence in the stem cell world, but not through direct state funding of research. Last year, ground was broken for the Wisconsin Institutes for Discovery, part of a $750 million multiyear strategy spearheaded by Governor Jim Doyle to make the state a leader in biotech and health sciences. But the state's direct involvement in stem cell research has been limited to $10.4 million in grants and loans to stem cell companies.

Former **Illinois** governor Rod Blagojevich signed an executive order in 2005 to create the Illinois Regenerative Medicine Institute. John Kessler, director of Northwestern University's Feinberg Clinical Neuroscience Research Institute, says the state gave out more than $10 million in grants in the subsequent 2 years, but the legislature never followed up with more money. Now, he suspects, "the time has passed."

–CONSTANCE HOLDEN

CREDIT: CALIFORNIA INSTITUTE FOR REGENERATIVE MEDICINE

Dream house. Construction on some facilities is delayed, including a global stem cell research center at the Buck Institute in California.

ScienceInsider

From the *Science* Policy Blog

Scientists around the world have been struggling to help a virologist who might have been **exposed to the Ebola virus**. An unnamed scientist at the Bernard Nocht Institute for Tropical Medicine in Hamburg, Germany, pricked her finger with a syringe during an experiment earlier this month. A team of world experts on the deadly disease eventually chose a new type of experimental vaccine developed in a Canadian lab and previously tested on monkeys. In 2003, researchers showed that a single shot of the virus offers protection in monkeys even if administered after exposure to Ebola. As of press time, it was still unknown whether the researcher had been infected.

The mad scramble for **millions of dollars in stimulus funds** has strained the Web site that handles federal grants, Grants.gov. According to data released in March, the site is designed to accommodate 2000 users at a time but was getting requests for 50% more than that. As a result, on 16 March, the system was down for 8 hours.

Dutch science minister Ronald Plasterk announced this week that the **170-year-old severed head of King Badu Bonsu II of Ghana** will be returned to the king's homeland after a writer found it preserved in formaldehyde in a medical research collection at Leiden University Medical Center last year.

The organizer of the **Copenhagen Climate Congress**, held earlier this month, debates with Stanford University ecologist Chris Field whether the event exaggerated the scientific consensus.

Finally, a public contest to name a new observatory module to be connected this year to the **international space station** has gone awry after Comedy Central's **Stephen Colbert** asked followers to add his name to the write-in ballots. His name came out on top, ahead of four suggested names.

For the full postings and more, go to **blogs.sciencemag.org/scienceinsider**.

Published by AAAS

Are You Ready to Become a Number?

Life could be a lot easier if every scientist had a unique identification number. The question is: Who should provide them?

A-1262-2007 AND A-1270-2007 ARE happy to be numbers—and they think you will be, too. The two clinical researchers at Maastricht University Medical Center in the Netherlands—named Jochen Cals and Daniel Kotz, respectively—find it bizarre that in this day and age, it can be next to impossible to find all the papers written by a given scientific author. Enter "Smith, J." into the PubMed search engine, they say, and you're deluged with more than 15,000 abstract titles. Good luck sorting out who wrote what.

That's why, in a paper in *The Lancet* last summer, the duo recommended that every scientist sign up for ResearcherID, a free system that promises to do away with such confusion by assigning every scientist a number. If everyone enrolled, they claimed, it would be much simpler to retrieve someone's complete publication record or to follow someone's career path. "It would make life a lot easier," says A-1262-2007.

He's not the only one to think so. With global scientific production growing fast, it's becoming harder and harder to tell authors apart. A universal numbering system could aid scientists trying to stay on top of the literature, help universities more readily track staff productivity, and enable funding agencies to better monitor the bang they're getting for their buck. An effective identification number might also make it easier to find information about an author's affiliations, collaborators, interests, or simply their current whereabouts.

ResearcherID, launched officially in January 2008, is only one in a wave of initiatives trying to pin a number on researchers. It's the creation of digital information company Thomson Reuters, which hopes to enhance the value of its paid services. Meanwhile, universities, librarians, national agencies, and publishers have devised, or are still hatching, potentially competitive identification systems, each with slightly different purposes in mind.

A-1262-2007 and A-1270-2007 endorsed ResearcherID not because it's perfect, they stress, but because it's the first global scheme ready and available now. But some predict that an ID scheme currently in development by CrossRef, an organization that unites more than 600 scientific publishers, has the potential to emerge as the dominant system, if only because publishers can force scientists to cooperate if they want to get their papers printed. Others say the U.S. National Center for Biotechnology Information (NCBI) may have a strong suit because it could incorporate its system into PubMed Central, the free and immensely popular database of medical and life sciences research at the National Institutes of Health (NIH), of which NCBI is part.

But for the moment, the plentitude of plans is a problem, some say, because to be truly useful, a numbering system has to be universal. "There are initiatives in four or five different silos," says Clifford Lynch, director of the Coalition for Networked Information (CNI), a Washington, D.C.–based group that promotes the use of technology in scholarly communication. "The lack of interconnection is striking."

Dr. Who?

The confusion over who's who in science has many sources. Common names such as James Smith and Mary Johnson are one—and with the number of published papers growing by an average of 3% annually, it's only getting worse. Some people also change their names when they get married or divorced, effectively splitting their scientific record in two. Adding to the confusion, journals have widely varying style rules for noting first names and initials. There's only one published scientist in the world with the last name of Varmus, for instance—that's

CREDIT: J. NEWFIELD/*SCIENCE*

Published by AAAS

Nobel laureate Harold Elliot Varmus—but his name appears on 352 scientific papers in six different ways.

Today's scientific explosion in Asia is fast exacerbating the problem. Names printed in Chinese characters are not usable in most online searching systems. For papers in English, Chinese authors usually "transliterate" their names using the so-called Pinyin system, which leads to many ambiguities. At least 20 different Chinese names, many of them common, are transliterated as "Wang Hong," for instance. Korean and Japanese names have the same problem. The Vietnamese use Roman script, but an estimated 40% of them have the family name Nguyen, which puts the Smiths to shame.

Of course, other information can help distinguish one author from another. The J. A. Smith who co-authored a 2008 paper on women, anger, and aggression is probably not the J. A. Smith who studied how to control the size of gold clusters in polyaniline. (And if you're in doubt, you can look at where they work.) Conversely, if the same e-mail address appears on two papers, it's a safe bet that they were written by one and the same researcher. But often, it's not so easy.

There are other problems that a numbering system could do away with, such as spelling errors. Of the more than 200 papers by French epidemiologist Antoine Flahault that are in one literature database, 14 are registered under the name "Flahaut." He can't wait to become a number.

Identity solution. Jochen Cals (*left*) and Daniel Kotz argue that a global system of unique identifiers, such as their ResearcherIDs, will help scientists better search research literature and work with colleagues.

CREDIT: APPIE DERKS/MAASTRICHT UNIVERSITY MEDICAL CENTRE

A fine balance

It's no surprise that Thomson Reuters was the first out of the gate with a worldwide system to assign unique numbers to researchers. Its livelihood, selling analyses of the scientific literature, depends on accurately matching papers with people.

Software can achieve that goal to a certain extent. So-called disambiguation algorithms can crawl through the literature and try to figure out which papers belong to the same author. They use names, as well as words in the abstract and all kinds of "metadata," such as affiliation, scientific field, co-authors, address, and citations. Thomson Reuters uses disambiguation software in its popular ISI Web of Knowledge. Reed Elsevier has built similar algorithms into Scopus, a rival literature search system launched in 2005.

At the moment, despite being two of the most popular literature search sites, neither PubMed nor Google Scholar uses disambiguation systems. Such software is expensive and time-consuming to develop, and the algorithms are far from perfect. They can incorrectly conclude that papers by different authors belong to one person, or fail to realize that various papers came from the same author.

There's a fine balance between these two types of mistakes, says Elsevier's Niels Weertman; if an algorithm reduces the number in one category, it usually increases the prevalence of the other. The software in Scopus errs on the side of caution; it only assigns two papers to the same person if it has a high degree of confidence. That means, for instance, that if you search for "Varmus" in Scopus, there appear to be two scientists by that name, one of whom wrote 338 papers and the other 14. When Weertman plugs his own last name into Scopus's name search field, the results include the works of Johannes Weertman and Julia Weertman, who have published many papers in the same journals and who are both professors emeriti at the department of Materials Science and Engineering at Northwestern University in Evanston, Illinois. (They're also married.) Their intellectual heritage is so hard to disentangle that Scopus cuts it up into more than 60 different clusters.

Because of such imprecision, disambiguation algorithms can't assign each scientist a single, unique number. (In Scopus, Varmus now has two numbers, whereas the Weertmans together have 65.) And that's why science information companies need human help. Elsevier, for instance, has staffers who "curate" the data by doing additional search work—mostly at offices in Asia—and manually merge separate groups of papers that belong to the same person.

Another strategy is to let scientists themselves take care of the job—after all, they should know which papers are part of their oeuvre. That's what motivated Thomson Reuters to launch ResearcherID. If you sign up—which some 30,000 scientists have done—you are first assigned a unique number. (Cals's number, A-1262-2007, means he was the 1262nd person to sign up in 2007.) Then you can "claim" the papers the company's software suggests are yours, coupling them to your number; you can also add others that the search engine missed—for instance because you wrote them before your divorce—or upload lists of your own citations.

For such a voluntary disambiguation system to work, scientists need an incentive, however. ResearcherID's carrot is that scientists can analyze citations to their papers, or place a "widget" on their Web site or blog that automatically retrieves a list of their most current papers whenever someone clicks on that page. They can also post a profile page with information about themselves on the ResearcherID site, much like people do on sites such as Facebook or LinkedIn. And like those sites, these services are free. Scopus currently doesn't allow users to register with a unique number, but it has plans to do so as well, Weertman says. Scientists can also suggest corrections to Scopus.

Publishers' plans

Some universities and research organizations have also begun setting up numbering systems. Part of the motivation stems from the advent of institutional repositories, online databases in which researchers can post copies of their papers and other data. Repositories are an answer to the pressure to make the fruits of taxpayer-funded research freely available to the public. They also help research managers track staff productivity and scientific impact. But again, achieving either goal is hard if you can't easily tell who's who—as the Weertmans at Northwestern demonstrate.

Several countries, meanwhile, have developed ID systems at the national level. In the Netherlands—a front-runner when it

comes to institutional repositories—every researcher has had a Digital Author Identifier (DAI) since 2007. The system was designed by SURF, a technology development foundation in which most research institutes and universities collaborate. So far, however, few Dutch scientists know about the numbers; Cals, for instance, wasn't aware he had one before he recommended ResearcherID in *The Lancet,* and he doubts that national numbers are very useful in an international endeavor such as science. But Gera Pronk, who helped develop DAIs, says national systems could eventually be knit together into an international one.

Another ID system is in the works at NIH, the biggest funder of biomedical research in the world. NIH wants to better track what its grantees are publishing, whether it's papers, book chapters, patents, or other output. NCBI Director David Lipman says his institute is consequently developing a unique identifier system for grantees that could later be expanded to all biomedical authors. Lipman has already discussed this idea with the editors of *Nature*, *Science*, and the *Proceedings of the National Academy of Sciences*, who have endorsed the concept.

Scientific publishers have their own reasons to support a numbering system: It would make it easier to do business. Giving scientists a number should speed up manuscript handling, help locate reviewers for a paper and detect conflicts of interest, facilitate royalty payments, and give marketing departments a leg up. For publishers, CrossRef was a logical candidate to develop a personal ID system; it already provides the infrastructure for Digital Object Identifiers (DOIs), the numbers that uniquely identify each published scientific article and that make it possible to click from one citation to the next on the Web.

The system now in development, called ContributorID, would ideally provide one identification with which a researcher could interact with any scientific publisher, whether as an author, journal editor, or reviewer, says CrossRef's Geoffrey Bilder. Whenever a research team submits a manuscript, each member would include a ContributorID number, establishing an enduring link to the paper's DOI. If publishers have trouble selling scientists on the system's benefits, such as doing away with a multitude of login data, they could bring out a stick: You can't publish without a number.

ContributorID would compete with Thomson Reuters and Elsevier, both of which are CrossRef members. Still, Weertman and James Pringle, vice president for product development at Thomson Reuters, say their companies won't necessarily oppose the plan, because there may be ways to cooperate. For instance, CrossRef is interested in using the disambiguation software developed by either company. And, Bilder points out, any universal numbering system, even one developed by a third party, could add value to both companies' products.

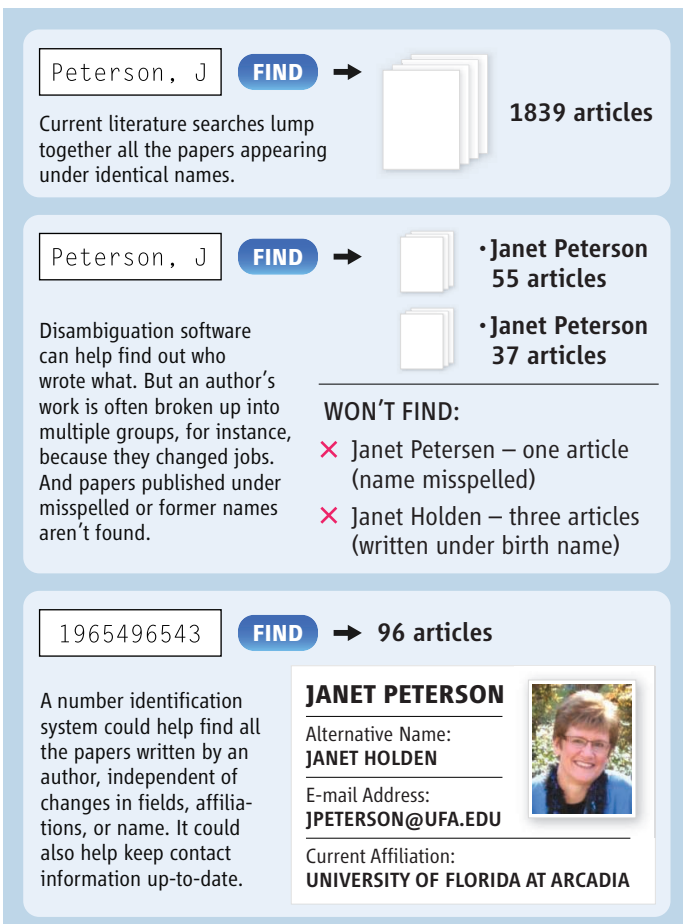

CREDIT: J. NEWFIELD/*SCIENCE*

Who controls it?

With so many initiatives, there's lots of discussion about which one could—or should—prevail. Because a numbering system would be for the ages, some say it shouldn't be in private hands or held by a single company. "I would be very worried if an individual publisher controlled this," says CNI's Lynch, adding that he would be "much more comfortable" if it were operated by NCBI or a broad group like CrossRef, whose membership includes so-called open-access publishers and scientific societies like AAAS, the publisher of *Science*. Given the power of CrossRef members to enforce the system, Lynch predicts that "it will probably carry the day." But Pronk says a publisher-operated system may remain unpalatable to universities; they are more likely to stick with their own, she says.

Meanwhile, some say the current lack of coordination is not just wasteful but could add to the confusion. Like people who have accounts at several social networking sites, researchers could end up with a whole series of numbers. Lipman says that may be the only way to make progress, however. "If we all had to sit down and talk until we agreed on a system, we would never get anything done," he says. And there's nothing wrong with letting a couple of systems evolve, he says; they can always be linked or merged later on.

Whichever system emerges victorious, it will still face problems. One is how to authenticate that the scientists claiming papers are who they say they are. ResearcherID does not currently verify that. "You can log in and claim every paper by Albert Einstein and have a lot of fun," Lynch says. Pringle says the system is "self-policing": If authors claim papers they have not actually written, others will protest soon enough, he says. Whether that really suffices remains to be seen. But for keeping track of NIH grantees or dealing with publishers, more secure identification systems are necessary, akin to those used for logging in to an online bank account.

Then there's the problem of what to do with the millions of old papers whose authors cannot help disambiguate their work because they are dead or no longer active. "Nobody has the time and money to do the detective work to get all the retrospective stuff 100% right," says Lynch. "It will always be a little probabilistic and flaky."

Unless that detective work was left to the wisdom of crowds, says Lipman. After all, if people are enthusiastic enough to set up Wikipedia pages about the most arcane topics, they may also be willing to help sort out who's who in 2 centuries of scientific literature.

–MARTIN ENSERINK

HYDROLOGY

California's Water Crisis: Worse to Come?

Perennially contentious issues of water management in California are being brought to a head by climate change and rising earthquake risks

California is now in its 3rd year of drought, and long-standing tensions over water are boiling to the surface. Last month, Governor Arnold Schwarzenegger declared a statewide water emergency, which could lead to widespread water rationing. Federal and state water managers announced that water deliveries would be drastically curtailed from the state's two major water projects, which serve tens of millions of people. Earlier this month, a pair of irrigation districts representing northern California farm communities pushed back, suing to keep the water flowing to their crops.

As bad as the situation is now, researchers warn that unless the state makes dramatic changes in the way it manages water, it's certain to get far worse. Especially vulnerable is the hub of California's freshwater system, the Sacramento–San Joaquin River Delta. A 2007 letter to Schwarzenegger written by members of a task force on the delta warned that it "is in crisis, and each day brings us closer to disaster."

The delta is the West Coast's largest estuary, channeling water from the northern Sierras into San Francisco Bay. Half of all Californians receive at least some of their water from two massive pumping stations in the southern part of the delta. One, the State Water Project, routes it to dozens of municipalities throughout northern and southern California. The other, the Central Valley Project, pipes it to farmers in the Central Valley, home to some of the richest farmland in the nation.

In February, Central Valley farmers were told that all water deliveries would be halted, and State Water Project managers said they would be forced to cut water deliveries to just 15% of normal. If those cuts come to pass, the upshot would likely be an economic hit of up to $2.8 billion and the loss of as many as 95,000 jobs, according to a new computer model developed by a trio of researchers at the University of California, Davis, led by resource economist Richard Howitt.

Heavy snows in the Sierras in late February and early March have brought some relief, boosting the region's snowpack back up to 90% of normal. "This will improve things slightly," says Howitt. Already, water levels in the state's reservoirs have increased markedly, and they are now at 70% of capacity for late March, according to the latest data from the California Department of Water Resources. Still, Howitt and others note, it will take a series of wet years to return to normal, and they warn that the delta's growing troubles threaten catastrophe.

Over the next few decades, a one-two punch of climate change and earthquakes is expected to change the delta dramatically. The delta contains some 1770 kilometers of levees holding back water from dozens of stadium-sized sunken "islands" inside which the land has subsided. By 2050, the chance of widespread levee failures is as high as 95%, due to runoff from the northern Sierras, which is predicted to be more concentrated in the late winter and early spring, and the increasing risk of earthquake, according to a report last summer by the Public Policy Institute of California (PPIC). If that occurs, salt water from the San Francisco Bay would rush in to fill the voids, dramatically increasing the salinity of water in the delta, possibly making it undrinkable. Adding sea-level rise to the equation—as climate models predict—brings the date of levee failures closer. "It will happen," says Ellen Hanek, a PPIC economist in San Francisco.

That realization is beginning to change long-standing water politics in the region. In 1982, Californians soundly defeated a measure to build a "peripheral canal" to divert Sacramento River water upstream of the delta and deliver it to farmers and urban residents farther south. The measure was opposed by a coalition of farmers and environmentalists, who saw it as a water grab by Los Angeles. "It became the third rail of water politics, because nobody wanted to touch it," Hanek says.

Until recently, no one has. But in January, The Nature Conservancy became the first environmental group to publicly support a modified peripheral canal. In addition to increasing the reliability of water deliveries to cities and farms, a peripheral canal is expected to improve habitat conditions for several species of endangered fish in the delta, says Anthony Saracino, the Conservancy's California water program director in Sacramento. That's because the current water projects remove water from the southern end of the delta, which pulls freshwater through the rest of the estuary toward the pumps. If those pumps were shut off and water instead diverted before entering the delta, "it would allow the estuary to have a more natural flow regime," Saracino says.

But making that change won't be easy. Farmers within the delta itself still oppose the change. And other stakeholders must be convinced that any future canal would be managed to ensure not only water deliveries to politically powerful cities and farms but also ecosystem health. Still, Saracino and others say it looks like the long-standing stalemate could be coming to an end. Says Saracino: "I think you're seeing real momentum building."

–ROBERT F. SERVICE

CREDIT: CALIFORNIA DEPARTMENT OF WATER RESOURCES

Delta blues. There is a 95% chance that levees will fail by 2050, according to a recent estimate.

Published by AAAS

SPACE SCIENCE

Can a Shotgun Wedding Help NASA And ESA Explore the Red Planet?

Tight budgets are pushing the U.S. and European space agencies to consider a truly collaborative series of missions to Mars. What would it mean for science?

Did Mars ever harbor life? The multibillion-dollar quest to find out faces an uncertain future on both sides of the Atlantic. The European Space Agency (ESA) lacks the money to carry out its ambitious blueprint for putting a sophisticated lander and rover on Mars's surface in 2016. And NASA is grappling with major cost increases and delays in its Mars Science Laboratory (MSL) that are eating up funding for future missions.

To avoid hanging separately, say scientists and managers in the United States and Europe, the two agencies must agree to hang together in an unprecedented partnership. This summer they intend to unveil a sweeping plan for a decade of collaboration that could kick off with a joint 2016 mission and culminate a decade later in the return of a martian sample to Earth. "This is a big change," says David Southwood, ESA science chief. "But we have to think about Mars differently." Adds his counterpart at NASA, Edward Weiler: "We've got to do this together."

The financial motivation for the new strategy is obvious. A sample return mission alone could run between $6 billion and $8 billion, far beyond the means of either agency. But the two agencies and scientific communities will first need to overcome a host of political, cultural, and technical challenges. Some Americans fear ESA is not yet ready to oversee complex missions on the martian surface. Europeans worry about being tied to NASA's annual budget wrangles. And both sides want the glory of landing rovers on Earth's neighbor.

Gaining weight

Cooperation between NASA and ESA is nothing new, of course. ESA has long been part of the international space station, and it provided the Huygens probe that plunged into Titan's atmosphere after riding on NASA's Cassini spacecraft to the Saturn system. Likewise, NASA is slated to pay for two important instruments aboard a 2016 ESA mission called ExoMars. But none of these projects is truly a joint effort. Instead, one agency—usually better-funded NASA—has had the final say, and the other agency's science has literally gone along for the ride. For the joint efforts now being discussed, each agency would take turns. For example, ESA and NASA are likely to alternate putting a lander on the surface, with the other providing a less expensive and technically challenging orbiter or related hardware.

The travails of ExoMars help to explain ESA's interest in a joint effort. Last year, the 17 nations that make up ESA approved $1.1 billion for ExoMars, some $195 million less than agency officials had requested (*Science*, 5 December 2008, p. 1447). The lander, which would open like a flower to reveal a 270-kg rover, would drill down 2 m to examine organics and conduct geochemical studies on whether life ever evolved and prospered on the planet. ESA's only other Mars mission, Mars Express, was a far more modest venture, and although its orbiter was a success after arriving in 2003, its U.K.-built Beagle 2 lander failed to survive the descent.

But the weight and complexity of ExoMars's planned scientific payload has grown alarmingly. The estimated weight of a geophysical package called Humboldt, for example, has tripled. Lifting additional weight requires extra fuel and a roomier spacecraft, which increase costs. "There is not enough [money] to fully realize ExoMars as planned," said Jorge Vago, ESA's ExoMars project scientist, at a meeting earlier this month near Washington, D.C., and "no mechanism for financial shortfalls." As a result, he says, scaling back the $1.56 billion project as well as bringing in U.S. participation "is unavoidable."

That effort is well under way. Last week, European engineers and scientists met in the Netherlands to decide the fate of 23 instruments, two of which would be NASA contributions. At the same time, Southwood is loath to scale it back too much. The ability to establish a presence on the Mars surface, he

Published by AAAS

says, will allow ESA to "stand shoulder to shoulder with Uncle Sam."

But some U.S. scientists worry that ESA lacks the experience to carry out such a difficult mission. "They have never successfully landed on Mars," notes G. Scott Hubbard, a former NASA official and now a physicist at Stanford University in Palo Alto, California. "And ExoMars is more complex than MSL."

Lean on me

NASA has long ruled the roost on solar system missions beyond Earth orbit, having a 3-decade-long track record of landing robots on Mars. But these days it needs a shoulder to lean on. Technical troubles and a $400 million cost increase for MSL recently forced Weiler to postpone the launch of the 900-kg rover by 2 years (*Science*, 12 December 2008, p. 1618). The overrun will eat into future Mars projects, endangering the agency's decade-old plan to send a probe to Mars every 2 years.

That strategy was meant to capitalize on a 1996 paper in which scientists presented possible evidence of fossilized life in a Mars meteorite—evidence that has since largely been discounted. The failure of two probes in 1999 led NASA to revamp that schedule, however, and last year then–NASA science chief S. Alan Stern put forward yet another plan to streamline Mars missions and speed up a sample return mission. Scientists said the plan was unrealistic, however, and Stern resigned shortly thereafter in a funding dispute with the NASA administrator.

Now NASA has decreed that future Mars missions must fit into the more constrained budget. The U.S. agency still plans to send an orbiter to Mars in 2016. One of the scientific instruments aboard the Mars Science Orbiter (MSO) would monitor trace gases such as methane while cameras would provide data on future landing sites. In addition, a communications package would beam information from future U.S. and ESA landers back to Earth.

However, overruns on MSL have left NASA managers with only $700 million for the mission, far less than needed. NASA has also pledged to fund two U.S.-built ExoMars instruments, and the $50 million growth in the initial $80 million budget for them would come out of the 2016 mission. To fit a mission into that amount of money, NASA has proposed limiting the number of instruments. But planetary scientists say the current MSO budget is unrealistic. "What can you do with $500 million?" asks John Mustard, a planetary scientist at Brown University and chair of NASA's Mars advisory panel. "Not much."

Given the dire budget situation, U.S. scientists seem to agree that cooperation with ESA is vital. But exactly how that will be done remains unclear. Some engineers and scientists favor a combined 2016 mission in which a U.S., European, or Russian rocket launches a NASA orbiter to Mars, which then drops ExoMars to the surface. In 2018, the two agencies would switch roles, with an ESA orbiter dropping NASA's proposed $1.3 billion to $1.6 billion Mars Prospector Rover. A network of landers designed to monitor Mars's geophysical health could follow in 2020. The first portion of a sample return mission would leave Earth in 2022, with the second half following in 2024. NASA would likely be responsible for getting the Mars sample into orbit, with an ESA craft bringing the sample home to Earth 2 years later.

In alignment. NASA's Edward Weiler (*left*) and ESA's David Southwood hope for a tentative agreement this summer on joint Mars missions.

That tag-team approach has its critics. Jean-Pierre Bibring, an ExoMars principal investigator with the Institute of Space Physics in Orsay, France, fears that combining the 2016 mission with U.S. and perhaps Russian components could delay it until 2018—5 years beyond its initial target. And he says that "if ExoMars meets its goals, then the 2018 lander makes no sense."

Bibring would prefer to see both sides do a sample return mission starting in 2018: "There is no other science rationale for waiting. The missions in between are really political and economic missions. They are a waste of time and money."

Flag size

Neither Weiler nor Southwood want to tip their hand before meeting in June. "We're still negotiating," says Southwood. The goal, he says, is to avoid the difficulty that goes along with integrating complicated pieces of hardware—from shipping risks to import restrictions—by making each agency responsible for separate pieces of every mission.

One key stumbling block is that Europe lacks the tradition of long-term planning that characterizes NASA's effort. The likelihood of ESA's many masters approving an entire series of very expensive flights to Mars during a severe economic downturn seems small. "There's a psychological barrier we're dealing with," acknowledges Southwood. "We've got to work with member states used to the idea of one mission at a time." At the same time, he and other Europeans note that NASA's penchant for long-term planning does not necessarily mesh with the uncertainty of Congress's annual budget process.

Weiler admits that cooperation with ESA is a hard sell. "I may be the only person in NASA who believes that this is the right thing to do," he says bluntly. "My toughest job is to get my view understood at all levels below me, and especially at certain NASA centers."

Those centers—particularly the Jet Propulsion Laboratory (JPL) in Pasadena, which has built previous Mars landers and rovers—may be loath to relinquish U.S. dominance of the Mars program. JPL has never been shy about using its industrial partners and the powerful California congressional delegation to ensure its central role in solar system exploration. But Weiler is betting that JPL's managers will realize that leading one Mars mission every 4 years is better than maintaining control over a bankrupt program.

There are subtler barriers to U.S.-European cooperation as well. American space scientists have less experience working with colleagues in other countries than do their counterparts. "There's a lot of ignorance," says Mustard, who has worked closely with French researchers for 2 decades. "So there's a lot of anxiety." And Europeans must contend with what Southwood says is "a bit of an inferiority complex" with NASA when it comes to managing major Mars projects.

But managers on both sides believe that the opportunity to do good science will ultimately trump all other concerns. Weiler admits that "psychology and nationalism … are tough nuts to crack." But he warns that if scientists want a strong Mars program, "flag size cannot matter."

–ANDREW LAWLER

CREDITS: FRED PROUSER/REUTERS/LANDOV; ROBYN BECK/AFP/GETTY IMAGES

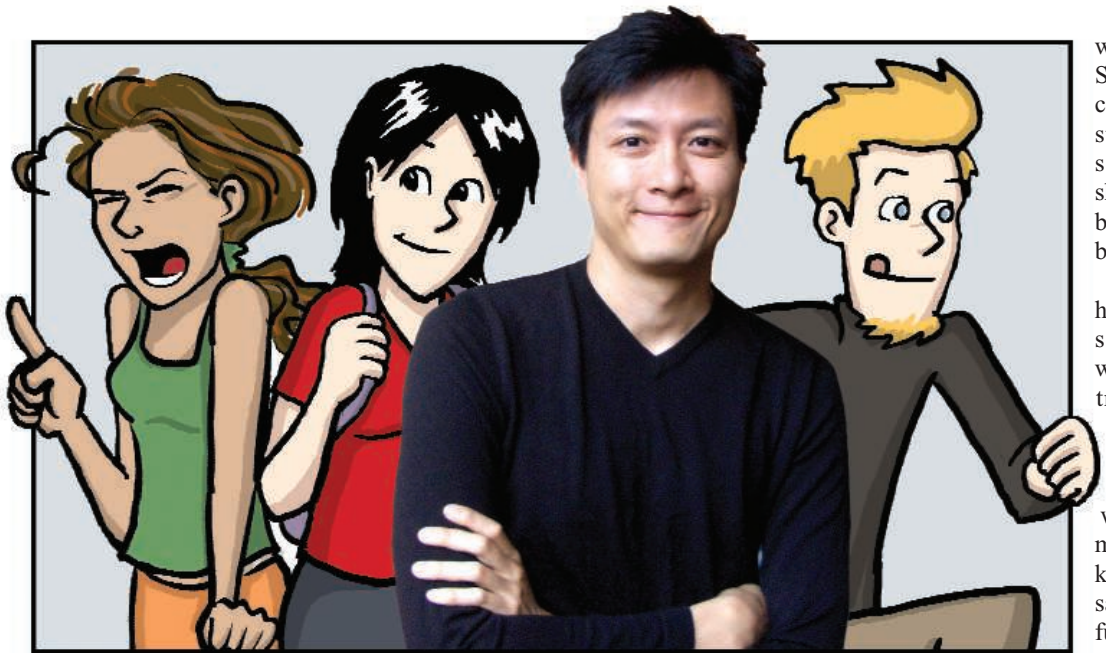

PROFILE: JORGE CHAM

Piled Higher and Deeper: The Everyday Life of a Grad Student

Jorge Cham's comic strip, capturing the trials and tribulations of grad school, became so popular that he left the lab for a career as a cartoonist and lecturer

Jorge Cham is not a Nobel laureate, but the popularity of his keynote lectures and his following in the scientific world are enough to make even the most distinguished professor green with envy. Cham, 33, is the brains behind the comic strip *Piled Higher and Deeper*—*PHD* for short—and it's made him a celebrity among graduate students, with 4.7 million visitors a year to his Web site and a battalion of fans in labs all over the planet. His fourth book, *Academic Stimulus Package*, is scheduled for publication this month.

Supervisors interested in learning what's on their students' minds might find *PHD* an illuminating place to start. After all, "every professor was once a graduate student," says Anthony Finkelstein, head of the Computer Sciences department at University College London (UCL) and a *PHD* fan. Cham's comic strip resonates with graduate students and professors alike because it deals with everyday frustrations of life in the lab—procrastination, dealing with advisers, serving on committees, lack of inspiration—and its appeal seems to be universal. "I live all those issues every day," says Martha Elena Ibarra, a molecular biology Ph.D. student at the Cinvestav laboratory in Irapuato, Mexico. "It makes you feel you're not the only one out there," says Shrikant Sundaram, an electrical engineering master's student at the University of Southern California in Los Angeles.

Cham, who is surprisingly low-key for somebody with such a sharp eye and an edge to his humor, grew up in Panama in a science-oriented family. Both of his parents have graduate degrees and taught at the University of Panama. "I guess you could say geekiness is in our genes," Cham says, "but they also instilled in us to value education and hard work."

As a child, Cham dreamed of becoming an engineer. "I was interested in machines and movement, so mechanical engineering seemed the best fit and robotics the most interesting to me within that," he says. He graduated from the Georgia Institute of Technology in Atlanta in 1997 with a bachelor's degree in mechanical engineering and got into cartooning almost by accident.

In the fall of 1997, a few weeks after he started a master's program in mechanical engineering at Stanford University in Palo Alto, California, the student newspaper *The Stanford Daily* put out a call for a new comic strip. Cham, his brother Jaime, who was also a graduate student at Stanford, and a few friends discussed some ideas for a comic strip over dinner. "My brother said he always thought there should be one about grad school, because that's when the real pain begins," Cham recalls.

Cham was enthused. Although he had doodled as a child and his school notebooks were filled with little drawings, he had never tried sketching comics before. "At the time, I was also reading a book about *Doonesbury*," the comic strip that has provided wry social and political commentary since 1970, "so I was kind of inspired in that way," he says. Despite being busy with a full load of classes and teaching assistant duties, Cham says, "I somehow thought it would be a good idea to draw a comic 5 days a week."

Cham proposed a comic strip that would center on the life (or lack thereof) of a group of overworked, underpaid, procrastinating graduate students and their terrifying advisers. *The Stanford Daily*'s editors liked the idea, and in October 1997, *Piled Higher and Deeper* was born. A few weeks later, Cham created the Web site on which, to this day, his comic strip is available for free.

From the beginning, *PHD* has featured a regular cast of characters: the nameless hero, suspiciously similar to the author himself; geeky Cecilia, the dedicated engineering student; Mike Slackenerny, who takes laziness to a whole new level; social scientist Tajel; the absent-minded Professor Jones; and the demanding Professor Smith. Cham insists that none of them is based on real people, but he acknowledges that he was inspired by colleagues "from the research center where I worked, to my cohort of classmates, to a lot of my brother's friends."

Online
sciencecareers.org
This article is part of a special **Science Careers** feature on scientists who have left the bench.

Split careers

Cham kept up the comic strip while he finished his master's degree and continued it during the 4 years he spent at Stanford studying for a Ph.D. His research was part of a multidisciplinary project to build a sturdy and fast six-legged robot—a design inspired by cockroaches—capable of maneuvering in bumpy terrains. Cham's role was to design the legs and joints. "He was a great student, creative and hardworking and very sharp," says Mark

CREDITS: JORGE CHAM

Published by AAAS

Cutkosky, Cham's Ph.D. adviser at Stanford. Cutkosky remembers his own graduate student days well enough to identify with the comic strip's characters. "Jorge's comics capture the special culture of academia, especially in technical fields, quite well," he says.

Cham's first book, *Piled Higher and Deeper: A Graduate Student Comic Strip Collection*, was published in 2002, during his last year at Stanford. But despite the growing success of the comic strip, he still planned to pursue a career in research. Cham started looking "very aggressively" for an academic job. He was short-listed for a job at the Massachusetts Institute of Technology (MIT) in Cambridge but didn't get it. "I always think that I was this close," he says with a hint of frustration. In the end, Cham stayed on the West Coast for a postdoc position at the California Institute of Technology (Caltech) in Pasadena researching neural prosthetics. The work was aimed at developing a system to help paralyzed people control external devices, such as a mouse pointer, with brain signals.

Cham's second collection of comic strips, *Life is tough and then you graduate*, was published in May 2005. By then, *PHD* fans had spread beyond Stanford, and his sister Laura volunteered to organize a book signing at MIT, where she was a graduate student. Cham thought it was a cool idea but says, "I offered to do a lecture instead, since it's a skill you learn as a Ph.D. anyway." He talked about the books and their characters, and the ups and downs of graduate student life. That talk launched his career as a speaker at conferences and student events worldwide.

His "The Power of Procrastination" lecture presents the comic strip and its characters, explores the pros and cons (mostly cons) of being a graduate student, and discusses the pros and cons (mostly pros) of procrastination. The result is "hilarious," says Finkelstein of UCL. Finkelstein says he considered several "worthy but dull options" for a keynote speech at the Computer Science 2008 Student Research Conference he was organizing at the University of Cambridge when someone suggested Cham. Finkelstein agreed immediately.

Feedback from the talk at Cambridge was excellent, he says. "[Cham's] message that research is mentally tough and potentially lonely strangely made the students more enthusiastic," Finkelstein adds.

Making choices

Coordinating his cartoonist activities with his research at Caltech became increasingly difficult, and Cham realized that the comic strip was "growing into something special." He dithered on whether to become a professional cartoonist or pursue his dream of becoming a professor. Cham says he's grateful for the advice Joel Burdick, his principal investigator at Caltech, gave him at the time. Burdick encouraged him "to pick one thing and be really good at it" and warned him not to be caught in artificial models of success, such as thinking that becoming a tenured professor at a major university is the only available option. Instead, Cham learned that "if you have the drive and the creativity, you can forge your own path" and "you can choose your own definition of success," he says.

Cham believes that part of his drive to become an academic was the thrill of achievement, and he realized that being "this close" to fulfilling his dream of getting an academic job at MIT was "actually pretty good. … So once I got that far, I just said to myself, 'You know, I don't need to be a professor anymore.' " So, in July 2005, Cham left Caltech to become a full-time cartoonist.

The *PHD* comic strip is still available for free on his Web site and syndicated for free in university newspapers. Cham makes his living with the sale of books, merchandise, and "The Power of Procrastination" lecture series. The business gives him little rest; Cham gave 46 lectures last year, more than a dozen of which were in Europe. Next month, he's scheduled to speak at five universities in four states and Canada.

Even though his graduate student years are definitely over, comic ideas are still plentiful: He posts new comics on his Web site "approximately 2.718 times a week." Cham draws mostly from his own experiences as a graduate student, although he is also inspired by fan mail and people he meets during his talks.

"Running a business can be really challenging," Cham says, and part of him misses working in a scientific institution and knowing that his research is part of something larger. However, there are quite a few signs that his work is far-reaching: His often-packed lectures usually include graduate students from many different disciplines, and seeing "art history scholars laughing along with biologists, English, and engineering majors is something I imagine rarely happens," Cham says. "Many people have come up to me to say the comics and the lecture are like therapy for them." Finkelstein agrees: Part of the appeal of *PHD*, he says, is that "while poking fun at the loneliness of research, [Cham] actually makes us realize that we are not alone."

–SARA COELHO

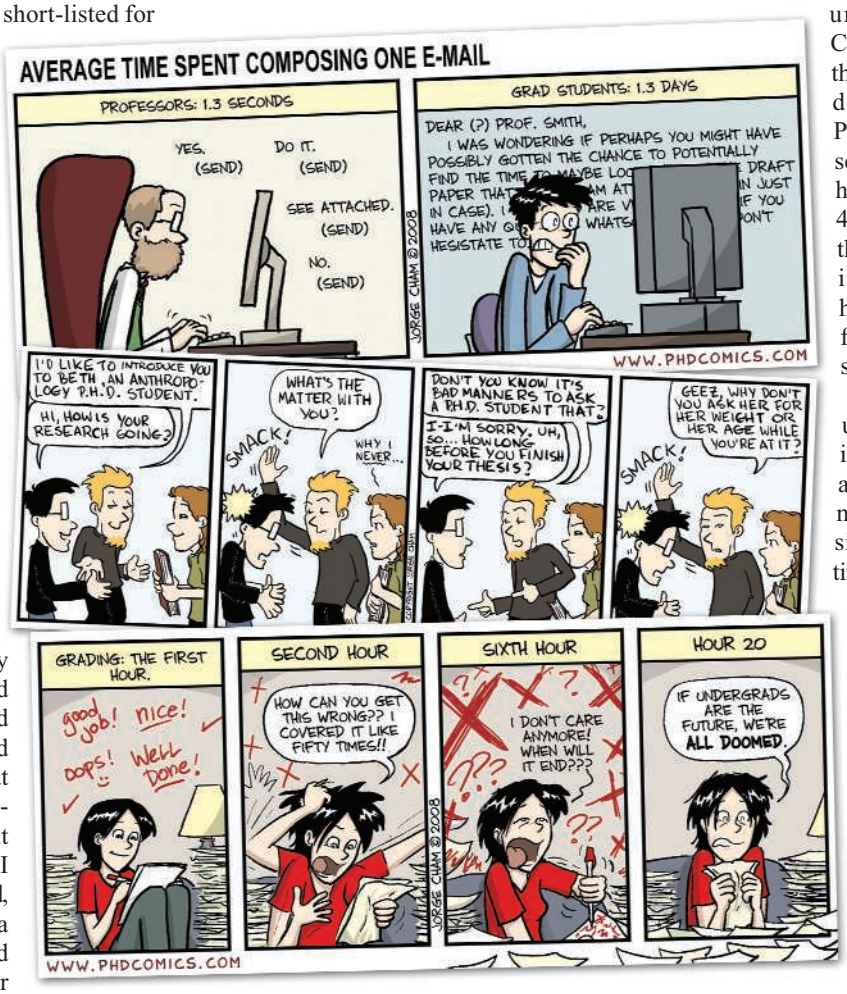

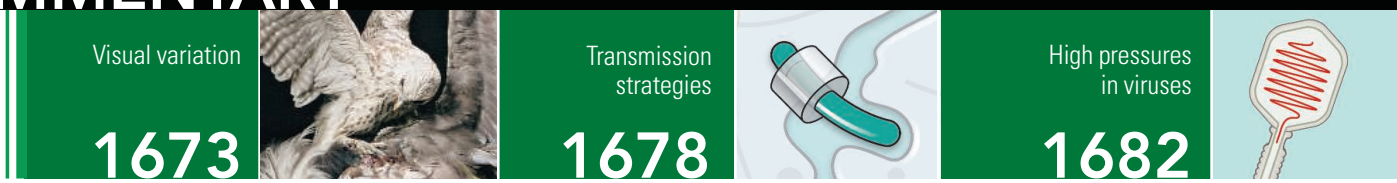

LETTERS

edited by Jennifer Sills

Sauropods Kept Their Heads Down

IN THEIR PERSPECTIVE "SAUROPOD GIGANTISM" (10 OCTOBER 2008, p. 200), P. M. Sander and M. Clauss assumed that in order to meet their high energy demands, these long-necked dinosaurs browsed in tall trees, as do today's giraffes. Recent museum reconstructions of *Barosaurus* and *Brachiosaurus* place the head about 9 meters above the chest, requiring the heart to generate about 750 mm Hg blood pressure. The problems associated with such hypertension, including extremely large hearts, have been considered (*1*), but the energy required to circulate the blood has not been appreciated.

This approach to the problem does not rely on knowledge of heart size or strength, but involves an estimate of the energy cost of the circulation, based on two axiomatic relationships between metabolic rate, blood flow rate, and blood pressure. First, the Fick Principle states that an animal's aerobic metabolic rate is proportional to blood flow rate (*2*). Second, the rate of work done by the left ventricle is proportional to the product of blood flow rate and mean arterial blood pressure (*3*). Therefore, cardiac work is proportional to the product of metabolic rate and blood pressure. Cardiac work averages about 10% of the metabolic rate in mammals that have a mean arterial blood pressure of about 100 mm Hg (*4*). An animal that produces 750 mm Hg would consequently have a cardiac work rate 7.5 times higher. Its metabolic rate would increase to 165%, and it would expend 45% of its total energy requirements just to circulate the blood. These percentages would be the same whether the animals were active or resting, high-energy endotherms or low-energy ectotherms. The high cost of high browsing makes it energetically more reasonable to keep the head down and move the neck horizontally rather than vertically (*5*).

ROGER S. SEYMOUR

Department of Ecology and Environmental Biology, University of Adelaide, Adelaide, SA 5005, Australia. E-mail: roger.seymour@adelaide.edu.au

References

1. R. S. Seymour, H. B. Lillywhite, *Proc. R. Soc. London Ser. B* **267**, 1883 (2000).
2. W. A. Calder III, *Size, Function, and Life History* (Dover Publications, Mineola, NY, ed. 2, 1996).
3. D. S. Loiselle, C. L. Gibbs, *Am. J. Physiol.* **237**, H90 (1979).
4. Z. M. Wang, T. P. O'Connor, S. Heshka, S. B. Heymsfield, *J. Nutr.* **131**, 2967 (2001).
5. K. A. Stevens, J. M. Parrish, *Science* **284**, 798 (1999).

Sauropod posture. Sauropods may not have used their long necks to lift their heads high, at least not for long periods of time.

CREDIT: MARK HALLETT PALEOART/PHOTORESEARCHERS, INC.

Response

WE VIEW THE LONG NECK AS CENTRAL TO THE unique gigantism of sauropod dinosaurs, but the controversy about whether sauropods kept their necks low (*1*, *2*) or carried them high (*3*–*6*) is not crucial to our argument. We did not claim that sauropods browsed preferentially on tall trees, although the schematic illustration accompanying our paper may have suggested otherwise. Instead, we posited that long necks allowed the sauropods to reach food that other animals could not (*6*). We also envisage sauropods feeding along lake shores and river banks. Their long necks would have allowed access to the most nutritious of bulk foods, *Equisetum* (*7*), without treading on potentially treacherous marshy ground.

Seymour's calculations suggest that sauropods did not elevate the head several meters above the heart for any length of time. This accords with computer modeling of zygapophyseal overlap in intervertebral joints (*1*, *2*) but not with evidence from the actual bones of *Camarasaurus* (*3*, *8*) or *Euhelopus* (*9*), which indicates that the neck could have been raised high above the body. In living long-necked animals (such as the ostrich and camel), zygapophyseal overlap is a poor predictor of dorsoventral neck mobility (*5*). The ability to raise the neck high is also suggested by the strong perimortem dorsoflexion of the neck in some sauropod skeletons and the relative size of the semicircular canals of *Brachiosaurus* (*10*).

The energy argument by Seymour does not exclude the possibility of a very high neck posture (*5*) during feeding but limits the situations in which a net energy gain would have resulted from a raised neck. Horizontal movements of the neck were preferable as long as sufficient food was available at low or medium heights. During food shortages, however, expenses for high cardiac output may have been offset by resources available only at greater heights.

P. MARTIN SANDER,[1]* ANDREAS CHRISTIAN,[2] CAROLE T. GEE[1]

Published by AAAS

[1]Division of Paleontology, Steinmann Institute, University of Bonn, D-53115 Bonn, Germany. [2]Institut für Biologie und Sachunterricht und ihre Didaktik, Universität Flensburg, Auf dem Campus 1, D-24943 Flensburg, Germany.

*To whom correspondence should be addressed. E-mail: martin.sander@uni-bonn.de

References and Notes

1. K. A. Stevens, J. M. Parrish, *Science* **284**, 798 (1999).
2. K. A. Stevens, J. M. Parrish, in *The Sauropods: Evolution and Paleobiology,* K. A. Curry Rogers, J. A. Wilson, Eds. (Univ. of California Press, Berkeley, CA, 2005), pp. 178–200.
3. G. S. Paul, *Mod. Geol.* **23**, 179 (1998).
4. A. Christian, *Mitteilungen aus dem Museum für Naturkunde in Berlin, Geowissenschaftliche Reihe* **5**, 271 (2002).
5. G. Dzemski, A. Christian, *J. Morphol.* **268**, 701 (2007).
6. A. Christian, G. Dzemski, *Fossil Rec.* **10**, 38 (2007).
7. J. Hummel *et al.*, *Proc. R. Soc. London Ser. B* **275**, 1015 (2008).
8. J. S. McIntosh, W. E. Miller, K. L. Stadtman, D. D. Gillette, *Brigham Young Univ. Geol. Stud.* **41**, 73 (1996).
9. C. Wiman, *Palaeontol. Sinica Ser. C* **6**, 1 (1929).
10. A. H. Clarke, *J. Vestibular Res.* **15**, 65 (2005).
11. The authors thank all members of DFG Research Unit 533 for discussion. This is contribution number 52 of this research unit.

Specimens Versus Sequences

IN HIS PERSPECTIVE "GENBANK—NATURAL history in the 21st century?" (24 October 2008, p. 537), B. J. Strasser claims that GenBank follows the tradition of natural history studies. I argue that GenBank is inconsistent with some important aspects of the tradition of natural history and it alone does not and will not constitute natural history.

First, GenBank has been designed to store molecular information about model organisms or humans, whereas natural history serves to explore and document biodiversity. GenBank's format is incapable of handling unique aspects of biodiversity studies such as diverse and large collections of specimens, and taxonomic uncertainties and revisions. Second, GenBank does not require vouchering of specimens, DNA extracts, or other molecular products, whereas the study of natural history always anchors information with specimens. Without such anchoring, revisionary work (which is part of the tradition of natural history) cannot be conducted. As a result, GenBank contains a considerable amount of unidentified or misidentified sequences (*1*–*3*). Third, GenBank is unlikely to reach amateurs in the way that natural history has. Study of natural history generally does not require expensive equipment and is exciting and rewarding. In comparison, DNA sequencing is costly, offers little aesthetic reward or recreational value, and requires specialist knowledge. It is hard to imagine amateurs comparing or exchanging their collections of DNA sequence instead of actual specimens.

Natural history documentation has many important facets, such as specimen locality data, images of morphology, and ecological notes. The Global Biodiversity Information Facility (www.gbif.org) and Morphbank (www.morphbank.net) are good examples. Specimen collections will continue serving as the primary record of natural history and biodiversity, while molecular data are supplementary.

GUANYANG ZHANG

Department of Entomology, University of California, Riverside, Riverside, CA 92521, USA. E-mail: Guanyang.Zhang@email.ucr.edu

References

1. P. D. Bridge, P. J. Roberts, B. M. Spooner, G. Panchal, *New Phytol*. **160**, 43 (2003).
2. R. H. Nilsson *et al.*, *PLoS ONE* **1**, e59 (2006).
3. G. Valkiūnas, C. T. Atkinson, S. Bensch, R. N. M. Sehgal, R. E. Ricklefs, *Trends Parasitol*. **24**, 247 (2008).

Response

ZHANG MISREPRESENTS THE PAST OF NATURAL history and the present of molecular sequence collection. His Letter reflects the exact tension I described in my paper between the naturalist and experimentalist perspectives.

First, although GenBank's objective may be to document model organisms, in February 2009 there were no fewer than 187,136 species represented in GenBank (*1*)—i.e., 5 to 10% of all known species. GenBank is thus already an extraordinary sampling of biological diversity, unmatched by any museums of natural history, and on par with the morphological databanks mentioned by Zhang.

Second, GenBank certainly contains a "considerable amount of unidentified or misidentified sequences," but all significant natural history museums likewise contain "unidentified and misidentified" specimens. Indeed, because systematic vouchering of specimens strengthens the reliability of the taxonomic assignment of sequence data (if the specimens are actually available to researchers), for more than a decade GenBank has included a data field for the specimen voucher. Presently, more than 623,000 sequences contain some kind of voucher information (*1*).

Third, sequence data in GenBank have indeed been provided mainly by professionals, although that might change very soon with the falling cost of genome sequencing. However, natural history collections are no different, given that most specimens have been identified by professionals, not by amateurs, as the history of taxonomy amply demonstrates (*2*). Zhang romanticizes natural history when he suggests that it "does not require expensive equipment"; most natural history endeavors have been anything but inexpensive. Surveys such as those of the fauna and flora of the West Indies in the 1780s, or of the American West in 1900 (*3*, *4*), were both characteristic Big Science projects, and the Kew Gardens or the American Museum of Natural History are not exactly cottage industries.

Zhang seems to fear that sequence data will replace specimen collections. He ignores the fact that natural history is not fundamentally about specimens, but about natural facts. Specimens are among these, but so are rocks, bones, and now molecular sequences. Thus, in his critique, Zhang repeats a concern that numerous naturalists have voiced since the beginning of the 20th century: that the experimental sciences would take over natural history. In the 1960s, molecular evolutionists led many of their naturalist colleagues to believe exactly that. They mocked the naturalists' methods based on morphological comparisons by asking "how many vertebrae does a sponge have?" (*5*).

In my Perspective, I argued that this controversy is becoming increasingly irrelevant in the 21st century, as the boundaries between specimen collections and molecular data collections are becoming increasingly blurred. With many GenBank sequences now linked to specimens in natural history museums, the convergence of specimen and sequence collections has proceeded smoothly precisely because both stand in the same tradition of natural history.

BRUNO J. STRASSER

Section of the History of Medicine, Yale University, New Haven, CT 06511, USA. E-mail: bruno.strasser@yale.edu

References

1. National Center for Biotechnology Information (www.ncbi.nlm.nih.gov).
2. J. Endersby, *Imperial Nature: Joseph Hooker and the Practices of Victorian Science* (Univ. of Chicago Press, Chicago, 2008).
3. L. L. Schiebinger, C. Swan, Eds., *Colonial Botany: Science, Commerce, and Politics in the Early Modern World* (Univ. of Pennsylvania Press, Philadelphia, 2005).
4. R. E. Kohler, *All Creatures: Naturalists, Collectors, and Biodiversity, 1850–1950* (Princeton Univ. Press, Princeton, NJ, 2006).
5. W. M. Fitch, E. Margoliash, *Science* **155**, 279 (1967).

EXHIBITIONS: ART AND EVOLUTION

The Darwinian Eye

Harriet Ritvo

Endless Forms
Charles Darwin, Natural Science and the Visual Arts

Diana Donald and Jane Munro, Curators

Yale Center for British Art, New Haven, CT. 12 February–3 May, 2009. Fitzwilliam Museum, Cambridge. 16 June–4 October, 2009. www.darwinendlessforms.org

Endless Forms
Charles Darwin, Natural Science and the Visual Arts

Diana Donald and Jane Munro, Eds.

Yale University Press, New Haven, CT, 2009. 358 pp. $75, £40. ISBN 9780300148268.

Darwin did not come up with his theory of evolution by natural selection in a "Eureka!" moment. As biographers have shown, he arrived at his big idea gradually after his five-year voyage on the Beagle, and he nurtured and refined it for longer still before exposing it to public scrutiny. As historians of science have shown, evolutionary theories had been current since before Darwin was born, propounded for both specialist and nonspecialist audiences.

Endless Forms: Charles Darwin, Natural Science and the Visual Arts, the fascinating and spectacular exhibit currently on display at the Yale Center for British Art—and appearing, with a somewhat different array of objects, at the University of Cambridge's Fitzwilliam Museum this summer—presents an additional context for Darwin's work. Darwin's world was saturated in images, and the exhibit compellingly illustrates the interplay between his ideas and the visual culture of his time. Although the opening room is dominated by Darwin the man, the exhibition as a whole is not structured around his life or his career. Even the introductory display juxtaposes popular images (including a statue of a gorilla abducting a nearly naked woman, a photograph of a man with skeletons and skulls of various primates, and a fanciful print of apes regarding the first human child) with the iconic portrait of the aged Darwin in a cloak, the famous final sentence from *On the Origin of Species* ("There is grandeur in this view of life …"), and two images that Darwin produced himself: an early sketch of his branching evolutionary tree and the diagram that ultimately appeared in *Origin*. (Unlike many naturalists of his time, Darwin was not a gifted artist.)

The entire exhibition is structured thematically, with sections devoted to the importance of visual evidence for natural history, the history of Earth, the struggle for existence, the relationship of people to other animals, the relationship of some people to other people, sexual selection, and the way that some late-19th-century artists used ideas associated with Darwin. This organization offers several important rewards. Each section spans at least the entire 19th century—that is, a longer period than that of Darwin's career or, indeed, his life. The range of items in each section reflects the variety of forms in which the themes could be represented. Particularly arresting are the mixture of two-dimensional displays (paintings, prints, photographs, drawings, maps, book or journal illustrations, and broadsides) with three-dimensional displays (statues, rocks, zoological and botanical specimens, scientific instruments, and several astonishing taxidermical tours de force) and the mixture of the imaginative (Edwin Landseer's anthropomorphic dog paintings or mythologized impressions of the emergence of humankind) with the naturalistic (a collection of insects or of photographs of human types). Many of the sections are connected by the increasing prominence of photography, with its ostensible promise of faithfulness to life.

For example, the understanding of the dynamism and length of geological history was an essential component of Darwin's evolutionary thought. *Endless Forms* illustrates the appeal that these emergent notions had to artists and amateurs as well as to serious naturalists. Painters such as J. M. W. Turner and Thomas Cole produced visions of the ancient (sometimes very ancient) world, while others incorporated new geological ideas in their images of such sublime settings as Niagara Falls. Naturalists exercised their imaginations on Earth's extinct ancient inhabitants, drawing the creatures and casting them in statues (of which the exhibit includes only some designs, rather than the enormous end products). Not content to admire such representations, the public began to collect its own smaller fossils along the beach cliffs, and this activity also became a subject for artists.

The exhibit is very full and very well selected. It contains many wonderful things. Perhaps the most wonderful (not least because of the effort and skill that must have been required to transport it intact from England) is a diorama, if that is the right word for a construction that can be viewed from all sides. Entitled *Struggle with the Quarry*, it shows a heron that, having caught an eel,

CREDIT: SEDGWICK MUSEUM OF EARTH SCIENCES, CAMBRIDGE UNIVERSITY

Robert Farren's *Duria Antiquior (An Earlier Dorset)* (circa 1850). Farren was one of the many artists who copied geologist Henry De la Beche's depiction of voracious ichthyosaurs and dueling pterosaurs, an 1830 watercolor widely distributed as a lithograph.

The reviewer is at the Department of History, Massachusetts Institute of Technology, Building E51-285, 77 Massachusetts Avenue, Cambridge, MA 02139, USA. E-mail: ritvo@mit.edu

John Hancock's *Struggle with the Quarry* (1851). One of a trio of taxidermy mounts depicting the stages of falconry.

is itself caught by a falcon controlled by a human falconer. (The falconer is only suggested; the other participants in the dramatic scene are stuffed.) The "Struggle for Existence" section contains diverse representations of animals' struggles with each other, either as predator and prey or as rivals. It also includes a few images that suggest the application of this idea to the members of Darwin's own society. Similarly close to home, the section on the "Descent of Humankind" juxtaposes predictably exoticized photographs of dark-skinned people from remote locations with an album of photographs of various British types.

To accompany the exhibition, curators Diana Donald (emerita, Manchester Metropolitan University) and Jane Munro (Fitzwilliam Museum) have edited a lavishly produced collection of essays. Most of the contributors are art historians or museum curators. The volume reproduces many of the items displayed in New Haven (along with many additional images), but it is much more than a catalogue. It offers thoughtful explorations of many of the ideas provocatively raised by the displays themselves. And anyone who visits "Endless Forms"—no matter how well acquainted in advance with Darwin's work or with his society or with his subject—will come away with many new answers and many new questions.

10.1126/science.1172248

BIOSCIENCE

Emerging Market Organisms

Jonathan M. W. Slack

Emerging Model Organisms
A Laboratory Manual. Volume 1

Cold Spring Harbor Laboratory Press, Cold Spring Harbor, NY, 2009. 604 pp. $158, £100. ISBN 9780879698263. Paper, $89, £55. ISBN 9780879698720. http://cshprotocols.cshlp.org/emo/

In the economy of modern competitive science, there can be few career outcomes more satisfactory for a bioscience professor than the successful introduction of a "new" model organism. If you are the first to domesticate a creature useful for experimental work, then everyone will use your protocols and refer to your papers. Second-generation labs will be founded by your students and postdocs. You will preside over the establishment of stock centers, genome sequencing, and the inevitable series of organism-specific international meetings. Finally, in the twilight of your career, you will be much venerated and in demand to give plenary lectures about the early days of risk and adventure that led to the creation of this particular new grant-consuming industry.

But how can you be sure that your chosen organism will hit the jackpot? *Emerging Model Organisms*, the first volume in a new series, introduces 23 "new" model organisms, each an eager candidate to capture market share. It covers two lower eukaryotes, three plants, and 18 types of animal. Each chapter briefly describes the organism and some of its principal applications before offering a series of lab protocols for activities such as obtaining embryos, making transgenics, or doing in situ hybridizations with the creature in question.

The idea of the "model organism" took root in the early days of molecular biology when *Escherichia coli* and its bacteriophages were adopted as vehicles to solve the problem of the molecular basis of inheritance. At the time, there was no guarantee that inheritance would have a common molecular basis in all organisms. But because it does, the discoveries made by a few labs in the 1940s and 1950s laid the basis for the whole of modern molecular biology—which now employs millions of people around the world. When contemplating the organisms discussed in this book, we necessarily ask, what are these creatures supposed to be models for? A model organism must exemplify some key general biological problem that can be solved relatively easily with it and that will turn out to have the same

A model butterfly. *Bicyclus anynana*, a tropical East African satyrid with seasonal polyphenism, offers a system for exploring evolutionary genetics and evolutionary developmental biology.

The reviewer is at the Stem Cell Institute, 2001 6th Street SE, Minneapolis, MN 55455, USA. E-mail: slack017@umn.edu

BROWSINGS

Mannahatta: A Natural History of New York City. Eric W. Sanderson; illustrations by Markley Boyer. Abrams, New York, 2009. 356 pp. $40, C$44, £19.99. ISBN 9780810996335.

In September 1609, explorer Henry Hudson arrived at the shore of the island now called Manhattan. Landscape ecologist Sanderson and artist Boyer depict the environments of the "island of many hills" then inhabited by the Lenape. Working with a very detailed 1782 map prepared by the British army during the Revolutionary War, they have matched the locations of long-vanished hills, ponds, woods, and wetlands to extant city blocks. In a Wildlife Conservation Society project (www.wcs.org/mannahatta), they used habitat requirements and ecological relations of biota historically recorded in New York to generate probable distributions of the earlier flora and fauna. Their comparisons of reconstructed landscapes and current cityscapes—such as these views of the Upper East Side (above)—will also be presented in an exhibit, *Mannahatta/Manhattan: A Natural History of New York City*, at the Museum of the City of New York (www.mcny.org), 20 May through 13 October 2009. In addition to looking back at the world glimpsed by Hudson, the authors sketch a green, sustainable Manhattan 400 years from now.

CREDITS: (LEFT) © MARKLEY BOYER/THE MANNAHATTA PROJECT/WILDLIFE CONSERVATION SOCIETY; (RIGHT) © STEPHEN AMIAGA

answer for more important but experimentally less tractable organisms, namely human beings or economically important domestic animals and crop plants.

There is a good case for some of these new, or not-so-new, organisms. Planarians regenerate their heads, something that we should all like to be able to do. None of the other standard model organisms in developmental biology will do this, which seems a pretty good reason for working on something that can. For most of the other 22 organisms, the justification lies in the realm of evolution. Some are developmental models that exemplify understudied taxa. For instance, *Ilyanassa*, a marine mud snail, is a representative of the spirally cleaving Lophotrochozoa. Others resemble ancestors thought to lie at important branch points of the evolutionary tree. These include choanoflagellates (sister group to Metazoa), sponges (basal Metazoa), the lamprey (basal vertebrate), and Polypterus (basal ray-finned fish). Still others differ slightly from already-studied taxa and thus provide opportunities to study small evolutionary changes in detail. These include "another nematode," *Pristionchus pacificus*; the blind cave fish, *Astyanax mexicanus*; the African butterfly *Bicyclus anynana*; and Darwin's finches. I am left somewhat unconvinced by all this. Even if we could catalog all the mutations that were fixed in the course of adjusting the beak sizes of Darwin's finches, would this really enable us to predict, or even understand, small evolutionary changes in other organisms?

For those who manage science funding, the book should pose the question: How many model organisms do we need? That issue is all the more urgent because there is a second volume of this series looming, so there will soon be another 20 or so organisms wanting to get their snouts, tentacles, probosci, or roots into the trough. We practitioners of academic life sciences feel we require a doubling of total expenditure about every five years to remain reasonably comfortable. Funding bodies have found this a difficult target to meet, and it will become even harder with so many more model organisms to feed.

The book's protocols reveal that not all the aspirant models are capable of being bred in the lab—something I would consider a basic requirement. The prize for extreme supply difficulty goes to Darwin's finches, whose eggs have to be collected under license in the Galapagos Islands. But there are other accessibility problems. At present, dogfish embryos can only be obtained from the Station Biologique in Roscoff, France, and the method for obtaining the demosponge *Amphimedon* begins "Snorkel at low tide to locate adult sponges." Unfortunately, the protocols themselves are unevenly distributed: none are provided for the cricket or dogfish, whereas *Bicyclus* gets 13.

Model organisms are usually considered unstoppable success stories. But this is not entirely true. One of the founders of molecular biology, Max Delbrück, worked on bacteriophage because he believed it was the simplest example of heredity available and therefore likely to be the easiest to solve. Later in his career, Delbrück turned to research on behavior. Again he chose what he felt was the simplest example, the fungus *Phycomyces* and its phototrophic growth movement. Alas, *Phycomyces* did not turn out to represent behavior in the wide sense that Delbrück had hoped; after an initial flurry of interest, publication numbers have been in slow decline since the 1970s.

The volume certainly raises interesting issues about what model organisms are for and how many we can afford. It may be a useful resource for researchers who tire of their current organism and seek a new one. But, in the end, a familiar warning is required: investments in emerging model organisms, like those in emerging markets, can go down as well as up.

10.1126/science.1171948

GRADUATE EDUCATION

Professional Science Master's Programs Merit Wider Support

A recent study shows the potential of an alternative career path in building a scientific work force.

Rita R. Colwell

The United States faces growing global competition in the development of innovative products and services, a challenge much like a "silent Sputnik" to which the nation must pay more attention (*1*). One component of the U.S. educational system that can help us meet that challenge is master's level education in the natural sciences.

In most fields in the natural sciences, master's degrees have long been viewed mainly as milestones en route to a doctorate, rather than destinations in their own right. But about a decade ago, foundations and universities began experimenting with new master's programs that develop advanced scientific knowledge and professional skills such as communication, project management, and commercialization. Most of these innovative Professional Science Master's (PSM) degree programs are interdisciplinary and provide hands-on learning through internships and team projects. They are not intended to displace traditional programs. Instead, they aim to engage students with professional goals and help them become scientists uniquely suited to the 21st-century workplace, equipped with a deeper and broader scientific knowledge than that acquired with a Bachelor of Science degree and the skills to apply it.

The experiment has yielded promising results. Beginning with seed money from the Alfred P. Sloan Foundation to establish individual PSM programs at existing institutions and an endowment from the W. M. Keck Foundation to establish the Keck Graduate Institute of Applied Life Sciences, the experiment has resulted in 128 PSM programs now under way at 64 universities in 23 states, producing about 600 graduates per year. (Examples of these PSM programs are listed in the table on the right.) The America COMPETES Act (Public Law 110-69) provides an opportunity for further growth by authorizing the National Science Foundation (NSF) to provide grants for the creation or expansion of up to 200 programs. With broader support from the community, these programs could engage and benefit far more students and employers, providing a powerful contribution to our nation's competitiveness. That was the conclusion of a recent study from the National Research Council, for which I served as chair (*2*).

The report committee found that many stu-

Professional Science Master's Programs*

Institution and Field	Description and Features
California State University, Chico Environmental Sciences	Targeted to scientists who want to improve their business skills, the program includes business training complemented by science training in fields such as agriculture, biology, chemistry, and engineering. www.csuchico.edu/psm
Middle Tennessee State University Biotechnology	Designed to prepare students for careers in the management of bioscience firms and organizations—specifically, research positions in laboratories applying biotechnology to problems in medicine, industry, and agriculture; and management positions in the biotechnology and pharmaceutical industries. Most students are full time. http://frank.mtsu.edu/~msps
University of Connecticut Applied Genomics	Designed to train scientists with interdisciplinary competency in genetics, molecular biology, and computational analysis. The program is intended to meet the needs of biotechnology and pharmaceutical companies and to prepare for genomics-related work in the law enforcement, legal, and political communities. www.smasters.uconn.edu/applied_genomics
Georgia Institute of Technology Bioinformatics	Designed to give students the knowledge and skills necessary to start a career in industry as a bioinformatics or biocomputing specialist. www.biology.gatech.edu/graduate-programs/bioinformatics/new/program_overview.php
Michigan State University Food Safety and Toxicology	The Online Master of Science in Food Safety Program was created in response to recognizing an undeniable need on the part of the food industry, government, and public health for their employees to be specifically educated in the many aspects of safeguarding our food supply. http://online.foodsafety.msu.edu
State University of New York at Buffalo Computational Chemistry	Focuses on how to apply existing chemical software to problems in quantum chemistry, molecular biology, environmental chemistry, and industrial chemistry, for example. Training in business and ethics is also included, and training in software development is available. The program is geared primarily to full-time students. http://professionalmasters.cas.buffalo.edu
Arizona State University Nanoscience	The program consists of interdisciplinary courses that provide a knowledge base required for full appreciation of research and innovation in nanoscience and nanotechnology. Students choose courses in physics, chemistry and biochemistry, materials science, biotechnology, and intellectual property and innovation. http://physics.asu.edu/graduate/psm/overview
Worcester Polytechnic Institute Quantitative Finance	Designed to prepare students for quantitative careers in the financial industry, including banks, insurance companies, and investment and securities firms. The curriculum includes mathematics and statistics courses along with studies in financial management, information technology, and/or computer science. www.wpi.edu/Academics/Depts/Math/Grad/financial.html

* From program Web sites and the Council of Graduate Schools.

R. R. Colwell is former director of the National Science Foundation, Distinguished University Professor at the University of Maryland and the Johns Hopkins Bloomberg School of Public Health, and Senior Advisor, Canon U.S. Life Sciences. She recently chaired a National Research Council committee that wrote the report *Science Professionals: Master's Education for a Competitive World*. E-mail: rcolwell@umiacs.umd.edu

Published by AAAS

dents who could have useful and interesting careers in the sciences shy away from graduate school, uncertain about both the length of study for the doctorate and the career outcomes. PSM degree programs, typically 2 years in length, offer a different path for these students, whose interests and talents might otherwise be lost to the scientific work force.

Indeed, the creation of PSM programs could provide the United States with a competitive advantage by both providing opportunities for more domestic students in graduate science and attracting international talent as well. PSM program data have already shown that these programs have attracted greater numbers of women than other graduate programs in similar fields; it is hoped that this can be extended to underrepresented minorities as well. Meanwhile, programs in areas such as bioinformatics have begun to attract large numbers of international students.

Those who follow the PSM path will likely find employers—whose work-force needs are evolving—eagerly awaiting them, our study found. Biotech companies, information technology firms, banks and financial companies, and government agencies have testified to their need for employees with the knowledge and skills these programs cultivate. And the salaries of those who hold master's degrees in science and engineering have grown faster over the last 10 years than salaries of those with bachelor's degrees or Ph.D.'s.

Members of this new cadre of science-trained professionals become investment analysts, science and technology acquisition managers, and forensic scientists. They work in emerging fields such as business intelligence, which uses data mining and mathematical modeling to solve business problems, and service science, which seeks ways to increase industry productivity and efficiency in the rapidly growing service economy. Some PSM graduates can be predicted to emerge as leaders in industry, government, and nonprofits.

In these jobs for which they are so well qualified, PSM graduates will benefit both individual employers and our nation's ability to compete in the global marketplace. The capacity to innovate depends not only on scientific discovery but also on the ability to translate new knowledge into products and services. This is where PSM graduates can have a major impact. To accomplish this on a broad scale—especially for expanding industries such as biotechnology, which increasingly are focused on production—current PSM programs need to be scaled up and new programs created, a challenge for the concerted action of government, universities, foundations, and employers.

The report recommends Congress take the lead by fully funding and expanding the PSM initiative it authorized at the NSF in the 2007 America COMPETES Act. Congress has now provided an initial $15 million at the NSF for the PSM through the American Recovery and Reinvestment Act, which became law in February. These funds are available through 30 September 2010. Congress has an opportunity to provide additional funding under the COMPETES Act authorization in the Fiscal Year 2010 Budget; after that, Congress will need to provide both new authorization and appropriation. This initiative should be expanded to include other federal science agencies.

Congress should also add scholarships for U.S. citizens who enroll in PSM programs. The typical cost of a program varies greatly, depending on the type of institution, and so far PSM students have had to fund their master's education. This is unlike many Ph.D. students who receive support through fellowships and research and teaching assistantships. However, it is not unlike students in professional programs in law, business, public policy, or medicine, who see the cost of such education as an investment in themselves that will pay off in the long run. Scholarships will allow many more students, particularly those from less advantaged backgrounds, to participate in PSM programs and will expand the number of domestic students who continue in science at the graduate level. In the meantime, many PSM programs are preparing to meet the educational needs of veterans who will benefit from the Post-9/11 Veterans Education Assistance Act, which became law in July 2008.

States, which have had a historic role in both higher education and economic development, must also play a role. They should regard PSM programs as critical to producing a cadre of science professionals who can manage and grow science- and technology-based industries in their states and regions and make wise investments to support them. In several states—North Carolina, New York, and California, for example—state universities have established systemwide plans for PSM programs across their campuses to meet key economic needs.

Universities, in turn, should continue to support existing programs, to create new ones, and to ensure that curricula evolve to reflect scientific developments and work-force needs. PSM programs have a responsibility within this context to engage in ongoing evaluation that will provide feedback on both processes and outcomes. This information will allow for midcourse corrections to increase program effectiveness.

Employers must be key partners in these efforts. PSM programs need to establish employer advisory boards and work with them to develop and evolve curricula and to develop linkages to the workplace. Employers can additionally sponsor student team projects, provide mentoring and internship opportunities for students, and hire graduates who meet their personnel needs.

To be sure, there are challenges in the development of PSM programs. A case must be made that funds for PSM development are a wise investment, justifying the opportunity costs. Individual faculty members also need to support these programs. While some do, others view master's level education only as an incidental step for doctoral students. Worse, they claim to be too busy to give it attention. With appropriate incentives—program resources, credit for program development in tenure review—surely, more faculty would participate in starting and sustaining these programs.

Professional organizations in the sciences have a role as well. These societies historically have focused on encouraging and supporting the work of a doctorate-educated work force, but many are now considering a broader role in advancing education. The professional societies should take master's education under their wings—creating committees to foster master's education, recognizing faculty who have led successful PSM programs, and serving as field-specific clearinghouses of information about the programs.

PSM programs can make a vital contribution to this century's work force, which needs employees who can work well in teams and across disciplines (*3*). It is time for leaders in government, education, and industry to show similar teamwork in supporting these programs—an investment to yield a talented group of scientists with the skills our nation requires most to meet the global challenges of the 21st century.

References and Notes

1. R. R. Colwell, *Bioscience* **58**, 3 (2008).
2. National Research Council, *Science Professionals: Master's Education for a Competitive World* (National Academies Press, Washington, DC, 2008); www.nap.edu/catalog.php?record_id=12064.
3. The PSM has also been endorsed in reports by the National Science Board, the President's Council of Advisors on Science and Technology, the Council on Competitiveness, the U.S. Chamber of Commerce, the Association of American Universities, the Council of Graduate Schools, and the National Governors Association [see Appendix I of the study report (*2*) for details].

10.1126/science.1171209

CELL BIOLOGY

The Art of Making an Exit

Bacteria can pass from one cell to another through a cytoskeletal structure that prevents host cell destruction.

Fredric Carlsson and Eric J. Brown

Pathogenic bacteria can replicate either outside or inside susceptible host cells. Outside the cells, they must evade or inhibit circulating host defense molecules such as antibodies, complement, and lectins, as well as professional phagocytes that function to kill the invading pathogens (*1*, *2*). But bacteria with an intracellular life-style face challenges too. They must get adequate nutrition from their intracellular milieu and spread to new host cells to sustain themselves in this niche. However, rupture of the host cell exposes bacteria to potent immune effectors in the extracellular milieu. To overcome this problem, bacteria have evolved strategies for direct cell-to-cell transmission, chiefly by exploiting the host cell's actin cytoskeleton (*3*). On page 1729 of this issue, Hagedorn *et al.* (*4*) describe a new actin-based strategy to promote spread of infection.

The best understood cell-to-cell transmission of bacteria is by *Listeria monocytogenes*, a foodborne occasional human pathogen. The bacterium polymerizes host cell actin to generate motive force that ultimately leads to a host cell membrane protrusion containing the microbe. The protrusions are subsequently ingested by neighboring cells. In the newly infected cell, *Listeria* are contained within a double-membrane vacuole, which they escape by lysing the vacuolar membranes. The bacteria thus take up residence in the cytosol of the new cell, where they polymerize actin and repeat the infectious cycle (*5*, *6*).

Much less is known about how other cytoplasmic bacteria spread from cell to cell, a problem addressed by Hagedorn *et al.* Using the genetically tractable model system of infection—*Dictyostelium discoideum* amoeba as a host cell and *Mycobacterium marinum* as the infectious microbe—the authors identified a bacteria-induced actin-containing structure—the "ejectosome"—by which cytosolic *M. marinum* exit infected cells in a nonlytic process (see the figure). Previous studies have shown that *M. marinum* escape from phagosomes and polymerize actin in the cytoplasm, leading to bacterial motility and cell-to-cell spread (*7*, *8*). Actin polymerization and motility depend on the host molecule Arp2/3, as is the case for *Listeria*. Activation of Arp2/3-mediated actin polymerization by *M. marinum* requires a member of the Wiskott-Aldrich syndrome protein (WASP) family, whereas *Listeria* bypasses this step for host Arp2/3 complex activation (*8*). The specific molecules on the surface of *M. marinum* required to activate actin polymerization and motility are not known, but the lipid-rich "waxy coat" of the bacterium is thought to participate because a lipid-binding region of N-WASP is necessary for bacterial recruitment of the Arp2/3 complex (*8*).

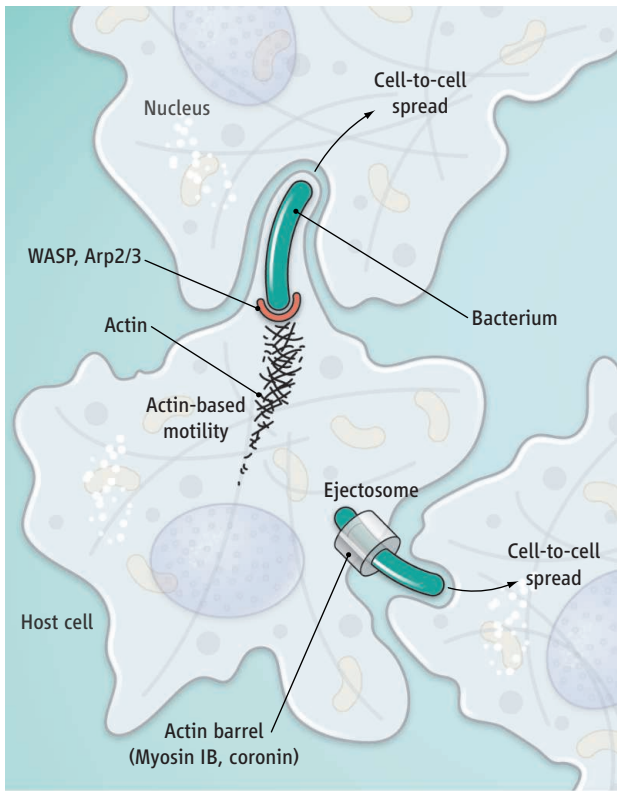

Moving out and about. *M. marinum* escapes from intracellular vacuoles in infected host cells and polymerizes actin into a tail that propels it forward, leading to membrane protrusions containing the bacterium. The protrusion is engulfed by adjoining cells. An independent mechanism of cell-to-cell spread is the ejectosome, an actin barrel through which a bacterium exits the host cell in a nonlytic process.

Pathogenic mycobacteria have a specialized secretion system required for virulence, called ESX-1, or type VII secretion (*9*). For both *M. marinum* and *M. tuberculosis*, ESX-1 is required for efficient cell-to-cell spread (*10*–*12*), but its role in this process has been poorly understood. ESX-1 causes direct host membrane damage (*10*), which may explain both phagosome escape (*10*) and lysis of the host cell plasma membrane (*13*), leading to spread of infection. However, this lytic model is challenged by Hagedorn *et al.*, who suggest a fundamentally different ESX-1–dependent exit strategy.

In *Dictyostelium*, *M. marinum* induces formation of a barrel-shaped, actin-containing structure surrounding a bacterium as it crosses the host cell plasma membrane in an outward journey. Importantly, although this process requires the ESX-1 secretion system, analysis with impermeable probes shows that bacterial egress is nonlytic—possibly because the host plasma membrane provides a dynamic and tight seal around the bacteria as they are exiting. The barrel-shaped ejectosome is thus fundamentally distinct from actin-mediated bacterial motility, and its genesis involves the host cell molecules RacH, Myosin IB, and coronin, but not Arp2/3. Although a few bacteria with short actin tails were observed, bacteria in the process of ejection were rarely associated with actin tails. Thus, the source of the force required to propel a bacterium through an ejectosome remains unknown. In *Dictyostelium*, ejection often occurred into the extracellular milieu. However, in infected metazoan hosts, if the ejection were to occur near a susceptible host cell, which is likely, this could facilitate spread of bacterial infection. Indeed, ESX-1 attracts uninfected macrophages to adhere to infected cells (*14*), and thus could facilitate this process. Does *M. marinum* coordinate both distinct mechanisms of actin polymerization during infection? The dependence of its cell-to-cell transmission on WASP proteins implies that Arp2/3-mediated actin polymerization has a

CREDIT: C. BICKEL/*SCIENCE*

Department of Microbial Pathogenesis, Genentech Inc., South San Francisco, 1 DNA Way, CA 94080, USA. E-mail: carlsson.fredric@gene.com; brown.eric@gene.com

Published by AAAS

role in transmission (*8*), and Hagedorn *et al.* implicate the ejectosome in this process as well. The authors did not observe prominent actin tails in infected *Dictyostelium*; whether actin-based motility plays less of a role in cell-to-cell spread in this host, or whether the shorter actin tails imply a different equilibrium between actin polymerization and depolymerization in *Dictyostelium*, is unclear. It could be that decreased motility facilitates ejectosome formation or that the prominent membrane protrusions induced by rapidly motile bacteria, as previously observed for *M. marinum* in macrophages (*7*), make ejectosomes more difficult to observe. Understanding whether these two modes of cell-to-cell spread represent alternative or complementary virulence strategies will shed light on the diverse biological functions of ESX-1.

Intriguingly, Hagedorn *et al.* also provide evidence that *M. tuberculosis* might use ejectosomes as an exit strategy, both in *Dictyostelium* and mammalian cells. *M. tuberculosis* is a major threat to human health globally, and there is an urgent need to improve our basic understanding of its pathogenesis. *M. tuberculosis* is unable to form actin tails (*15*), implying that this feature of *M. marinum* virulence might not apply to *M. tuberculosis* pathogenesis. Even the ability of *M. tuberculosis* to escape phagosomes in mammalian cells is extremely controversial. Characterizing the molecular mechanisms of ejectosome-mediated exit in mammalian cells, and addressing the importance of ESX-1–mediated ejectosome escape to mycobacterial pathogenesis in general, and *M. tuberculosis* in particular, will be important challenges for the future.

References

1. M. W. Hornef, M. J. Wick, M. Rhen, S. Normark, *Nat. Immunol.* **3**, 1033 (2002).
2. D. M. Underhill, A. Ozinsky, *Annu. Rev. Immunol.* **20**, 825 (2002).
3. J. M. Stevens, E. E. Galyov, M. P. Stevens, *Nat. Rev. Microbiol.* **4**, 91 (2006).
4. M. Hagedorn, K. H. Rohde, D. G. Russell, T. Soldati, *Science* **323**, 1729 (2009).
5. E. Gouin, M. D. Welch, P. Cossart, *Curr. Opin. Microbiol.* **8**, 35 (2005).
6. L. G. Tilney, D. A. Portnoy, *J. Cell Biol.* **109**, 1597 (1989).
7. L. M. Stamm *et al.*, *J. Exp. Med.* **198**, 1361 (2003).
8. L. M. Stamm *et al.*, *Proc. Natl. Acad. Sci. U.S.A.* **102**, 14837 (2005).
9. A. M. Abdallah *et al.*, *Nat. Rev. Microbiol.* **5**, 883 (2007).
10. L. Y. Gao *et al.*, *Mol. Microbiol.* **53**, 1677 (2004).
11. K. M. Guinn *et al.*, *Mol. Microbiol.* **51**, 359 (2004).
12. N. van der Wel *et al.*, *Cell* **129**, 1287 (2007).
13. I. C. Koo *et al.*, *Cell Microbiol.* **10**, 1866 (2008).
14. H. E. Volkman *et al.*, *PLoS Biol.* **2**, e367 (2004).
15. L. M. Stamm, E. J. Brown, *Microbes Infect.* **6**, 1418 (2004).

10.1126/science.1172254

BIOCHEMISTRY

Through a Mirror, Differently

Crystal structures elucidate how some enzymes can bind many different molecules, including mirror-image isomers.

Jonathan A. Sheps

Enzyme-catalyzed reactions are typically stereospecific, affecting only one of a given pair of mirror-image isomers. This arises from a close fit between substrate molecules and the binding surfaces of proteins. But some enzymes do not conform to this expectation. For example, P-glycoprotein (P-gp) catalyzes the movement of dozens of distinct classes of compounds—from peptides to steroids, including pairs of stereoisomers—across cellular membranes. How does it perform this feat? On page 1718 of this issue, Aller *et al.* (*1*) report crystal structures of a mammalian P-gp, both with and without a stereo pair of inhibitor molecules bound to it. The results show how P-gp recognizes multiple substrates via specific, but multiple and partially overlapping, binding sites.

P-gp is the leading cause of multidrug resistance in cancer, where a single genetic change can lead to its overexpression, frustrating chemotherapy treatments. Since P-gp was first identified in the 1970s (*2*), there has been some understandable disbelief that a single protein could interact directly with the full range of molecules whose intracellular concentrations it controls.

P-gp is a membrane-bound adenosine triphosphatase that is a member of a large family of adenosine triphosphate (ATP)–dependent transporter proteins, the ABC (ATP-binding cassette) gene family. Members of this family are present in all living cells, where they carry out various essential roles by transporting molecules across cellular membranes (*3*). Indeed, the three-dimensional structures presented by Aller *et al*. strongly resemble those of related multidrug resistance proteins from bacteria, suggesting that the mechanisms coupling substrate recognition with transport may be the same throughout this protein family (*4*, *5*).

Molecular genetic and biochemical studies of P-gp in model systems—including in vitro

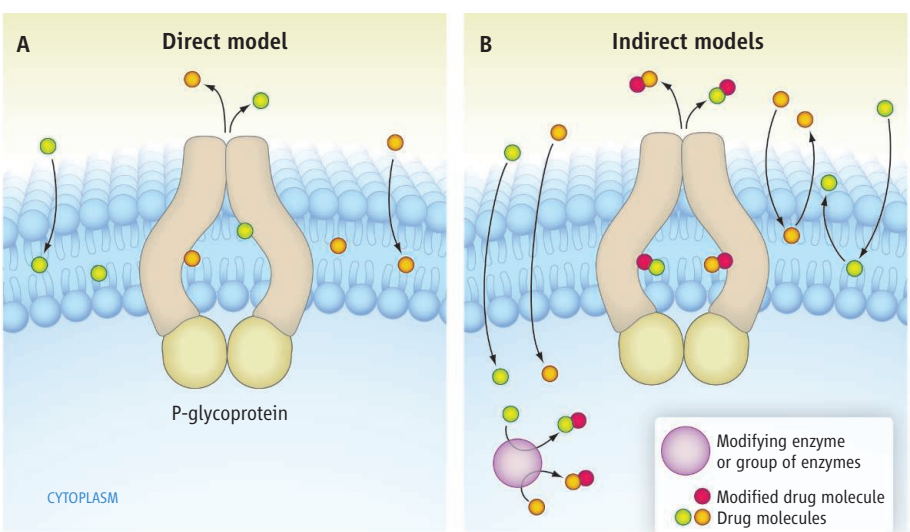

Different views of P-gp action. The direct transport model (**A**) posits that many different drug molecules are recognized by different sites on P-gp before efflux. In contrast, indirect models (**B**) suggest either that drug molecules are modified by enzymes in the cell, creating a common recognition feature for recognition and efflux by P-gp, or that the activity of P-gp alters the cell membrane so as to render it impermeable to the drugs. The P-gp crystal structures reported by Aller *et al.* provide support for the direct transport model (panel A).

CREDIT: P. HUEY/*SCIENCE*

Cancer Genetics and Developmental Biology, BC Cancer Research Centre, British Columbia Cancer Agency, Vancouver, BC V5Z 1L3 Canada. E-mail: jsheps@bccrc.ca

cultures of mammalian cells as well as bacteria expressing other ABC transporters—have led most researchers to believe that P-gp operates by directly binding and transporting multiple types of substrate molecules out of cells (*6*) (see the figure, panel A). Nevertheless, controversy remains. Alternative models have been proposed in which P-gp alters a single cellular feature, such as intracellular pH and/or membrane fluidity, which then alters the permeability of cell membranes to multiple drugs (*7*), or a common enzymatic modification of multiple drugs provides a core feature recognized by the transporter (*8*) (see the figure, panel B).

The direct transport model is supported by transport assays using purified P-gp reconstituted into artificial lipid membrane systems. These assays suggested that P-gp can extract its substrates directly from the inner lipid leaflet of the membrane bilayer (*9*), that the transporter can bind at least two substrate molecules simultaneously, and that substrates can interact with one another while bound to the transporter (*10*), thus modulating one another's binding kinetics.

The new crystal structures confirm several features of the direct transport model, for example, showing that the substrate-binding pocket of P-gp is open at its sides to the inner leaflet of the membrane. One of the substrate-bound crystals shows two molecules of SSS-QZ59 (the SSS isomer of QZ59, a cyclic hexapeptide) bound simultaneously and asymmetrically to the protein, whereas co-crystals of the protein with RRR-QZ59 show a single molecule binding in a position that partially overlaps both of its isomer's binding sites. By offering physical confirmation of multiple drug recognition, this work moves us closer to a resolution of this debate. In so doing, it marks the culmination of an epoch in the multidrug-resistance field.

The finding of multiple substrate binding, and especially of two substrate molecules binding simultaneously to the P-gp structure, opens the door to detailed explanations of the wealth of previous biochemical findings in this system. For instance, crystallization of P-gps with additional substrates should permit a mechanistic explanation for the observed cooperativity between substrates bound at different sites. Future prospects for rational drug design based on these crystal structures are not limited to the discovery of new drugs targeting P-gp. They also include prediction of interactions between pairs of drugs that are P-gp substrates. Given that P-gp is expressed in the blood-brain barrier as well as major organs of drug elimination such as the liver and kidneys, this work is relevant to the pharmacology of many drugs, well beyond the cancer treatment context in which P-gp first became known.

References

1. S. G. Aller *et al.*, *Science* **323**, 1718 (2009).
2. M. M. Gottesman, V. Ling, *FEBS Lett.* **580**, 998 (2006).
3. M. Dean, A. Rzhetsky, R. Allikmets, *Genome Res.* **11**, 1156 (2001).
4. R. J. Dawson, K. P. Locher, *Nature* **443**, 180 (2006).
5. R. J. Dawson, K. P. Locher, *FEBS Lett.* **581**, 935 (2007).
6. H. W. van Veen, C. F. Higgins, W. N. Konings, *Res. Microbiol.* **152**, 365 (2001).
7. C. Rauch, A. Pluen, *Eur. Biophys. J.* **36**, 121 (2007).
8. B. T. Zhu, *Mol. Carcinog.* **25**, 1 (1999).
9. A. B. Shapiro, V. Ling, *Eur. J. Biochem.* **250**, 122 (1997).
10. A. B. Shapiro, V. Ling, *Eur. J. Biochem.* **250**, 130 (1997).

10.1126/science.1172428

CHEMISTRY

Producing Transportation Fuels with Less Work

New reaction chemistry may reduce the energy input and carbon dioxide emissions from processes that convert coal into liquid fuels.

Diane Hildebrandt,[1] David Glasser,[1] Brendon Hausberger,[1] Bilal Patel,[1] Benjamin J. Glasser[2]

The long-term strategy for reducing emissions of carbon dioxide (CO_2) and other greenhouse gases is to replace fossil fuels with renewable resources. In the short term, liquids derived from fossil resources will be used to power transportation, in part because liquid fuels have an established production and delivery infrastructure as well as high energy density. Liquid fuels are overwhelmingly derived from increasingly scarce crude oil, and it would thus be beneficial to make liquid fuels from other sources, such as coal and biomass (*1*, *2*).

One reason why liquid transportation fuels are derived from petroleum instead of coal is that converting coal into liquids is much more energy-intensive. Thus, substantially less CO_2 is released in the production of a gallon of gasoline derived from petroleum than in the production of fuel from coal-to-liquids (CTL) processes (*1*). The carbon atoms in coal are largely bonded to one another in graphitic networks, and breaking these bonds requires a large energy input. Energy is also needed to supply hydrogen to the process. We outline reaction chemistry and processing designs that could dramatically reduce these energy inputs and minimize the amount of CO_2 emissions that would be emitted or mitigated by other costly strategies, such as carbon capture and sequestration (*3*).

There are many methods that convert carbon-rich sources into liquid fuels, including pyrolysis, direct liquefaction, and indirect liquefaction, which proceeds through gasification such as the Fischer-Tropsch (FT) and methanol-to-olefins (MTO) processes (*2*, *4*). Of these, the FT process

$$3C + 4H_2O \rightarrow 2CO + 4H_2 + CO_2 \rightarrow 2(-CH_2-) + 2H_2O + CO \quad (1)$$

(where CO is carbon monoxide and $-CH_2-$ represents the alkane products) has been successfully implemented on the largest scale industrially (*2*, *5*) but is very inefficient in that a large part of the carbon fed into the process ends up as CO_2, either directly or indirectly from fuel consumption for heating the reaction (*5*). However, FT technology gasifies the coal so that unwanted ash, heavy metals, and sulfur can be removed (*2*).

To identify more efficient ways to run chemical processes, theoretical tools have been developed that can look at the industrial plant as a whole (*6*–*9*), even at the level of rethinking the reaction chemistry. These tools assess what would happen if we could operate the plant as efficiently as possible (that is, near thermodynamic reversibility).

For example, thermodynamic principles have been applied to examine the production of molecular hydrogen (H_2) by thermochemical cycles (*6*). By analyzing reversible processes, limits can be placed on the best performance that can be achieved for a given cycle. For example, H_2 could be produced through chemical reactions powered directly

[1]Centre of Material and Process Synthesis, Department of Chemical and Metallurgical Engineering, University of the Witwatersrand, Johannesburg 2050, South Africa. [2]Department of Chemical and Biochemical Engineering, Rutgers University, Piscataway, NJ 08854, USA. E-mail: diane.hildebrandt@wits.ac.za

by the heat from a nuclear reactor, such as zinc reacting with water to produce zinc oxide and H_2. The zinc is recovered by heat-driven decomposition of zinc oxide. A thermodynamic analysis has shown that the currently proposed thermochemical cycles for producing H_2 cannot compete with electrolysis of water through direct use of electricity (*6*).

Thermodynamic analysis of reversible processes can be coupled with theoretical efficiencies to allow comparison of real processes. Such an analysis was performed for direct H_2 use for transportation, and the findings were compared with other strategies for reducing greenhouse emissions and U.S. oil imports (*6*, *10*). This work has brought to light serious concerns about the feasibility of an H_2 economy.

However, recent work suggests a path forward for the sustainable production of liquid hydrocarbon fuel for transportation that would make use of H_2 produced from carbon-free energy, such as solar or wind (*1*, *11*). These processes add H_2 to the syngas (CO and H_2) produced from gasification of biomass, and convert this mixture to liquid fuels via the FT process. If H_2 is coupled with coal as the carbon source to produce liquid hydrocarbons via FT, then there is potentially no additional CO_2 release to the atmosphere in replacing crude oil with coal (*1*).

A disadvantage of these approaches is that they borrow inputs from alternative energy sources. A different strategy is to improve the energy use in the FT process, and a thermodynamic analysis has revealed a somewhat paradoxical route that pushes the initial steps toward a more oxidized initial product, CO_2, rather than CO, and then feeds CO_2 and H_2 into the hydrocarbon synthesis part of the process (*9*).

To understand how this improvement works, consider that steps that require large inputs of work and heat are potential sources of inefficiency (*12*–*14*). For example, if the CTL process produces alkanes from a feed of coal and water (see the figure), the overall process requires 58 kJ/mol of heat per $–CH_2–$ unit to be added. In addition, the reversible process requires about 41 kJ/mol of work to be added, which, in a facility that produces 80,000 barrels per day, amounts to at least 350 MW of work that must be added (*9*).

The two steps of the CTL process can be viewed as a heat engine (see the figure). The first step is a high-temperature endothermic reaction that converts the solid coal into gases. This heat input, by virtue of its temperature, carries work W_{in} that must be equal to or greater than the Gibbs free energy change of this process. The second step, the FT synthesis reaction, is a low-temperature exothermic process that emits heat and carries work W_{out} out with it. Again, W_{out} should be equal to the Gibbs free energy of this reaction for this step to be reversible. The net work for the overall process is the difference between W_{in} and W_{out} and is equal to the change in the Gibbs free energy of the overall reaction.

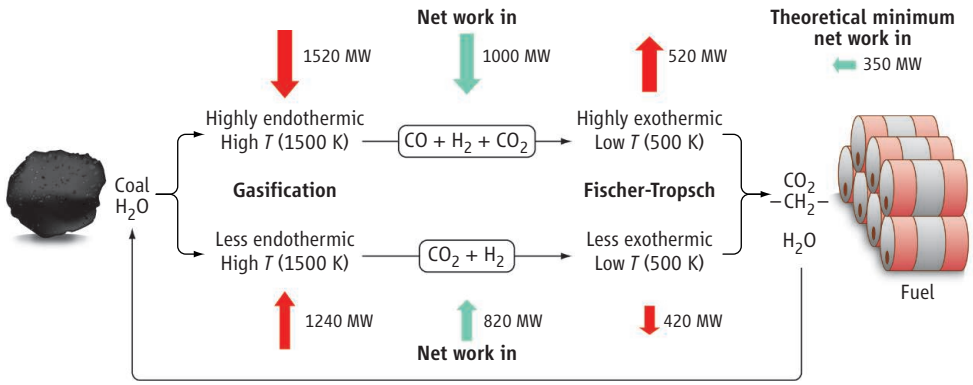

Reducing the work. Improvements in efficiency of the Fischer-Tropsch process can be achieved with a carbon dioxide and hydrogen route, rather than the traditional carbon monoxide and hydrogen route. The processes shown would produce 80,000 barrels of liquid fuel per day and have a theoretical minimum work of 350 MW; the work (via heat) inputs for each stage and for the overall processes are shown as red and green arrows.

The conventional FT process is inefficient because it requires too much work to be put in the gasifier and emits too much work from the FT reactor. The gasification process adds more than four times as much work as is needed to run the plant reversibly. Even if electricity is generated from the steam produced in the FT process, the net work added is still nearly three times the minimum amount needed.

More efficient operation requires decreasing both W_{in} and W_{out}. A way to run both reactions to achieve this goal is for the gasifier not to produce CO and H_2 but rather CO_2 and H_2, which is a less endothermic process (*9*, *15*). Furthermore, making fuel from CO_2 and H_2 is less exothermic (see the figure). The synthesis reaction may not go directly via the new gas mixture, but when combined with the reverse water-gas shift reaction, which converts CO_2 and H_2 to CO and H_2O, the process

$$3C + 6H_2O \rightarrow 3CO_2 + 6H_2 \rightarrow$$
$$2(–CH_2–) + 4H_2O + CO_2 \qquad (2)$$

is feasible. Water can be recycled in both cases, and in the second process, can pump heat back into the gasification section. The CO_2 gasification process requires adding about 20% less work to the gasifier than would be required by the CO route. If work is recovered from the heat rejected from the synthesis reactors, the net work required by the overall process in an 80,000 barrels per day facility is 820 MW—nearer the optimum (350 MW) than the conventional route (1000 MW). This process would produce 0.5 MT less CO_2 per year than the conventional route (15% reduction) (*9*).

Note that the second part of the new process also represents a direct way of using CO_2. If H_2 is produced via nuclear, wind, or solar energy, this process becomes a method for consuming CO_2 and may bypass the difficulties in the direct use of H_2 as a fuel (*1*). Technological advances developed for CTL readily transfer to processes for converting natural gas to liquids, and eventually could be adapted to biomass sources.

References

1. R. Agrawal *et al.*, *Proc. Natl. Acad. Sci. U.S.A.* **104**, 4828 (2007).
2. S. Lee, J. G. Speight, S. K. Loyalka, *Handbook of Alternative Fuel Technologies* (CRC Press, Boca Raton, FL, 2007).
3. M. C. Sheppard, R. H. Socolow, *AIChE J.* **53**, 3022 (2007).
4. O. Levenspiel, *Ind. Eng. Chem. Res.* **44**, 5073 (2005).
5. P. Mukoma, D. Glasser, D. Hildebrandt, *Ind. Eng. Chem. Res.* **45**, 5928 (2006).
6. R. Shinnar, F. Citro, *Chem. Eng. Prog.* **103**, 10 (2007).
7. B. Patel, D. Hildebrandt, D. Glasser, B. Hausberger, *Ind. Eng. Chem. Res.* **46**, 8756 (2007).
8. M. Yamamoto, M. Ishida, *Energy Convers. Manage.* **43**, 1271 (2002).
9. D. Hildebrandt, D. Glasser, B. Hausberger, B. Patel, paper presented at the 1st World CTL Conference, Paris, 3 to 4 April 2008.
10. R. Shinnar, F. Citro, *Science* **313**, 1243 (2006).
11. R. Agrawal, M. Offutt, M. P. Ramage, *AIChE J.* **51**, 1582 (2005).
12. I. L. Leites, D. A. Sama, N. Lior, *Energy* **28**, 55 (2003).
13. H. Oaki, M. Ishida, *J. Chem. Eng. Jpn.* **15**, 52 (1982).
14. B. Patel, D. Hildebrandt, D. Glasser, *Ind. Eng. Chem. Res.* **44**, 3529 (2005).
15. D. Hildebrandt, D. Glasser, B. Hausberger, international patent application WO/2007/122498 (2007).

10.1126/science.1168455

VIROLOGY

Pressurized Viruses

Many viruses depend on extremely high pressures to deliver their genomes.

William M. Gelbart and Charles M. Knobler

Unlike all living organisms, most viruses have genomes that consist of single-stranded (ss) RNA rather than double-stranded (ds) DNA. These ssRNA viruses replicate within hours and evolve faster than any organism; their genomes mutate rapidly because—unlike dsDNA—ssRNA replication does not involve proofreading corrections. However, the less common dsDNA viruses enjoy another unique feature: The pressures in them have been found to be as high as 50 atmospheres (*1*–*3*)—more than 10 times the pressures found anywhere else in a living system. How do these high pressures arise, and what roles do they play in viral infectivity?

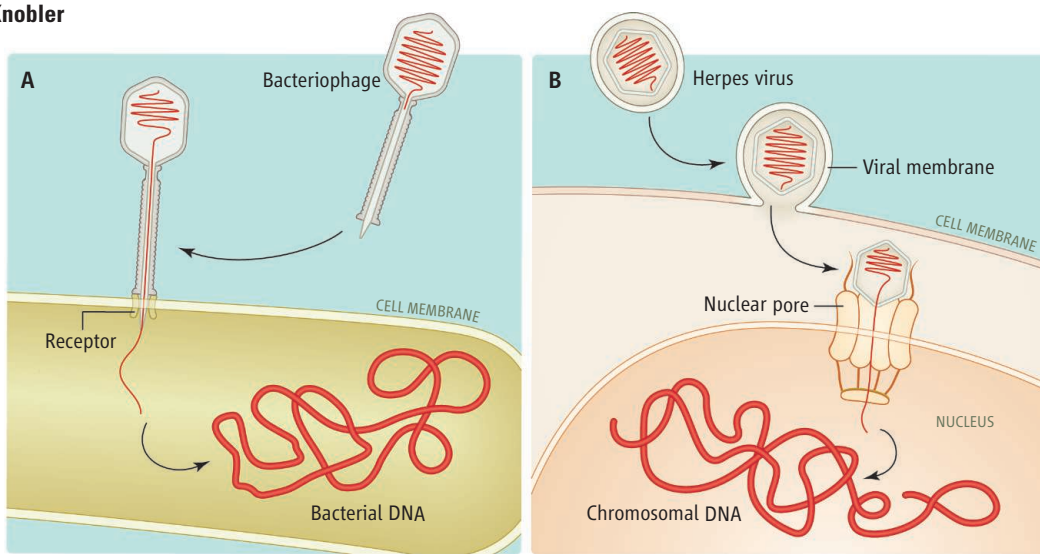

Pressure-driven delivery. (**A**) Upon binding of its tail to a receptor in the outer membrane of the bacterium, the phage injects its DNA genome into its host's cytoplasm. (**B**) A mammalian DNA virus like herpes simplex sheds its membrane upon fusing with that of the host cell; its capsid then binds to a nuclear pore and injects its DNA into the nucleus.

A dsDNA virus consists of its genome surrounded by a single-protein-thick shell or capsid, whose subunits are bound to one another only by hydrophobic, electrostatic, and hydrogen-bonding forces. To package the genome into the preformed capsid, a motor protein must exert forces larger than 50 pN (*4*–*6*)—much larger than the forces exerted by other motor proteins such as RNA polymerase and kinesin. And to withstand the resulting pressures of 50 atmospheres, the protein shell must tolerate tensions of almost 100 mN/m, many times higher than the critical tension of a lipid bilayer membrane.

The biological reason why DNA viruses are so strongly pressurized is to deliver their genomes to the cytoplasm or nucleus of their host cell; the physical reason is that DNA is difficult to compress and yet is confined in a small capsid volume. The capsids must be small because thousands of copies of them must fit into host cells only micrometers in diameter. Consistent with this fact, spherical viruses are ~20 nm to 200 nm in diameter. This range of 10 in diameter corresponds to a range of 10^3 in volume. The smallest viruses—satellite viruses that depend on other viruses for additional gene products—have space for just one gene, whereas the largest ones—the recently discovered mama viruses (*7*)—can fit as many as 1000 genes.

For example, the capsid of the bacterial virus phage λ has an inner radius of ~25 nm; the enclosed DNA genome involves 50 genes, with a total length of 17,000 nm. To fit this length of genome into this volume, the DNA must be essentially close-packed. Indeed, x-ray studies (*8*) have shown that the DNA in bacteriophages is mostly hexagonal close-packed, with interaxial spacings as small as those in crystalline DNA.

At these distances, under physiological conditions, the repulsions between neighboring double-helical portions correspond to pressures of tens of atmospheres (*9*). In contrast, DNA is much more weakly confined in cell nuclei, where it is wound in histone complexes 10 nm in diameter at a density less than one-tenth that in phage capsids, thereby allowing access to transcription factors and other DNA binding proteins.

In 2001, Kindt *et al.* (*10*) provided the first estimate of the packaging forces in DNA viruses. With phage λ in mind, they calculated the force needed to package DNA into a shell whose radius (25 nm) is half the DNA persistence length (50 nm) and a small fraction of the full DNA contour length (17,000 nm). The persistence length is the radius into which DNA can be bent by thermally available energy; to bend it more strongly, work needs to be done by an applied force. The authors predicted the packaging force to increase from a few to tens of piconewtons when 75% of the DNA is packaged. On the basis of measured values of DNA-DNA interactions and bending energies, Tzlil *et al.* (*3*) predicted pressures as high as 50 atmospheres, dominated by the strong self-repulsions of the confined DNA.

Also in 2001, Smith *et al.* (*4*) performed a tour-de-force experiment addressing these issues: a single-molecule measurement of the force exerted by the packaging protein of bacteriophage ϕ29. As in the theory described above, they found that the force increases sharply from a few to tens of piconewtons when about 75% of the genome is packaged. Two years later, Evilevitch *et al.* (*1*) measured the pressure in bacteriophage λ by inhibiting the ejection of its DNA with a counterbalancing osmotic pressure, and found pressures consistent with those predicted by theory (*3*). Subsequent experiments showed that the capsid pressure can be reduced by shortening the genome or by adding salts that permeate the capsid and decrease DNA self-repulsions (*2*). Single-molecule measurements of packaging forces in phages λ (*5*) and T4 (*6*) have provided further evidence that capsid forces and pressures are determined by salt concentrations and the ratio of genome volume to capsid volume, that is, by the strength of DNA-DNA repulsions.

Given these results, high pressures and forces should be a signature of any virus that

Department of Chemistry and Biochemistry, University of California, Los Angeles, CA 90095, USA. E-mail: gelbart@chem.ucla.edu

CREDIT: P. HUEY/SCIENCE

Published by AAAS

delivers its genome by ejection/injection (rather than by disassembly of its capsid). Most of these pressurized viruses are likely to be bacteriophages, which generally do not enter their host cell but rather inject their genome upon binding to the outer cell membrane (see the figure, panel A). The genome involved must be dsDNA, because single-stranded nucleic acid is easily compressible and hence does not get sufficiently pressurized upon being confined.

It is thus no coincidence that most bacterial viruses have dsDNA genomes. In contrast, plant and animal viruses, whose capsids generally enter the cytoplasm of their host cells and then disassemble, mostly have ssRNA genomes. On the other hand, a mammalian dsDNA virus such as herpes, whose capsid enters the cytoplasm of its host cell by passing through the outer cell membrane, must still inject its genome into the nucleus upon binding to a nuclear pore complex (see the figure, panel B). The pressure in its capsid should be comparable to those in bacteriophages. The motor protein that packages its genome is thus expected to exert forces as high as tens of piconewtons.

In many phage life cycles, the freshly replicated, not-yet-packaged DNA genomes are linked together in a polymer. High-resolution cryoelectron microscopy studies on phage P22 (*11*) have revealed the configuration of the packaged DNA and shown how the motor protein complex acts as a pressure sensor when a certain density of DNA is achieved. At this point, packaging stops and the DNA is cut.

As always, new understanding raises new questions. For example, because the host cell cytoplasm has an osmotic pressure of several atmospheres, phage ejection stops when the capsid pressure drops to a few atmospheres; what drives delivery of the rest of the genome? In some cases, it is transcription of the genes that have already been delivered; in others, it may involve the influx of water through the phage to accommodate the growth of the host bacterium (*12*).

State-of-the-art biophysical studies will help to elucidate these and other issues, such as how capsids can withstand pressures on the order of 50 atmospheres. Notable among these studies are the reconstitution of bacteriophage λ "from scratch" (*13*), the probing of elastic properties of individual viruses by atomic force microscopy (*14*), the observation of genome ejection from single viruses by fluorescence microscopy (*15*), and the simulation of protein capsid assembly, as well as single-molecule manipulations and high-resolution cryoelectron microscopy. Much as phages played key roles in the development of molecular biology and the genetic engineering revolution, pressurized viruses are likely to be central to the emerging field of physical virology.

References and Notes

1. A. Evilevitch, L. Lavelle, C. M. Knobler, E. Raspaud, W. M. Gelbart, *Proc. Natl. Acad. Sci. U.S.A.* **100**, 9292 (2003).
2. P. Grayson *et al.*, *Virology* **348**, 430 (2006).
3. S. Tzlil, J. Kindt, W. M. Gelbart, A. Ben-Shaul, *Biophys. J.* **84**, 1616 (2003).
4. D. E. Smith *et al.*, *Nature* **413**, 748 (2001).
5. D. N. Fuller *et al.*, *J. Mol. Biol.* **373**, 1113 (2007).
6. D. N. Fuller D. M. Raymer, V. Kottadiel, V. B. Rao, D. E. Smith, *Proc. Natl. Acad. Sci. U.S.A.* **104**, 16868 (2008).
7. D. Raoult *et al.*, *Science* **306**, 1344 (2004); published online 14 October 2004 (10.1126/science.1101485).
8. W. C. Earnshaw, S. C. Harrison, *Nature* **268**, 598 (1977).
9. D. C. Rau, V. A. Parsegian, *Biophys. J.* **61**, 246 (1992).
10. J. Kindt, S. Tzlil, A. Ben-Shaul, W. M. Gelbart, *Proc. Natl. Acad. Sci. U.S.A.* **98**, 13671 (2001).
11. G. C. Lander *et al.*, *Science* **312**, 1791 (2006); published online 17 May 2006 (10.1126/science.1127981).
12. P. Grayson, I. J. Molineux, *Curr. Opin. Microbiol.* **10**, 401 (2007).
13. H. Gaussier, Q. Yang, C. E. Catalano, *J. Mol. Biol.* **357**, 1154 (2006).
14. J.-P. Michel *et al.*, *Proc. Natl. Acad. Sci. U.S.A.* **103**, 6184 (2006).
15. S. Mangenot, M. Hochrein, J. Radler, L. Letellier, *Curr. Biol.* **15**, 430 (2005).

16. Supported by NSF grant CHE-0714411.

10.1126/science.1170645

IMMUNOLOGY

Dangers In and Out

The immune system relies on specific signaling molecules to dampen its response to injury while maintaining the capacity to fight infection.

Marco E. Bianchi and Angelo A. Manfredi

Every organism faces a bewildering array of threats, pathogens foremost among them. But how does the immune system distinguish between an infection and trauma? Both elicit similar inflammatory immune responses. On page 1722 of this issue, Chen *et al*. (*1*) explain why and how the immune system responds appropriately in either scenario.

All mammals have an impressive arsenal of molecules and cells specialized to fight pathogens. Adaptive immunity, in the form of antibody production by B cells and the instruction of "killer" or cytotoxic T cells, is a critical component of the body's defenses. However, this is only a second line of defense that selectively recognizes microbes attacking for a second time. Without a first line of defense—innate immunity—mammals would succumb to pathogens still unrecognized by B and T cells.

The broad outlines of our current understanding were first sketched 20 years ago by Charles Janeway (*2*), starting from the idea that the immune system cannot recognize pathogens individually, because the information required is huge and would rapidly become obsolete. Pathogens continually evolve, confounding the ability of the immune system to recognize them. Instead, immune cells recognize broad molecular patterns rather than detailed features of specific pathogens. Such pathogen-associated molecular patterns (PAMPs) comprise molecular structures that are found in microbes but not in host tissues. Moreover, PAMPs are essential for the survival or the pathogenicity of microbes; thus, they cannot simply do away with PAMPs to evade recognition by the immune system.

Toll-like receptor 4 (TLR4) was the first receptor to be identified that recognizes PAMPs (*3*). It recognizes lipopolysaccharide, a component of the outer membrane of Gram-negative bacteria. As the name implies, it is related to Toll, a receptor involved in pathogen recognition in the fly *Drosophila melanogaster*. Thus, Toll-like receptors are evolutionarily ancient, although their number in mammals has grown to about one dozen.

When cells of the innate immune system—such as macrophages, mast cells, natural killer cells, and dendritic cells—encounter a PAMP, they secrete cytokines and chemokines, soluble molecules that signal "danger" to other cells. The most immediate response is inflammation at the site of infection, and the recruitment of additional immune cells, including neutrophils. Importantly, neutrophils "shoot at first sight," releasing reactive oxygen species and proteases, thereby causing extensive collateral damage to the host tissue. Usually, the intruding pathogens are eliminated, and the adaptive immune system "remembers" their identity in case the organism is reinfected by

San Raffaele University, Faculty of Medicine, and San Raffaele Scientific Institute, via Olgettina 58, 20132 Milano, Italy. E-mail: bianchi.marco@hsr.it

the same pathogens; eventually, the tissue is reconstructed and healed. Inflammation, therefore, is a damaging but essential response, and becomes a problem only when it is excessive, or persists (chronic inflammation).

This picture of pathogen infection is complicated by the fact that physical trauma (such as a wound or a broken bone) causes many of the same effects as invading pathogens, including inflammation. Indeed, pathogens are thought to be initially recognized by the immune system precisely because they cause tissue damage (*4*). How, then, does the immune system recognize tissue damage? Damage-associated molecular patterns (DAMPs) were postulated as the counterparts to PAMPs, with the important distinction that DAMPs should be endogenous—the body's own molecules—just as the PAMPs should be pathogen-borne and thus exogenous. For example, the molecule high mobility group box 1 (HMGB1) fits the hypothetical description of an endogenous danger signal (*5*) and instructs adaptive immunity in ways similar to those elicited by exogenous danger signals (*6*). HMGB1 is a component of chromatin, the DNA-protein complex that makes up chromosomes, and thus normally resides in the cell nucleus. The release of HMGB1 by cells that have died as a result of tissue trauma signals "danger" to neighboring cells and to the immune system. Importantly, HMGB1 is also recognized by the pattern recognition receptors TLR2, TLR4, and TLR9, as well as by the receptor of advanced glycation endproducts, another "danger" receptor (*7*–*9*). Thus, trauma and pathogens (DAMPs and PAMPs) engage the same immune cell receptors, neatly explaining why they elicit the same inflammatory responses, although the molecular details are still largely unknown.

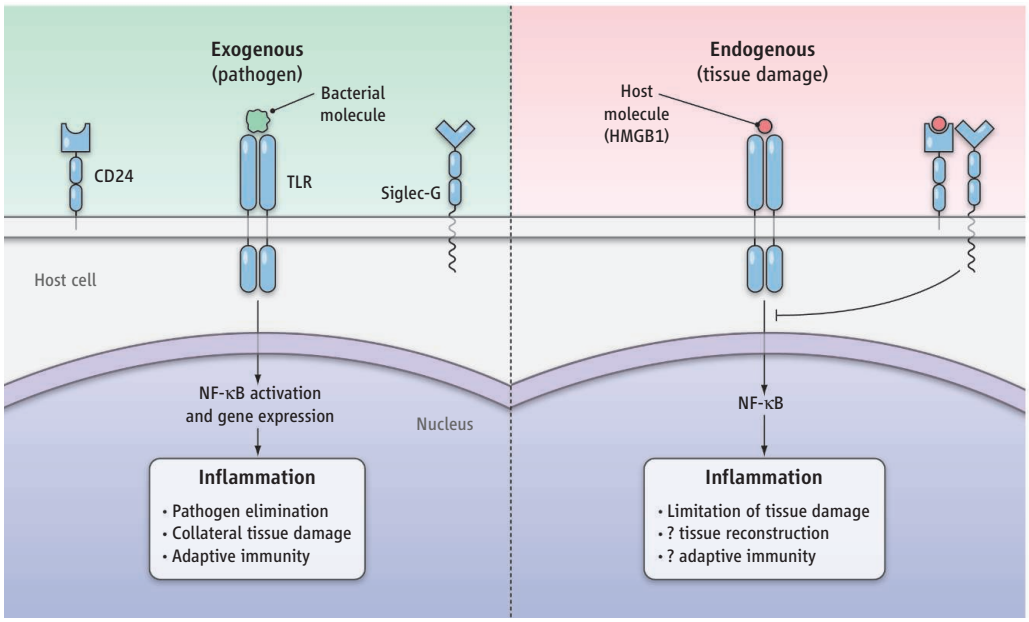

Danger signals. Exogenous and endogenous signals, such as bacterial and host cell molecules, respectively, elicit the inflammatory response through the same Toll-like receptors on immune cells. However, a specific signaling pathway limits the response to endogenous signals. This may prevent a runaway immune response to injuries.

Yet, some outcomes must be different between the two scenarios. Chen *et al.* explored how these partly different outcomes occur by inducing liver necrosis in mice with an excess of acetaminophen. This treatment causes the release of HMGB1, and thus leads to inflammation in the absence of any pathogen. The authors found that mice lacking CD24, a membrane protein expressed by immune and stem cells, developed an inflammatory response that was more powerful and lethal than that in wild-type mice. In fact, HMGB1 was found to directly associate with CD24 and Siglec-G, a member of the sialic acid–binding immunoglobulin-like lectin family. Mice lacking Siglec-G also were sensitive to inflammation due to acetaminophen-induced liver necrosis. CD24 does not contain a cytosolic domain, and signals through Siglec-G, which contains an immune receptor tyrosine-based inhibitory motif (ITIM). ITIMs are cytosolic domains that reduce activation of nuclear factor κB (NF-κB), which is a transcription factor activated by both DAMPs (*10*) and PAMPs (*11*) and is essential for many aspects of the inflammatory response, including the secretion of cytokines and chemokines. The CD24-Siglec complex also recognizes heat shock proteins, another class of endogenous danger signals, but does not respond to lipopolysaccharide or poly-(dI:dC), two exogenous danger signals.

Signaling pathways negatively regulate Toll-like receptor responses to PAMPs as a control for excessive inflammation during infection. It now appears that endogenous danger signals activate a different "braking circuit" that is specific for DAMPs (see the figure). This dampens the immune response to injury and limits collateral damage to the tissue. Interestingly, both HMGB1 and Toll-like receptors appeared early in evolution, but only more modern vertebrates have CD24 and Siglecs. It appears that this particular braking circuit is an add-on to the ancient activating system.

Can the braking circuit also moderate adaptive immunity (which first appeared with fishes), so as to avoid autoimmune responses? CD24 has already been implicated in autoimmunity, and genetic variations in CD24 influence the susceptibility to autoimmune diseases, including multiple sclerosis and lupus (*12*). The CD24-Siglec system might also respond to the various complexes that HMGB1 forms with lipopolysaccahride, interleukin-1β, single-stranded DNA, and nucleosomes. At least one of these complexes, nucleosome-bound HMGB1, is implicated in dendritic cell activation and the production of autoantibodies (*13*). Can the HMGB1-CD24-Siglec system limit the more severe forms of sterile inflammation, such as sepsis? The growing insight into how the immune system distinguishes between internal and external danger is likely to have a substantial impact on therapeutic approaches.

References

1. G.-Y. Chen, J. Tang, P. Zheng, Y. Liu, *Science* **323**, 1722 (2009); published online 5 March 2009 (10.1126/science.1168988).
2. C. A. Janeway Jr., *Cold Spring Harb. Symp. Quant. Biol.* **54**, 1 (1989).
3. R. Medzhitov, P. Preston-Hurlburt, C. A. Janeway Jr., *Nature* **388**, 394 (1997).
4. P. Matzinger, *Annu. Rev. Immunol.* **12**, 991 (1994).
5. P. Scaffidi, T. Misteli, M. E. Bianchi, *Nature* **418**, 191 (2002).
6. P. Rovere-Querini *et al.*, *EMBO Rep.* **5**, 825 (2004).
7. J. S. Park *et al.*, *J. Biol. Chem.* **279**, 7370 (2004).
8. S. Ivanov *et al.*, *Blood* **110**, 1970 (2007).
9. J. Tian *et al.*, *Nat. Immunol.* **8**, 487 (2007).
10. R. Palumbo *et al.*, *J. Cell Biol.* **19**, 33 (2007).
11. T. Kawai, S. Akira, *Trends Mol. Med.* **13**, 460 (2007).
12. Y. Liu, P. Zheng, *Trends Immunol.* **28**, 315 (2007).
13. V. Urbonaviciute *et al.*, *J. Exp. Med.* **295**, 3007 (2008).

10.1126/science.1172794

CREDIT: C. BICKEL/*SCIENCE*

SCIENCE DIPLOMACY

Syrian, U.S. Science and Health Leaders to Explore Cooperation

High-level science, medical, and higher education officials from Syria and the United States agreed to explore future cooperation in health, agriculture, scholar exchanges, and other areas during 4 days of talks in Damascus.

Diplomacy in Damascus. Syrian and U.S. officials recommended science and education cooperaton across a range of fields.

The delegation met for more than an hour with Syrian President Bashar al-Assad, with discussion focused on the central role of science and education in meeting a nation's economic and social needs. The Americans also joined with some of Syria's most influential leaders in research, education, and government for wide-ranging talks, with the hope that science diplomacy could help open a new chapter in relations between the two countries.

The 10-member U.S. delegation was assembled by the Center for the Study of the Presidency and Congress (CSPC) and included Nobel laureate David Baltimore, the immediate past chairman of the AAAS Board of Directors, and two senior AAAS executives. The visit came at a time of new dialogue between the two nations, and both sides characterized the meetings as cordial and constructive.

"Successful cooperation between the United States and Syria in science, education, and health care will serve to help break through political barriers and negative perceptions and serve as a cushion in times of political disagreement," said U.S. delegation leader Pamela Scholl, president of the Dr. Scholl Foundation and a member of the Center's Board of Trustees.

"I was a little apprehensive before the U.S.-Syria dialogue got under way," said delegation sponsor Wafic Saïd, a Syrian-born businessman and philanthropist. "We had essentially brokered a blind date between two highly distinguished delegations, and we had no idea whether they would take to each other. As it turned out, both sides worked together with mutual respect and genuine enthusiasm and we were able to identify concrete opportunities for future collaboration of benefit to both countries."

Though planning for the meetings had been under way for months, the delegation's visit coincided with steps by the administration of U.S. President Barack Obama to explore a possible thaw with Syria, which has been at odds with the United States over a range of regional issues. And it reflects the growing ambition of independent diplomacy efforts by researchers and research organizations in the United States who are making science-based overtures to Iran, Cuba, North Korea, and other nations where governmental relations are strained or nonexistent.

The delegation arrived in Damascus on 9 March, and after a reception that night, the Americans and their Syrian counterparts spent 3 full days in talks and in visits to research and education centers and cultural and historic sites. The Syrian delegation, headed by Dr. Fawaz Akhras, medical director of Cardiac and Medical Healthcare Services at Cromwell Hospital in London, made presentations on Syria's health care and higher education systems and its plans for science- and technology-driven innovation.

Bilateral working groups made a series of recommendations, which were adopted by the delegations. Among them: focus on collaboration in water, energy, and agriculture, where there is joint capacity and mutual interest; help Syrian hospitals win accreditation; consider establishment of a Syrian-American institute for advanced medical practices to help develop programs for medical technicians and nurses; increase exchanges involving science and engineering students and faculty; and look into how the U.S. visa system limits such exchanges.

Delegation member Vaughan Turekian, AAAS's chief international officer, said that in the meeting with Assad, the Syrian president spoke in detail of two top priorities: water use and conservation in agriculture, and building an integrated system of innovation. Turekian, who also directs the AAAS Center for Science Diplomacy, described the meeting as "very productive."

"Throughout the visit, we were welcomed with enthusiasm and warmth," Turekian said. "Though challenges remain, both sides acknowledged that the tensions have gone on for far too long. The visit was an important demonstration of the potential for better relations."

The visit was hosted by Damascus University, and university President Wael Mualla sat on the Syrian delegation. The British Syrian Society, with Akhras serving as co-chair, facilitated the meeting. Among others on the U. S. delegation were Theodore Kattouf, former U. S. ambassador to Syria and the United Arab Emirates; and Norman P. Neureiter, director of the AAAS Center for Science, Technology and Security Policy and senior adviser to the Center for Science Diplomacy.

The U.S. delegation's visit was conceived last fall during discussions between Saïd, who sits on the British Syrian Society's board of directors; CSPC President David M. Abshire, former U.S. ambassador to NATO; and Dr. Hrant Semerjian, a prominent Washington, D.C., physician. The Richard Lounsbery Foundation and the Center for Science Diplomacy also helped organize the meetings.

AAAS ANNUAL MEETING

S&T Leaders Urge New Era of Climate, Energy Policy

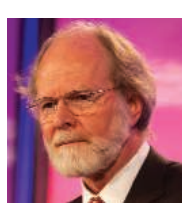

James J. McCarthy

CHICAGO—One hundred and fifty years after Charles Darwin published his elegant demonstration of how natural forces shape a diverse and ever-changing world, scientists at the AAAS Annual Meeting in Chicago warned that those forces are being overwhelmed by human impact.

In his plenary address to open the 2009 meeting, outgoing AAAS President James J. McCarthy said the natural world explored by Darwin is disappearing, overtaken by a

CREDITS: (SYRIA PHOTO) COURTESY OF DAMASCUS UNIVERSITY; (DR. JAMES J. MCCARTHY PHOTO) COURTESY OF COLELLAPHOTO.COM

Published by AAAS

"distinctly new era" in which human activity has left an indelible mark on climate and habitat.

From McCarthy to planetary scientist Susan W. Kieffer to former U.S. Vice President Al Gore, the meeting's key speakers joined in a sobering perspective on Earth's transformation, conceding that certain trends in climate change may now be irreversible.

But they urged the thousands of researchers, policy-makers, educators, and students in attendance to join the search for strategies that will allow humans to halt and perhaps reverse their damaging impact. "The choices to be made are not simple ones," said McCarthy, "but the choices we make today will have profound effect decades out."

While many attendees welcomed the promise of a new U.S. president who supports science and is committed to protecting the climate, McCarthy and others emphasized that significant political challenges lie ahead.

The team of science advisers assembled by President Barack Obama is without equal, said McCarthy, "but these people will need all of our support as this new administration moves aggressively to solve the economic and energy security problems…and at the same time assumes a new role as an international leader in global efforts to curb anthropogenic climate change."

Addressing an audience of 3000, Gore asked scientists to use their knowledge and their respected status in the community to press for broad, swift changes in energy and environmental policies. "We have a full-blown political struggle to communicate the truth," said the 2007 Nobel Peace Prize winner. "And those of you who have not been engaged in trying to communicate effectively in your communities…this is no time to sit back."

Underscoring the need for action, Stanford University biologist Christopher Field offered an ominous update on rising greenhouse gas levels, in a symposium that was widely covered by U.S. and international news media.

A massive release of carbon from shrinking forests and melting permafrost may soon "act like a foot on the accelerator pedal for atmospheric CO_2," warned Field, who is working on the next consensus report from the Intergovernmental Panel on Climate Change. "We are basically looking now at a future climate that is beyond anything that we've considered seriously in climate policy."

Kieffer, a MacArthur Fellow at the University of Illinois Urbana-Champaign, called for the creation of a "CDC for Planet Earth"—an organization that could respond to ocean acidification, spreading deserts, and degraded soils in the same way that the U.S. Centers for Disease Control and Prevention now responds to health crises.

Even as the twin troubles of climate change and a faltering worldwide economy loomed over many of the Chicago symposia, attendees found time to celebrate Darwin's legacy in topics as diverse as the chemistry of kissing and the end of the universe. Local students visited the Field Museum of Natural History during AAAS's Public Science Day to chat with scientists about the role of evolution in modern research.

And in a nod to the great naturalist's interest in human evolution, a team led by Max Planck geneticist Svante Pääbo announced a rough draft of the Neandertal genome at the start of the meeting. The Neandertal project and others like it are bringing about a "second golden age in evolutionary science," said molecular biologist Sean B. Carroll, who suggested in his plenary talk that today's researchers "share the same sense of surprise and discovery" as Darwin and his contemporaries. — *Becky Ham*

ENERGY AND CLIMATE

The Problem with Coal, the Promise of Efficiency

Solar and wind power get a lot of favorable buzz, and nuclear power is always provocative. But at a Washington, D.C., forum sponsored by Hitachi Ltd. and co-organized by the Brookings Institution and AAAS, researchers and business leaders suggested that to protect Earth's climate, it is immediately important to control the harmful impact of coal and use its power more efficiently.

That prescription could have enormous impact as energy demand and greenhouse gas emissions accelerate in the early 21st century, the experts said. The United States and China remain heavily dependent on coal; clean-coal technologies are still experimental and likely to be expensive. And renewable power sources, while promising, aren't yet ready to fill the gap, said Tadahiko Ishigaki, chairman of Hitachi America.

But the forum generated a surprising, albeit cautious, optimism: Efficiency could be the most readily available, least expensive, and most effective approach to reducing emissions.

"Energy efficiency is the near-term essential thing to do because we can wake up and start doing it tomorrow morning," said William Moomaw, director of the Center for International Environment and Resource Policy at Tufts University.

The 5 March forum convened about 400 people to hear discussion under the theme "Meeting Energy Needs, Reducing Environmental Impact." Speakers came from Japan, Brazil, and the United States; Hitachi, Brookings, and AAAS each organized a panel.

Though they covered a broad range of issues, coal was a recurring theme—a power source so important, and so damaging, that speakers insisted it should be an urgent focus of climate policy, science diplomacy, and technological innovation.

In a keynote speech, U.S. Senator John Kerry (D–MA) warned that despite two decades of global discussion, conditions are deteriorating. Carbon dioxide emissions from human sources have grown four times faster in the last 8 years than in the 1990s, he said. CO_2 concentrations in the atmosphere have gone up 33% faster, surpassing the worst-case emission scenarios envisioned by the Intergovernmental Panel on Climate Change.

In that context, coal is "the most intractable problem," said *Science* reporter Eli Kintisch, who moderated one panel. While dozens of coal-fired power plants have recently been cancelled in the United States, speakers noted such plants still account for 50% of the nation's power, and 70% in China. In India, coal-related industries employ 26 million people.

Coal will remain a key power source, several speakers said. And until other sources come online, conservation and efficiency are the best means for reducing demand for electricity—and emissions from coal-fired plants. Kerry cited a recent report by McKinsey & Company which found that energy efficiency alone could yield almost 40% of needed emission reductions.

"Energy efficiency is the world's greatest resource," said Kateri Callahan, president of the Alliance to Save Energy. The United States has "turned to it time and again over the past 30 years to power our economy."

Without past efficiency improvements, Callahan explained, the nation would need to produce 50% more energy today than it does. And the 2007 federal law phasing out incandescent bulbs by 2014 will save as much energy as all other federal appliance standards adopted since 1980.

Panelist Takashi Hatchoji, the chief environmental strategy officer at Hitachi, said that by 2025, the company plans to cut emissions associated with its products by 100 million tons compared to 2005. The key, he said, will be using technological innovation to achieve efficiency in a range of applications, from home appliances to hybrid trains to processes for making steel and cooling massive data centers.

Other speakers described projects that seem sprung from science fiction, but which are all under study: nuclear power fueled by thorium, which is more efficient and poses fewer risks than uranium; industrial processes that extract CO_2 from coal-fired power plants and turn it into cement-like calcium carbonate; and harvesting solar and geothermal power in the American Southwest to power the whole nation.

Physicist Martin Hoffert, a professor emeri- tus at New York University, is exploring how satellites could beam solar energy down to Earth. He and others called for a new era of federal research and development investment in high-risk ventures that could permanently shift the energy-climate paradigm.

As a nation, "our unique talent …has been in breaking the rules and doing things that have never been done before," Hoffert said. "I think this is our destiny."

It may be the world's destiny, as well.

Queen Succession Through Asexual Reproduction in Termites

Kenji Matsuura,[1]* Edward L. Vargo,[2] Kazutaka Kawatsu,[3] Paul E. Labadie,[2] Hiroko Nakano,[1] Toshihisa Yashiro,[1] Kazuki Tsuji[4]

It is unknown how diverse the mating systems of termites, which include inbreeding and asexual reproduction, are and how they are maintained. Termite colonies are founded by one king and one queen, which produce the rest of the colony (*1*, *2*). In the subterranean termites (Rhinotermitidae), secondary neotenic reproductives are produced upon the death of the primary queen and/or king, which may engage in inbreeding for many generations (*3*).

We collected and censused 30 natural colonies of *Reticulitermes speratus* at five field sites. In all but one, the primary queen had been replaced by numerous secondary queens; in the exception, both the primary queen and 128 secondary queens were present (fig. S1 and S2) with 55.4 ± 12.4 (mean ± SEM, $n = 30$) queens present on average. All 1660 secondary queens collected were nymphoid, that is, neotenic reproductives with wing buds differentiated from nymphs (fig. S1). In contrast, 19 of 21 colonies had a single primary king; two had a single secondary king. These results suggest that primary kings live longer than primary queens and that replacement of the primary king may be rare.

Unmated primary queens of *R. speratus* can found colonies through thelytokous, automictic parthenogenesis with terminal fusion (*2*, *4*), but whether parthenogenetic reproduction is part of the breeding system in colonies containing a single king is unknown. Genetic analyses of seven representative colonies (Fig. 1) for different locations with five microsatellite loci (observed heterozygosities from 0.543 to 0.957) were used to genotype 135 secondary queens, one primary queen, six primary kings, one secondary king, 140 workers, and 40 alate nymphs. Nearly all of the secondary queens genotyped (131 of 135) were homozygous at all five loci for alleles from the primary queen (*5*), but none had alleles that could be attributed to the king. Hence, these secondary queens were produced by parthenogenesis (Fig. 1A). Additionally, secondary queens were related to their mother primary queen by one ($r = 0.99$, $SE_{jackknife} = 0.01$, $n = 7$ colonies) but were unrelated to the primary king from the same nest ($r = -0.07$, $SE_{jackknife} = 0.09$, $n = 7$ colonies). In contrast, 100% of the workers (140 of 140, Fig. 1B) and 95% of the alate nymphs (38 of 40, Fig. 1C) were produced by sexual reproduction. Thus, *R. speratus* colonies are composed of secondary queens that are almost exclusively produced parthenogenetically by the founding primary queens, whereas workers and alates are produced by normal sexual reproduction (Fig. 1).

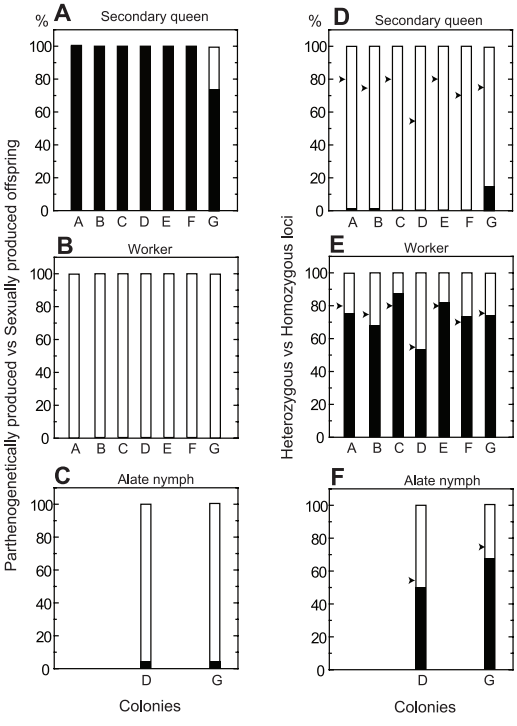

Fig. 1. Respective proportion of parthenogenetically produced offspring (black) and sexually produced offspring (white) in secondary queens (**A**), workers (**B**), and alate nymphs (**C**). Proportion of heterozygous loci (black) and homozygous loci (white) in secondary queens (**D**), workers (**E**), and alate nymphs (**F**). The amounts of heterozygosity expected for offspring produced by outcrossing of the primary king and the primary queen are indicated by arrowheads.

Heterozygosity of workers in colonies headed by secondary queens was as high ($H_o = 0.733$ over all loci) as that expected for offspring produced by outcrossing of the primary king and the primary queen ($H_e = 0.736$; G total = 8.63, df = 7, $P = 0.28$, G test; Fig. 1E). Likewise, there was no significant reduction of heterozygosity in nymphs produced in colonies with secondary queens ($H_o = 0.585$, $H_e = 0.65$; G total = 3.92, df = 2, $P = 0.06$; Fig. 1F), although occurrence of two parthenogenetic nymphs lowered overall heterozygosity somewhat. Further evidence for the lack of inbreeding in *R. speratus* colonies is provided by the low inbreeding coefficient of workers, which did not differ significantly from zero ($F_{IT} = 0.014$, $SE_{jackknife} = 0.048$, over all loci).

By using parthenogenesis to produce secondary queens, primary queens increase their reproductive output while retaining the transmission rate of their genes to descendants and maintaining genetic diversity in the workers and new primary reproductives even after they themselves are replaced (fig. S3). The lack of consanguineous matings in this breeding system may also benefit primary kings because the offspring produced by outcrossing between the king and parthenogenetic queens may have greater fitness than those produced by king-daughter inbreeding. These findings, together with similar reports from the phylogenetically distant ants (*6*–*8*), show that eusociality with its attendant caste structure and unique life histories can generate novel reproductive and genetic systems with mixed modes of reproduction that can provide important insights into the advantages and disadvantages of sexual reproduction.

References and Notes

1. J. S. Shellman-Reeve, *Proc. R. Soc. London Ser. B* **266**, 137 (1999).
2. K. Matsuura, T. Nishida, *Popul. Ecol.* **43**, 119 (2001).
3. B. L. Thorne, J. F. A. Traniello, E. S. Adams, M. Bulmer, *Ethol. Ecol. Evol.* **11**, 149 (1999).
4. K. Matsuura, M. Fujimoto, K. Goka, *Insectes Soc.* **51**, 325 (2004).
5. Materials and methods are available as supporting material on *Science* Online.
6. M. Pearcy, S. Aron, C. Doums, L. Keller, *Science* **306**, 1780 (2004).
7. D. Fournier *et al.*, *Nature* **435**, 1230 (2005).
8. K. Ohkawara, M. Nakayama, A. Satoh, A. Trindl, J. Heinze, *Biol. Lett.* **2**, 359 (2006).
9. We are grateful to K. Shimizu, E. Hasegawa, S. Dobata, and N. E. Pierce for discussion and to W. Booth, D. R. Tarpy, K. Ross, L. Keller, and C. Schal for comments on the manuscript. Funded by the Japan Society for the Promotion of Science (K.M., K.T.) and the Program for Promotion of Basic Research Activities for Innovative Biosciences (K.M.).

Supporting Online Material

www.sciencemag.org/cgi/content/full/323/5922/1687/DC1
Materials and Methods
Figs. S1 to S3
Tables S1 to S8
References

12 December 2008; accepted 17 February 2009
10.1126/science.1169702

[1]Laboratory of Insect Ecology, Graduate School of Environmental Science, Okayama University, Okayama 700-8530, Japan. [2]Department of Entomology and W. M. Keck Center for Behavioral Biology, North Carolina State University, Raleigh, NC 27695–7613, USA. [3]Laboratory of Insect Ecology, Graduate School of Agriculture, Kyoto University, Kyoto 606-8502, Japan. [4]Faculty of Agriculture, University of the Ryukyus, Okinawa 900-0213, Japan.

*To whom correspondence should be addressed. E-mail: kenjijpn@cc.okayama-u.ac.jp

Fermi Observations of High-Energy Gamma-Ray Emission from GRB 080916C

The Fermi LAT and Fermi GBM Collaborations*

Gamma-ray bursts (GRBs) are highly energetic explosions signaling the death of massive stars in distant galaxies. The Gamma-ray Burst Monitor and Large Area Telescope onboard the Fermi Observatory together record GRBs over a broad energy range spanning about 7 decades of gamma-ray energy. In September 2008, Fermi observed the exceptionally luminous GRB 080916C, with the largest apparent energy release yet measured. The high-energy gamma rays are observed to start later and persist longer than the lower energy photons. A simple spectral form fits the entire GRB spectrum, providing strong constraints on emission models. The known distance of the burst enables placing lower limits on the bulk Lorentz factor of the outflow and on the quantum gravity mass.

Gamma-ray bursts (GRBs) are the most luminous explosions in the universe and are leading candidates for the origin of ultrahigh-energy cosmic rays (UHECRs). Prompt emission from GRBs from ~10 keV to ~1 to 5 MeV has usually been detected, but occasionally photons above 100 MeV have been detected by the Energetic Gamma-Ray Experiment Telescope (EGRET) (*1*) and more recently by Astro-rivelatore Gamma a Immagini LEggero (AGILE) (*2*). Observations of gamma rays with energies >100 MeV are particularly prescriptive because they constrain the source environment and help understand the underlying energy source. Although there have been observations of photons above 100 MeV (*3*–*5*), it has not been possible to distinguish competing interpretations of the emission (*6*–*8*). The Fermi Gamma-ray Space Telescope, launched on 11 June 2008, provides broad energy coverage and high GRB sensitivities through the Gamma-ray Burst Monitor (GBM) and the Large Area Telescope (LAT) (*9*). The GBM consists of 12 sodium iodide (NaI) detectors, which cover the energy band between 8 keV and 1 MeV, and two bismuth germanate (BGO) scintillators, which are for the energy band between 150 keV and 40 MeV. The LAT is a pair conversion telescope with the energy coverage from below 20 MeV to more than 300 GeV (supporting online text). In this paper, we report detailed measurements of gamma-ray emission from the GRB 080916C detected by the GBM and LAT.

Observations. At 00:12:45.613542 UT (T_0) on 16 September 2008 the GBM flight software triggered on GRB 080916C. The GRB produced large signals in 9 of the 12 NaI detectors and in one of the two BGO detectors. Analysis of the data on the ground localized the burst to a right ascension (RA) = $08^h07^m12^s$, declination

*The full list of authors and affiliations is presented at the end of this paper.

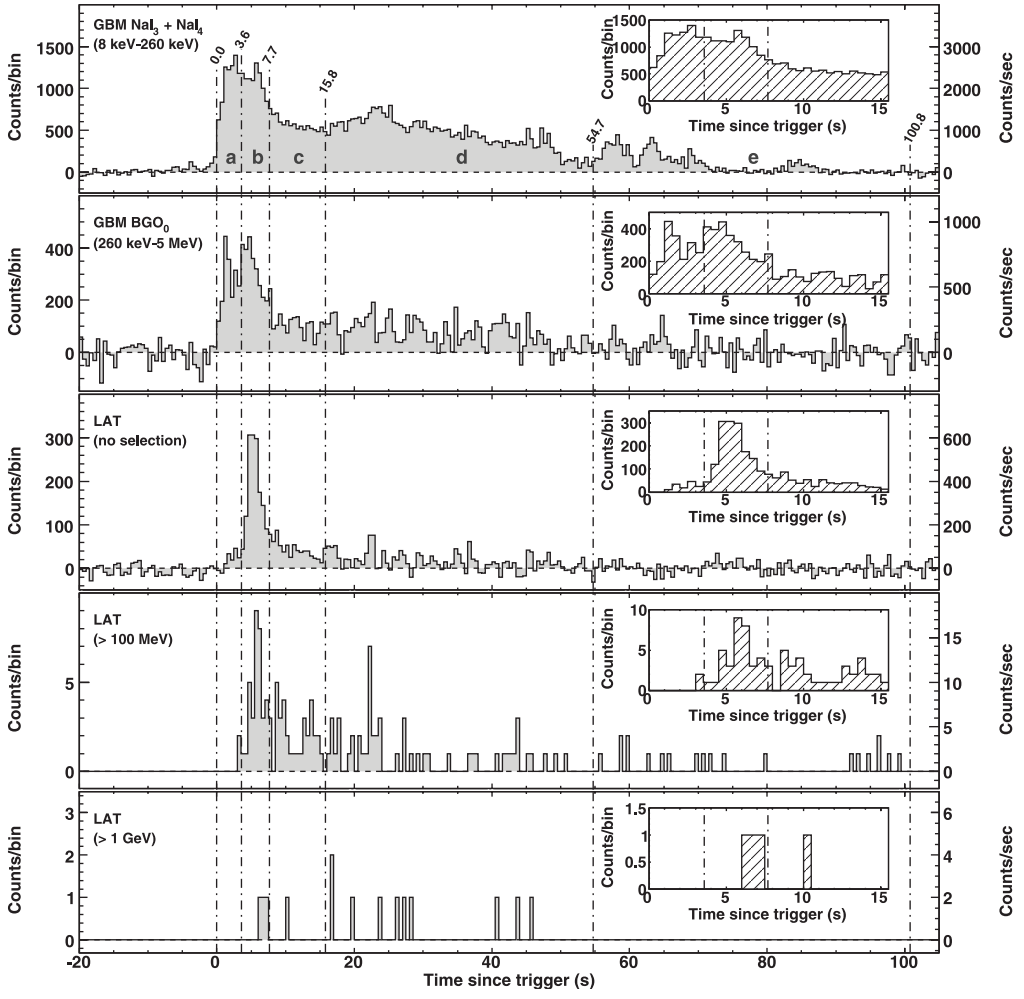

Fig. 1. Light curves for GRB 080916C observed with the GBM and the LAT, from lowest to highest energies. The energy ranges for the top two graphs are chosen to avoid overlap. The top three graphs represent the background-subtracted light curves for the NaI, the BGO, and the LAT. The top graph shows the sum of the counts, in the 8- to 260-keV energy band, of two NaI detectors (3 and 4). The second is the corresponding plot for BGO detector 0, between 260 keV and 5 MeV. The third shows all LAT events passing the onboard event filter for gamma-rays. (**Insets**) Views of the first 15 s from the trigger time. In all cases, the bin width is 0.5 s; the per-second counting rate is reported on the right for convenience.

(Dec.) = −61°18′00″ (*10*), with an uncertainty of 2.8° at 68% confidence level (C.L.).

At the time of the trigger, the GRB was located ~48° from the LAT boresight, and on-ground analysis revealed a bright source consistent with the GRB location. Using the events collected during the first 66 s after T_0, within 20° around the GBM burst position, the LAT provided a localization of RA = $07^h59^m31^s$, Dec. = −56°35′24″ (*11*) with a statistical uncertainty of 0.09° at 68% C.L. (0.13° at 90% C.L.) and a systematic uncertainty smaller than ~0.1° (movie S1).

Follow-up x-ray and optical observations revealed a fading source at RA = $07^h59^m23.24^s$, Dec. = −56°38′16.8″ (±1.9″ at 90% C.L.) (*12*) by Swift/X-Ray Telescope (XRT) and RA = $07^h59^m23.32^s$, Dec. = −56°38′18.0″ (±0.5″) (*13*, *14*) by Gamma-Ray Burst Optical/Near-Infrared Detector (GROND), respectively, consistent with the LAT localization within the estimated uncertainties. GROND determined the redshift of this source to be z = 4.35 ±0.15 (*15*). The afterglow was also observed in the near-infrared band by the Nagoya-SAAO 1.4 m telescope (IRSF) (*16*). The x-ray light curve of the afterglow from T_0 + 61 ks to T_0 + 1306 ks shows two temporal breaks at about 2 and 4 days after the trigger (*17*). The light curves before, between, and after the breaks can be fit with a power-law function with decay indices ~−2.3, ~−0.2. and ~−1.4, respectively.

The light curve of GRB 080916C, as observed with Fermi GBM and LAT, is shown in Fig. 1. The total number of LAT counts after background subtraction in the first 100 s after the trigger was >3000. For most of the low-energy events, however, extracting reliable directional and energy information was not possible. After we applied standard selection cuts (*9*) for transient sources with energies greater than 100 MeV and directions compatible with the burst location, 145 events remained (panel 4), and 14 events had energies > 1 GeV (panel 5).

Because of the energy-dependent temporal structure of the light curve, we divided the light curve into five time intervals (a, b, c, d, and e) delineated by the vertical lines (Fig. 1). The GRB light curve at low energy has two bright peaks, one between 0 and 3.6 s after the trigger (interval a) and one between 3.6 and 7.7 s (interval b). The two peaks are distinct in the BGO light curve but less so in the NaI. In the LAT detector the first peak is not significant though the light curve shows evidence of activity in time interval a, mostly in events below 100 MeV. Above 100 MeV, peak b is prominent in the LAT light curve. Interval c coincides with the tail of the main pulse, and the last two intervals reflect temporal structure in the NaI light curve and have been chosen to provide enough statistics in the LAT energy band for spectral analysis. The highest energy photon was observed during interval d: $E_h = 13.22^{+0.70}_{-1.54}$ GeV. Most of the emission in peak b shifts toward later times as the energy increases (inset).

Spectral analysis. We performed simultaneous spectral fits of the GBM and LAT data for each of the five time bins described above and shown in Fig. 1 (see Fig. 2 for an example of the fits). GBM NaI data from detectors 3 and 4 were selected from 8 keV to 1.0 MeV, as well as BGO detector 0 data from 0.26 to 40 MeV. LAT photons were selected by using the "transient" event class (*9*) for the energies from 100 MeV to 200 GeV. This event class provides the largest effective area and highest background rates among the LAT standard event classes, which is appropriate for bright sources with small backgrounds like this burst. This combination of the GBM and LAT data results in joint spectral fits by using forward-folding techniques covering over 7 decades of energy [supporting online material (SOM) text].

The spectra of all five time intervals are well fit by the empirical Band function (*18*), which smoothly joins low- and high-energy power laws. The first time interval, with a relative paucity of photons in the LAT, also has the most distinct spectral parameter values. The low-energy photon index α is larger (indicating harder emission), and the high-energy photon index β is smaller (indicating softer emission), consistent with the small number of LAT photons observed at this time. After the first interval there was no significant evolution in either α or β, as is evident in Fig. 3. In contrast, E_{peak}, the energy at which the energy emission peaks in the sense of energy per photon energy decade, evolved from the first time bin to reach its highest value in the second time bin, then softened through the remainder of the GRB. The higher E_{peak} and overall intensity of interval b, combined with the hard value of β that is characteristic of the later intervals, are the spectral characteristics that lead to the emission peaking in the LAT light curve (Fig. 1). The spectrum of interval b with a Band function fit is shown in Fig. 2. Comparing the parameters of this interval to the ensemble of EGRET burst detections, we find that the flux at around 1 MeV and β are similar to those for GRB 910503 and that E_{peak} resembles that for GRB 910814 (*19*).

We searched for deviations from the Band function, such as an additional component at high energies (*5*). Three photons in the fourth time bin had energies above 6 GeV. We tried modeling these high-energy photons with a power law as an additional high-energy spectral component. Compared to the null hypothesis that the data originated from a simple Band GRB function, adding the additional power-law component resulted in a probability of 1% that there was no additional spectral component for this time bin; with five time bins, this is not strong evidence for any additional component. Our sensitivity to higher-energy photons may be reduced at z ~ 4.35 through absorption by extragalactic background light (EBL). Because the effect of various EBL models ranges widely, from leaving the single time bin spectral-fit probability of an extra component unchanged (*20*) to decreasing the

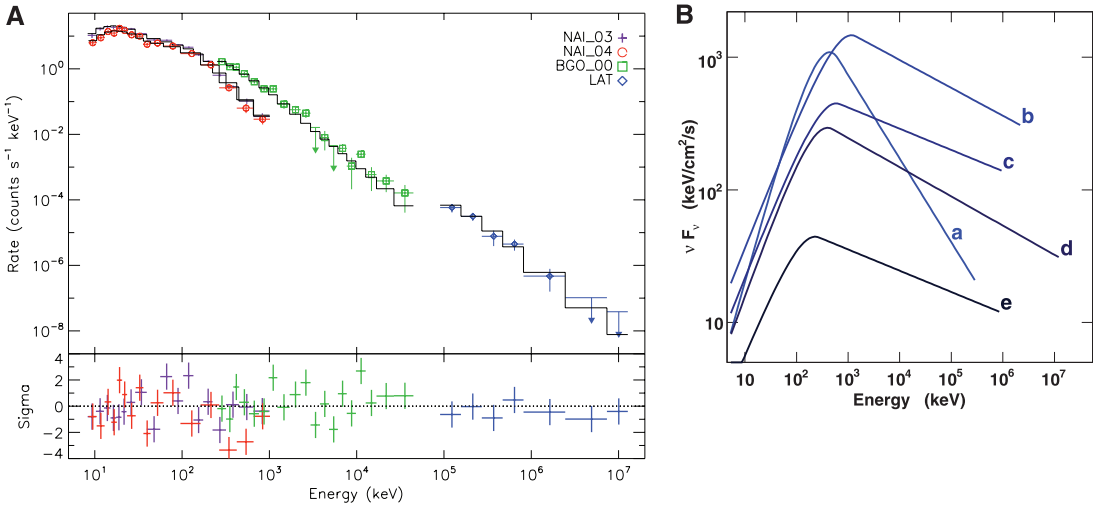

Fig. 2. (**A**) Count spectrum for NaI, BGO, and LAT in time bin b: The data points have 1σ error bars, whereas upper limits are 2σ. The histograms show the number of counts obtained by folding the photon model through the instrument response models. Spectra for time intervals a to e over the entire energy fit range are available in figs. S1 to S5. (**B**) The model spectra in νF_ν units for all five time intervals, in which a flat spectrum would indicate equal energy per decade of photon energy, and the changing shapes show the evolution of the spectrum over time. The curves end at the energy of the highest-energy photon observed in each time interval.

spectral-fit plausiblity of its absence to 0.03% (*21*), we cannot use EBL absorption effects in our estimation of significance.

Long-lived emissions. Although the light curves shown in Fig. 1 indicate that during interval e the spiky structures typical of prompt GRB emission appear to be dying out, the emission persisted in some of the GBM NaI detectors at a low level out to nearly T_0 + 200 s. The lack of pulse structure and the background-limited nature of the NaI detectors make this emission difficult to associate conclusively with the GRB, but the excess above background in the 12 NaI detectors occurred in the ratios expected for the geometry of the detectors relative to the burst direction. In addition, this type of low-level, extended emission is a known phenomenon in at least some long GRBs (*22*), so we associate it with the GRB and fit the spectrum with a power-law index of −1.92 ± 0.21 (1σ uncertainty). Emission beyond T_0 + 200 s fell below the threshold of the GBM detectors. Because of much lower instrumental backgrounds in the LAT, a high-energy decaying component might be seen for a longer time. The most suitable class to study faint sources with minimum backgrounds ("diffuse") was used to select events within 15° of the GROND localization coordinates between T_0 + 100 s and T_0 + 1400 s, which were then examined for possible connection with the GRB source. The interval up to T_0 + 200 s was treated separately for correlation with contemporaneous data from the GBM. The upper bound was chosen because, after T_0 + 1400 s, the GRB off-axis angle increased from 50° to 62°, resulting in decreased effective area.

We performed unbinned maximum likelihood fits of a power-law spectral function for a point source at the GROND-determined burst location in these two time intervals. Contributions from instrumental, Galactic, and extragalactic components were included in the fit, as well as the bright source Vela (which is located 13° from the GRB). Both time intervals show the presence of significant flux. For the final time interval, T_0 + 200 to T_0 + 1400 s, the fit yields a flux of (6.4 ± 2.5) × 10^{-6} γ cm^{-2} s^{-1} for E > 100 MeV with a power-law photon index of −2.8 ± 0.5 at a significance of 5.6σ. The fitting process does not assign individual photons to particular sources; it predicts, however, that 10.4 of the fitted photons originated from the GRB. If the position of the point source is left free instead of fixed to the GROND localization, the fit yields a source position of RA = $07^h57^m33^s$, Dec. = −57°00′00″ with an uncertainty of 0.51° at 90% C.L. This location is 0.45° from, and in agreement with, the GROND GRB position. To solidify the association of this extended emission with the GRB, we performed the same source detection procedure for data from T_0 − 900 s to T_0, and no emission was observed. A search for emission beyond T_0 + 1400 s was also fruitless.

We therefore associate this long-lived component with the GRB and include it as a sixth and a seventh time interval for comparison with the early-time emission (Fig. 4). In the LAT data, a constantly declining high-energy flux with a power-law decay index of −1.2 ± 0.2 is seen throughout T_0 + 1400 s (red points, Fig. 4). On the other hand, the flux in the GBM band shows a slower decay initially and an apparent break in the light curve at ~ T_0 + 55 s. The power-law decay indices are about −0.6 and −3.3 before and after the break, respectively. Previous reports (*3*, *5*) have provided tantalizing clues that distinct high-energy components may be a feature of some GRBs.

Interpretation. The Fermi observations of GRB 080916C show that the event energy spectra up to ~100 s are consistent with a single model (Band function), suggesting that a single emission mechanism dominates.

Between 10 keV and 10 GeV in the observer's frame, we measure a fluence $f = 2.4 \times 10^{-4}$ ergs cm^{-2}, which gives at $z = 4.35$ an apparent isotropic energy release for a standard cold dark matter cosmology with cosmological constant $\Omega_\Lambda = 0.73$, $\Omega_m = 0.27$, and a Hubble's constant of 71 km s^{-1} Mpc^{-1} of $E_{iso} \cong 8.8 \times 10^{54}$ ergs (SOM text). This is ~4.9 times the Solar rest energy and therefore strongly suggests on energetic grounds, for any stellar mass progenitor, that the GRB outflow powering this emission occupied only a small fraction ($\lesssim 10^{-2}$) of the total solid angle and was collimated into a narrow jet. A comparison with the previous highest measured $E_{iso} = 2.0 \times 10^{54}$ from 20 keV to 2 MeV shows the fluence and E_{iso} for GRB 080916C in this energy range are 1.2×10^{-4} ergs cm^{-2} and 4.3×10^{54} ergs, respectively. This earlier burst, GRB 990123 (*23*), was detected up to ≈20 MeV by the EGRET Total Absorption Shower Counter instrument.

High-energy γ rays from such intense regions can be strongly attenuated by lower-energy photons via pair production. The pair-production opacity can be reduced if the emission region is moving toward us at highly relativistic speeds—a

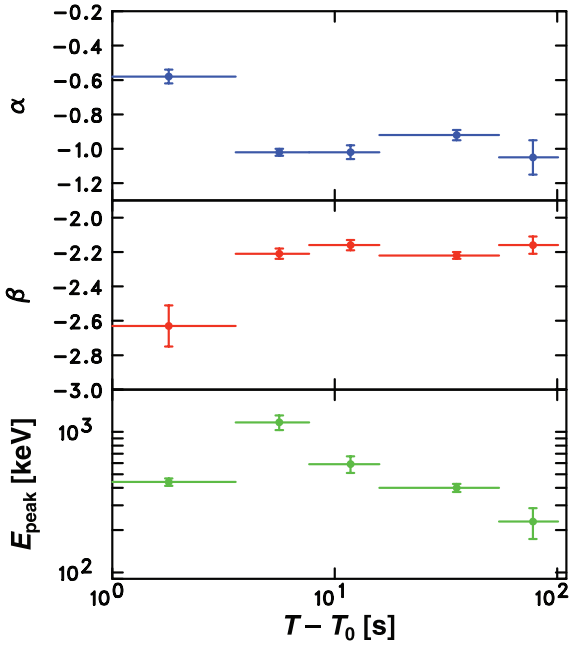

Fig. 3. Fit parameters for the Band function, α, β, and E_{peak} as a function of time. Error bars indicate 1σ uncertainty.

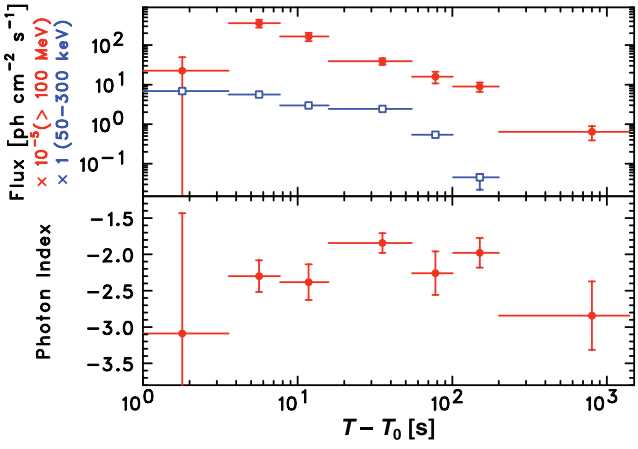

Fig. 4. Fluxes (**top**) for the energy ranges 50 to 300 keV (shown in blue open squares) and above 100 MeV (red solid squares) and power-law index as a function of the time from T_0 to T_0 + 1400 s [(**bottom**) LAT data only]. The red points are obtained by spectral fits of the LAT-only data for all time intervals. The blue points are obtained with the Band functions listed in Table 1 for the first five intervals and a power-law fit with index −1.90 ± 0.05 for the sixth interval.

relativistic jet with Lorentz factor Γ also explains the intensity and rapid variability of GRB γ rays (*24*–*28*). The observed correlated variability of the GBM and LAT emissions indicates that photons formed co-spatially, with the lower-energy (GBM) photons providing target photons that can interact with higher energy γ rays to produce electron-positron pairs. By using the Band function as the target radiation field and setting to unity the optical depth $\tau_{\gamma\gamma}$ to γ-ray pair production attenuation of the highest-energy observed photon, we calculate Γ_{min}, the minimum bulk Lorentz factor (supporting online text) (Fig. 5). For $z = 4.35$, we obtain $\Gamma_{min} = 608 \pm 15$ and 887 ± 21 in time bins d and b, respectively. For a spherical emitting shell of radius R, the observed variability time Δt and Γ_{min} can be used to set a lower limit on the emission radius, $R > \Gamma_{min}^2 c\Delta t/(1+z) = 8.9 \times 10^{15}(\Gamma_{min}/890)^2(\Delta t/2\ s)[5.35/(1+z)]$ cm. Similarly large prompt emission radii were inferred for other GRBs on different grounds (*29*, *30*).

The delayed onset of the GRB 080916C LAT pulse, which coincides with the rise of the second peak in the GBM light curve (Fig. 1), suggests a common origin in a region spatially distinct from the first GBM pulse. In the framework of the internal-shocks model for the prompt emission of GRBs (*27*, *28*), where intermittent winds of relativistic plasma are ejected by a newly formed black hole and collide to form shocks and accelerate particles, the two emission regions could arise from two different pairs of colliding shells, with variations in physical conditions leading to nonthermal electrons with different spectral hardnesses.

An alternative explanation for the delayed onset of the LAT emission is that a volume becomes filled with radiation that attenuates the high-energy photons until a later time when the emitting region expands and becomes optically thin. A γγ pair-production opacity effect would, however, produce a high-energy spectral softening or cutoff, whereas in all cases the combined GBM/LAT data are well fit with simple models by using the Band parameterization. Moreover, internal γ-ray opacity models predict that high-energy photons should also be detected in the rising portion of the GBM emission while they can still escape the source, before the increased photon density attenuates the γ rays (*31*). Lastly, in hadronic models associated with UHECR and high-energy neutrino production, the delay of the LAT emission could be a consequence of the time needed to accelerate protons or ions to energies where they can radiate by photopion or proton synchrotron radiation and generate an electromagnetic cascade (*32*–*34*). It is, however, unclear whether such models can reproduce the observed 10-keV to 10-GeV spectrum.

Before our observations, a high-energy (≳100 MeV) tail was observed most clearly from GRB 940217 (*3*) in observations by EGRET. The continuous high-energy tail in GRB 080916C could be due to the delayed arrival of the SSC emission in the GeV energy band during the afterglow phase (*35*). The observations, however, lack the predicted spectral hardening expected as the GeV emission changes from prompt synchrotron to afterglow SSC radiation. The LAT high-energy tail could also result from angle-dependent scattering effects (*36*) or from cascades induced by ultrarelativistic ions accelerated in GRBs (*8*).

The lack of two distinct emission components in the spectra up to ~10 GeV throughout the burst is compatible with a nonthermal synchrotron origin of the radiation. This is the favored emission mechanism at keV to MeV energies (*27*) and can indeed reach $\sim 30(\Gamma/1000)[5.35/(1+z)]$ GeV (*37*). Nonthermal synchrotron radiation should, however, be accompanied by a synchrotron self-Compton (SSC) spectral component produced from electrons that Compton upscatter their synchrotron photons to gamma-ray energies potentially in the LAT energy band. The apparent lack of an SSC component indicates that the magnetic energy density is much higher than the electron energy density (SOM text) or that the SSC νF_ν spectrum peaks at >>10 GeV and thus cannot be detected, which requires a typical electron Lorentz factor $\gamma_m \sim (E_{peak}^{SSC}/E_{peak}^{syn})^{1/2} >> 100$.

In addition to these considerations, sensitivity to a high-energy additional spectral component is reduced because EBL can absorb high-energy photons via pair-production interactions. In GRB 080916C, we did not observe a spectral cutoff that might be a signature of EBL, nor does the observation of a 13.2-GeV photon discriminate between EBL models (SOM text). However, if EBL is hiding an additional spectral component, we may be underestimating the energetics of GRB 080916C.

The high photon energies and large distance of GRB 080916C can test a prediction of some quantum gravity models that energy dispersion exists in the speed of photons, high-energy photons traveling slower and therefore arriving to us later than low-energy photons (*38*). In the linear approximation, the difference in the arrival times Δt is proportional to the ratio of photon energy difference to the quantum gravity mass, $\Delta E/M_{QG}$, and depends on the distance the photons traveled. The arrival time of the $13.22^{+0.70}_{-1.54}$ GeV photon relative to T_0, $t = 16.54$ s, is a conservative upper limit on its Δt relative to ~MeV photons and implies a robust lower limit on the quantum gravity mass, $M_{QG} > 1.3 \times 10^{18}$ GeV/c^2 (SOM text). We have used the low-end of the 1σ confidence intervals of both z and E_h in cal-

Table 1. Fit parameters for the Band function A, α, β, and E_{peak} as a function of time. Uncertainties are statistical in nature; the maximum possible systematic errors on the parameter values are comparable to their statistical errors (SOM text). Times are relative to trigger time T_0 = 00:12:45.613542 UT.

Time bin and range (s)	A (γ cm^{-2} s^{-1} keV^{-1})	α	β	E_{peak} (keV)	Flux 50 to 300 keV (γ cm^{-2} s^{-1})	Flux 100 MeV to 10 GeV (γ cm^{-2} s^{-1})
a: 0.004 to 3.58	$(55 \pm 2) \times 10^{-3}$	-0.58 ± 0.04	-2.63 ± 0.12	440 ±27	6.87 ± 0.12	$(2.5 \pm 1.6) \times 10^{-4}$
b: 3.58 to 7.68	$(35 \pm 1) \times 10^{-3}$	-1.02 ± 0.02	-2.21 ± 0.03	1170 ±140	5.63 ± 0.09	$(4.8 \pm 0.6) \times 10^{-3}$
c: 7.68 to 15.87	$(21 \pm 1) \times 10^{-3}$	-1.02 ± 0.04	-2.16 ± 0.03	590 ±80	2.98 ± 0.06	$(1.7 \pm 0.2) \times 10^{-3}$
d: 15.87 to 54.78	$(19.4 \pm 0.7) \times 10^{-3}$	-0.92 ± 0.03	-2.22 ± 0.02	400 ±26	2.44 ± 0.03	$(7.1 \pm 0.9) \times 10^{-4}$
e: 54.78 to 100.86	$(5.2 \pm 0.9) \times 10^{-3}$	-1.05 ± 0.10	-2.16 ± 0.05	230 ±57	0.54 ± 0.02	$(1.5 \pm 0.4) \times 10^{-4}$

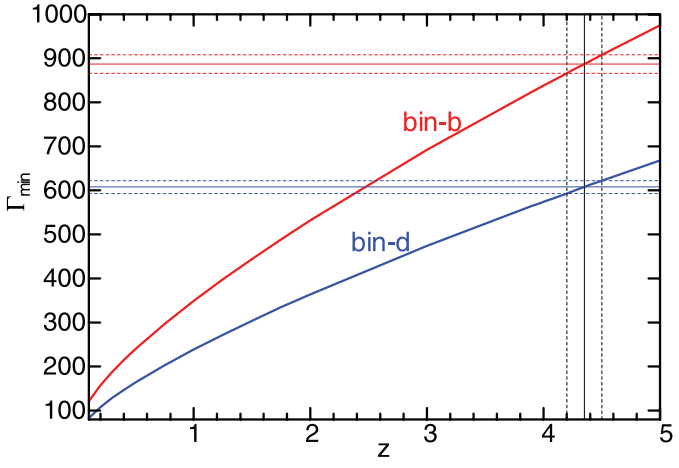

Fig. 5. The minimum Lorentz factor Γ_{min} as a function of redshift z for two different pulses in the γ-ray light curve. The value of Γ_{min}, defined by the condition that the γ-ray absorption opacity $\tau_{\gamma\gamma} = 1$, is derived for 3 GeV and 13 GeV photons and variability time scales $\Delta t = 2.0$ s and 20 s in time bins b and d, respectively.

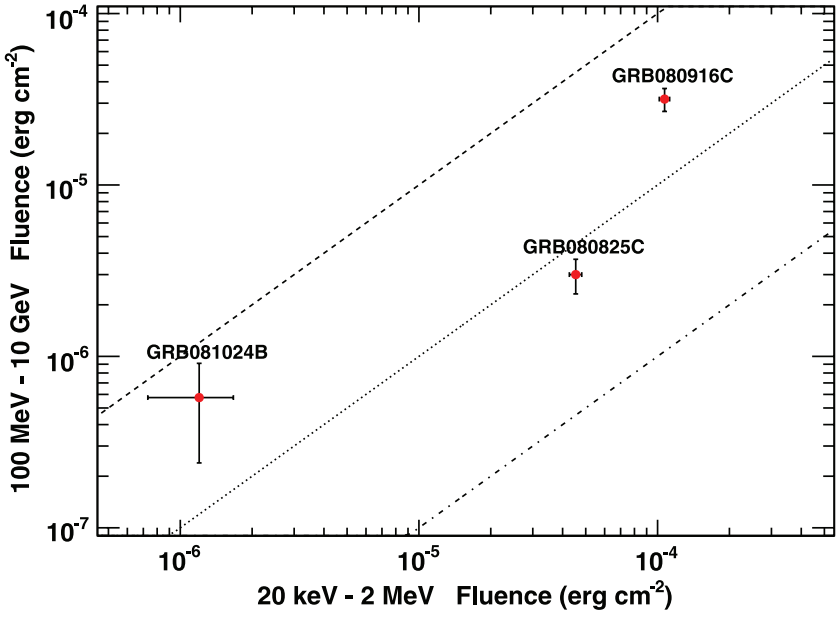

Fig. 6. Low- and high-energy gamma-ray fluences of three GRBs observed with both Fermi instruments. Both energy ranges are two decades. The diagonal lines indicate constant ratios between the two fluences: dashed, LAT and GBM fluences are equal; dotted, LAT fluence is 10% of GBM fluence; dot-dash, LAT fluence is 1% of GBM fluence.

culating M_{QG}. This lower limit is only one order of magnitude smaller than the Planck mass, 1.22×10^{19} GeV/c^2.

In the first 5 months since triggering was enabled on 14 July 2008, GBM triggered on 58 GRBs within the LAT field of view: Besides GRB 080916C (discussed here), two additional events were also seen with the LAT. The first was GRB 080825C (*39*), and the third was GRB 081024B, the first short GRB observed with the LAT (*40*, *41*). Figure 6 shows the LAT (100 MeV to 10 GeV) versus the GBM (20 keV to 2 MeV) fluences measured during the entire duration of each event. GRB 080916C stands out in both instruments, enabling better statistics in its spectral and timing analyses. Moreover, unlike the other two events, GRB 080916C has a redshift measurement, enabling determinations of lower limits for the bulk Lorentz factor of its ejecta and of the quantum gravity mass M_{QG}.

Figure 6 raises questions about the relation between the low and high energy emission. In no case have we detected a high-energy excess that would imply a distinct spectral component such as an SSC peak. The constraints are, however, weaker for GRBs 081024B and 080825C, which have fewer detected counts with which we could fit additional components. We observe in all three GRBs a delay in the onset of the LAT ($E >$ 100 MeV) photons with respect to the lower energy GBM photons. This trend is an important clue for unraveling the GRB phenomenon.

References and Notes

1. B. L. Dingus, *Astrophys. Space Sci.* **231**, 187 (1995).
2. A. Giuliani *et al., Astron. Astrophys*. in press; preprint available online at http://arxiv.org/abs/0809.1230 (2008).
3. K. Hurley *et al*., *Nature* **372**, 652 (1994).
4. D. N. Wren, D. L. Bertsch, S. Ritz, *Astrophys. J.* **574**, L47 (2002).
5. M. M. Gonźalez *et al*., *Nature* **424**, 749 (2003).
6. J. Granot, D. Guetta, *Astrophys. J.* **598**, L11 (2003).
7. J. Katz, *Astrophys. J.* **432**, L27 (1994).
8. C. D. Dermer, A. Atoyan, *New J. Phys.* **8**, 122 (2006).
9. W. B. Atwood *et al.*, http://arxiv.org/abs/0902.1089 (2008).
10. A. Goldstein, A. vander Horst, *GCN Circ. 8245* (2008).
11. H. Tajima *et al., GCN Circ. 8246* (2008).
12. M. Perri *et al., GCN Circ. 8261* (2008).
13. C. Clemens *et al., GCN Circ. 8257* (2008).
14. C. Clemens *et al., GCN Circ. 8272* (2008).
15. J. Greiner *et al*., http://arxiv.org/abs/0902.0761 (2009).
16. T. Nagayama *et al., GCN Circ. 8274* (2008).
17. G. Stratta *et al., GCN Rep. 166.1* (2008).
18. D. Band *et al*., *Astrophys. J.* **413**, 281 (1993).
19. M. Baring, *Astrophys. J.* **650**, 1004 (2006).
20. S. Razzaque, C. D. Dermer, J. D. Finke, *Astrophys. J.*, in press; preprint available at http://arxiv.org/abs/0807.4294 (2008).
21. F. W. Stecker, M. A. Malkan, S. T. Scully, *Astrophys. J.* **648**, 774 (2006).
22. V. Connaughton, *Astrophys. J.* **567**, 1028 (2002).
23. M. S. Briggs *et al*., *Astrophys. J.* **524**, 82 (1999).
24. J. H. Krolik, E. A. Pier, *Astrophys. J.* **373**, 277 (1991).
25. E. E. Fenimore, R. I. Epstein, C. Ho, *Astron. Astrophys. Suppl. Ser.* **97**, 59 (1993).
26. Y. Lithwick, R. Sari, *Astrophys. J.* **555**, 540 (2001).
27. P. Mészáros, *Annu. Rev. Astron. Astrophys.* **40**, 137 (2002).
28. T. Piran, *Phys. Rep.* **314**, 575 (1999).
29. P. Kumar *et al*., *Mon. Not. R. Astron. Soc.* **376**, L57 (2007).
30. J. L. Racusin, *Nature* **455**, 183 (2008).
31. J. Granot, J. Cohen-Tanugi, E. do Couto e Silva, *Astrophys. J.* **677**, 92 (2008).
32. J. P. Rachen, P. Mészáros, *Phys. Rev. D* **58**, 123005 (1998).
33. C. D. Dermer, *Astrophys. J.* **574**, 65 (2002).
34. S. Razzaque, P. Mészáros, E. Waxman, *Mod. Phys. Lett. A* **20**, 2351 (2005).
35. R. Sari, A. A. Esin, *Astrophys. J.* **548**, 787 (2001).
36. X. Y. Wang, Z. Li, P. Mészáros, *Astrophys. J.* **641**, L89 (2006).
37. A. A. Pe'er, E. Waxman, *Astrophys. J.* **613**, 448 (2004).
38. G. Amelino-Camelia *et al*., *Nature* **393**, 763 (1998).
39. A. Bouvier *et al., GCN Circ. 8183* (2008).
40. N. Omodei, *GCN Circ. 8407* (2008).
41. V. Connaughton, M. S. Briggs, *GCN Circ. 8408* (2008).
42. A. A. Abdo, J. Finke, and S. Razzaque are National Research Council Research Associates. A. J. van der Horst is a NASA Postdoctoral Program Fellow. The Fermi LAT Collaboration acknowledges the support of a number of agencies and institutes. These include NASA and the Department of Energy in the United States; the Commissariat à l'Energie Atomique and the Centre National de la Recherche Scientifique/Institut National de Physique Nucléaire et de Physique des Particules in France; the Agenzia Spaziale Italiana and the Istituto Nazionale di Fisica Nucleare in Italy; the Ministry of Education, Culture, Sports, Science and Technology (MEXT), High Energy Accelerator Research Organization (KEK), and Japan Aerospace Exploration Agency (JAXA) in Japan; and the K. A. Wallenberg Foundation, the Swedish Research Council, and the Swedish National Space Board in Sweden. J.C. is a Royal Swedish Academy of Sciences Research fellow supported by a grant from the K. A. Wallenberg foundation. The Fermi GBM Collaboration acknowledges the support of NASA in the United States and Deutsches Zentrum für Luft- und Raumfahrt in Germany and thanks L. Gibby, A. English, and F. Kroeger.

***List of authors and affiliations:** A. A. Abdo,[1] M. Ackermann,[2] M. Arimoto,[3] K. Asano,[3] W. B. Atwood,[4] M. Axelsson,[5,6] L. Baldini,[7] J. Ballet,[8] D. L. Band,[9,10] G. Barbiellini,[11,12] M. G. Baring,[13] D. Bastieri,[14,15] M. Battelino,[5,16] B. M. Baughman,[18] K. Bechtol,[3] F. Bellardi,[8] R. Bellazzini,[8] B. Berenji,[3] P. N. Bhat,[18] E. Bissaldi,[19] R. D. Blandford,[2] E. D. Bloom,[2] G. Bogaert,[20] J. R. Bogart,[2] E. Bonamente,[21,22] J. Bonnell,[10] A. W. Borgland,[2] A. Bouvier,[2] J. Bregeon,[7] A. Brez,[7] M. S. Briggs,[18]* M. Brigida,[23,24] P. Bruel,[20] T. H. Burnett,[25] D. Burrows,[26] G. Busetto,[14,15] G. A. Caliandro,[23,24] R. A. Cameron,[2] P. A. Caraveo,[27] J. M. Casandjian,[8] M. Ceccanti,[7] C. Cecchi,[21,22] A. Celotti,[28] E. Charles,[2] A. Chekhtman,[1,29] C. C. Cheung,[10] J. Chiang,[2] S. Ciprini,[21,22] R. Claus,[2] J. Cohen-Tanugi,[30] L. R. Cominsky,[31] V. Connaughton,[18] J. Conrad,[5,16,32] L. Costamante,[2] S. Cutini,[33] M. DeKlotz,[34] C. D. Dermer,[1]* A. de Angelis,[35] F. de Palma,[23,24] S. W. Digel,[2] B. L. Dingus,[36] E. do Couto e Silva,[2] P. S. Drell,[2] R. Dubois,[2] D. Dumora,[37,38] Y. Edmonds,[2] P. A. Evans,[39] D. Fabiani,[7] C. Farnier,[30] C. Favuzzi,[23,24] J. Finke,[1] G. Fishman,[40] W. B. Focke,[2] M. Frailis,[35] Y. Fukazawa,[41] S. Funk,[2] P. Fusco,[23,24] F. Gargano,[24] D. Gasparrini,[33] N. Gehrels,[10,42] S. Germani,[21,22] B. Giebels,[20] N. Giglietto,[23,24] P. Giommi,[33] F. Giordano,[23,24] T. Glanzman,[2] G. Godfrey,[2] A. Goldstein,[18] J. Granot,[43] J. Greiner,[19] I. A. Grenier,[8] M.-H. Grondin,[37,38] J. E. Grove,[1] L. Guillemot,[37,38] S. Guiriec,[30] G. Haller,[2] Y. Hanabata,[41] A. K. Harding,[10] M. Hayashida,[2] E. Hays,[10] J. A. Hernando Morata,[44] A. Hoover,[36] R. E. Hughes,[17] G. Jóhannesson,[2] A. S. Johnson,[2] R. P. Johnson,[4] T. J. Johnson,[10,42] W. N. Johnson,[1] T. Kamae,[2] H. Katagiri,[41] J. Kataoka,[3] A. Kavelaars,[2] N. Kawai,[3,45] H. Kelly,[2] J. Kennea,[26] M. Kerr,[25] R. M. Kippen,[36] J. Knödlseder,[46] D. Kocevski,[2] M. L. Kocian,[2] N. Komin,[8,30] C. Kouveliotou,[40] F. Kuehn,[17] M. Kuss,[7] J. Lande,[2] D. Landriu,[8] S. Larsson,[5,32] L. Latronico,[7] C. Lavalley,[30] B. Lee,[47] S.-H. Lee,[2] M. Lemoine-Goumard,[37,38] G. G. Lichti,[19] F. Longo,[11,12] F. Loparco,[23,24] B. Lott,[37,38] M. N. Lovellette,[1] P. Lubrano,[21,22] G. M. Madejski,[2] A. Makeev,[1,29] B. Marangelli,[23,24] M. N. Mazziotta,[24] S. McBreen,[19,48] J. E. McEnery,[10] S. McGlynn,[5,16] C. Meegan,[40] P. Mészáros,[26] C. Meurer,[5,32] P. F. Michelson,[2] M. Minuti,[7] N. Mirizzi,[23,24] W. Mitthumsiri,[2] T. Mizuno,[41] A. A. Moiseev,[9] C. Monte,[23,24] M. E. Monzani,[2] E. Moretti,[11,12] A. Morselli,[49] I. V. Moskalenko,[2] S. Murgia,[2] T. Nakamori,[3] D. Nelson,[2] P. L. Nolan,[2] J. P. Norris,[50] E. Nuss,[30] M. Ohno,[51] T. Ohsugi,[41] A. Okumura,[52] N. Omodei,[7] E. Orlando,[19] J. F. Ormes,[50] M. Ozaki,[51] W. S. Paciesas,[18] D. Paneque,[2] J. H. Panetta,[2] D. Parent,[37,38] V. Pelassa,[30] M. Pepe,[21,22] M. Perri,[33] M. Pesce-Rollins,[7] V. Petrosian,[2] M. Pinchera,[7] F. Piron,[30] T. A. Porter,[4] R. Preece,[40] S. Rainò,[23,24] E. Ramirez-Ruiz,[53] R. Rando,[14,15] E. Rapposelli,[7] M. Razzano,[7] S. Razzaque,[1] N. Rea,[54]† A. Reimer,[2] O. Reimer,[2] T. Reposeur,[37,38] L. C. Reyes,[55] S. Ritz,[9,42] L. S. Rochester,[2] A. Y. Rodriguez,[54] M. Roth,[25] F. Ryde,[5,16] H. F.-W. Sadrozinski,[4] D. Sanchez,[20] A. Sander,[17] P. M. Saz Parkinson,[4] J. D. Scargle,[56] T. L. Schalk,[4] K. N. Segal,[9] C. Sgrò,[7] T. Shimokawabe,[3] E. J. Siskind,[57] D. A. Smith,[37,38] P. D. Smith,[17] G. Spandre,[7] P. Spinelli,[23,24] M. Stamatikos,[10] J.-L. Starck,[8] F. W. Stecker,[10] H. Steinle,[19] T. E. Stephens,[10] M. S. Strickman,[1] D. J. Suson,[58] G. Tagliaferri,[59] H. Tajima,[2]* H. Takahashi,[41] T. Takahashi,[51] T. Tanaka,[2] A. Tenze,[7] J. B. Thayer,[2] J. G. Thayer,[2] D. J. Thompson,[10] L. Tibaldo,[14,15] D. F. Torres,[54,60] G. Tosti,[21,22] A. Tramacere,[2,61] M. Turri,[2] S. Tuvi,[2]

T. L. Usher,[2] A. J. van der Horst,[40] L. Vigiani,[7] N. Vilchez,[46] V. Vitale,[49,62] A. von Kienlin,[19] A. P. Waite,[2] D. A. Williams,[4] C. Wilson-Hodge,[40] B. L. Winer,[17] K. S. Wood,[1] X. F. Wu,[26,63,64] R. Yamazaki,[41] T. Ylinen,[5,16,65] M. Ziegler[4]

[1]Space Science Division, Naval Research Laboratory, Washington, DC 20375, USA. [2]W. W. Hansen Experimental Physics Laboratory, Kavli Institute for Particle Astrophysics and Cosmology, Department of Physics and SLAC National Accelerator Laboratory, Stanford University, Stanford, CA 94305, USA. [3]Department of Physics, Tokyo Institute of Technology, Meguro City, Tokyo 152-8551, Japan. [4]Santa Cruz Institute for Particle Physics, Department of Physics, and Department of Astronomy and Astrophysics, University of California at Santa Cruz, Santa Cruz, CA 95064, USA. [5]The Oskar Klein Centre for Cosmo Particle Physics, AlbaNova, SE-106 91 Stockholm, Sweden. [6]Department of Astronomy, Stockholm University, SE-106 91 Stockholm, Sweden. [7]Istituto Nazionale di Fisica Nucleare, Sezione di Pisa, I-56127 Pisa, Italy. [8]Laboratoire AIM, CEA-IRFU/CNRS/Université Paris Diderot, Service d'Astrophysique, CEA Saclay, 91191 Gif sur Yvette, France. [9]Center for Research and Exploration in Space Science and Technology (CRESST), NASA Goddard Space Flight Center, Greenbelt, MD 20771, USA. [10]National Aeronautics and Space Administration (NASA) Goddard Space Flight Center, Greenbelt, MD 20771, USA. [11]Istituto Nazionale di Fisica Nucleare, Sezione di Trieste, I-34127 Trieste, Italy. [12]Dipartimento di Fisica, Università di Trieste, I-34127 Trieste, Italy. [13]Department of Physics and Astronomy, Rice University, MS-108, Post Office Box 1892, Houston, TX 77251, USA. [14]Istituto Nazionale di Fisica Nucleare, Sezione di Padova, I-35131 Padova, Italy. [15]Dipartimento di Fisica "G. Galilei," Università di Padova, I-35131 Padova, Italy. [16]Department of Physics, Royal Institute of Technology (KTH), AlbaNova, SE-106 91 Stockholm, Sweden. [17]Department of Physics, Center for Cosmology and Astro-Particle Physics, The Ohio State University, Columbus, OH 43210, USA. [18]University of Alabama in Huntsville, Huntsville, AL 35899, USA. [19]Max-Planck Institut für Extraterrestrische Physik, 85748 Garching, Germany. [20]Laboratoire Leprince-Ringuet, École Polytechnique, CNRS/IN2P3, Palaiseau, France. [21]Istituto Nazionale di Fisica Nucleare, Sezione di Perugia, I-06123 Perugia, Italy. [22]Dipartimento di Fisica, Università degli Studi di Perugia, I-06123 Perugia, Italy. [23]Dipartimento di Fisica "M. Merlin," dell'Università e del Politecnico di Bari, I-70126 Bari, Italy. [24]Istituto Nazionale di Fisica Nucleare, Sezione di Bari, 70126 Bari, Italy. [25]Department of Physics, University of Washington, Seattle, WA 98195-1560, USA. [26]Pennsylvania State University, 525 Davey Laboratory, University Park, PA 16802, USA. [27]INAF (Istituto di Astrofisica Spaziale e Fisica Cosmica), I-20133 Milano, Italy. [28]Scuola Internazionale Superiore di Studi Avanzati (SISSA), 34014 Trieste, Italy. [29]George Mason University, Fairfax, VA 22030, USA. [30]Laboratoire de Physique Théorique et Astroparticules, Université Montpellier 2, CNRS/IN2P3, 34095 Montpellier, France. [31]Department of Physics and Astronomy, Sonoma State University, Rohnert Park, CA 94928-3609, USA. [32]Department of Physics, Stockholm University, AlbaNova, SE-106 91 Stockholm, Sweden. [33]Agenzia Spaziale Italiana (ASI) Science Data Center, I-00044 Frascati (Roma), Italy. [34]Stellar Solutions Incorporated, 250 Cambridge Avenue, Suite 204, Palo Alto, CA 94306, USA. [35]Dipartimento di Fisica, Università di Udine and Istituto Nazionale di Fisica Nucleare, Sezione di Trieste, Gruppo Collegato di Udine, I-33100 Udine, Italy. [36]Los Alamos National Laboratory, Los Alamos, NM 87545, USA. [37]CNRS/IN2P3, Centre d'Études Nucléaires Bordeaux Gradignan, UMR 5797, Gradignan, 33175, France. [38]Université de Bordeaux, Centre d'Études Nucléaires Bordeaux Gradignan, UMR 5797, Gradignan, 33175, France. [39]Department of Physics and Astronomy, University of Leicester, Leicester, LE1 7RH, UK. [40]NASA Marshall Space Flight Center, Huntsville, AL 35805, USA. [41]Department of Physical Science and Hiroshima Astrophysical Science Center, Hiroshima University, Higashi-Hiroshima 739-8526, Japan. [42]University of Maryland, College Park, MD 20742, USA. [43]Centre for Astrophysics Research, University of Hertfordshire, College Lane, Hatfield AL10 9AB, UK. [44]European Organization for Nuclear Research (CERN), CH-1211 Geneva, Switzerland. [45]Cosmic Radiation Laboratory, Institute of Physical and Chemical Research (RIKEN), Wako, Saitama 351-0198, Japan. [46]Centre d'Étude Spatiale des Rayonnements, CNRS/UPS, BP 44346, F-30128 Toulouse Cedex 4, France. [47]Orbital Network Engineering, 10670 North Tantau Avenue, Cupertino, CA 95014, USA. [48]University College Dublin, Belfield, Dublin 4, Ireland. [49]Istituto Nazionale di Fisica Nucleare, Sezione di Roma "Tor Vergata," I-00133 Roma, Italy. [50]Department of Physics and Astronomy, University of Denver, Denver, CO 80208, USA. [51]Institute of Space and Astronautical Science, Japan Aerospace Exploration Agency (JAXA), 3-1-1 Yoshinodai, Sagamihara, Kanagawa 229-8510, Japan. [52]Department of Physics, Graduate School of Science, University of Tokyo, 7-3-1 Hongo, Bunkyo-ku, Tokyo 113-0033, Japan. [53]University of California Observatories/Lick Observatories, Santa Cruz, CA 95064, USA. [54]Institut de Ciencies de l'Espai (IEEC-CSIC), Campus UAB, 08193 Barcelona, Spain. [55]Kavli Institute for Cosmological Physics, University of Chicago, Chicago, IL 60637, USA. [56]Space Sciences Division, NASA Ames Research Center, Moffett Field, CA 94035-1000, USA. [57]NYCB Real-Time Computing Incorporated, Lattingtown, NY 11560-1025, USA. [58]Department of Chemistry and Physics, Purdue University Calumet, Hammond, IN 46323-2094, USA. [59]INAF Osservatorio Astronomico di Brera, I-23807 Merate, Italy. [60]Institució Catalana de Recerca i Estudis Avançats (ICREA), 08010 Barcelona, Spain. [61]Consorzio Interuniversitario per la Fisica Spaziale (CIFS), I-10133 Torino, Italy. [62]Dipartimento di Fisica, Università di Roma "Tor Vergata," I-00133 Roma, Italy. [63]Joint Center for Particle Nuclear Physics and Cosmology (J-CPNPC), Nanjing 210093, China. [64]Purple Mountain Observatory, Chinese Academy of Sciences, Nanjing 210008, China. [65]School of Pure and Applied Natural Sciences, University of Kalmar, SE-391 82 Kalmar, Sweden.

*To whom correspondence should be addressed. E-mail: michael.briggs@nasa.gov (M.S.B.); htajima@slac.stanford.edu (H.T.); charles.dermer@nrl.navy.mil (C.D.D.).
†Present address: Sterrenkundig Institut "Anton Pannekoek," 1098 SJ Amsterdam, Netherlands.

Supporting Online Material
www.sciencemag.org/cgi/content/full/1169101/DC1
SOM Text
Figs. S1 to S7
Movie S1

27 November 2008; accepted 11 February 2009
Published online 19 February 2009;
10.1126/science.1169101
Include this information when citing this paper.

Comprehensive Characterization of Genes Required for Protein Folding in the Endoplasmic Reticulum

Martin C. Jonikas,[1,2,3,4] Sean R. Collins,[1,3,4] Vladimir Denic,[1,3,4]* Eugene Oh,[1,3,4] Erin M. Quan,[1,3,4] Volker Schmid,[5] Jimena Weibezahn,[1,3,4] Blanche Schwappach,[5] Peter Walter,[2,3] Jonathan S. Weissman,[1,3,4]† Maya Schuldiner[1,3,4]‡

Protein folding in the endoplasmic reticulum is a complex process whose malfunction is implicated in disease and aging. By using the cell's endogenous sensor (the unfolded protein response), we identified several hundred yeast genes with roles in endoplasmic reticulum folding and systematically characterized their functional interdependencies by measuring unfolded protein response levels in double mutants. This strategy revealed multiple conserved factors critical for endoplasmic reticulum folding, including an intimate dependence on the later secretory pathway, a previously uncharacterized six-protein transmembrane complex, and a co-chaperone complex that delivers tail-anchored proteins to their membrane insertion machinery. The use of a quantitative reporter in a comprehensive screen followed by systematic analysis of genetic dependencies should be broadly applicable to functional dissection of complex cellular processes from yeast to human.

The endoplasmic reticulum (ER) is responsible for the folding and maturation of secreted and membrane proteins. External stress or mutations can compromise ER folding, contributing to diseases such as diabetes and neurodegeneration (*1*, *2*). The specialized milieu of the ER is composed of a large number of proteins that aid the structural maturation of itinerant proteins (*3*, *4*). Although many of these ER folding factors have been extensively studied, the full range of proteins contributing to this process is unknown, and how they function together is poorly understood.

Systematic identification of genes contributing to ER folding. We exploited the cell's endogenous sensor of ER protein folding status, Ire1p, to identify genes in *Saccharomyces cerevisiae* that contribute to structural maturation of secretory proteins. In response to misfolded proteins in the ER, the transmembrane sensor Ire1p activates the transcription factor Hac1p (*5*), which in turn transcriptionally up-regulates a distinct set of genes (*6*, *7*) in a process called the unfolded protein response (UPR). We used a reporter system in which a Hac1p-responsive promoter drives green fluorescent protein (GFP) expression (*8*) (Fig. 1A). To correct for nonspecific expression changes, we coexpressed a red fluorescent protein (RFP) from a constitutive *TEF2* promoter and used the ratio of GFP/RFP as our reporter of UPR signaling. A titration of the ER stress-inducing reducing agent dithiothreitol (DTT) demonstrated that this reporter quantitatively responds to misfolding of ER proteins (Fig. 1B).

With use of synthetic genetic array methodology (*9*), we introduced the reporter into ~4500 strains from the *S. cerevisiae* deletion library (*10*),

[1]Department of Cellular and Molecular Pharmacology, University of California, San Francisco, San Francisco, CA 94143, USA. [2]Department of Biochemistry and Biophysics, University of California, San Francisco, San Francisco, CA 94143, USA. [3]Howard Hughes Medical Institute, University of California, San Francisco, San Francisco, CA 94143, USA. [4]California Institute for Quantitative Biomedical Research, San Francisco, CA 94143, USA. [5]Faculty of Life Sciences, University of Manchester, Manchester M13 9PT, UK.

*Present address: Department of Molecular and Cellular Biology, Harvard University, Cambridge, MA 02138, USA.
†To whom correspondence should be addressed. E-mail: weissman@cmp.ucsf.edu
‡Present address: Department of Molecular Genetics, Weizmann Institute of Science, Rehovot 76100, Israel.

and the median single-cell fluorescence of each strain was measured by using high-throughput flow cytometry (*11*, *12*) (fig. S1 and table S1). The UPR showed significant basal induction, which allowed us to identify genes whose deletion caused either up-regulation (399 hits with $P < 0.01$, explicitly modeling our experimental error) or down-regulation (334 hits with $P < 0.01$) of the reporter. We found limited overlap between the genes

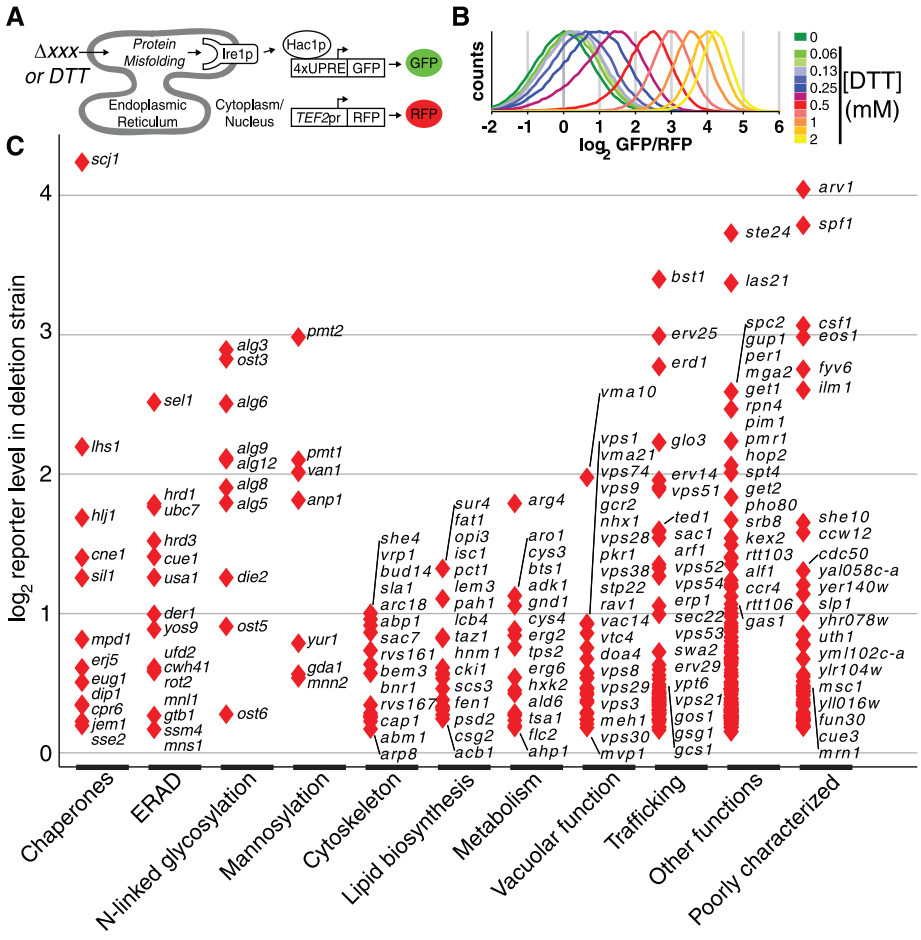

Fig. 1. Quantitative screen for gene deletions that perturb UPR signaling. (**A**) Strategy for quantifying UPR levels in deletion strains. (**B**) GFP/RFP reporter ratios as a function of concentration of DTT, a reducing agent that causes protein misfolding in the ER. (**C**) UPR reporter levels of up-regulator hits by functional category.

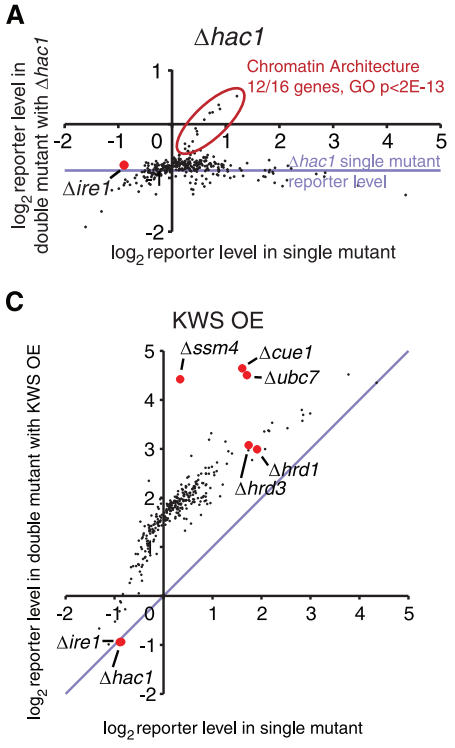

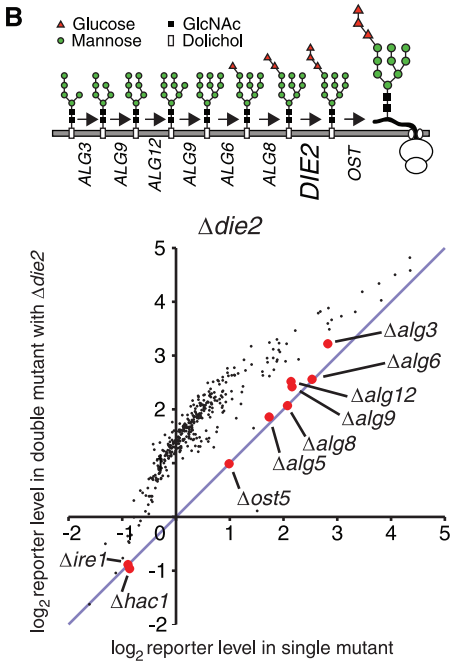

Fig. 2. Double mutant analysis provides information on functional dependencies between genes. (**A**) Double mutant (DM) plot of Δ*hac1*. Each point represents a gene. *X* coordinate represents the reporter level of a strain deleted for that gene in a wild-type (WT) background. *Y* coordinate represents the reporter level in a double mutant lacking the same gene and additionally deleted for a second gene (in this case, *HAC1*). The horizontal blue line indicates the reporter level in the Δ*hac1* single mutant. Circled in red are up-regulators whose reporter induction is *HAC1*-independent, which are highly enriched for chromatin architecture factors. (**B**) (Top) Schematic of the lumenal steps of the N-linked glycan synthesis pathway. (Bottom) DM plot for Δ*die2*/*alg10*. (**C**) DM plot depicting genetic interactions between deletion mutants and overexpression (OE) of the ERAD substrate KWS.

whose deletion induces the UPR and the genes that were previously shown by microarray analysis to be transcriptionally up-regulated by the UPR (*7*) [fig. S2 and table S2; see also (*10*, *13*)]. Thus, although defining the UPR targets was fundamental to our understanding of how cells respond to ER stress, it provides a limited view of the processes constitutively required for folding in the ER.

Overview of gene deletions affecting the UPR. Proteins whose deletion caused up-regulation of the reporter were highly enriched for localization throughout the secretory pathway (fig. S3 and table S3) (*14*), including the ER as well as the Golgi, vacuole, and endosome. As expected, chaperones (*15*) and genes in the N-linked glycosylation (*16*) and ER-associated degradation (ERAD) (*17*) pathways featured among the top hits (Fig. 1C). However, deletion of genes involved in many other processes, including O-mannosylation, glycophosphatidylinositol anchor synthesis, lipid biosynthesis, multiple steps of vesicular trafficking, and ion homeostasis, caused similarly high reporter inductions (table S1). Moreover, the UPR up-regulators included several dozen poorly characterized genes, some whose deletion caused reporter induction that rivaled the strongest hits.

The diversity of functions contributing to ER integrity presented a major obstacle in our efforts to understand how these unexpected factors function together to support protein folding in the ER. To overcome this, we explored their functional dependencies by systematically quantifying how the phenotype caused by loss of one gene was modulated by the absence of a second. Systematic analysis of genetic interactions, using growth rate as a phenotype, has been used extensively to determine gene function (*9*, *18*–*23*). We sought to generalize this strategy by using ER stress as a quantitative phenotype. Accordingly, we quantified GFP reporter levels in over 60,000 strains containing pairwise deletions among 340 of our hits (*12*).

Genetic interactions illuminate functional relations. Three examples illustrate the utility of the double mutant analysis. First, comparison of the GFP levels in the presence and absence of *IRE1*/*HAC1* differentiated between the subset of up-regulators whose deletion affected protein folding in the ER (i.e., GFP induction was dependent on the Ire1p/Hac1p pathway) from those, like chromatin architecture genes, that were directly affecting expression of the reporter (Fig. 2A and table S4).

In a second example, UPR levels of pairwise deletions with Δ*die2*/*alg10*, the enzyme that performs the last step in the synthesis pathway for N-linked glycans, illustrated our ability to define genes acting in a linear pathway (Fig. 2B). Most double mutants showed a typical increase in fluorescence that was dictated solely by the reporter levels of the single mutants. Notably, a specific subset of the double mutants had the same reporter level as the single mutant, indicative of "fully masking" epistatic interactions in which the function of one gene is completely dependent on the presence of a second one. Indeed, the genes that we find to be epistatic to *DIE2* include the full set of factors that act immediately upstream of Die2p in the synthesis of N-linked sugars (*16*).

The utility of aggravating genetic interactions, in which pairs of deletions lead to exaggerated folding defects, was illustrated in a third example in which we overexpressed the constitutively misfolded and rapidly degraded membrane protein KWS (*24*) in deletion strains that were hits in our screen (Fig. 2C). KWS degradation is mediated by a well-defined subset of the ERAD machinery, including the E3 ubiquitin ligase Ssm4p/Doa10p and the E2 ubiquitin-conjugating complex Ubc7p and Cue1p (*24*). The role of these factors in mitigating the stress caused by overexpression of KWS is revealed in our data by the strongly aggravating interaction between their deletions and KWS overexpression. In contrast, other ERAD components, which do not act on KWS, including the Hrd1p/Hrd3p E3 ligase complex (*24*), show typical reporter levels.

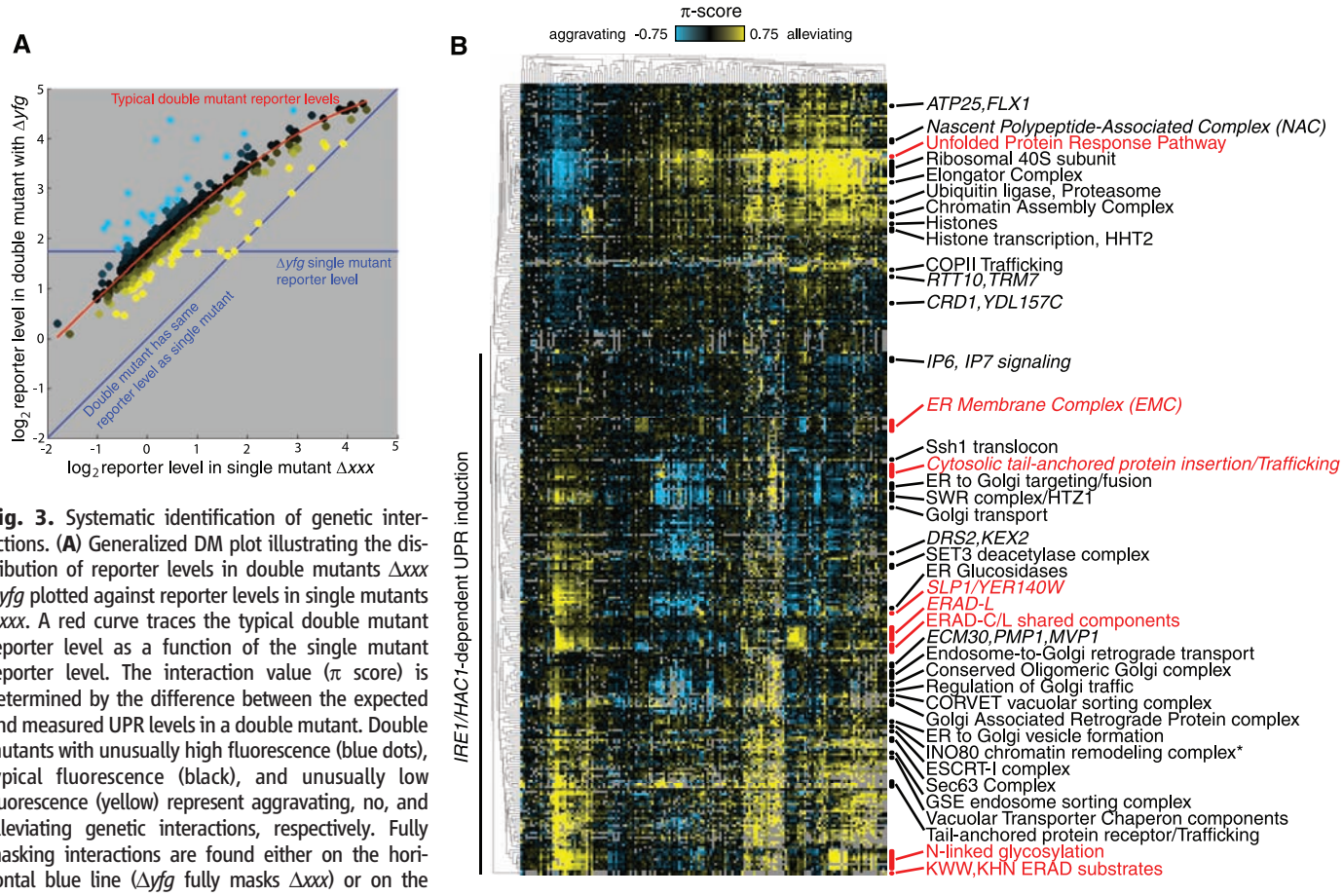

Fig. 3. Systematic identification of genetic interactions. (**A**) Generalized DM plot illustrating the distribution of reporter levels in double mutants Δ*xxx* Δ*yfg* plotted against reporter levels in single mutants Δ*xxx*. A red curve traces the typical double mutant reporter level as a function of the single mutant reporter level. The interaction value (π score) is determined by the difference between the expected and measured UPR levels in a double mutant. Double mutants with unusually high fluorescence (blue dots), typical fluorescence (black), and unusually low fluorescence (yellow) represent aggravating, no, and alleviating genetic interactions, respectively. Fully masking interactions are found either on the horizontal blue line (Δ*yfg* fully masks Δ*xxx*) or on the diagonal blue line (Δ*xxx* fully masks Δ*yfg*). (**B**) Hierarchical clustering of a genetic interaction map based on systematic π score analysis. To the right of the map, functional clusters are labeled (table S5). Clusters referred to in the text are highlighted in red; those containing previously unknown components are marked in italics.

Phenotypic interaction score (π score) quantifies functional relations. Strongly aggravating and fully masking interactions as described above are only a subset of the broader range of possible genetic interactions in which pairs of perturbations lead to a continuum of exacerbated (aggravating) or attenuated folding defects. We sought to quantify these systematically by developing a phenotypic interaction score or "π score" that describes the degree to which a double mutant UPR reporter level differs from that expected from the two single mutant levels. A simple empirical multiplicative model accurately predicted the typical double mutant reporter levels when we accounted for saturation of the reporter [Fig. 3A; see (*12*)]. The π score for each double mutant was given by the difference between the typical levels expected from the reporter levels of the two single mutants and the measured UPR reporter levels in the double mutant. Thus, negative π scores (exaggerated inductions) represent aggravating interactions, and positive π scores (unusually low inductions) represent alleviating interactions, with the fully masking interactions being a subset of the positive π scores.

Systematic identification of functional groups through phenotypic interaction maps. In growth-based studies, the pattern of genetic interactions of a mutation provides a signature that can be used to group genes by function (*20*, *21*, *25*). Analogous hierarchical clustering on the double mutant π scores yielded a map with a high density of precise functional clusters (Fig. 3B and fig. S4). This analysis accurately grouped over 100 of the previously well-characterized genes into 22 functions spanning a wide range of processes (table S5). Among genes whose deletions directly affected the ER folding environment (i.e., caused Ire1p/Hac1p-dependent reporter induction), our map grouped not only the ERAD and glycosylation machinery discussed above but also many other processes, including those in the distal secretory pathway (Fig. 3B). Our map also accurately clustered multiple functions that act downstream of *HAC1*, including the chromatin assembly complex, core histones, and histone chaperones.

Genetic interactions identify functional hierarchies. Within the functional groups defined above, the specific double mutant phenotypes revealed the extent to which the activities of individual components depended on each other. For example, all of the known components of the ERAD-L machinery needed for disposal of misfolded lumenal proteins (*17*) formed a tight cluster. The double mutant phenotypes of Δ*hrd3* revealed the expected full dependence of *YOS9*, *DER1*, and *USA1* on *HRD3* (Fig. 4A) (*17*). In contrast, only partial epistasis was seen with the E2 Ubc7p and its membrane anchor, Cue1p, consistent with their known roles in other branches of ERAD and the ability of another E2, Ubc1p, to partially substitute in their absence (*26*). In addition, the clustering analysis suggested that *YLR104W* is a previously unknown component of ERAD that acts upstream of *HRD3* and *USA1* (perhaps by delivering a subset of ERAD targets to the Hrd1p ligase) (table S6). Our complete list of genetic interactions, which includes over 500 full masking relations among 213 genes, should provide a resource of functional predictions for the community (table S6). For example, our data suggest that *YDR161W* is closely functionally related to the nascent polypeptide-associated complex. We also provide a MATLAB script to display double mutant plots for any gene in our data set (*12*).

Analysis of phenotypic interactions reveals previously unknown pathways important for ER protein folding. By using this systematic approach, we identified a pathway involving a conserved (table S9) multiprotein transmembrane complex. The poorly characterized genes *YCL045C*, *YJR088C*, *YKL207W*, *YGL231C*, *KRE27*, and *YLL014W* all clustered together and showed strongly alleviating interactions among themselves (Fig.

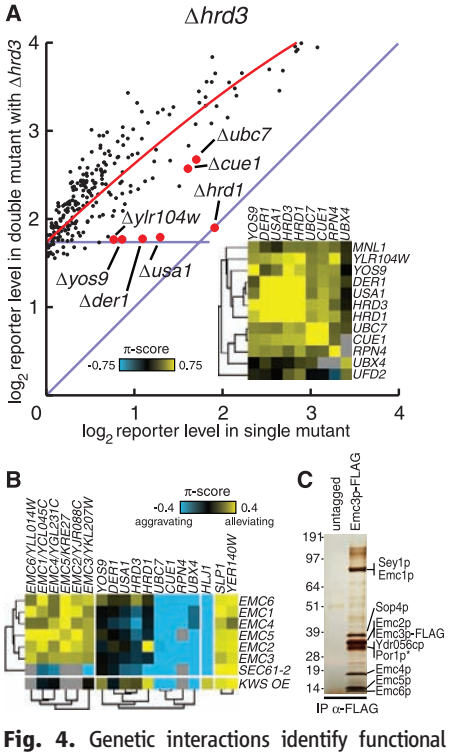

Fig. 4. Genetic interactions identify functional dependencies of uncharacterized proteins. (**A**) DM plot of Δ*hrd3*. (Inset) Enlargement of a region of Fig. 3B, showing genetic interactions of the ERAD cluster. (**B**) Selected genetic interactions of the EMC. (**C**) SDS–polyacrylamide gel electrophoresis analysis of immunoprecipitation of Emc3p-FLAG and associated proteins; protein identities were determined by mass spectrometry. The specificity of the Por1p interaction has not been evaluated.

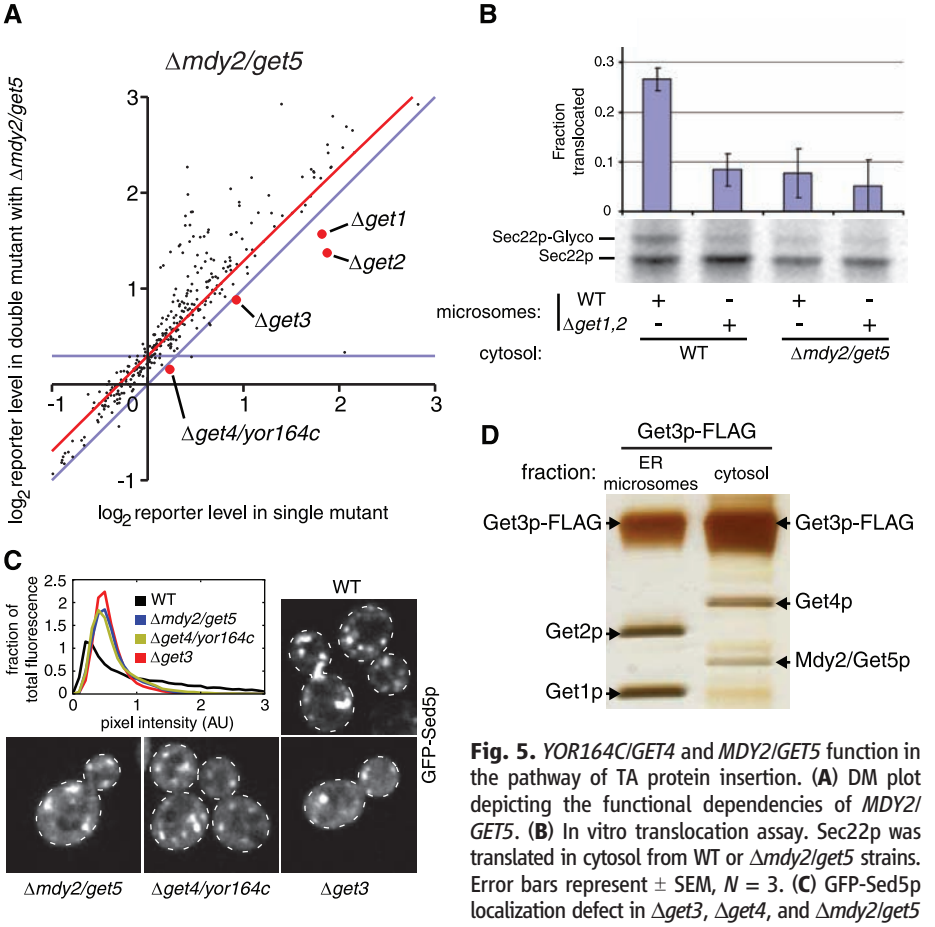

Fig. 5. *YOR164C*/*GET4* and *MDY2*/*GET5* function in the pathway of TA protein insertion. (**A**) DM plot depicting the functional dependencies of *MDY2*/*GET5*. (**B**) In vitro translocation assay. Sec22p was translated in cytosol from WT or Δ*mdy2*/*get5* strains. Error bars represent ± SEM, *N* = 3. (**C**) GFP-Sed5p localization defect in Δ*get3*, Δ*get4*, and Δ*mdy2*/*get5* strains. The images of at least 20 cells per strain with similar average fluorescence were quantified to determine the distribution of each strain's total fluorescence across pixels of different intensities. (**D**) Silver stain of immunoprecipitation of Get3-FLAGp from ER microsomes and cytosol; protein identities were determined by mass spectrometry.

4B), a signature of factors that cooperate to carry out a single function (*21*). Immunoprecipitation of FLAG-tagged Ykl207wp revealed that proteins encoded by these genes form an apparently stoichiometric complex (Fig. 4C). Accordingly we termed this the ER membrane protein complex (EMC) and named the genes from this cluster *EMC1* through *EMC6*. Although the precise biochemical roles of the EMC will have to wait for future studies, our data suggest that loss of the EMC leads to accumulation of misfolded membrane proteins: The pattern of genetic interactions of strains deleted for EMC members most closely resembled that seen in a strain overexpressing the misfolded transmembrane protein Sec61-2p (a mutated form of the Sec61 translocon) (*27*) and is similar to the pattern of a strain overexpressing the misfolded transmembrane protein KWS (*24*). This shared pattern includes strong aggravating interactions with Δ*ubc7* and Δ*cue1*, whose gene products are known to be involved in elimination of misfolded membrane proteins (*17*), but minimal interactions with other ERAD components.

A second cluster containing two conserved yet uncharacterized proteins (Yer140wp and Slp1p) show robust alleviating interactions with EMC components (Fig. 4B), as well as with each other. In support of a functional link between Yer140wp and Slp1p, these two proteins are suggested to be in a physical complex (*28*). The finding of two conserved protein complexes that are functionally dependent on each other underscores the value of this genetic data in identifying uncharacterized pathways required for ER folding.

Genetic interactions identify components of the tail-anchored protein biogenesis machinery. As a final example, we focused on Yor164c/Get4p and Mdy2/Tma24/Get5p because our analysis implicated them in tail-anchored (TA) protein biogenesis. TA proteins are an important class of transmembrane proteins, which includes soluble *N*-ethylmaleimide–sensitive factor attachment protein receptor (SNARE) trafficking factors (*29*, *30*). TA proteins have a single C-terminal transmembrane domain, which is inserted into the ER membrane through the action of the recently discovered GET pathway: the Get3p/Arr4p adenosine triphosphatase (and its mammalian homolog Asna1/TRC40) binds newly synthesized TA proteins and brings them to the ER via the ER membrane receptor complex formed by Get1p/Mdm39p and Get2p/Hur2p/Rmd7p (*31*–*33*). Our double mutant analysis pointed to a role of Yor164c/Get4p and its physical interaction partner, Mdy2p/Get5p (*34*), in the GET pathway because Δ*get4* and Δ*mdy2*/*get5* tightly clustered with Δ*get3* (fig. S5). Additionally, loss of *GET3* fully masked the effect of Δ*get4* and Δ*mdy2*/*get5* (Fig. 5A). Moreover, these deletions partially suppressed the UPR induction of Δ*get1* and Δ*get2*, a phenomenon previously seen with other phenotypes for Δ*get3* (*32*).

Several observations support a role for *GET4* and *MDY2*/*GET5* in TA protein biogenesis. First, cytosolic extracts from strains lacking Mdy2p/Get5p had a defect in insertion of the model TA substrate Sec22p into ER microsomes (Fig. 5B). Second, several of the in vivo phenotypes characteristic of loss of GET members are also observed in Δ*get4* and Δ*mdy2*/*get5* strains. These include a highly significant ($P < 10^{-30}$, Mann-Whitney *U*) relocalization of TA protein GFP-Sed5p from punctate Golgi structures to a more diffuse pattern (Fig. 5C and fig. S7) (*12*) as well as mislocalization of the peroxisomal TA protein, GFP-Pex15p, to mitochondria (fig. S8) (*32*). Consistent with a defect in Sed5 biogenesis, loss of Get4p or Mdy2p/Get5p led to secretion of HDEL proteins, a phenotype that is seen in other GET deletion strains (fig. S9). Third, immunoprecipitation revealed that Get4p and Mdy2p/Get5p bind Get3p in the cytosol (Fig. 5D). Mdy2p/Get5p also colocalized with Get3p and TA proteins to punctate protein aggregates that form in Δ*get1* strains (*32*) (figs. S10 and S11). Localization of Get3 to these puncta is dependent on Get4p and Mdy2p/Get5p but not vice versa (figs. S10 to S12), suggesting that Get4p and Mdy2p/Get5p help deliver TA proteins to Get3p in the cytosol for trafficking to the ER membrane. Interestingly, Get4p and Mdy2p/Get5p have been suggested to be peripherally associated with ribosomes (*34*), where they could potentially capture nascent TA proteins. Thus, whereas Get4p and Mdy2p/Get5p are localized outside of the secretory pathway and initially may have appeared to be false positives, our double mutant analysis revealed how they affect ER protein folding.

Perspective. Our work reveals the range of processes that make the ER a robust folding compartment and yields both a list of components and a blueprint for their functional interdependence. These factors include a wide range of activities such as chaperones, glycosylation enzymes, and ERAD components as well as trafficking pathways, transcriptional regulatory networks, modulators of lipid and ion composition, and vacuolar function. The diversity of activities found supports and extends the recent view in which ER protein folding homeostasis (proteostasis) emerges from the dynamic interplay between folding, degradation, and export processes (*35*, *36*). From a practical perspective, our studies provide a rational starting point for efforts to modulate the ER folding capacity to intervene in disease (*36*).

More broadly, dissecting complex cellular processes represents a major challenge in cell biology. Deletion libraries and RNA interference (RNAi) approaches now make it possible to identify important factors rapidly (*37*). But this in turn creates a bottleneck in their functional characterization, which classically requires specialized gene-by-gene follow-up studies. Our approach in effect allows hundreds of different secondary screens to be carried out in parallel to explore systematically the functional interdependencies of hits, thus providing a foundation for focused mechanistic investigations. Given the large number of potential ways of creating proximal reporters for different aspects of biology, our strategy for generalizing systematic quantitative genetic analysis should be broadly applicable to other processes and organisms, including mammals, through the use of double RNAi treatments.

References and Notes

1. J. H. Lin, P. Walter, T. S. Yen, *Annu. Rev. Pathol.* **3**, 399 (2008).
2. D. Scheuner, R. J. Kaufman, *Endocr. Rev.* **29**, 317 (2008).
3. D. N. Hebert, M. Molinari, *Physiol. Rev.* **87**, 1377 (2007).
4. E. S. Trombetta, A. J. Parodi, *Annu. Rev. Cell Dev. Biol.* **19**, 649 (2003).
5. D. Ron, P. Walter, *Nat. Rev. Mol. Cell Biol.* **8**, 519 (2007).
6. R. Casagrande *et al.*, *Mol. Cell* **5**, 729 (2000).
7. K. J. Travers *et al.*, *Cell* **101**, 249 (2000).
8. M. G. Pollard, K. J. Travers, J. S. Weissman, *Mol. Cell* **1**, 171 (1998).
9. A. H. Y. Tong *et al.*, *Science* **294**, 2364 (2001).
10. G. Giaever *et al.*, *Nature* **418**, 387 (2002).
11. J. R. Newman *et al.*, *Nature* **441**, 840 (2006).
12. Materials and methods are available as supporting material on *Science* Online.
13. E. A. Winzeler *et al.*, *Science* **285**, 901 (1999).
14. W. K. Huh *et al.*, *Nature* **425**, 686 (2003).
15. B. Bukau, J. Weissman, A. Horwich, *Cell* **125**, 443 (2006).
16. A. Helenius, M. Aebi, *Annu. Rev. Biochem.* **73**, 1019 (2004).
17. K. Nakatsukasa, J. L. Brodsky, *Traffic* **9**, 861 (2008).
18. L. Decourty *et al.*, *Proc. Natl. Acad. Sci. U.S.A.* **105**, 5821 (2008).
19. H. S. Girgis, Y. Liu, W. S. Ryu, S. Tavazoie, *PLoS Genet.* **3**, 1644 (2007).
20. X. Pan *et al.*, *Cell* **124**, 1069 (2006).
21. M. Schuldiner *et al.*, *Cell* **123**, 507 (2005).
22. D. Segre, A. Deluna, G. M. Church, R. Kishony, *Nat. Genet.* **37**, 77 (2005).
23. R. P. St Onge *et al.*, *Nat. Genet.* **39**, 199 (2007).
24. S. Vashist, D. T. Ng, *J. Cell Biol.* **165**, 41 (2004).
25. A. H. Y. Tong *et al.*, *Science* **303**, 808 (2004).
26. R. Friedlander, E. Jarosch, J. Urban, C. Volkwein, T. Sommer, *Nat. Cell Biol.* **2**, 379 (2000).
27. T. Sommer, S. Jentsch, *Nature* **365**, 176 (1993).
28. S. R. Collins *et al.*, *Mol. Cell. Proteomics* **6**, 439 (2007).
29. L. Burri, T. Lithgow, *Traffic* **5**, 45 (2004).
30. N. Borgese, S. Brambillasca, P. Soffientini, M. Yabal, M. Makarow, *Biochem. Soc. Trans.* **31**, 1238 (2003).
31. V. Favaloro, M. Spasic, B. Schwappach, B. Dobberstein, *J. Cell Sci.* **121**, 1832 (2008).
32. M. Schuldiner *et al.*, *Cell* **134**, 634 (2008).
33. S. Stefanovic, R. S. Hegde, *Cell* **128**, 1147 (2007).
34. T. C. Fleischer, C. M. Weaver, K. J. McAfee, J. L. Jennings, A. J. Link, *Genes Dev.* **20**, 1294 (2006).
35. W. E. Balch, R. I. Morimoto, A. Dillin, J. W. Kelly, *Science* **319**, 916 (2008).
36. T. W. Mu *et al.*, *Cell* **134**, 769 (2008).
37. M. Boutros, J. Ahringer, *Nat. Rev. Genet.* **9**, 554 (2008).

38. We thank C.-S. Chin for flow cytometry software development; C. Boone, D. Breslow, N. Krogan, D. Ng, and C. Wang for reagents; K. Thorn for microscopy assistance; S. Zhou, D. King, G. Cagney, and N. Krogan for mass spectrometry analyses; J. Metz, P. Nittler, A. Carroll, J. Hill, J. Ihmels, S. Wang, and C. Chu for technical help; R. Andino, T. Aragon, A. Battle, N. Bradshaw, J. DeRisi, N. Friedman, J. Hollien, J. Newman, D. Koller, R. Kupferman, H. Madhani, L. Osherovich, F. Papa, and members of the Weissman, Walter, and Schwappach labs for stimulating discussion; B. Toyama for graphics; and M. Bassik, D. Breslow, O. Brandman, S. Churchman, and S. Neher for comments on the manuscript. This work was supported by the Howard Hughes Medical Institute (J.S.W. and P.W.), the NSF (M.C.J. and E.M.Q.), the International Human Frontier Science Program (M.S. and J.W.), an NIH K99/R00 award (M.S.), a European Molecular Biology Organization long-term fellowship (J.W.), the Deutsche Forschungsgemeinschaft (V.S.), and the Wellcome Trust (B.S.).

Supporting Online Material

www.sciencemag.org/cgi/content/full/323/5922/1693/DC1
Materials and Methods
Figs. S1 to S12
Tables S1 to S12
References

3 November 2008; accepted 27 January 2009
10.1126/science.1167983

Lubrication at Physiological Pressures by Polyzwitterionic Brushes

Meng Chen,[1]* Wuge H. Briscoe,[1]† Steven P. Armes,[2] Jacob Klein[1,3]‡

The very low sliding friction at natural synovial joints, which have friction coefficients of $\mu < 0.002$ at pressures up to 5 megapascals or more, has to date not been attained in any human-made joints or between model surfaces in aqueous environments. We found that surfaces in water bearing polyzwitterionic brushes that were polymerized directly from the surface can have μ values as low as 0.0004 at pressures as high as 7.5 megapascals. This extreme lubrication is attributed primarily to the strong hydration of the phosphorylcholine-like monomers that make up the robustly attached brushes, and may have relevance to a wide range of human-made aqueous lubrication situations.

The rubbing of opposing bones during the articulation of mammalian joints is mediated by layers of articular cartilage coating their surfaces that provide particularly efficient lubrication as they slide past each other (*1*, *2*). The associated very low friction at the high pressures of human joints such as hips or knees, with friction coefficients $\mu < 0.002$, has to date not been emulated in human-made systems. Model studies (*3*–*7*) between smooth sliding surfaces bearing neutral or charged polymer brushes demonstrated sliding friction coefficients as low as $\mu < 0.001$, which are values lower than with any other boundary lubricant system. As noted (*8*, *9*), in earlier studies with polymer brushes (*3*–*6*), the friction increases sharply at mean pressures $P > \sim 0.3$ MPa, which is far below the 5 MPa or more at which low friction persists in nature. In the present work, we sought to overcome the limitations of these earlier studies (*3*–*6*). We used polymer brushes, which make good boundary lubricants because they do not bridge the intersurface gap, that are strongly attached to each surface so as to resist being sheared off and that are highly hydrated so as to use the very efficient lubrication afforded by hydration sheaths that has been previously observed (*10*, *11*).

Brushes of the polymer poly[2-(methacryloyloxy) ethyl phosphorylcholine] (pMPC) were grown from the surfaces of macroinitiator-coated mica sheets that were premounted onto cylindrical lenses for surface force balance (SFB) measurements (*12*, *13*). After calibration in dry air, control measurements of the normal forces (F_n) and shear forces (F_s) between the macroinitiator-coated mica surfaces were performed (*12*, *14*) as a function of their absolute separation D and their sliding velocity v_s [$F_n(D)$ and $F_s(D, v_s)$, respectively]. Measurements were performed both in polymer-free water and after incubation in a 0.3% w/v pMPC homopolymer solution in order to compare them with the subsequent pMPC brush profiles. These controls, shown in Fig. 1, reveal the high friction associated with the macroinitiator alone (Fig. 1, B and C) before the growing of the polymer layers. They also show that the pMPC homopolymer does not adsorb onto the macroinitiator-bearing mica (Fig. 1A), which confirms that surface growth of the polymer results in true brush formation. After the polymer brushes were grown via direct polymerization from the surface, $F_n(D)$ and $F_s(D, v_s)$ profiles between the brush layers were measured in water and in aqueous $NaNO_3$ solutions up to physiological salt concentrations.

Figure 2 shows the typical F_n versus D profiles between pMPC brush–bearing mica surfaces in the standard crossed-cylinder SFB configuration in pure water and at salt concentrations of ~0.01 M and ~0.1 M $NaNO_3$ (the pMPC brush and its monomer structure are shown in Fig. 2A, inset). Some contraction of the pMPC brushes is seen in the salt solutions relative to those in the pure water. The highest normal loads F_n applied are some two or more orders of magnitude higher than those in earlier brush studies (*4*, *5*) that used the SFB. This leads to substantial flattening at the contact region, as indicated in the photo of the interference fringes (Fig. 2B and schematically in Fig. 2C), from which the contact area A between the surfaces is measured directly (the mean pressures P across the flattened contact area are given by $P = F_n/A$). Comparison with the control profiles

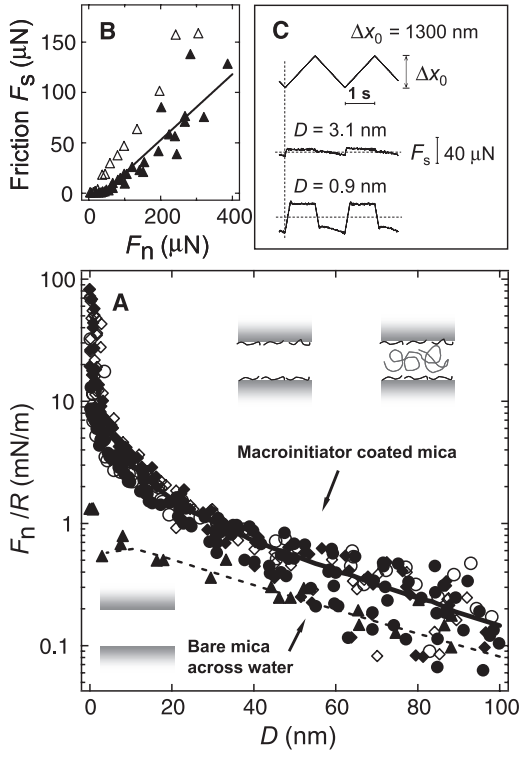

Fig. 1. Control measurements of (**A**) F_n versus D profiles and (**B** and **C**) of F_s between bare mica and between macroinitiator-coated mica surfaces across water and across a pMPC homopolymer solution. (A) Solid triangles indicate forces between bare mica in pure water on approach [normalized as $F_n(D)/R$, where $R \approx 1$ cm is the mean surface curvature radius]. The dashed line is a fit to the Derjaguin-Landau-Vervey-Overbeek theory based on a numerical solution of the nonlinear Poisson-Boltzmann equation (*32*) for a 1:1 electrolyte concentration $c = 5 \times 10^{-5}$ M, with constant surface potential $\psi_0 = -80$ mV and Hamaker constant $A = 2 \times 10^{-20}$ J. Solid and open circles indicate $F_n(D)$ profiles between macroinitiator-coated (20 min of incubation) mica in pure water on approach and separation, respectively. Solid and open diamonds indicate profiles between macroinitiator-coated mica after 13 hours of incubation in 0.3% w/v pMPC homopolymer [M_w = 22,000; M_w/M_n = 1.3, where M_w and M_n are, respectively, the weight and number average molecular weights] in aqueous solution on approach and separation, respectively. The solid line is a guide to the eye. The illustrations show schematically the configurations corresponding to the three control measurements; the short chains (black) represent the macroinitiator, and the longer random-coil chains represent the pMPC homopolymer in solution. (B) A summary of friction force F_s versus load, extracted from traces as in (C), between macroinitiator-coated surfaces in water (open triangles) and in 0.3% w/v MPC homopolymer solution (solid triangles); the solid line corresponds to friction coefficient $\mu = 0.33$. (C) Typical F_s versus time traces between two macroinitiator-coated mica surfaces in water at different D values in response to laterally applied motion of the top mica surface (top trace).

[1]Physical and Theoretical Chemistry Laboratory, University of Oxford, Oxford OX1 3QZ, UK. [2]Department of Chemistry, University of Sheffield, Sheffield S3 7HF, UK. [3]Weizmann Institute, Rehovot 76100, Israel.

*Present address: Procter and Gamble (Beijing) Technical Centre, Floor 5-8, Tongfang Building, 18 Shuangqing Road, Haidian District, Beijing 100084, People's Republic of China. †Present address: School of Chemistry, University of Bristol, Bristol BS8 1TS, UK.

‡To whom correspondence should be addressed. E-mail: jacob.klein@weizmann.ac.il

from Fig. 1A in the absence of polymer brushes (the dotted and dashed curves in Fig. 2A) reveals the extension of the unperturbed brushes from the macroinitiator layer, whereas fits to the force profiles provide more detailed information on the brush characteristics (*12*, *13*). The profiles both on approach and separation of the surfaces (characteristic of brush interactions) are similar as is in particular their insensitivity to repeated shear up to the highest compressions, which shows the robustness of the layers toward resisting friction and shear-off (*15*).

Characteristic traces of F_s versus time as two pMPC brushes slide past each other under different loads or compression ratios (corresponding to different surface separations) and salt concentrations, taken directly from the SFB, are shown in Fig. 3. Traces both at low compressions (higher D values) (Fig. 3, left) and high compressions (lower D values) (Fig. 3, right) show that the shear forces remain very weak—within the noise level of the SFB—up to mean contact pressures of ~2 to 2.5 MPa and then increase measurably with the load, up to the largest loads applied. Such traces are characteristic of all pMPC brushes and salt concentrations studied; that the traces are unchanged in time indicates there is no detectable wear of the layers over the range of parameters studied. Shear force results are summarized in Fig. 4 and Table 1. These show that the friction coefficient μ (taken as the slope of the F_s versus F_n plot) is in the range of values $\mu \approx (1.5 \pm 1) \times 10^{-3}$ up to the highest mean contact pressures applied, $P \approx 7.5$ MPa (~75 atmospheres). The values of μ, though remaining very low, are seen to increase slightly within this range as the salt concentration increases. The variation of the shear or friction force with v_s is shown in Fig. 4B, revealing a weak $F_s(v_s)$ dependence over three orders of magnitude in v_s.

Our findings show that brushes of pMPC, a polyzwitterion whose monomers carry the phosphorylcholine (PC) group (as occurs in naturally occurring phospholipid headgroups), can reduce friction to levels previously seen only in natural joints (μ on the order of 0.001 at pressures of 5 MPa or more). Earlier studies (*4*, *5*) between polymer brush–coated surfaces showed similarly low friction coefficients but only at very much lower pressures. At higher pressures, the coefficient of friction became large, either because of entanglement or vitrification of the brushes (*4*) or as a result of the increasing frictional shear at these pressures removing from the surface the relatively weakly attached charged brushes (*5*). What is the

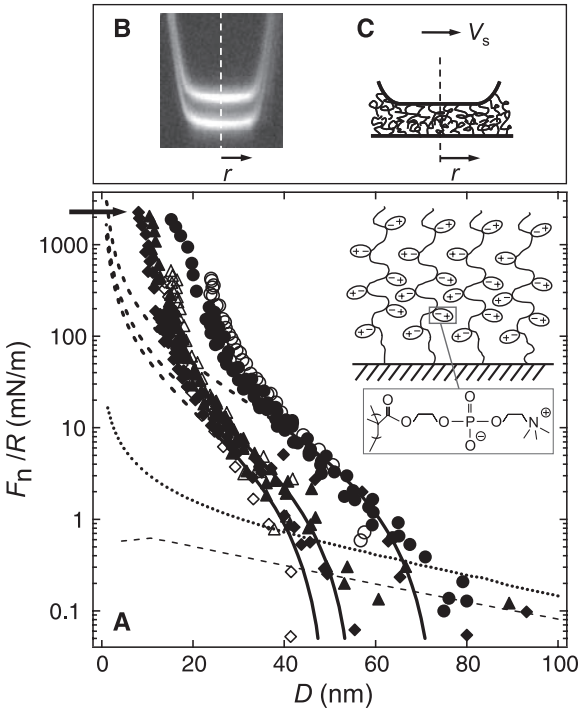

Fig. 2. Normal interactions between pMPC brush–coated mica surfaces across water and across aqueous salt solutions (normalized as above). (**A**) Normal force profiles: circles, water (no added salt); triangles, 8.7 mM $NaNO_3$; diamonds, 88.6 mM $NaNO_3$. Solid and open symbols indicate compression and decompression, respectively. Different incubation times in the macroinitiator solution (20 min and 2 hours) were used, with a polymerization time of 1.5 hours in each case (the layers are designated as 20-1.5 and 2-1.5, respectively). The pMPC layers are 2-1.5 brushes (*12*). Before solvation, the brushes were characterized (*12*, *13*) with x-ray photoelectron spectroscopy, multiple-beam interference, x-ray reflectometry, and atomic force micoscopy, which revealed a uniform smooth layer (root mean square roughness, 0.4 nm), whereas from a fit to the data (solid curves) (*12*) we estimate mean interanchor spacings $s = 3.5 \pm 1$ nm and unperturbed brush-heights $L = 37 \pm 5$, 28 ± 5, and 25 ± 5 nm for the solvated brushes at respective increasing salt concentrations. The brush-chain polydispersity is estimated at ~1.2 (*12*, *13*). The pMPC brush-like configuration and its monomer structure are also shown. The dashed and dotted lines summarize the brush-free controls between bare and between macroinitiator-coated mica, respectively, from Fig. 1A. (**B**) Equal chromatic order interference fringes revealing the flattening of the mica surfaces at a high load, indicated by the arrow in (A). (**C**) The schematic configuration corresponding to (B) (with contact area $A \cong \pi r^2$).

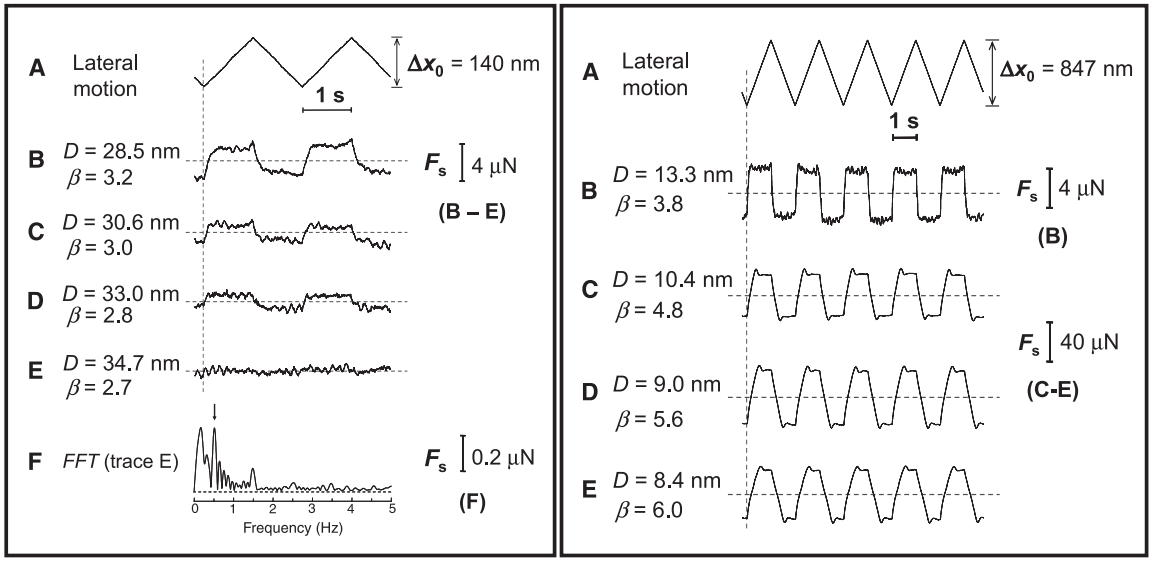

Fig. 3. Typical F_s versus time traces between pMPC-coated mica surfaces taken directly from the SFB. (**Left**) 20-1.5 brushes in pure water. (**Right**) 2-1.5 brushes in ~0.1 M salt solution (*12*). The top trace A in each column is the lateral motion applied to the top surface, whereas traces B to E are the corresponding shear forces transmitted between the surfaces at the compression ratios β (2*L*/*D*) shown. Trace F is a frequency (ω) analysis of trace E, where the magnitude of F_s (ω) at the drive frequency (arrow) is used to reveal the onset of frictional force above any systematic signal (*5*, *10*) at large D values.

mechanism underlying the very low friction in the present study?

Earlier studies with charged brushes attributed comparably low friction coefficients (at much lower pressures) to a combination of factors. At low to moderate pressures, interpenetration (and therefore entanglement) of the opposing brushes was suppressed by configurational entropy effects (*4*, *6*, *16*). At the higher compressions of the present study, such interpenetration during the sliding is attributed instead to a self-regulation mechanism within the interfacial region (*6*, *17*). According to this, the mutual interpenetration zone of the sliding brushes, where the viscous dissipation leading to frictional drag occurs, has a thickness δ. This thickness varies so that the relaxation rate of the polymer moieties within it equals the shear rate within the zone; that is, $[1/\tau(\delta)] \approx (v_s/\delta)$, where τ is the relaxation time of the polymer moieties. Such self-regulation can readily be seen to lead to a weak dependence of friction on v_s, which is in line with the observed data at high loads (Fig. 4B), and a similar variation has been seen earlier for friction between sliding highly compressed brushes (*17*). Qualitatively, this occurs because at higher sliding velocities the extent of brush interpenetration decreases so that the overall frictional drag varies more weakly with increasing v_s than if the interpenetration zone remained at a constant thickness (*6*, *17*). At elevated pressures, lubrication by charged brushes was previously attributed to counterion osmotic pressure (*5*), together with the lubricating action of hydration layers surrounding the charged monomers. In the present study, the overall-neutral zwitterionic chains have no counterions associated with them so that osmotic pressure due to trapped counterions cannot be playing a role. The effect of any counterions associated with the residual charge of the underlying macroinitiator-coated mica is negligible. The primary mechanism underlying the low friction observed must therefore be attributed almost exclusively to the high level of hydration of the zwitterionic PC groups on the monomers. These are known to bind around 15 to 25 or more water molecules per monomer [depending on the method of measurement (*18*–*23*)]. Similar strongly bound hydration layers about such phosphorylcholine-coated biomaterials are also responsible for repelling proteins from their surfaces (*22*, *24*).

Water molecules in hydration layers have been shown to act as very efficient lubricants in the case of hydrated ions trapped between charged surfaces (*10*). This results from the water molecules being tenaciously attached, on an average over time, to the enclosed ionic charges so that the resistance to dehydration leads to their ability to support a large pressure. At the same time, the hydration water molecules are able to rapidly exchange with other hydration or free water molecules (*10*, *25*) and so are able to behave fluidly when sheared at rates lower than these exchange (relaxation) rates. This, we believe, is also the origin of the low friction in the present system and, together with the stronger attachment of the chains grown directly from the surface, ensures the robust nature of the brushes when compared with the polyelectrolyte chains that were sheared off (*15*). We attribute the ability of the hydration shells about the (methacryloyloxy)ethyl phosphorylcholine (MPC) monomers to lubricate at much higher mean pressures (relative to those at which previously studied polyelectrolyte brushes were removed by friction) to the higher and more tenacious hydration (*18*–*21*, *23*) of their PC groups. The slight increase in the friction coefficient with increasing salt concentration (Table 1) may be attributed to some salting-out of the pMPC monomers at the higher salt concentration [as has been observed in other PC systems (*26*)], leading to reduced hydration of the monomers and thus to less efficient lubrication. Such an effect would also explain the small contraction of the brush height at the higher salt concentrations (Fig. 2).

A large reduction in wear of polymer/metal hip implants has recently been achieved (*27*) by growing a pMPC layer from a polyethylene acetabular surface. The corresponding μ ~ 0.1 was not especially low. It is likely that this value of μ is dominated by a small number of high-friction asperity contacts between the sliding surfaces, which are far rougher than the mica substrate in our experiments, or by the bridging of the pMPC chains between the acetabular surface and the metal countersurface to which they may adsorb. This would result in higher friction relative to the values we measured between two pMPC brushes. A comparably high friction coefficient, ~0.1, was also measured (*28*) in a recent pin-on-disk tribological study between pMPC-coated surfaces under water.

Finally, in view of their similarly low friction at comparably high pressures, it is of interest to consider the relevance of our study to mechanisms of

Table 1. Friction coefficients between pMPC brush–coated mica surfaces sliding past each other at mean pressures *P* (in the range of 2 to 7.5 MPa) at different salt concentrations. Details about the water purification can be found in (*12*).

Aqueous solution	Friction coefficient
Pure water	0.00043 ± 0.0001
0.01 M $NaNO_3$	0.001 ± 0.0004
0.1 M $NaNO_3$	$0.0026^{+0.0005}_{-0.001}$

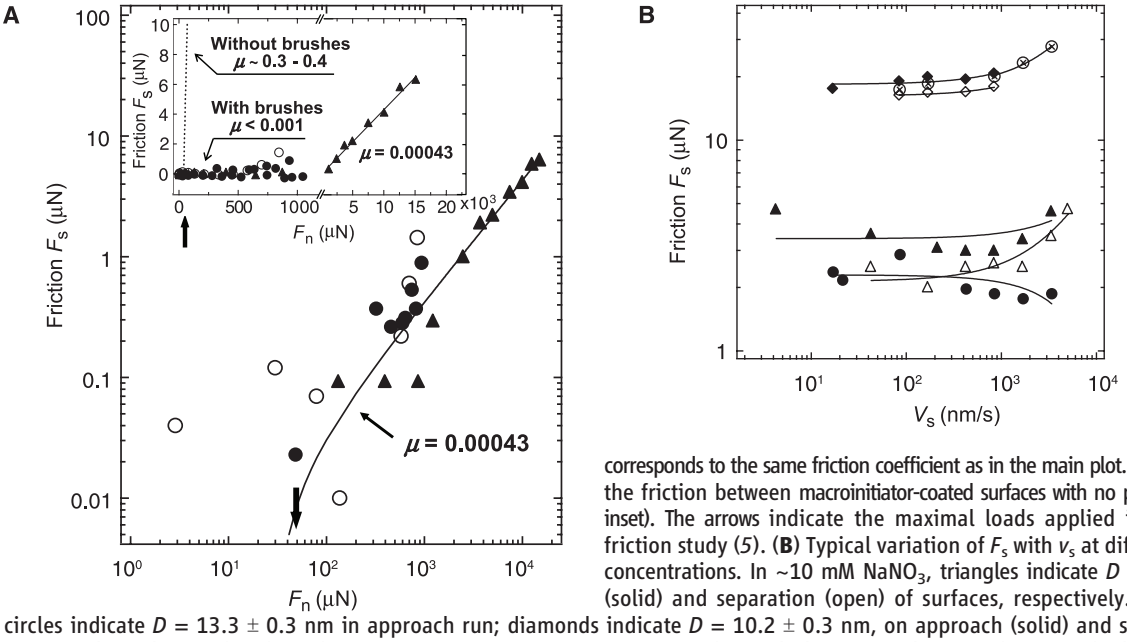

Fig. 4. Variation of friction F_s with load F_n and with sliding velocity v_s between pMPC brush–coated surfaces. (**A**) Variation of F_s with F_n for both 20-1.5 (circles) and 2-1.5 (triangles) brushes across water; within the scatter there is little systematic difference between these two brushes. Solid circles, approach; open circles, separation. There is a double logarithmic scale; the solid curve corresponds to μ = 0.00043. (Inset) The same data on a linear scale; the solid line for F_n > 1.5 mN corresponds to the same friction coefficient as in the main plot. The sharply rising dotted line is the friction between macroinitiator-coated surfaces with no pMPC brushes (based on Fig. 1, inset). The arrows indicate the maximal loads applied in the polyelectrolyte brush friction study (*5*). (**B**) Typical variation of F_s with v_s at different compressions and salt concentrations. In ~10 mM $NaNO_3$, triangles indicate D = 13 ± 0.3 nm on approach (solid) and separation (open) of surfaces, respectively. In ~100 mM $NaNO_3$, solid circles indicate D = 13.3 ± 0.3 nm in approach run; diamonds indicate D = 10.2 ± 0.3 nm, on approach (solid) and separation (open) of surfaces, respectively; and crossed circles indicate D = 8.5 ± 0.3 nm, in separation run. There is little variation between data sets whether on approach or separation of surfaces and whether in ~10 mM or 100 mM salt.

lubrication between articular cartilage surfaces. Biological lubrication at such synovial joints, despite many decades of study, is not yet well understood at the molecular level (*29*–*31*). Recent models have focused on the role of pressurized interstitial water (*31*) and of macromolecules at the outer cartilage surface (*30*). Our system of synthetic polyzwitterionic brushes polymerized from molecularly smooth mica surfaces does not have a clear analog at the cartilage surface, at which macromolecular components of the cartilage and the synovial fluid surrounding it are likely to be present [including proteins, hyaluronic acid, proteoglycans, glycoproteins, and lipidic molecules (*30*)]. The detailed role of these in the lubrication process, as well as of the cartilage substrate itself, has yet to be clarified. Moreover, cartilage is softer and much rougher than mica, though at these high pressures it may deform affinely (*30*); experiments on similarly soft and roughened brush-coated surfaces could potentially provide insight into the mechanisms that are operative in cartilage-cartilage friction. The highly hydrated PC-like monomers on our pMPC chains provide very efficient lubrication. The structure of these is similar to that of lipid headgroups, which provides some context for the recent controversial suggestion that lipid multilayers may have a role in mediating synovial lubrication (*29*), particularly in view of recent findings on the mechanism of boundary lubrication under water (*11*). Finally, although our polyzwitterionic brushes have no direct analog at cartilage surfaces, our results underline the possible importance at such surfaces of highly hydrated macromolecules in both chondroprotective and lubrication roles.

We have shown that brushes of a biocompatible polyzwitterion, pMPC, are capable of providing extremely efficient lubrication in aqueous media with coefficients of friction $\mu \approx 0.001$ at mean pressures up to 7.5 MPa, which are comparable to values in human synovial joints. We attribute the low friction at the high pressure primarily to the lubricating action of tenaciously attached but labile water molecules about the strongly hydrated MPC monomers. Our results may have relevance for boundary lubrication in human-made systems in aqueous or physiological media, as in biomedical devices, in which friction and wear are often an issue.

References and Notes

1. C. W. McCutchen, *Fed. Proc.* **25**, 1061 (1966).
2. D. Swann, K. J. Bloch, D. Swindell, E. Shore, *Arthritis Rheum.* **27**, 552 (1984).
3. A. N. M. Forster, J. W. Mays, S. M. Kilbey, *J. Polym. Sci. Part B Polym. Phys.* **44**, 649 (2006).
4. J. Klein, E. Kumacheva, D. Mahalu, D. Perahia, L. Fetters, *Nature* **370**, 634 (1994).
5. U. Raviv *et al.*, *Nature* **425**, 163 (2003).
6. P. Schorr, T. Kwan, M. Kilbey, S. G. Shaqfeh, M. Tirrell, *Macromolecules* **36**, 389 (2003).
7. J. P. Gong *et al.*, *J. Am. Chem. Soc.* **123**, 5582 (2001).
8. D. Gourdon *et al.*, *Langmuir* **24**, 1534 (2008).
9. S. Lee, N. D. Spencer, *Science* **319**, 575 (2008).
10. U. Raviv, J. Klein, *Science* **297**, 1540 (2002).
11. W. H. Briscoe *et al.*, *Nature* **444**, 191 (2006).
12. Materials and methods are available as supporting material on *Science* Online.
13. M. Chen, W. H. Briscoe, S. P. Armes, H. Cohen, J. Klein, *ChemPhysChem* **8**, 1303 (2007).
14. J. Klein, E. Kumacheva, *J. Chem. Phys.* **108**, 6996 (1998).
15. This robustness is consistent with the nature of the pMPC brushes' attachment to the mica and the shear forces applied. For an area per macroinitiator $A_m \approx 16$ nm^2 (*13*) and a mean pressure P, the shear force acting on a single macroinitiator molecule [$F_{s(m)}$] through the chains growing from it is given by $F_{s(m)} = \mu P A_m$. Because the chains are attached covalently to the initiation sites, any detachment due to shear is expected to commence at the weaker bonds attaching the macroinitiator to the mica. These bonds (on average ~18 such bonds per macroinitiator) each have a net adhesion energy $\varepsilon_1 \approx k_B T$ (k_B is the Boltzmann constant and T is the temperature) arising from replacement of counterions at the negatively charged mica surface by the positively charged quaternary $-N^+(CH_3)_3$ groups on the macroinitiator. In the worst-case scenario, all the $F_{s(m)}$ during sliding will act on one of the quaternary groups at the surface, and this may initiate the "unzipping" of the macroinitiator from the mica. Putting $\mu = 0.001$ and $P = 7.5$ MPa gives $F_{s(m)} = 1.2 \times 10^{-13}$ N. This is smaller than the force $f_1 \approx \varepsilon_1/\delta$ that is needed to detach a single $-N^+(CH_3)_3$ group from the mica, where δ is on the order of 1 Å or less. Putting $\delta = 1$ Å gives $f_1 \approx 4 \times 10^{-11}$ N. Thus, the friction force on a macroinitiator at the highest pressures we apply is too weak (by a factor of 100 or more) to detach even a single bond anchoring the macroinitiator to the mica surface, which is consistent with our observations of the robustness of the pMPC layer toward resisting shear under all conditions in our study.
16. T. Witten, L. Leibler, P. Pincus, *Macromolecules* **23**, 824 (1990).
17. R. Tadmor, J. Janik, L. J. Fetters, J. Klein, *Phys. Rev. Lett.* **91**, 115503 (2003).
18. E. A. Disalvo *et al.*, *J. Argent. Chem. Soc.* **92**, 1 (2004).
19. M. Yaseen, J. R. Lu, *Langmuir* **22**, 5825 (2006).
20. G. Pabst, M. Rappolt, H. Amenitsch, P. Laggner, *Phys. Rev. E Stat. Phys. Plasmas Fluids Relat. Interdiscip. Topics* **62**, 4000 (2000).
21. J. F. Nagle *et al.*, *Biophys. J.* **70**, 1419 (1996).
22. K. Ishihara *et al.*, *J. Biomed. Mater. Res.* **39**, 323 (1998).
23. L. J. Lis, M. McAlister, N. Fuller, R. P. Rand, V. A. Parsegian, *Biophys. J.* **37**, 657 (1982).
24. W. Feng *et al.*, *Biointerphases* **2**, 34 (2007).
25. F. A. Cotton, G. Wilkinson, *Advanced Inorganic Chemistry* (Wiley, New York, ed. 5, 1998), pp. 1288–1289.
26. M. Rappolt, G. Pabst, H. Amenitsch, P. Laggner, *Colloids Surf. A Physicochem. Eng. Asp.* **183-185**, 171 (2001).
27. T. Moro *et al.*, *Nat. Mater.* **3**, 829 (2004).
28. M. Kobayashi *et al.*, *Soft Matter* **3**, 740 (2007).
29. B. A. Hills, G. D. Jay, *J. Rheumatol.* **29**, 200 (2002).
30. J. Klein, *Proc. Inst. Mech. Eng. Part J J. Eng. Tribol.* **220**, 691 (2006).
31. S. Park, K. D. Costa, G. A. Ateshian, *J. Biomech.* **37**, 1679 (2004).
32. D. Y. C. Chan, R. M. Pashley, L. R. White, *J. Colloid Interface Sci.* **77**, 283 (1980).

33. We thank A. L. Lewis (Biocompatibles Ltd.) for kind donation of the MPC monomer; X. Y. Chen for synthesis of the macroinitiator; I. E. Dunlop, S. Perkin, and W. Feng for help and advice; and P. Pincus for a discussion. S.P.A. is the recipient of a Royal Society Research Merit Award. W.H.B. thanks the Taiho Kogyo Tribology Research Foundation for support. This work was supported by the Engineering and Physical Sciences Research Council, the Petroleum Research Fund (grant 45694-AC7), the Charles McCutchen Foundation, and the Minerva Foundation at the Weizmann Institute.

Supporting Online Material

www.sciencemag.org/cgi/content/full/323/5922/1698/DC1
Materials and Methods
References

5 December 2008; accepted 21 January 2009
10.1126/science.1169399

Controlled Formation of Sharp Zigzag and Armchair Edges in Graphitic Nanoribbons

Xiaoting Jia,[1] Mario Hofmann,[2] Vincent Meunier,[3] Bobby G. Sumpter,[3] Jessica Campos-Delgado,[4] José Manuel Romo-Herrera,[4] Hyungbin Son,[2] Ya-Ping Hsieh,[2] Alfonso Reina,[1] Jing Kong,[2] Mauricio Terrones,[4] Mildred S. Dresselhaus[2,5]*

Graphene nanoribbons can exhibit either quasi-metallic or semiconducting behavior, depending on the atomic structure of their edges. Thus, it is important to control the morphology and crystallinity of these edges for practical purposes. We demonstrated an efficient edge-reconstruction process, at the atomic scale, for graphitic nanoribbons by Joule heating. During Joule heating and electron beam irradiation, carbon atoms are vaporized, and subsequently sharp edges and step-edge arrays are stabilized, mostly with either zigzag- or armchair-edge configurations. Model calculations show that the dominant annealing mechanisms involve point defect annealing and edge reconstruction.

Graphene, a single sheet of graphite, has attracted a lot of research interest since it first became experimentally accessible in 2004 (*1*–*5*). Its two-dimensional (2D) structure and the near massless behavior of its charge carriers provide unique transport properties. Graphene nanoribbons, which are quasi-1D graphene nanostructures, exhibit a bandgap between the valence and conduction band states. The bandgap depends on both the edge type and ribbon width (*6*), which is typically a few nanometers, making graphene nanoribbons a very interesting material for potential electronics applications (*7*). Theoretical and experimental studies show that the edges of graphene nanoribbons strongly influence their electronic and magnetic properties (*8*, *9*). Therefore, much effort has been devoted to studying the edges in graphitic nanomaterials (*10*–*18*). Although atomically smooth edges are essential for many applications, it is difficult to produce such edges by conventional physico-chemical methods. For example, lithographic etching and

chemical methods usually provide rough edges (*19*) that contribute to carrier scattering. Furthermore, characterizing the edges and identifying the edge structure has been a challenge.

With an integrated transmission electron microscope–scanning tunneling microscope (TEM-STM) system [see supporting online material (SOM)], we are able to produce atomically smooth zigzag or armchair edges from defective rough edges that are observed in specially prepared graphitic nanoribbons (*20*). The graphitic nanoribbon samples are produced by a chemical vapor deposition process (*20*), as summarized in the SOM (fig. S1A). An individual nanoribbon sample is attached to the sample holder at one end and to the STM tip at the other end; these ends also serve as the two electrodes. As we apply a voltage (up to 1.6 V) over the length (315 nm) of a 66-nm-wide ribbon, the current (*I*)–versus–voltage (*V*) curve shows (Fig. 1A) the onset of a nonlinear regime (at 1.6 V), where the resistance decreases with increasing input energy (Fig. 1B). As current flows, the degree of crystallinity of the ribbon improves rapidly (Fig. 1, C and D), and the sample thickness decreases, until all the graphene layers evaporate and the sample breaks from the middle (fig. S1B). From the edge terminations observed in Fig. 1E, we conclude that the majority of edges are either zigzag or armchair after Joule heating.

It is important to note that in the lower voltage (quasi-linear) regime below 1.6 V (see Fig. 1A), carbon atoms mainly vaporize because of knock-on effects caused by the electron irradiation (*21*), and edges start reconstructing via Joule annealing. However, at higher applied voltages (1.6 V), the preferred reconstruction-crystallization effects induced by the high temperature caused by Joule heating are seen in going from Fig. 1, C to D, indicating that the activation energy of atoms forming zigzag or armchair edges is lower than for other edge configurations. Other types of edges are seen infrequently because a mixture of zigzag and armchair edges is metastable due to an energy penalty at the edge junctions. Figure 1F depicts the reconstructed graphitic material shown in Fig. 1D. The measured in-plane lattice spacing for our ribbons is 0.24 ± 0.02 nm, consistent (within the accuracy of our TEM measurements) with literature values for graphite [which is $\sqrt{3}a_{c-c}$, where a_{c-c} is the nearest-neighbor carbon-to-carbon distance (*22*)]. As a result of carbon atom vaporization and Joule heating, the defective graphitic edges in the as-grown nanoribbon sample crystallize (fig. S2) and finally become atomically sharp and highly crystalline. The maximum length of the smooth edges observed after the process in Fig. 1E is ~29 nm. The mechanism of reconstruction or crystallization for the nanoribbons and edges is attributed primarily to the carbon atom vaporization, the current flow along the ribbon and edges, and the high temperature associated with the resistive Joule heating (see SOM).

The graphitization steps of carbon at high temperatures have been described by Goma and Oberlin (*23*, *24*). Here the graphitization process culminates in the thermal crystallization of wavy and wrinkled layers into long in-plane crystalline domains by ~2100°C with *c*-axis stacking order starting to develop above 2300°C and identified with crystalline graphite. For our ribbon samples, we observed the transformation of AA stacking into ABAB stacking, and we attribute these transformations mainly to the high temperatures reached (above 2000°C) in the nonlinear voltage regime. To verify that a high temperature is achieved by

[1]Department of Materials Science and Engineering, Massachusetts Institute of Technology, Cambridge, MA 02139–4307, USA. [2]Department of Electrical Engineering and Computer Science, Massachusetts Institute of Technology, Cambridge, MA 02139–4307, USA. [3]Computer Science and Mathematics Division and Center for Nanophase Materials Sciences, Oak Ridge National Laboratory (ORNL), Post Office Box 2008, Oak Ridge, TN 37831–6367, USA. [4]Laboratory for Nanoscience and Nanotechnology Research (LINAN) and Advanced Materials Department, Instituto Potosino de Investigación Científica y Tecnológica, Camino a la Presa San José 2055, Col. Lomas 4a. sección, San Luis Potosí 78216, México. [5]Department of Physics, Massachusetts Institute of Technology, Cambridge, MA 02139–4307, USA.

*To whom correspondence should be addressed. E-mail: millie@mgm.mit.edu

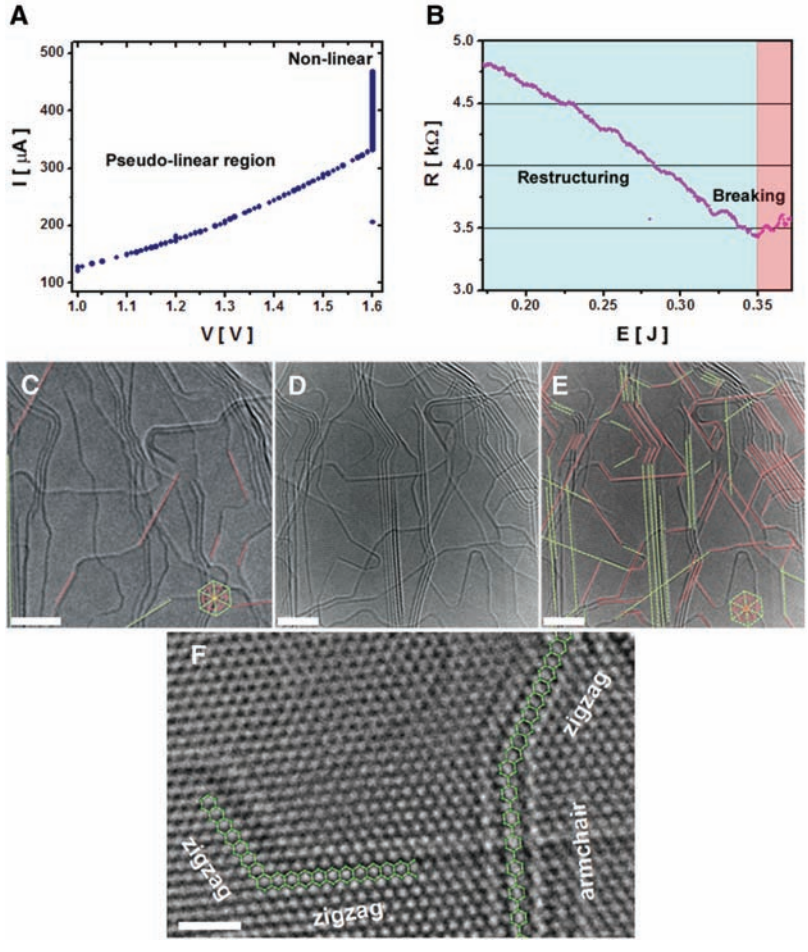

Fig. 1. Crystallization and edge formation in graphitic nanoribbons. (**A**) *I* versus *V* curve during Joule heating, indicating three regimes: (i) a linear regime from 1 to 1.25 V, (ii) a slowly increasing slope regime from 1.25 to 1.6 V, and (iii) a rapidly increasing slope regime at 1.6 V. (**B**) Resistance versus input energy at 1.6 V applied bias. (**C**) Ribbon sample before Joule heating, showing very few zigzag (pink lines) and armchair edges (green lines). (**D**) The same ribbon sample after Joule heating (for 10 min at 1.6 V), in which most of the edges seen are either zigzag or armchair edges, as indicated in (**E**). The inset hexagons indicate the zigzag- or armchair-edge orientations associated with the lattice patterns in (C) and (E). (**F**) High-magnification image of the annealed sample showing that well-defined zigzag-armchair and zigzag-zigzag edges are formed. The green hexagons in (E) help with the identification of the atomic structure at the armchair and zigzag edges. Scale bars in (C), (D) and (E), 4 nm; in (F), 1 nm.

resistive Joule heating in the suspended graphitic nanoribbons, Pt nanoparticles were deposited on an as-prepared ribbon (fig. S4). Upon Joule heating (with an applied bias below 2V), the Pt nanoparticles evaporate from the center region of the nanoribbon surface (fig. S5), thus indicating that a high temperature is achieved by Joule heating along the freely suspended ribbon (see SOM).

The dynamics of the edge reconstruction are shown in Fig. 2, A to D, and fig. S3. In Fig. 2, A to D, we see a time resolved sequence of a three-layered graphene edge structure placed on top of another few-layered graphene sheet with a zigzag-armchair-zigzag-armchair edge configuration forming 150° angles (note that the angles between zigzag and armchair edges can be 30°, 90°, or 150°). As we apply a bias voltage of 1.6 V (high annealing temperatures), the armchair edge above the zigzag edge starts to evaporate, resulting in the upward movement of the zigzag edge (red arrows) with a speed of 2.3 nm/min. This low speed at the investigated high temperatures indicates that the necessary activation energy is much larger than the activation energy of defect migration observed by Jin *et al.* (*25*) in carbon nanotubes. Eventually, as shown in Fig. 2D, the armchair edge is eliminated, and the lower zigzag edge joins with the upper zigzag edge and forms a stable zigzag-zigzag junction.

In Fig. 2E, the edge motion direction and speed are plotted for 14 experiments over the

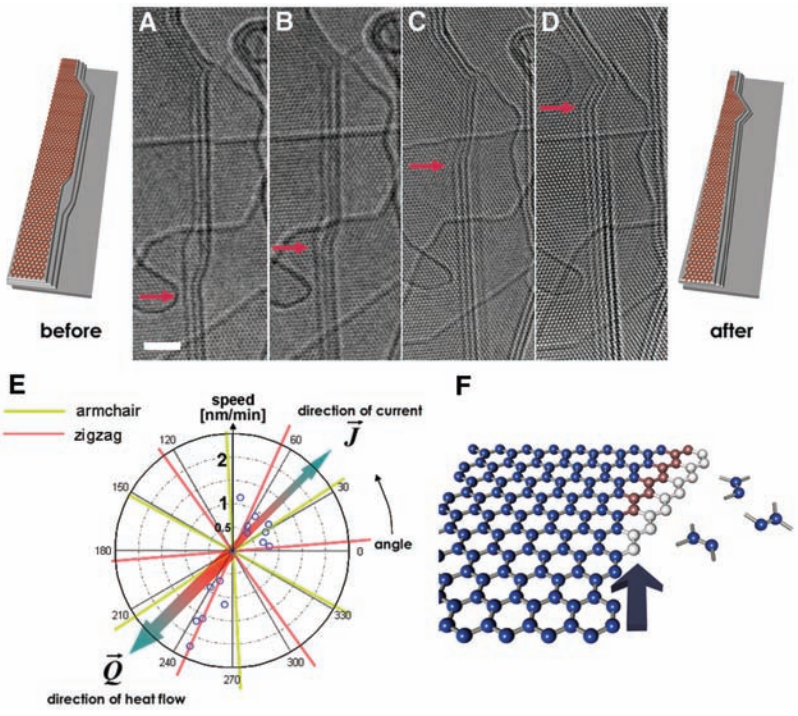

Fig. 2. Edge motion under Joule heating inside the TEM. (**A**) Three-layer zigzag-armchair-zigzag-armchair edge array. The red arrow indicates the position of the zigzag-armchair edge junction at the beginning of the annealing process. After some time of Joule heating, the junction moves up [(**B**) and (**C**)], keeping the short zigzag-edge length almost unchanged. Eventually, the zigzag edge joins with the upper zigzag edge, forming a stable zigzag-zigzag-armchair edge array (**D**). The sketches on the left of (A) and on the right of (D) are the simulated structures of (A) and (D), respectively. (**E**) Plot of the speed (in the radial direction) and angle (in the counterclockwise direction) of the edge motion relative to the current and heat flow directions. (**F**) A scenario for the motion of carbon atoms near edges and edge junctions, as C_2 dimers are evaporated from edges. As a row of the carbon atoms near the zigzag edge move away from the edge (first white colored balls and then red colored balls) upon heating, the zigzag-armchair edge junction (indicated by a black arrow) moves upward by $3a_{c\text{-}c}$. Scale bar in (A), 2 nm.

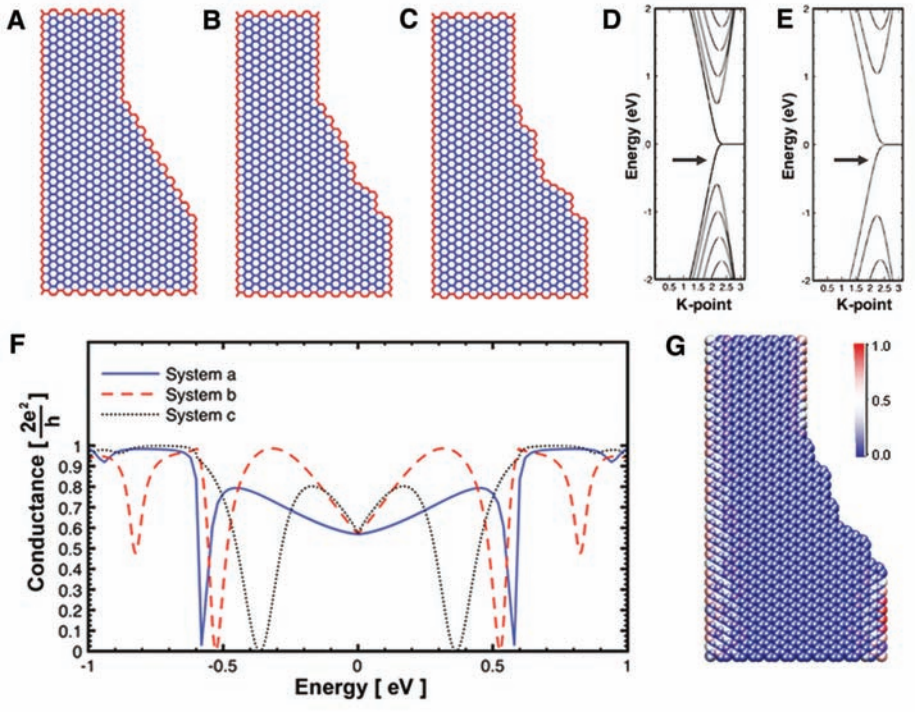

Fig. 3. Electronic and transport properties of graphene nanoribbon heterojunctions based on a single π-orbital tight-binding model (the Fermi energy is located at $E = 0$ eV). (**A** to **C**) Three models considered here where the details of the edges are highlighted in red. In each case, the two electrodes consist of two zigzag-edge nanoribbons [$N_{zig} = 44$ and 24, using notation from (*29*)]. The electronic properties of the individual electrodes are represented in (**D**) and (**E**) for the large and small ribbons, respectively. The conductance corresponding to systems (A) to (C) is presented in (**F**). For system (C), the amplitude of the scattered wave function (current-carrying state) is shown in (**G**); it is normalized such that the maximum amplitude is 1. The figure in (G) confirms that, close to the Fermi level, the current-carrying state in the zigzag taper is localized along the zigzag edges (zero amplitude at the inner part of the figure) and that the tapered part of the junction presents a high electrical resistance.

ribbon sample, similar to that shown in Fig. 2, A to D. From Fig. 2E, we see that the edge motion mostly follows either zigzag or armchair crystallographic orientations, and that the speed of edges moving along the heat flow direction $\vec{Q}$ (from the middle of the ribbon to the two electrodes acting as heat sinks) is higher (2 nm/min) than that along the current flow direction $\vec{J}$ (from the STM probe to the sample holder) when the two are antiparallel (1 nm/min). Edge motion along other directions is not favored. A scenario for the dissociation of carbon atoms from edges and the resulting motion of the edge junctions is given in Fig. 2F.

The reason why thermal energy is dissipated at an edge hetero-junction is because it is the location of the largest electrical resistance. Therefore, quasi-metallic [zigzag-edged or one-third of armchair-edged graphene nanoribbons (*26*)] systems should be preferred. Joule heating involves both current flow and atomic vibrations. Carbon nanoribbons do not show any specific phonon associated with a given edge type (there is no special phonon localized on the edges themselves) (*27*). Point (localized) defects are associated with large amplitude vibrations, and these are likely to be annealed first. In addition, zigzag-edged graphene ribbons are the only graphene structures which have electronic states that are localized along their edges (*9*). Because the electronic dispersion is quite large (Fig. 3, D and E), the electronic flow in zigzag-edged nanoribbons occurs mainly along these zigzag edges. When a zigzag edge meets a non-zigzag edge, the electronic flow is reduced, and the system acts as if a large resistance were introduced at the junction. Therefore, heating will result and will cause electron flow away from the edge junction or, if enough energy is dissipated at the junction, will result in a modification of the structure. In that case, provided that sufficient energy is dissipated in this manner, the atomic structure will rearrange locally (fig. S6) until electronic flow is reestablished. Starting from a zigzag edge, this can take place if the structure is annealed into a zigzag edge. For this reason, zigzag-zigzag junctions are the favored junction formation (Fig. 1). This zigzag edge formation mechanism is therefore local, because it is due to a high local resistance at the edge intersection.

To verify this hypothesis, we considered the three junctions shown in Fig. 3, A to C, which differ in the structure of the tapered edge: In Fig. 3A, the junction is made by an armchair edge, whereas the junctions in Fig. 3, B and C, are a mixture of edge geometries. The conductance of the hetero-junctions between zigzag and armchair edges is considerably reduced because of the fact that transmission is hindered on those non-zigzag edges where no electronic state is present. The scattering amplitude of a current-carrying state close to E = 0 eV is shown in Fig. 3G, highlighting the appearance of a large, localized resistance where the zigzag edge is interrupted. In turn, this resistance results in local heating and subsequent annealing into an all–zigzag edge system.

A nonlocal transformation mechanism can be invoked to account for the formation of semimetallic conducting armchair edges. For larger current flow, the structure can also anneal into a conducting armchair-edge system, as the current is allowed to flow, albeit not along the edges themselves. The effect is nonlocal in nature because, even though the edge structure governs the semi-metallicity of the whole structure, the current flow in the nonlocal case mostly appears away from the edges.

Experimentally, we found that more zigzag edges are initially formed at high temperatures, which is an indication that local processes are dominant. Conversely, armchair-edged ribbons, although found in less abundance, are considerably longer (Figs. 1 and 2), lending support to an operative nonlocal mechanism. Also, it is important to note that armchair edges evaporate easily when compared with the zigzag edges (Fig. 2). Molecular dynamics calculations (fig. S6) show that a C–C unit located at the armchair edge dissociates preferentially; the energy required to vaporize a C–C unit from the armchair edge is 6.7 eV, whereas that of a zigzag edge is considerably higher (~11 eV).

The Joule annealing process and its associated current flow create stable "edge arrays" (see Fig. 1D and Fig. 2, A to D). These edge arrays indicate that an offset is present between the edges of two adjacent layers. The results of a careful measurement of the edge-to-edge distances in these edge arrays is plotted in Fig. 4A, which shows clear peaks at 0.34-, 0.38-, and 0.43-nm edge-to-edge distances. These distances correspond to the offset of adjacent edges of differently stacked graphene layers (Fig. 4A). Of particular interest, the evolution of the edge arrays (Fig. 4B) after 10 min of irradiation and Joule annealing shows a clear increase for the AB stacked zigzag edges and a decrease of the AA stacked zigzag edges. This observation is attributed to the fact that the ABAB stacked configuration is thermodynamically more stable than AA stacking (*28*) and is consistent with the Goma-Oberlin mechanism (*23*).

We demonstrated the efficient shaping of graphitic nanoribbon edges into zigzag or armchair edges via Joule heating inside a TEM-STM system. This structural transformation is mainly attributed to the vaporization of carbon edges that reconstruct at high temperatures, in which the resistive Joule heating and the preferred current flow along specific edges play a vital role. The theoretical edge evolution model reveals that the specific edge formation is stimulated as a means to provide an easy path for current flow between intersecting zigzag and conducting armchair edges. This means that the efficient formation of all zigzag-edge ribbons could be achieved by careful limitation of the flowing current. These results open up a possible

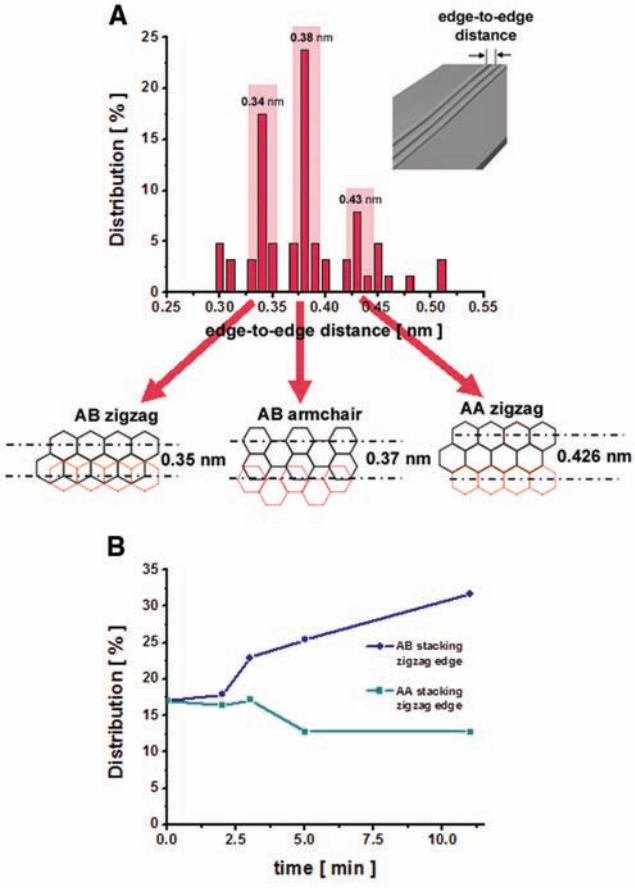

Fig. 4. Edge arrays and their time evolution. (**A**) The experimental edge-to-edge distances in the edge arrays show three peaks at 0.34, 0.38, and 0.43 nm. These peaks correspond to the offset of two adjacent AB stacked zigzag edges, AB stacked armchair edges, and AA stacked zigzag edges, respectively, as indicated in the inset of (A). (**B**) Of all the edges obtained from analysis of Fig. 1D, the percentage of AB stacked zigzag edges increases from 17 to 32%, whereas the percentage of AA stacked zigzag edges decreases from 17 to 13% after a 10-min anneal, indicating that the AB stacked layer configuration is more stable than AA stacking. Error of points is 2%.

way of generating atomically well-defined edges that make graphene-based electronics possible.

References and Notes

1. K. S. Novoselov *et al.*, *Science* **306**, 666 (2004).
2. K. S. Novoselov *et al.*, *Proc. Natl. Acad. Sci. U.S.A.* **102**, 10451 (2005).
3. Y. Zhang, Y. W. Tan, H. L. Stormer, P. Kim, *Nature* **438**, 201 (2005).
4. J. C. Meyer *et al.*, *Nature* **446**, 60 (2007).
5. A. K. Geim, K. S. Novoselov, *Nat. Mater.* **6**, 183 (2007).
6. Y. W. Son, M. L. Cohen, S. G. Louie, *Nature* **444**, 347 (2006).
7. X. Li, X. Wang, L. Zhang, S. Lee, H. Dai, *Science* **319**, 1229 (2008); published online 23 January 2008 (10.1126/science.1150878).
8. T. Enoki, Y. Kobayashi, K. Fukui, *Int. Rev. Phys. Chem.* **26**, 609 (2007).
9. K. Nakada, M. Fujita, G. Dresselhaus, M. S. Dresselhaus, *Phys. Rev. B* **54**, 17954 (1996).
10. K. Wakabayashi, *Phys. Rev. B* **64**, 125428 (2001).
11. L. G. Cançado *et al.*, *Phys. Rev. Lett.* **93**, 047403 (2004).
12. L. G. Cançado, M. A. Pimenta, B. R. A. Neves, M. S. S. Dantas, A. Jorio, *Phys. Rev. Lett.* **93**, 247401 (2004).
13. P. Shemella, Y. Zhang, M. Mailman, P. M. Ajayan, S. K. Nayak, *Appl. Phys. Lett.* **91**, 042101 (2007).
14. L. Yang, C. H. Park, Y. W. Son, M. L. Cohen, S. G. Louie, *Phys. Rev. Lett.* **99**, 186801 (2007).
15. X. Wang *et al.*, *Phys. Rev. Lett.* **100**, 206803 (2008).
16. T. C. Li, S. P. Lu, *Phys. Rev. B* **77**, 085408 (2008).
17. F. Cervantes-Sodi, G. Csányi, S. Piscanec, A. C. Ferrari, *Phys. Rev. B* **77**, 165427 (2008).
18. L. Tapasztó, G. Dobrik, P. Lambin, L. P. Biró, *Nat. Nanotechnol.* **3**, 397 (2008).
19. M. Y. Han, B. Özyilmaz, Y. Zhang, P. Kim, *Phys. Rev. Lett.* **98**, 206805 (2007).
20. J. Campos-Delgado *et al.*, *Nano Lett.* **8**, 2773 (2008).
21. F. Banhart, *Rep. Prog. Phys.* **62**, 1181 (1999).
22. B. T. Kelly, *Physics of Graphite* (Applied Science Publishers, London, 1981).
23. J. Goma, A. Oberlin, *Thin Solid Films* **65**, 221 (1980).
24. J. N. Rouzaud, A. Oberlin, C. Beny-Bassez, *Thin Solid Films* **105**, 75 (1983).
25. C. Jin, K. Suenaga, S. Iijima, *Nano Lett.* **8**, 1127 (2008).
26. Y. W. Son, M. L. Cohen, S. G. Louie, *Phys. Rev. Lett.* **97**, 216803 (2006).
27. M. Vandescuren, P. Hermet, V. Meunier, L. Henrard, Ph. Lambin, *Phys. Rev. B* **78**, 195401 (2008).
28. S. Latil, V. Meunier, L. Henrard, *Phys. Rev. B* **76**, 201402 (2007).
29. D. A. Areshkin, D. Gunlycke, C. T. White, *Nano Lett.* **7**, 204 (2007).
30. We thank Z. Ren, S. Chen, B. I. Yakobson, S. Gradecak, G. Dresselhaus, and G. Chen for valuable and fruitful discussions, and E. Gracia-Espino for providing the Pt-coated ribbons that we used in some experiments.

This work was supported by NSF grant Nanoscale Interdisciplinary Research Teams CTS-05-06830. We also thank Consejo Nacional de Ciencia y Tecnología (CONACYT)–Mexico for grants 56787 (Laboratory for Nanoscience and Nanotechnology Research–LINAN), 45772 (M.T.), 41464–Interamerican Collaboration (M.T.), 2004-01-013/SALUD-CONACYT (M.T.), and Ph.D. scholarships (J.C.-D. and J.M.R.-H.). A portion of the present research was supported in part by the Laboratory Directed Research and Development Program of ORNL, managed by UT-Battelle, by the Division of Materials Science and Engineering, U.S. Department of Energy, and by the Center for Nanophase Materials Sciences, sponsored by the Division of Scientific User Facilities, U.S. Department of Energy (V.M. and B.G.S.). A patent that is related to the production of these graphic nanoribbons has been submitted by some of the authors and holds the U.S. patent application number 12/042,544.

Supporting Online Material

www.sciencemag.org/cgi/content/full/323/5922/1701/DC1
Materials and Methods
SOM Text
Figs. S1 to S6
References

6 October 2008; accepted 10 February 2009
10.1126/science.1166862

Graphene at the Edge: Stability and Dynamics

Çağlar Ö. Girit,[1,2] Jannik C. Meyer,[1,2] Rolf Erni,[3] Marta D. Rossell,[3] C. Kisielowski,[3] Li Yang,[1,2] Cheol-Hwan Park,[1,2] M. F. Crommie,[1,2] Marvin L. Cohen,[1,2] Steven G. Louie,[1,2] A. Zettl[1,2]*

Although the physics of materials at surfaces and edges has been extensively studied, the movement of individual atoms at an isolated edge has not been directly observed in real time. With a transmission electron aberration–corrected microscope capable of simultaneous atomic spatial resolution and 1-second temporal resolution, we produced movies of the dynamics of carbon atoms at the edge of a hole in a suspended, single atomic layer of graphene. The rearrangement of bonds and beam-induced ejection of carbon atoms are recorded as the hole grows. We investigated the mechanism of edge reconstruction and demonstrated the stability of the "zigzag" edge configuration. This study of an ideal low-dimensional interface, a hole in graphene, exhibits the complex behavior of atoms at a boundary.

Graphene, a single atomic layer of carbon atoms bonded in a hexagonal lattice, is one of few materials that are stable in two dimensions (*1*) and free-standing when suspended (*2*). This unexpected stability (*3*), combined with its exotic band structure and other unusual physical properties (*4*), has led to a considerable amount of experimental research (*5*–*11*). Of the many theoretical studies of graphene, a substantial portion are devoted to the physics of graphene edges, whose structure in narrow graphene ribbons is predicted to have a major impact on their electronic properties (*12*, *13*). Experimental studies of the graphene edge have lagged behind, mainly due to the difficulty of atomically resolving and characterizing the boundaries of graphene sheets, but would give insight into the one-dimensional (1D) interface of a purely 2D structure.

The traditional method of obtaining atomic resolution on surfaces and edges is scanning tunneling microscopy (STM) or atomic force microscopy (AFM). Although there are several atomically resolved AFM/STM studies of graphene (*14*–*16*), as well as studies of step edges in graphite (*17*), there are several problems in observing dynamics of the edge atoms with scanning probe techniques. First, typical scan speeds are on the order of minutes to hours, which may be too slow to capture the movement of atoms. Second, the highest resolution and stability is obtained at cryogenic temperature, where the dynamics may be frozen out. Finally, the sample is usually on a substrate, which can strongly influence the behavior of atoms both in the bulk and at the edge. To observe dynamics on a time scale of seconds, the only alternative to scanning probe microscopes with comparable spatial resolution is the transmission electron microscope (TEM). Indeed, the dynamics of atom columns composed of heavy atoms were observed in this manner (*18*).

Traditional TEMs lack the necessary resolution at the low operating voltages required to avoid immediate sample damage. Previous 100 to 200 kV TEM studies of few-layer graphitic materials showed that some microscopes have difficulty resolving the lattice and are not capable of atomically resolving edges (*19*–*21*), making image interpretation ambiguous. By using the Transmission Electron Aberration-corrected Microscope monochromated (TEAM 0.5) (*22*), capable of sub-Ångstrom resolution even at 80 kV, we imaged every carbon atom in the lattice of suspended single-layer graphene (*23*). We employed the same microscope to record the dynamics of carbon atoms on the edge of a hole in a graphene sheet. The sample was prepared as described previously (*24*), and details of the microscope configuration can be found in (*23*). The entire experiment was conducted in the high-vacuum environment ($<10^{-7}$ mbar) of the microscope chamber.

Movie S1 shows the evolution of the hole within a suspended graphene sheet. Each frame averages 1 s of exposure, and the frames themselves are 4 s apart. The carbon atoms are shown as white because the spherical aberration was chosen to be negative (*25*). The spatial sampling is 26 ± 4 pm/pixel, determined by fitting for the measured atomic positions and using the known atomic spacing of 1.42 Å. Figure 1A shows the first frame of the sequence. The hole, initially formed through prolonged irradiation by the electron beam, is clearly visible near the center of the frame and is surrounded by the hexagonal carbon lattice. The structures lining the boundary of the frame are adsorbates

[1]Department of Physics, University of California at Berkeley, Berkeley, CA 94720, USA. [2]Materials Sciences Division, Lawrence Berkeley National Laboratory, Berkeley, CA 94720, USA. [3]National Center for Electron Microscopy, Lawrence Berkeley National Laboratory, Berkeley, CA 94720, USA.

*To whom correspondence should be addressed. E-mail: azettl@berkeley.edu

most likely deposited during the process of suspending the graphene sheet. Every carbon atom in the lattice is resolved, including those at the edge of the hole. Although there is a possibility that edge atoms could be terminated by hydrogen or other functional groups, there is no reason experimentally to indicate that this is the case, and the results of simulation show that this would not have an effect on the observed dynamics (*26*). As the sheet is suspended, small drifts in the *z* direction can occasionally move it out of the focal plane of the microscope. To account for this, a focal adjustment was made between frames 29 and 30, which represents a time gap of less than 1 minute.

Figure 1, B and C, showing frames 9 and 10 of movie S1, respectively, depict the basic mechanism by which the hole changes shape. While motion of the atoms is expected to occur faster than the 1-s sampling time in the experiment, it is the "meta-stable" configurations of the edge that are recorded. The dashed line in Fig. 1, B and C, circles a hexagon which "loses" two atoms, indicated by red diamonds, as a result of either knock-on damage from the electrons in the beam or migration to vacant sites nearby. For an 80-keV incident electron, the maximum energy that can be transferred to a carbon atom is 15.8 eV (*27*). The knock-on energy threshold for ejection of an in-lattice carbon atom with three bonds is 17 eV, corresponding to a beam energy of 86 keV (*28*), and hence those atoms are not ejected. However, this threshold drops below the maximum transfer energy to 15 eV for sites with a neighboring vacancy (*29*) and may be even less in our case, where atoms at the edge may have several vacant next-nearest-neighbor sites. The lower energy mechanism of beam-induced ejection of atoms from the edge, as opposed to the surface, is referred to as sputtering and is responsible for the overall enlargement of the hole.

The energy barrier for migration of a carbon atom to various nearby vacant sites is expected to be less than the 15 eV necessary for sputtering. Indeed, ab initio density functional theory (DFT) calculations within the local density approximation give a barrier height of 0.3 to 6.6 eV for unterminated edges (*26*). Because of the much smaller energy threshold for atom migration, these events should occur more frequently than hole enlargement, and this is what is observed. Movie S1 and subsequent figures show that the hole growth time scale is on the order of minutes, in contrast to less than a second for edge reconfiguration. Figure 1, B and C, shows the appearance of two carbon atoms (blue dots) at previously vacant sites. This may be a result of migration of the two atoms indicated by red diamonds or from another region of the hole. It is also possible that the region of the hole obscured by adsorbates acts as a carbon atom reservoir, which can replenish sites that are made vacant. Those adsorbates are likely rich in carbon and more reactive than graphene, providing atoms for "repair" of the lattice but at a slower rate than beam-induced ejection, leading to an overall growth of the hole. These competing mechanisms result in the rich dynamics observed in the movie.

To investigate whether a model can reproduce the experimental observations, we simulate the evolution of the graphene hole with a kinetic Monte Carlo method (*26*, *30*). We manually define a hole in a graphene lattice and describe the edge dynamics in terms of three different mechanisms: the beam-induced ejection of carbon atoms along the edge, the addition of carbon atoms from a virtual reservoir, and the migration of dangling carbon atoms from one site to another. The ejection probability incorporates the effect of energy input from the electron beam. The addition probability, smaller than the ejection probability, accounts for the possibility of obtaining carbon atoms from either the imperfect vacuum in the microscope or adsorbates near the hole. These two probabilities are estimated to be much smaller than the migration probabilities and thus set by hand. The migration probabilities (up to the third nearest-neighbor sites) are determined by the factor $e^{-\frac{\Delta E}{k_B T}}$, where ΔE is the relevant energy barrier height obtained from DFT calculations and T is an effective temperature corresponding to the energy input from the electron beam. In the movie of simulated hole growth (movie S2), the time step is not necessarily that of the experimental movie (movie S1). The dynamics, as characterized by Figs. 2 and 3, are remarkably similar to that observed experimentally and show the emergence of long-range order and the mechanism of edge reconfiguration.

Figure 2 shows typical examples from the experiment of edge configurations with a high degree of order. The outlined region of the hole in Fig. 2A is entirely "armchair," and that in Fig. 2B

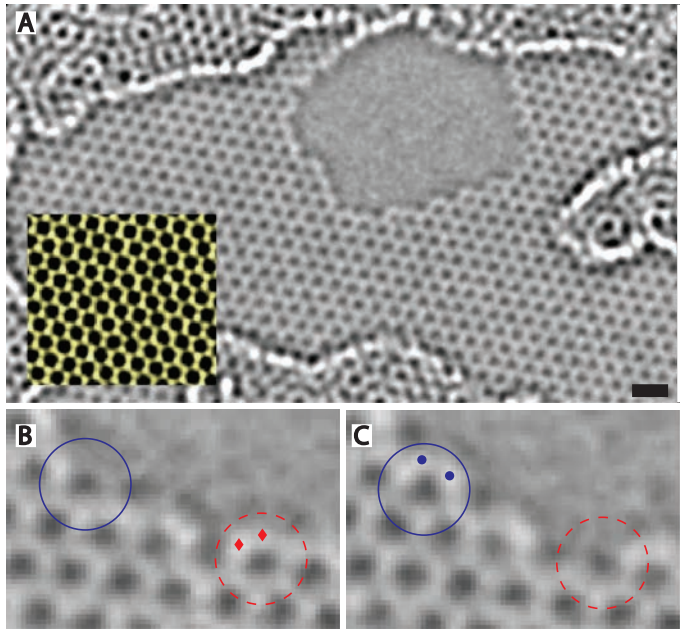

Fig. 1. (**A**) Aberration-corrected TEM image of a hole in a single layer of graphene produced by prolonged irradiation (frame 1 of Movie S1). Individual carbon atoms are resolved as white spots. Structures lining the perimeter are adsorbates. Scale bar is 5 Å. (Inset) Averaged series of images showing the atomically resolved graphene lattice. (**B**) and (**C**) Two still frames (9 and 10) in the evolution of the hole, with (C) following 4 s after (B). Two carbon atoms (red diamonds in the dashed circle) are removed while two carbon atoms nearby (blue dots) bind to their neighbors to close a hexagon (solid circle). The measured lattice constant is 2.5 Å ± 0.2 Å.

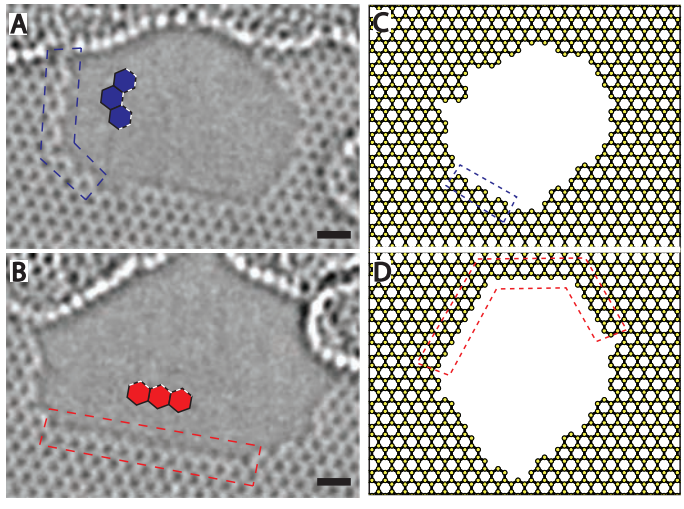

Fig. 2. Edge configurations. Aberration-corrected TEM image of (**A**) an armchair (frame 24) and (**B**) zigzag (frame 55) configuration of carbon atoms at the edge of a hole in graphene. The inset diagrams exemplify an armchair (upper panel) and zigzag (lower panel) arrangement. The armchair edge, roughly 12 hexagons long, makes a 60° turn at the lower left-hand corner. The zigzag edge is a continuous segment 12 hexagons long. Examples of the emergence of long-range order in the simulation of hole growth are (**C**), frame 113, with a 7-hexagon armchair segment at the edge of the simulated hole and (**D**), frame 223, an extremely long (19 hexagon) zigzag edge interrupted by two 60° turns.

is entirely "zigzag." These two configurations are defined in the inset diagrams of Fig. 2, A and B, respectively. Each ordered edge spans about 12 hexagons. The existence of such long-range order indicates that these configurations are stable, at least for periods of time longer than the 1 s to capture the frame. Such long-range order is also observed in the simulation, as shown in Fig. 2, C and D, where a 7-hexagon armchair edge and a 19-hexagon zigzag edge are identified, respectively. Long armchair edges are much less prevalent than zigzag edges in the simulation. This is also the case experimentally, although not as pronounced, and results from the greater stability of the zigzag edge.

The beam-induced ejection of atoms, and the resultant migration and edge reconfiguration, changes the shape of the hole, as shown in Fig. 3A. An armchair sequence at a corner of the hole transforms over the course of 4 s, or one frame, into a zigzag sequence. The blue dots in the upper frame indicate two carbon atoms that were removed from the armchair edge, and the red diamonds in the lower frame indicate four atoms added to form the zigzag edge. At a corner, or for a short segment, such a transformation would only involve the migration, addition, or removal of a handful of atoms, but the exact sequence of events is unknown. For long, uniform segments such as in Fig. 2, B or D, where the edge is aligned with the zigzag direction of the lattice, a transformation to armchair is difficult. Similar behavior is again observed in the simulation, where the rearrangement of atoms can also interconvert armchair and zigzag edges. The simplest example of such an event is shown in Fig. 3B, where three atoms on a zigzag edge (red diamonds, upper frame) disappear and within four frames, two others appear (blue dots, lower frame) to form an armchair edge.

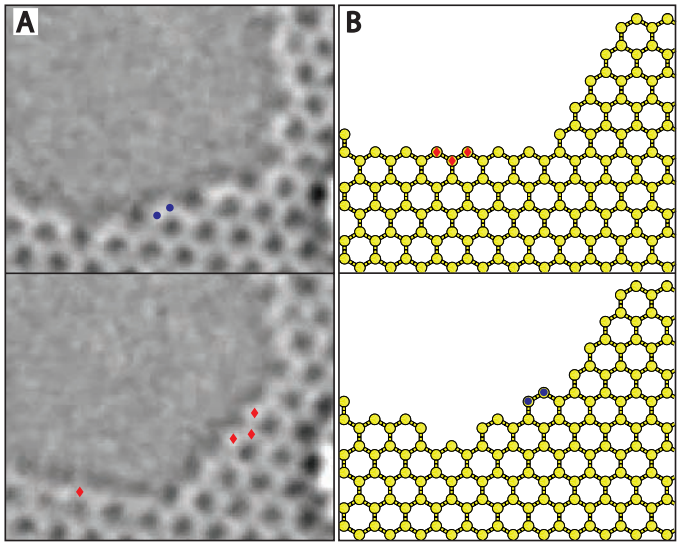

Fig. 3. Edge reconfiguration. (**A**) Conversion of an armchair edge (top) to a zigzag edge (bottom) over the course of two frames, 14 and 15, taken at a 4-s interval. The two atoms marked as blue dots in the upper frame are gone in the lower frame, where four new carbon atoms are indicated as red diamonds. The 7- hexagon armchair edge is transformed into a 9-hexagon zigzag edge with a 60° turn. The transformation occurs due to migration of atoms along the edge. (**B**) Similar behavior is observed in the kinetic Monte Carlo simulation of hole growth, where three zigzag atoms (red diamonds, top) from frame 235 disappear and two armchair atoms (blue dots, bottom) appear in frame 239. Both frames in (B) have been flipped vertically.

In Fig. 4, we analyze the data in an attempt to understand the growth of the hole as a function of time and demonstrate the stability of the zigzag edge configuration. Figure 4A shows a flattened image averaging all 110 recorded frames. First, the images are registered by taking the initial frame, isolating a region of the lattice far from the hole, and shifting all subsequent frames into alignment (*30*). Then the pixel values are averaged over all frames to produce an image. The advantage of such a representation is that it will highlight structures along the edge that appear often, even though those structures may change rapidly from frame to frame. Faint hexagons are fleeting, located in regions where the hole quickly grew in size, whereas well-contrasted hexagons are more stable and existed throughout most of the recording. One observes that the most prominent edge structure is of the zigzag type, with the bottom and lateral sides of the hole aligned in the zigzag directions of the lattice. The faint hexagons are concentrated on the left and right sides of the hole, where the hole grew quickly. The dashed line indicates a path of pixels along which the time development is shown in Fig. 4B. The pixel values along the path are lined on the horizontal axis, with the vertical axis time going from top to bottom. The hexagons are indicated by alternating bands of black and white, with the hole a uniform gray. Here, one directly sees the growth of the hole along the cut in Fig. 4A. The hole expands by roughly three hexagons both to the left and the right within the first 50 frames and then stabilizes with about two hexagons on the left side and one on the right. This stable configuration corresponds to the formation of zigzag edges on the left and right of Fig. 4A. The lateral regions of the hole, which started with more armchair or mixed-type edges, stabilize in a state that is more zigzag in nature. A similar slice taken perpendicular to the bottom edge of the hole (not shown) indicates a slower growth of the hole in that direction, indicating that it is difficult to erode the long zigzag edge. To further analyze the hole growth, the outline of the hole was determined algorithmically for each frame. All such outlines were averaged over all frames to produce the image in Fig. 4C. Faint lines indicate regions where the outline quickly

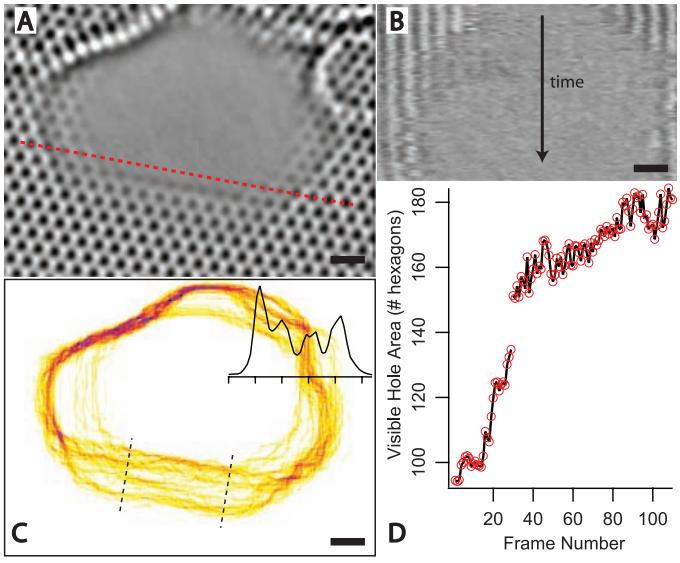

Fig. 4. Growth of hole in graphene. (**A**) Average intensity map constructed by averaging pixel values over all 110 frames of movie S1 after frame registration. Faint hexagons in the interior have been gradually removed by knock-on damage from the electron beam. Scale bar is 5 Å. (**B**) Time development of the pixel values along the dashed line in (A). The left end of the dashed line corresponds to the left side of (B). The frame number increases from top to bottom, and the scale bar is 5 Å along the *x* axis (position) and 30 frames, or 120 s, along the *y* axis (time). The opening of the hole is visible as a reduction in the number of black-and-white bands, corresponding to hexagons, scanning downwards. (**C**) Average, over all frames, of the perimeter of the hole. Darker segments of lines correspond to regions through which the perimeter passed more often than lighter segments. The hole opened quickly in the horizontal direction, as observed in (B), but near the bottom edge, the presence of four dark bands indicates that those configurations of the perimeter were more stable and the hole opened less quickly in the direction of the black dashed line. Scale bar is 5 Å. (Inset) The profile of pixel values along the dashed line shows four peaks corresponding roughly to the graphene lattice constant. Tick spacing, 2 Å. (**D**) The visible area of the hole, normalized by the area of a single hexagon, 5.17 $Å^2$, as a function of frame number. The missing line segment indicates the 30-s gap between frames 29 and 30.

changed shape and darker ones where the outline of the hole was more constant. The analysis of the lateral and bottom regions is similar to the above, except that one clearly sees four bands on the bottom (between dashed lines) aligned along the zigzag direction. This indicates once more that the hole was more stable along that direction and that the hexagons remained in place longer. An averaged line profile over those bands shows four peaks (inset, Fig. 4C), with a mean spacing of 2.1 Å, close to the lattice constant of 2.46 Å. Finally, in Fig. 4D, the area within the hole, as determined from the outlines, is computed and plotted as a function of frame number. We see the sharp increase in area within the first 50 frames as the hexagons along the left and right edges of the hole are removed, and then the hole growth slows down as a more stable configuration and a larger hole is produced. This global analysis of the edge stability is complemented by a site-by-site analysis of the zigzag fraction (fig. S1).

A simple model can account for the stability of zigzag edges observed in both experiment and simulation by considering the effect of ejecting an atom at the edge for each chirality (fig. S2). Half of the atoms along a zigzag or armchair edge are bonded to two neighboring atoms, and the other half are bonded to three neighboring atoms. Naively, we expect that the atoms most likely to be ejected by the electron beam are those with two neighboring atoms. The removal of such an atom from a zigzag edge leaves a vacancy without creating any dangling carbon atoms, those bonded to only a single neighbor. However the removal of such an atom from an armchair edge does leave a dangling carbon atom, which can easily migrate and fill a vacancy elsewhere on the edge, as the calculations predict (*30*). For an armchair configuration, two atoms are needed to repair the edge: the atom that was ejected and the neighboring dangling atom that migrated away. In a zigzag edge, only the ejected atom needs replacement. Hence, the zigzag edge is more stable under electron irradiation at this energy, and the argument holds even when the ejection of atoms along the edge with three neighbors is considered.

The images, simulation, and analysis presented here show the complicated dynamics that occur at the atomic edge of a single-layer graphene sheet. The TEAM microscope provides real-time atomic resolution, and the electron beam at 80 keV acts as an energy bath that allows the dynamics of edge reconstruction and hole growth to be observed. In our study of the edge configuration, we demonstrate the stability of the armchair and zigzag arrangements and quantify their evolution with time. Although the reconfiguration occurs on a time scale on the order of seconds, with a comparable contribution of armchair and zigzag sites, the long-term stability of zigzag edges is elucidated through a time-average analysis and explained by a simple model.

References and Notes

1. K. S. Novoselov *et al.*, *Science* **306**, 666 (2004).
2. J. C. Meyer *et al.*, *Nature* **446**, 60 (2007).
3. K. S. Novoselov *et al.*, *Proc. Natl. Acad. Sci. U.S.A.* **102**, 10451 (2005).
4. A. K. Geim, K. S. Novoselov, *Nat. Mater.* **6**, 183 (2007).
5. K. S. Novoselov *et al.*, *Nature* **438**, 197 (2005).
6. Y. Zhang, Y.-W. Tan, H. L. Stormer, P. Kim, *Nature* **438**, 201 (2005).
7. Y. Zhang *et al.*, *Nat. Phys.* **4**, 627 (2008).
8. S. Y. Zhou *et al.*, *Nat. Phys.* **2**, 595 (2006).
9. T. Ohta, A. Bostwick, T. Seyller, K. Horn, E. Rotenberg, *Science* **313**, 951 (2006).
10. J. S. Bunch *et al.*, *Science* **315**, 490 (2007).
11. C. Lee, X. Wei, J. W. Kysar, J. Hone, *Science* **321**, 385 (2008).
12. L. Yang, C.-H. Park, Y.-W. Son, M. L. Cohen, S. G. Louie, *Phys. Rev. Lett.* **99**, 186801 (2007).
13. Y.-W. Son, M. L. Cohen, S. G. Louie, *Nature* **444**, 347 (2006).
14. V. W. Brar *et al.*, *Appl. Phys. Lett.* **91**, 122102 (2007).
15. G. M. Rutter *et al.*, *Science* **317**, 219 (2007).
16. M. Ishigami, J. H. Chen, W. G. Cullen, M. S. Fuhrer, E. D. Williams, *Nano Lett.* **7**, 1643 (2007).
17. L. Tapaszto, G. Dobrik, P. Lambin, L. P. Biro, *Nat. Nano.* **3**, 397 (2008).
18. A. V. Martin, K. Ishizuka, C. Kisielowski, L. J. Allen, *Phys. Rev. B* **74**, 172102 (2006).
19. J. C. Meyer, C. O. Girit, M. F. Crommie, A. Zettl, *Nature* **454**, 319 (2008).
20. J. Campos-Delgado *et al.*, *Nano Lett.* **8**, 2773 (2008).
21. M. H. Gass *et al.*, *Nat. Nano.* **3**, 676 (2008).
22. C. Kisielowski *et al.*, *Microsc. Microanal.* **14**, 454 (2008).
23. J. C. Meyer *et al.*, *Nano Lett.* **8**, 3582 (2008).
24. J. C. Meyer, C. O. Girit, M. F. Crommie, A. Zettl, *Appl. Phys. Lett.* **92**, 123110 (2008).
25. K. W. Urban, *Science* **321**, 506 (2008).
26. Materials and methods are available as supporting material on *Science* Online.
27. R. F. Egerton, F. Wang, P. A. Crozier, *Microsc. Microanal.* **12**, 65 (2006).
28. B. W. Smith, D. E. Luzzi, *J. Appl. Phys.* **90**, 3509 (2001).
29. V. H. Crespi, N. G. Chopra, M. L. Cohen, A. Zettl, S. G. Louie, *Phys. Rev. B* **54**, 5927 (1996).
30. A. F. Voter, in *Proceedings of the NATO Advanced Study Institute on Radiation Effects in Solids* (Springer, Berlin, 2006), pp. 1–23.

31. The National Center for Electron Microscopy is supported by the Department of Energy under contract DE-AC02-05CH11231. The TEAM project is supported by the Department of Energy, Office of Science, Office of Basic Energy Sciences. Ç.G., J.M., and A.Z. were supported by the Director, Office of Energy Research, Office of Basic Energy Sciences, Materials Sciences, and Engineering Division, of the U.S. Department of Energy under contract DE-AC02-05CH11231, through the sp^2-bonded nanostructures program. L.Y., C.-H.P., M.L.C., and S.G.L. were supported by the National Science Foundation and by the Director, Office of Science, Office of Basic Energy Science, Division of Material Sciences and Engineering, U.S. Department of Energy. Ç.G. thanks P. Vollhardt, V. W. Brar, and Y. Zhang for interesting discussions.

Supporting Online Material

www.sciencemag.org/cgi/content/full/323/5922/1705/DC1
Materials and Methods
Figs. S1 and S2
References
Movies S1 and S2

9 October 2008; accepted 30 January 2009
10.1126/science.1166999

Reversible Interactions with para-Hydrogen Enhance NMR Sensitivity by Polarization Transfer

Ralph W. Adams,[1] Juan A. Aguilar,[1] Kevin D. Atkinson,[1] Michael J. Cowley,[1] Paul I. P. Elliott,[1]* Simon B. Duckett,[1]† Gary G. R. Green,[2] Iman G. Khazal,[1] Joaquín López-Serrano,[1] David C. Williamson[1]

The sensitivity of both nuclear magnetic resonance spectroscopy and magnetic resonance imaging is very low because the detected signal strength depends on the small population difference between spin states even in high magnetic fields. Hyperpolarization methods can be used to increase this difference and thereby enhance signal strength. This has been achieved previously by incorporating the molecular spin singlet para-hydrogen into hydrogenation reaction products. We show here that a metal complex can facilitate the reversible interaction of para-hydrogen with a suitable organic substrate such that up to an 800-fold increase in proton, carbon, and nitrogen signal strengths are seen for the substrate without its hydrogenation. These polarized signals can be selectively detected when combined with methods that suppress background signals.

The wide variety of applications of nuclear magnetic resonance (NMR) (*1*–*3*) are limited by the technique's extremely low inherent sensitivity. Here we describe an approach that uses hyperpolarized spins derived from para-hydrogen (para-H_2) (*4*) to sensitize the NMR experiment without actually incorporating para-H_2 into the molecule that is to be probed. Specifically, we show that high-resolution NMR spectra can be collected for a range of molecules and nuclei with detected signal strengths up to 800 times greater than would be normally achievable with an unpolarized sample. This improvement facilitates the collection of diagnostic high-resolution ^{1}H, ^{13}C, ^{15}N, and ^{19}F NMR spectra and magnetic resonance images of selected signals in a fraction of the time that would normally be necessary. When optimized, this route is predicted to increase proton sensitivity by up to four orders of magnitude (*5*) such that the routine single shot characterization of materials, even at picomole levels, will become possible (*6*).

The relative weakness of NMR signals exhibited by nuclei with a nonzero magnetic moment results from the way the original energy levels split in a magnetic field (*7*). The bulk magnetic moment for an ensemble of such nuclei is determined by the Boltzmann population of each energy level. In general, the difference in the energy between these levels is so small that almost-equal spin populations exist across them. For example, in a magnetic field of 9.4 T such as that found in routine high-resolution NMR spectrometers, the difference in spin population will only be around 1 in 32,000 for ^{1}H. Unfortunately, ^{1}H nuclei are the most sensitive, and, for ^{19}F, ^{31}P, ^{13}C, and ^{15}N, the next most common nuclei to be studied, the sensitivity problem is even more acute, with the associated signal decreasing by factors of 1.2, 15, 64, and 10^{4} respectively. The problem is further exacerbated when the natural abundance of ^{13}C (1.108%) and ^{15}N (0.37%) isotopes are taken into account, meaning the effective differences in sensitivity scale from 1 in 32,000 for ^{1}H to 1 in 120 million and 1 in 8.7 billion in these nuclei, respectively. As a result of this, general routine human imaging experiments are restricted to measuring the ^{1}H signals coming from water and lipid in tissues. Furthermore the direct detection of nonproton signals can require many hours of measurement even in NMR spectroscopy.

A number of "hyperpolarization" methods have been developed (*8*–*18*) to enhance signal strength by transferring nonequilibrium nuclear spin polarizations. The method of dynamic nuclear polarization (DNP), as reviewed by Kemsley (*10*), creates a non-Boltzmann spin population by transfer of polarization from an unpaired electron. Recently this approach has been demonstrated to usefully enhance ^{13}C and ^{15}N signals by factors that exceed 10,000 (*11*–*14*). Currently, however, this method requires long polarization times (often over 6 hours), normally uses water and methanol as solvents, and is unable to detect enhanced proton signals routinely.

We tackled the sensitivity problem in a different way by using para-H_2 as the source of polarization. Para-H_2 has the advantage that it can be prepared easily and stored at room temperature for months. Previously, studies with para-H_2 were limited to those involving the formation of hydrogenation products containing para-H_2–derived protons (*15*). For example, Pines *et al.* recently used it to image heterogeneous hydrogenation reactions through the detection of polarized protons of propane (*16*). More usually, however, the imaging of ^{13}C-based magnetization was targeted because such nuclei can be polarized by para-H_2–based hydrogenation reactions in low magnetic field, as demonstrated by Bargon *et al.* (*17*) and exploited by Golman *et al.* (*12*). In these hydrogenative processes, the newly formed reaction products contain protons originating from a single para-H_2 molecule, and they can produce strongly enhanced NMR signals in the reaction product provided the reaction does not change the magnetic arrangement of these coupled atoms (*15*).

The need for a suitable hydrogen acceptor, however, reflects an important limitation of the existing approach. Nonetheless, the ability to increase proton signal strengths in such products by 32,000 with para-H_2 and hence detect picomoles of material in a single scan has been established (*6*, *18*). In order to generalize the use of para-H_2 as a source of polarization, a method for the transfer of polarization without the direct hydrogenation of materials is needed. We show that the temporary association of a substrate and para-H_2 via a transition metal center in low magnetic field can achieve just this. Thus, NMR signal amplification by reversible exchange (NMR-SABRE) is achieved without any chemical modification of the hyperpolarized material. As an example, we used the labile complex $[Ir(H)_2(PCy_3)(substrate)_3][BF_4]$, which is formed by the reaction of $[Ir(COD)(PCy_3)(MeCN)][BF_4]$ (where Cy is cyclohexyl and COD is cyclooctadiene) with para-H_2 and an excess of the substrate to be polarized (*5*, *19*). Notably, the same observations can be made on a range of materials and metal templates according to the concept illustrated in Fig. 1.

We first illustrate this effect by using pyridine as the substrate where the iridium dihydride complex $[Ir(H)_2(PCy_3)(pyridine)_3][BF_4]$ is formed.

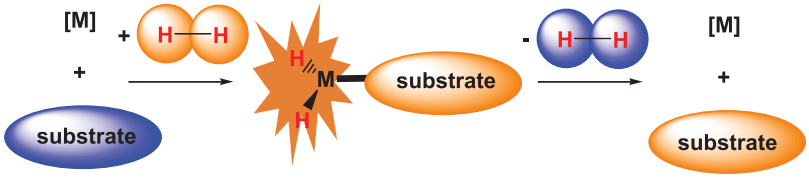

Fig. 1. Schematic representation of the magnetization transfer process.

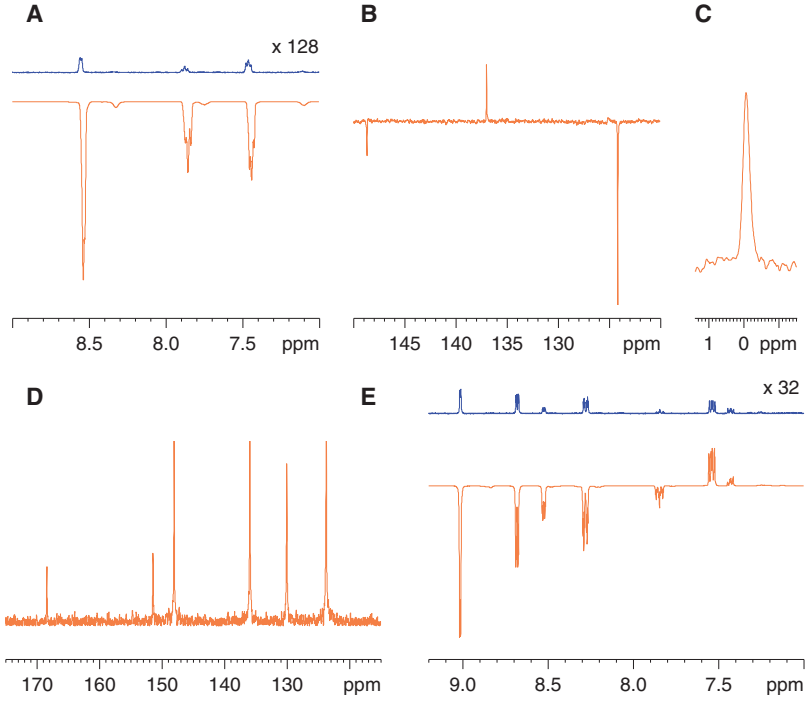

Fig. 2. Single scan NMR spectra of samples containing a templating medium, the indicated substrate, and para-H_2 at 295 K in d_4-methanol where the polarization transfer step was achieved in a 2×10^{-2} T field. ppm indicates parts per million. (**A**) The ^{1}H control trace (top) of 6 nmol of pyridine with 128-fold vertical expansion relative to the bottom ^{1}H trace that was recorded immediately after polarization transfer. (**B**) Polarized ^{1}H decoupled ^{13}C trace of the same sample after refocusing. (**C**) Polarized ^{1}H decoupled ^{15}N trace, with refocusing, of a sample containing 25 nmol of ^{15}N labeled pyridine. (**D**) Polarized ^{1}H decoupled ^{13}C trace after refocusing, in magnitude, of a sample containing 50 μmol of nicotinamide. (**E**) The ^{1}H NMR spectrum of the same nicotinamide sample showing the control trace (top), with a 32-fold vertical expansion relative to the polarized trace (bottom) with transfer in a 0.5×10^{-4} T field.

[1]Department of Chemistry, University of York, Heslington, York, YO10 5DD, UK. [2]York Neuroimaging Centre, The Biocentre York Science Park, University of York, Heslington, York, YO10 5DG, UK.

*Present address: Department of Chemical and Biological Sciences, University of Huddersfield, Queensgate, Huddersfield, HD1 3DH, UK.

†To whom correspondence should be addressed. E-mail: sbd3@york.ac.uk

The single scan ^{1}H NMR spectrum shown in Fig. 2A was recorded after the sample was first polarized in a magnetic field of around 2×10^{-2} T and contains signals with enhanced intensity for the three proton sites of the pyridine substrate. All that is necessary to achieve this result is to shake the sample in a low magnetic field (movie S1). This dissolves fresh para-H_2 from the head space above the solvent, allowing it to associate with the metal complex and thereby activating the polarization transfer process in the solution. Specifically, the signals for free pyridine at δ 7.84, 8.54, and 7.43 appear in the downward direction that is most simply described as emission. After the sample is then left in the NMR spectrometer for 10 minutes, the resulting NMR spectrum demonstrates that the pyridine's magnetic states have returned to their more usual Boltzmann distribution through relaxation. We note that the resonances illustrated for free pyridine in Fig. 2A can be described as hyperpolarized.

When the region of the ^{1}H NMR spectrum containing the pyridine signals is examined in more detail, weaker signals for the bound pyridine ligands within the host-ligand complex $[Ir(H)_2(PCy_3)(pyridine)_3][BF_4]$ are also seen to show this emission character. We conclude therefore that, while at low field, spontaneous polarization transfer occurs between para-H_2 and the pyridine substrate that is in temporary association with the metal template. Furthermore, substrate exchange with that bound in the host-ligand template during this period leads to the buildup of hyperpolarization in free pyridine. When these enhanced signals are compared with those without enhancement, up to 550-fold increase in signal strength is observed. The enhancement achieved by using this simple process is realized after just a few seconds of contact with the sample in low field (movie S1).

This enhancement effect is not just limited to proton signals because the corresponding ^{13}C (Fig. 2B) and ^{15}N resonances (Fig. 2C) of pyridine are also polarized. Furthermore, these effects can be regenerated by simply removing the sample from the spectrometer and bringing it into contact with fresh para-H_2 in low magnetic field. When the hyperpolarized ^{13}C NMR spectrum is compared with that obtained when a standard ^{13}C NMR spectrum is recorded, it would take 670,000 scans to achieve equal signal intensity to that seen with only one scan after the para-H_2 enhancement process (*5*). The time saved through this 823-fold signal enhancement has been estimated to exceed 3 months assuming that the individual measurements are separated by a 20-s recovery delay and use 90° observation pulses. If the NMR spectra of 100% ^{13}C-enriched materials were compared with those obtained from para-H_2 enhancement of the unenriched material, an eightfold gain in sensitivity would still be apparent. Of course these enriched materials could themselves be easily polarized and therefore yield even larger signals.

These methods can be extended beyond pyridine, and in Fig. 2D we illustrate a ^{13}C spectrum of nicotinamide that is collected in the same way; 345-fold ^{1}H signal enhancements have been quantified for this system on the basis of spectra such as that shown in Fig. 2E. All of the ^{13}C resonances for nicotinamide are enhanced, although not to the same degree (*5*). We note that 3-fluoropyridine, nicotine, pyridazine, quinoline, quinazoline, quinoxaline, and dibenzothiophene also show enhancement and that ^{19}F and ^{31}P signals can also be detected (*5*). These substrates associate weakly with the metal complex through their basic donor sites, thereby facilitating the polarization transfer step. NMR spectra representative of these materials can be found in figs. S2 and S3.

We recently described a gradient-based NMR method called only parahydrogen spectroscopy (OPSY) that suppresses signals derived from nuclei with thermally equilibrated spin state populations while allowing the observation of signals from para-H_2–derived protons found in hydrogenation products (*20*). This method works by selectively probing the longitudinal two-spin order term that is generated for coupled spins derived from para-H_2 while dephasing terms from the usual thermal magnetization through the use of pulsed field gradients. When it is applied, all thermal signals are successfully suppressed and those for the hyperpolarized molecules still remain. As a result, NMR spectra of polarized substrates can be recorded in the presence of a protio solvent. The corresponding ^{1}H-selected OPSY spectral trace showing signals for polarized pyridine, collected in protio methylenechloride, is shown in Fig. 3A.

This polarization transfer process is predicted to generate spin states that are unaffected by dipole-dipole relaxation mechanisms and as such to have long lifetimes in low field (*5*). The potential impact of long-lived states in NMR has been highlighted by Levitt in a different context (*21*). The OPSY-based ^{1}H NMR spectrum in Fig. 3B was recorded 150 s after polarization. This illustrates the presence of the longitudinal two-spin order magnetic state associated with a pair of coupled hydrogen atoms within polarized pyridine.

These results suggest a route for the use of naturally occurring molecules as contrast agents in magnetic resonance imaging (MRI). In this regard, Fig. 4 shows two separate single-average true fast imaging with steady state precession (True-FISP)–based MRI images of pyridine collected over 0.7 s on an 8-mm sample tube containing cylinders of 1-mm internal diameter (*22*). We collected the first trace on a 0.5-mm slice by using polarized pyridine in d_4-methanol, whereas the second was collected on the same sample after the pyridine polarization had decayed, albeit over a 20-mm slice thickness with half the in-plane resolution in both directions; this introduces an inherent 160-fold increase in signal strength between the two measurements before any additional signal enhancement is considered. Even under the latter conditions, no image is visible, illustrating both the viability of this approach in MRI and that the sensitivity gain is over 160-fold.

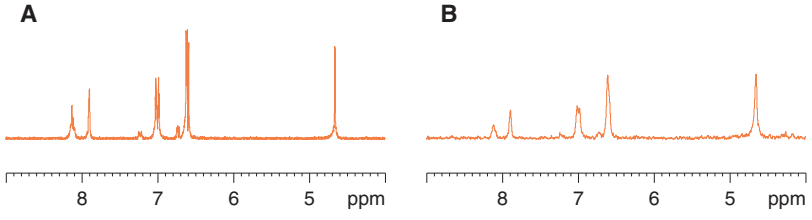

Fig. 3. (**A**) Unlocked ^{1}H NMR spectrum recorded in protio-CH_2Cl_2 by using the OPSY filtration sequence to suppress background signals, which illustrates the detection of 60 μmol of polarized pyridine in a single scan. (**B**) The ^{1}H NMR spectrum recorded on the same sample by using the same pulse sequence but recorded 150 s after the low field polarization step.

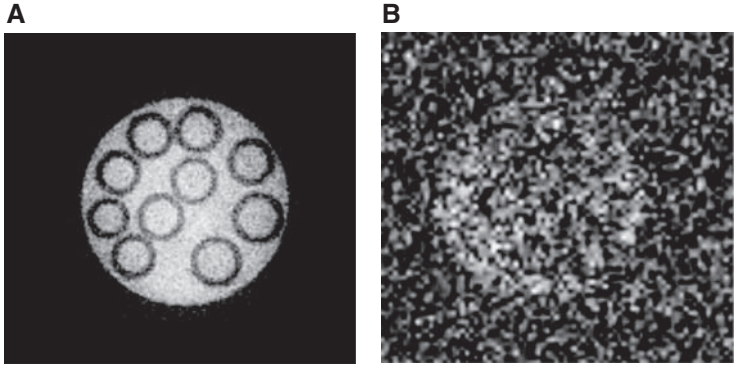

Fig. 4. Single average ^{1}H True-FISP MRI images of an 8-mm sample tube containing glass cylinders with 1-mm internal diameter showing (**A**) signals from polarized pyridine in d_4-methanol within a 0.5-mm slice and (**B**) signals from the same sample after the decay of polarization for a 20-mm slice thickness.

The procedures described in this paper are relatively cheap to implement and can produce large amounts of hyperpolarized materials in a short time. Furthermore, the video sequence (movie S1) illustrates the simplicity of the measurement process that we have described. The method can be used on routine proton-based MRI instruments without the need to exploit other magnetically active nuclei that provide much weaker signals. Given the opportunities that hyperpolarized methods have been shown to offer for the development of real-time metabolic imaging applications, the results presented here take us a step further toward the goal of responsive high-sensitivity MR-based methods for the diagnosis of disease (*10*).

References and Notes

1. R. R. Ernst, *Angew. Chem. Int. Ed. Engl.* **31**, 805 (1992).
2. K. Wuthrich, *Angew. Chem. Int. Ed.* **42**, 3340 (2003).
3. P. G. Morris, *Nuclear Magnetic Resonance Imaging in Medicine and Biology* (Oxford Univ. Press, Oxford, 1986).
4. C. R. Bowers, D. P. Weitekamp, *J. Am. Chem. Soc.* **109**, 5541 (1987).
5. Materials and methods are available as supporting material on *Science* Online.
6. N. J. Wood, J. A. Brannigan, S. B. Duckett, S. L. Heath, J. Wagstaff, *J. Am. Chem. Soc.* **129**, 11012 (2007).
7. P. Zeeman, *Nature* **78**, 369 (1908).
8. B. Driehuys, *Science* **314**, 432 (2006).
9. L. Schroder, T. J. Lowery, C. Hilty, D. E. Wemmer, A. Pines, *Science* **314**, 446 (2006).
10. J. Kemsley, *Chem. Eng. News* **86**, 12 (2008).
11. J. H. Ardenkjaer-Larsen *et al.*, *Proc. Natl. Acad. Sci. U.S.A.* **100**, 10158 (2003).
12. K. Golman, J. H. Ardenaer-Larsen, J. S. Petersson, S. Mansson, I. Leunbach, *Proc. Natl. Acad. Sci. U.S.A.* **100**, 10435 (2003).
13. L. Frydman, D. Blazina, *Nat. Phys.* **3**, 415 (2007).
14. M. E. Merritt *et al.*, *Proc. Natl. Acad. Sci. U.S.A.* **104**, 19773 (2007).
15. D. Blazina, S. B. Duckett, J. P. Dunne, C. Godard, *Dalton Trans.* 2601 (2004).
16. L. S. Bouchard *et al.*, *Science* **319**, 442 (2008).
17. L. T. Kuhn, J. Bargon, *Top. Curr. Chem.* **276**, 25 (2007).
18. M. S. Anwar *et al.*, *Phys. Rev. Lett.* **93**, 040501 (2004).
19. R. H. Crabtree, M. Lavin, L. Bonneviot, *J. Am. Chem. Soc.* **108**, 4032 (1986).
20. J. A. Aguilar, P. I. P. Elliott, J. Lopez-Serrano, R. W. Adams, S. B. Duckett, *Chem. Commun.* **2007**, 1183 (2007).
21. M. Carravetta, M. H. Levitt, *J. Chem. Phys.* **122**, 214505 (2005).
22. A. Oppelt *et al.*, *Electromedica* **54**, 15 (1986).

23. This work was supported by the University of York, the White-Rose Health Innovation Partnership, the Engineering and Physical Sciences Research Council, the Medical Research Council, Biotechnology and Biological Sciences Research Council, the Spanish Ministry of Education and Science [Project Consolider ORFEO (CSD 2007-00006)], and Bruker Bio-Spin. We thank Bruker Bio-Spin, R. Perutz, P. Walton, M. Hymers, S. Johnson, M. Mortimer, and K. Armour for advice and helpful discussions. We have filed a patent application, P115707GB, based on this work.

Supporting Online Material

www.sciencemag.org/cgi/content/full//323/5922/1708/DC1
Materials and Methods
SOM Text
Figs. S1 to S7
Movie S1
References

24 November 2008; accepted 9 February 2009
10.1126/science.1168877

Increasing Hyperpolarized Spin Lifetimes Through True Singlet Eigenstates

Warren S. Warren,* Elizabeth Jenista, Rosa Tamara Branca, Xin Chen

The sensitivity limitations for magnetic resonance imaging of organic molecules have recently been addressed by hyperpolarization methods, which prepare excess nuclear spin polarization. This approach can increase sensitivity by orders of magnitude, but the enhanced signal relaxes away in tens of seconds, even in favorable cases. Here we show theoretically that singlet states between strongly coupled spins in molecules can be used to store and retrieve population in very-long-lived disconnected eigenstates, as long as the coupling between the spins substantially exceeds both the couplings to other spins and the resonance frequency difference between them. Experimentally, 2,3-carbon-13–labeled diacetyl has a disconnected eigenstate that can store population for minutes and is read out by hydration to make the two spins inequivalent.

Magnetic resonance imaging of different endogenous and exogenous molecules in tissue and living organisms holds the promise of resolving metabolic pathways and diagnosing early disease states, thus broadly affecting pharmaceutical development and molecular medicine. However, magnetic resonance is extremely insensitive, mainly because even very large magnetic fields induce only a very small nuclear magnetization at room temperature. For example, hydrogen atoms in a 7-T imager have ~0.0001 of the bulk magnetization they would have if all spins were aligned in the same direction. As a result, virtually all clinical magnetic resonance images measure water signal, and localized magnetic resonance spectroscopy is challenging and slow.

This signal limitation has spurred the development of so-called hyperpolarization methods, which commonly produce bulk magnetizations of 20% or more. Although the first applications used spin-polarized noble gases (*1*) (for instance, ^{3}He and ^{129}Xe), in recent years attention has turned to two methods that can hyperpolarize molecules: (i) para-H_2 addition across double bonds (*2*–*4*) and (ii) dynamic nuclear polarization (DNP) (*5*–*13*). The DNP methodology in particular is very versatile, and hundreds of different molecules have been polarized, but virtually all in vivo work has focused on one molecule (^{13}C-labeled pyruvate), largely because the population relaxation time T_1 is relatively long (40 s at 14.1 T). The polarized nuclei can undergo metabolic reactions before the nuclear magnetic resonance (NMR) signal returns to thermal equilibrium and becomes undetectable. Generically, ^{13}C T_1 values are tens of seconds for carbons without attached protons (and much shorter with attached protons), and hydrogen T_1 values are shorter still. This lifetime permits some important metabolic processes to be studied, but it is vastly shorter than the lifetimes associated with other molecular imaging modalities (e.g., ^{18}F positron emission tomography, which decays in ~2 hours).

We present a practical approach to storing and retrieving population from very-long-lived spin states in a fairly wide range of molecular targets. The key is understanding and exploiting symmetry effects and the way they are altered by chemical reactions. To begin, suppose a molecule has two spin-1/2 nuclei that are isolated (meaning that they are not coupled to any other spins) and are chemically equivalent (*14*, *15*) (meaning that they have the same resonance frequency, usually because of symmetry). The molecule then has what we will call a "disconnected eigenstate." The singlet energy level [$2^{-1/2}(\alpha_1\beta_2 - \beta_1\alpha_2)$, where α_n and β_n are the two possible states of spin n] is an eigenstate of the internal molecular Hamiltonian and has no dipole moment connecting it to the other three triplet levels [$\alpha_1\alpha_2$, $\beta_1\beta_2$, and $2^{-1/2}(\alpha_1\beta_2 + \beta_1\alpha_2)$]. The simplest example is H_2 itself, where molecules in the singlet state (called para-H_2) can actually be chemically separated from the other (ortho) form and can persist almost indefinitely in the gas phase.

The triplet levels support two allowed transitions with the same energy, making the scalar spin-spin "J" coupling unobservable in this molecule (or for that matter in water, which has the same symmetry). Singlet states also have no substantial interactions with external magnetic fields, as long as the field does not break the symmetry between the spins, so they are protected from the interactions that cause T_1 relaxation. Of course, pairs of isolated, chemically equivalent spins are found in only a handful of molecules; in addition, the lack of interaction with external fields implies that the signal we need to measure is unobservable.

As an alternative, several groups (*16*–*18*) have elegantly demonstrated lengthening of singlet-state lifetimes in molecules with inequivalent spins. In these experiments, the singlet state is not an eigenstate, so without any intervention it would rapidly evolve into unprotected states. However,

Department of Chemistry and Center for Molecular and Biomolecular Imaging, Duke University, Durham, NC 27708, USA.

*To whom correspondence should be addressed. E-mail: warren.warren@duke.edu

it can be forced to be a pseudo-eigenstate either by removing frequency differences with multiple spin echoes or by lowering the magnetic field to such an extent that the resonance frequencies are essentially the same. The signal can then be observed by permitting free evolution in a high field. Both approaches give clear lifetime increases, but neither is practical for magnetic resonance imaging. Multiple spin-echo sequences rapidly exceed safe power dissipation limits in tissue, and rapidly shuttling patients in and out of a magnet induces vertigo and nausea. In addition, at the microscopic level, both of these approaches must have their limitations. Relaxation is dominated by the local components of the magnetic field fluctuating near the resonance frequency, and if two sites are physically inequivalent, these fluctuations are expected to be poorly correlated, even if the resonance frequencies are nearly the same.

Here, we show that, in many cases, we can take advantage of chemistry to access and retrieve population from long-lived states and that disconnected eigenstates suitable for this storage exist in a fairly wide range of molecules. A test system that demonstrates both concepts is 2,3-^{13}C–labeled diacetyl [$CH_3(^{13}C{=}O)(^{13}C{=}O)CH_3$]. Diacetyl is formed in butter during ripening by the organism *Streptococcus lactis cremoris*, it is the source of the buttery flavor in wine and beer (at typical concentrations of a few micrograms per milliliter) (*19*), and it is added to soft margarines, producing concentrations in air commonly of ~100 parts per million (ppm) during cooking (*20*). However, there are concerns about extremely long-term inhalation (at chemical manufacturing plants), which has recently been implicated in bronchiolitis obliterans (*21*).

^{13}C-labeled diacetyl was prepared from $^{13}C_2$ oxalate, which was reacted with *N*,*N*′-dimethylethylenediamine to afford 2,3-$^{13}C_2$-1,4-dimethylpiperazine-2,3-dione (97% yield). Two equivalents of methyl magnesium bromide were added to the piperazine dione to produce the dimethyl piperazine *N*,*O*-acetal. Crude acetal was hydrolyzed with 10% aqueous HCl to yield 2,3-$^{13}C_2$ diacetyl, which was purified by fractional distillation. The carbonyl carbons in diacetyl are chemically equivalent, so at modest resolution (as is commonly achieved in an imaging system), the spectrum is expected to have only a single line. Neat 2,3-^{13}C diacetyl does have a single-line carbon spectrum, but the carbon spectrum in water has five lines. The monohydrate $CH_3(^{13}C{=}O)[^{13}C(OH)_2CH_3]$ (Fig. 1), with two inequivalent carbons and a scalar coupling $J_{C\text{–}C}$ = 45 Hz, is the majority species (*22*); the dihydrate is undetectable. Equilibrium can be shifted back to diacetyl by changing the solvent, and the rate of interconversion is pH-dependent. At pH 7, inversion of the diacetyl alone causes recovery in 8 s, which gives the rate of dehydration; inversion of all lines causes diacetyl to recover in 22 s.

Preparation of the singlet state requires perturbation of the αβ and βα populations from their equilibrium 25%. Hyperpolarization does not do this efficiently by itself. For example, 20% nuclear polarization (60% α, 40% β) would imply $\alpha_1\beta_2$ and $\beta_1\alpha_2$ populations of 24% (only 1% from equilibrium) and would waste most of the potential signal. However, because all the energy levels in the hydrate are accessible, suitable pulse sequences can manipulate the αβ and βα populations. The simplest is inversion of one line in one of the doublets (e.g., $\alpha_1\alpha_2 \rightarrow \alpha_1\beta_2$), which in this example would interchange the 36% $\alpha_1\alpha_2$ and 24% $\alpha_1\beta_2$ populations. Dehydration converts the sum of the $\alpha_1\beta_2$ and $\beta_1\alpha_2$ populations (in this case, 60%) evenly among the singlet $\alpha_1\beta_2 - \beta_1\alpha_2$ and triplet $\alpha_1\beta_2 + \beta_1\alpha_2$ of diacetyl; the singlet population in this case is 30%, six times farther from equilibrium than that produced by DNP alone. After this dehydration step, the population should be locked for a very long time, as discussed later, unless it exchanges back to the hydrate.

Figure 2 demonstrates this lifetime extension, both with and without hyperpolarization. The left side of Fig. 2 shows the result of selectively inverting only one line in thermally polarized monohydrate, then checking populations with a small flip-angle probe pulse after a variable delay. With a very long delay (50 s, top) the free induction decay (FID) from the monohydrate looks like the normal FID, which has a null at $t = 1/2J$ (10 ms), because each pair of lines separated by frequency J in Fig. 1 destructively interferes at that time. However, deviations of the αβ and βα population from their equilibrium values cause a characteristic alternation of the peak intensities [or, equivalently, FID signal at $t = 1/(2J)$]. For short delays between the selective inversion pulse and the probe pulse (10 s), the signal is large at $t = 1/2J$, also as expected. Figure 2A shows that population then flows rapidly into diacetyl as expected, but when it returns to the monohydrate (~30 s), it has excess αβ and βα population consistent only with a long-lived state (the singlet).

With hyperpolarization, this population could be readily converted back to observable signal in the hydrate (excess population in $\alpha_1\beta_2$ and $\beta_1\alpha_2$ implies dipolar order, which can be converted to

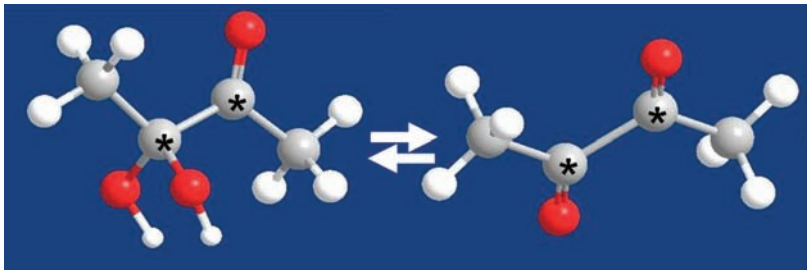

Fig. 1. The hydrate of 2,3-^{13}C diacetyl (**left**) has two inequivalent carbons (denoted by asterisks) whose resonance frequency differs by 110 ppm (~8 kHz in our magnet). The 45-Hz C–C scalar coupling splits both carbon lines into doublets, making all four energy levels accessible. The dehydrated version (**right**) has the same resonance frequency for both carbons and has a disconnected eigenstate. The αβ and βα populations in the hydrate are thus readily perturbed by radiofrequency pulses. Dehydration locks part of this population in the long-lived disconnected state; rehydration makes it observable again.

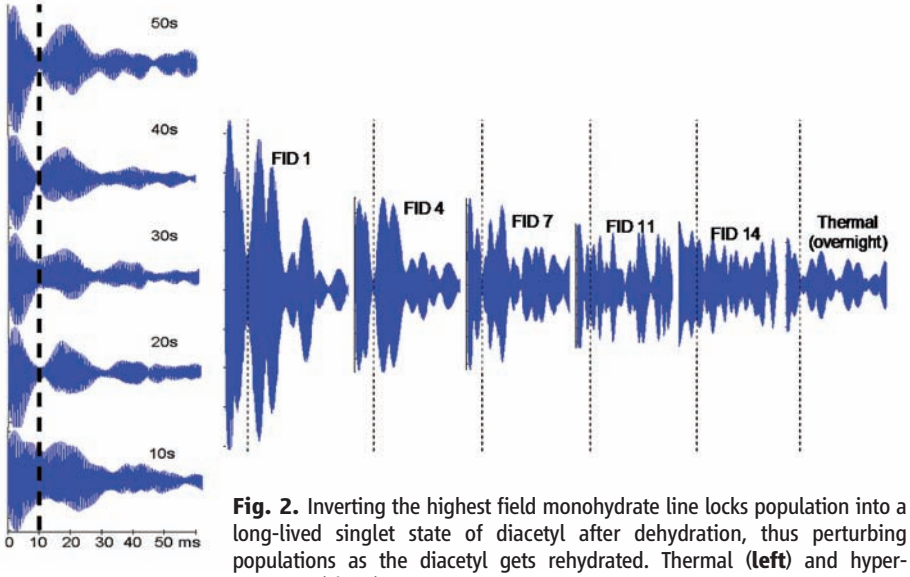

Fig. 2. Inverting the highest field monohydrate line locks population into a long-lived singlet state of diacetyl after dehydration, thus perturbing populations as the diacetyl gets rehydrated. Thermal (**left**) and hyperpolarized (**right**) FIDs are shown of only the portion of the spectrum around the monohydrate peaks. For equilibrium magnetization, the line splitting implies that the FID should vanish at $t = 1/2J$ (vertical dotted lines). The signal at that point directly measures excess population in $\alpha_1\beta_2$ and $\beta_1\alpha_2$ states, which is perturbed here by population flow from $\alpha_1\beta_2 - \beta_1\alpha_2$ in diacetyl.

observable signal with a 45° pulse and delay), dramatically extending the effective hyperpolarized lifetime. This procedure differs from most hyperpolarization experiments, where small-pulse flip angles are used to conserve the signal for multiple shots; singlet diacetyl is unaffected by radio frequency pulses, so large flip angles do not deplete the stored population. Equilibrium is readily shifted away from the hydrate by the addition of acetone, thus permitting the singlet state to last longer as a spin reservoir.

For the right side of Fig. 2, we started by hyperpolarizing diacetyl in water, achieving ~20% nuclear polarization. We then inverted one line of the monohydrate and followed with immediate 3:1 dilution with acetone. Dilution slowed the rate of hydration and helped to preserve any locked population produced by dehydration of the monohydrate. Individual spectra were acquired by 45° pulses with 10-s time separation. The dynamics are complex (for example, the equilibrium is being shifted), but useful insights can be gained by following only at the FID from hydrate peaks (Fig. 2B). The first FIDs have excess signal at $t = 1/2J$ (vertical dotted lines), as expected from the selective inversion. At intermediate times (sufficient for dehydration and mixing of the acetone), the FIDs look similar to the thermal ones (averaged over 360 shots). Most interestingly, the later FIDs have signal higher than thermal, and the structure is very complex. In the case of FID 14, for example, the preceding 45° pulses should have depleted all but 1% of the hyperpolarized signal, and relaxation should have depleted all but 0.1%, so less than 10^{-5} should remain in the absence of singlet effects.

Figure 3 shows the result of an experiment similar to Fig. 2, except that this time we used perdeuterated diacetyl. We generated excess $\alpha_1\beta_2$ and $\beta_1\alpha_2$ population, diluted with acetone, then applied a series of 45° pulses, both before and after the addition of excess water. Before the water addition, hyperpolarization goes away because of the ~30-s T_1 relaxation time and population depletion by the pulses themselves; at the time of the water injection, ~3% of the initial hyperpolarized signal is still present. The water injection permits rehydration, thus making the stored singlet population accessible. Within seconds after the injection, the signal more than triples and, in this case, is still readily observable for minutes.

Shifting the equilibrium with acetone in vivo would not be feasible. As diacetyl does not have a dipole moment, it can migrate to a nonpolar phase [for instance, it is mostly found in the fatty phase in butter (*23*)], and we picture one ultimate application of this agent as a "reporter molecule" in a delivery system [for example, functionalized or temperature-sensitive liposomes or functionalized ultrasound contrast agents, including commercially available agents that are based on encapsulated perfluorocarbons (*24*)].

To understand how general these results would be, it is important to recognize that the high-resolution spectrum of diacetyl is more complicated than that of para-H_2 or water because the two carbons are chemically equivalent but not isolated. Each carbon is coupled differently to the two methyl groups (the C–H couplings are 6.4 Hz and –1.1 Hz). Such couplings generate simple splitting patterns in most molecules. For example, Fig. 4A shows the carbonyl region ^{13}C NMR spectrum of the singly carbon-labeled species (2-^{13}C diacetyl), where the two different couplings to three hydrogens each generate a quartet of quartets. Fig. 4B also shows the spectrum of acetone [$CH_3(^{13}C{=}O)CH_3$], which leads to a septet because the six hydrogens are equivalent. Both of these results would be obvious to a practicing organic chemist. However, Fig. 4C shows the superficially very complicated spectrum of 2,3-^{13}C diacetyl. The complexity arises from addition of the C–C coupling (~45 Hz) and hides a secret: The carbon singlet state is nearly a disconnected eigenstate.

The bottom panels of Fig. 4 show simulations (using WindNMR-Pro) that unravel the complexity by varying the coupling $J_{C\text{-}C}$ between the two carbons. If $J_{C\text{–}C} = 0$ (Fig. 4D), the doubly labeled and singly labeled spectra are identical, and inspection of the energy levels shows that the carbon singlet is not an eigenstate: The two different scalar couplings readily connect this state to others with the same overall symmetry, but with ($\alpha\beta + \beta\alpha$) as the carbon component. However, if $J_{C\text{–}C}$ is much larger than all other couplings (Fig. 4E), the spectrum changes dramatically. It collapses back into a septet, similar to the acetone spectrum, except that the splitting is not a real coupling; rather, it is the 2.65-Hz average of the couplings between the near and far methyl groups. This is an example of a "deceptively simple spectrum" (*25*–*27*). It can be explored by exact calculations, which readily show that the spectrum comes entirely from transitions involving $\alpha\beta + \beta\alpha$ as a carbon state, which is delocalized over the two carbons and is coupled equally to each hydrogen. The $\alpha\beta - \beta\alpha$ state is a disconnected eigenstate; hence, it is long-lived.

Smaller spin systems that would have similar properties (e.g., the case of two coupled pairs of chemically equivalent spins) (*28*) were solved analytically decades ago, and it would have been possible to draw the same conclusions about disconnected eigenstates from those analytic solutions. For example, consider 2,3-^{13}C diacetylene (H–C≡^{13}C–^{13}C≡C–H). This would be called an AA′XX′ system in standard NMR parlance, where A and X stand for the two different NMR-active nuclei (here ^{13}C and H) and the primes indicate that there are two different couplings between A and X. We expect 12 lines associated with the carbon (A) transitions, not 1, and the singlet state is generally mixed with many other states. Careful inspection of (*28*) shows that the critical parameters are the ratios $(J \pm J')/(J_{A\text{–}A} - J_{X\text{–}X})$, where J and J' are the two different A–X couplings. Here this ratio would be small, and the exact result (or a simple perturbation theory analysis) would show the worst overlap of a carbon singlet state with a true spin eigenstate to be $\{1 - 0.25[(J - J')/(J_{A\text{–}A} -$

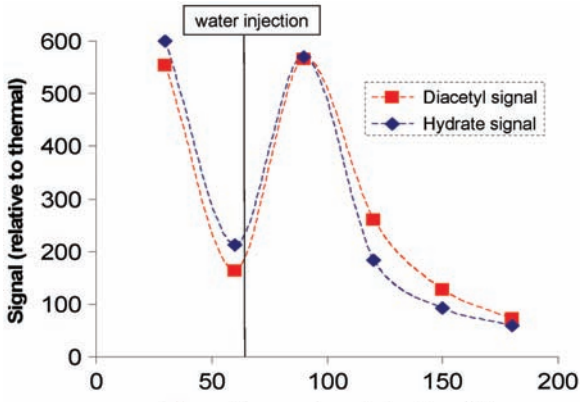

Fig. 3. Hyperpolarized perdeuterated diacetyl monohydrate was pulsed to perturb the $\alpha_1\beta_2$ and $\beta_1\alpha_2$ populations, diluted in acetone, then probed with a series of 45° pulses (both before and after addition of excess water). The dramatic increase in signal with rehydration reflects the unlocking of long-lived population stored in the diacetyl disconnected eigenstate.

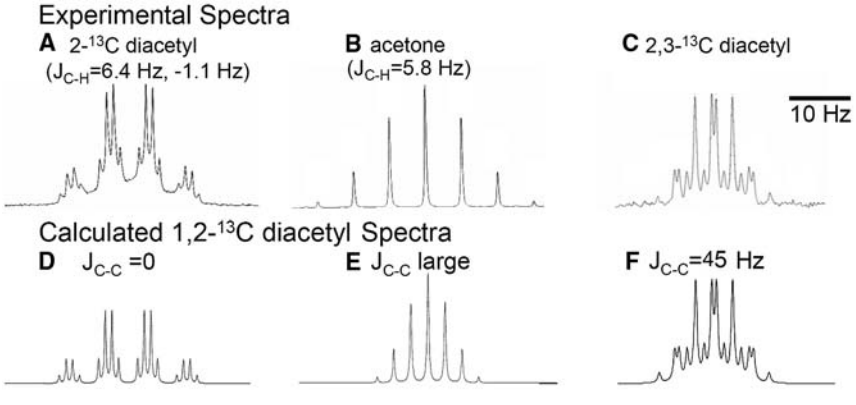

Fig. 4. (A to F) Experimental and theoretical spectra validating the presence of disconnected eigenstates (even in molecules such as diacetyl) without magnetically equivalent spins.

$J_{X-X})]^2\}$. We then expect the singlet lifetime lengthening to be on the order of $[(J_{A-A} - J_{X-X})/(J - J')]^2$. However, the importance of disconnected eigenstates was apparently not appreciated, in part because, in the absence of hyperpolarization and a mechanism to populate the state, the associated state has no obvious applications.

The perturbation calculation is easily extended to diacetyl, where the ratio $(J \pm J')/(J_{A-A} - J_{X-X})$ is also small (the minus sign gives the larger value in cases such as ours, where the couplings have opposite signs). Although the spectra in Fig. 4, C and F, are quite complex, assuming the couplings have the same value as in the hydrate (which gives the excellent spectral fit in Fig. 4F) shows that the overlap of the singlet state with an eigenstate is better than 0.96. This result is also readily verified by precise numerical analysis of this eight-spin system, and thus we predict more than an order-of-magnitude lengthening of the spin lifetime. In effect, the strong coupling between the two carbons quenches communication with other spins—virtually all the spectral complexity comes from the other three carbon states, and singlet-to-triplet interconversion is slow. Of course, perdeuteration dramatically reduces even this limited singlet-triplet mixing and further increases the lifetime.

The advantage of the perturbation theory calculation is that it lets us discuss the generic case. The generalization is more subtle than one might expect. The common case of magnetic equivalence [where the two spins have the same resonance frequency and each of the two spins is coupled identically to every other spin (*12*)] does not necessarily produce a disconnected eigenstate. For example, any two of the spins in a freely rotating methyl group are magnetically equivalent, but the energy level diagram for three equivalent spins produces no fully disconnected states, so the immunity to environmental perturbations is not present. The only possible disconnected eigenstate for two spins is the singlet; for a larger even number of spins with enough symmetry [e.g., benzene (*29*)] other disconnected states exist, although they might be difficult to access in practice.

The critical constraint for producing a disconnected eigenstate is that the coupling between two spins substantially exceeds both the couplings to other spins and the resonance frequency difference between the spins. Systems of interest as hyperpolarized contrast agents have two nearby H, ^{13}C, ^{15}N, ^{19}F, or ^{31}P atoms that satisfy this constraint. They have a precursor where the two atoms are inequivalent (hence permitting hyperpolarization of the $\alpha_1\beta_2$ population), which can be converted to the contrast agent by chemical manipulation in a time that is short compared with the normal T_1. Finally, they have a biological pathway that again makes them inequivalent, permitting detection of the hyperpolarization. Diacetyl in vivo satisfies these conditions. Partition in vivo between hydrophobic and hydrophilic phases would modulate the exchange rate (drastically reducing the water concentration and, hence, lengthening the time to convert from singlet); even ignoring hydration, the first metabolite is acetoin with inequivalent carbons. More generally, the simplest case is two equivalent adjacent carbons or nitrogens without directly bonded hydrogens, as in diacetyl, naphthalene, and oxolin (an antiviral compound) or in many derivatives of pyridazine or phthalazine, which have recently been shown to have vascular endothelial growth factor receptor–2 inhibitory activity (*30*). In other cases, deuteration can essentially eliminate the coupling to outside nuclei, as could very weak irradiation (far less than is necessary when the spin systems differ in their chemical shift frequency). At moderate fields, even molecules with not-quite-equivalent spins (such as the 3,4-^{13}C versions of L-dopa or dopamine) might be usable, as the degradation pathway leads to compounds such as HVA with substantial asymmetry.

References and Notes

1. J. R. MacFall *et al.*, *Radiology* **200**, 553 (1996).
2. C. R. Bowers, D. P. Weitekamp, *J. Am. Chem. Soc.* **109**, 5541 (1987).
3. J. Natterer, J. Bargon, **31**, 293 (1997).
4. K. Golman *et al.*, *Magn. Reson. Med.* **46**, 1 (2001).
5. A. Abragam, M. Goldman, *Rep. Prog. Phys.* **41**, 395 (1978).
6. K. Golman, J. H. Ardenkjaer-Larsen, J. S. Petersson, S. Mansson, I. Leunbach, *Proc. Natl. Acad. Sci. U.S.A.* **100**, 10435 (2003).
7. D. A. Hall *et al.*, *Science* **276**, 930 (1997).
8. J. Kurhanewicz, R. Bok, S. J. Nelson, D. B. Vigneron, *J. Nucl. Med.* **49**, 341 (2008).
9. K. Golman *et al.*, *Cancer Res.* **66**, 10855 (2006).
10. M. E. Merritt *et al.*, *Proc. Natl. Acad. Sci. U.S.A.* **104**, 19773 (2007).
11. I. J. Day, J. C. Mitchell, M. J. Snowden, A. L. Davis, *Magn. Reson. Chem.* **45**, 1018 (2007).
12. C. Gabellieri *et al.*, *J. Am. Chem. Soc.* **130**, 4598 (2008).
13. E. R. McCarney, B. L. Armstrong, M. D. Lingwood, S. Han, *Proc. Natl. Acad. Sci. U.S.A.* **104**, 1754 (2007).
14. The nomenclature used here is explained more fully, with specific examples, in textbooks such as (*15*).
15. E. D. Becker, *High Resolution NMR: Theory and Chemical Applications* (Academic, San Diego, 2000), pp. 171–175.
16. M. Carravetta, O. G. Johannessen, M. H. Levitt, *Phys. Rev. Lett.* **92**, 153003 (2004).
17. M. Carravetta, M. H. Levitt, *J. Chem. Phys.* **122**, 214505 (2005).
18. P. Ahuja, R. Sarkar, P. R. Vasos, G. Bodenhausen, *J. Chem. Phys.* **127**, 134112 (2007).
19. G. del Campo, M. C. Carmen Lajo, *Analyst (London)* **117**, 1343 (1992).
20. See http://seattlepi.nwsource.com/dayart/20071221/DiacetylProducts2.pdf for a study done by the *Seattle Post-Intelligencer* in December 2007.
21. F. G. B. G. J. van Rooy, *Am. J. Respir. Crit. Care Med.* **176**, 498 (2007).
22. R. P. Bell, *Adv. Phys. Org. Chem.* **4**, 1 (1966) and references therein.
23. W. H. Hoecker, B. W. Hammer, *J. Dairy Sci.* **25**, 175 (1942).
24. J. Å. Jakobsen *et al.*, *Eur. Radiol.* **15**, 941 (2005).
25. R. J. Abraham, H. J. Bernstein, *Can. J. Chem.* **39**, 216 (1961).
26. F. A. L. Anet, *Can. J. Chem.* **39**, 2262 (1961).
27. J. I. Musher, E. J. Corey, *Tetrahedron* **18**, 791 (1962).
28. J. A. Pople, W. G. Schneider, H. J. Bernstein, *Can. J. Chem.* **35**, 1060 (1957).
29. A. Saupe, *Z. Naturforsch.* **20a**, 572 (1965).
30. A. S. Kiselyov, V. V. Semenov, D. Milligan, *Chem. Biol. Drug Des.* **68**, 308 (2006).

31. This work was supported by the NIH under grant EB02122 and by the North Carolina Biotechnology Center. We thank D. Bhattacharyya for his help in determining optimal conditions to hyperpolarize diacetyl; M. Jenista for help with calculations; T. Ribiero for his assistance in running NMR spectra; L. Bouchard for discussions of singlet character in strongly coupled systems; and S. Craig, E. Toone, D. Coltart, and M. S. Warren for particularly useful discussions on the chemistry of these compounds. A provisional patent has been submitted on this work by W.S.W. and Duke University.

27 October 2008; accepted 2 February 2009
10.1126/science.1167693

Greatly Expanded Tropical Warm Pool and Weakened Hadley Circulation in the Early Pliocene

Chris M. Brierley,[1]* Alexey V. Fedorov,[1]*† Zhonghui Liu,[2]* Timothy D. Herbert,[3] Kira T. Lawrence,[4] Jonathan P. LaRiviere[5]

The Pliocene warm interval has been difficult to explain. We reconstructed the latitudinal distribution of sea surface temperature around 4 million years ago, during the early Pliocene. Our reconstruction shows that the meridional temperature gradient between the equator and subtropics was greatly reduced, implying a vast poleward expansion of the ocean tropical warm pool. Corroborating evidence indicates that the Pacific temperature contrast between the equator and 32°N has evolved from ~2°C 4 million years ago to ~8°C today. The meridional warm pool expansion evidently had enormous impacts on the Pliocene climate, including a slowdown of the atmospheric Hadley circulation and El Niño–like conditions in the equatorial region. Ultimately, sustaining a climate state with weak tropical sea surface temperature gradients may require additional mechanisms of ocean heat uptake (such as enhanced ocean vertical mixing).

The early Pliocene [~5 to 3 million years ago (Ma)] is often considered the closest analog to the effects of contemporary global warming on Earth's climate. Indeed, the external factors that control the climate system—the intensity of sunlight incident on Earth's surface, global geography (*1*, *2*), and, most important, the atmospheric concentration of CO_2 (*3*)—were similar to present-day conditions. However, high latitudes were warmer, continental ice sheets were largely absent from the Northern Hemisphere, and the sea level was ~25 m higher than today (*4*, *5*).

The climate of the tropics was also quite different. The sea surface temperature (SST) contrast between the eastern and western equatorial Pacific was very small, and cold surface waters were almost absent from coastal upwelling zones off the western coasts of Africa and the Americas (*6*–*10*). These climate conditions are often called a "permanent El Niño" or permanent El Niño–like state (*11*). This term describes the long-term mean state of the ocean-atmosphere system. In contrast, the modern, intermittent El Niño is the warm phase of a quasi-periodic climate oscillation, which affects weather and climate patterns worldwide every 4 to 5 years (*12*, *13*). Interannual climate variability may have also existed in the Pliocene (*14*), but only during times when the equatorial SST gradient exceeded some critical value (*12*).

This study focuses on the meridional distribution of SST and its effects on the early Pliocene climate. Understanding changes in this distribution, including variations in the meridional extent of the ocean tropical warm pool, is essential for understanding mechanisms responsible for the gradual transition from the warmer Pliocene to the cooler Pleistocene. It has been hypothesized that the early Pliocene had a relatively deep ocean thermocline in the tropics and that the subsequent shoaling of the thermocline signaled the transition to a colder climate (*6*). A reduced meridional gradient is required to sustain a deeper tropical thermocline (see below).

We first examined the evolution of the meridional SST gradient over the past 4 million years in the eastern tropical Pacific (Fig. 1, A and C). We used orbitally resolved records from two Ocean Drilling Program (ODP) sites: Site 1012 (32°N, 118°W) from the California margin, and Site 846 (3°S, 91°W) from the eastern Pacific cold tongue just south of the equator (Fig. 1B). Both data sets are based on alkenone-derived estimates of SST (*15*). The new data from ODP Site 1012 agree overall with previously published results from ODP Site 1014 (*8*); however, the present data set has much higher resolution, allowing precise temporal alignment of equatorial and subtropical records.

According to these data, the mean temperature contrast between the two sites evolved from a very small value of ~2°C at 4 Ma to 7°C by 2 Ma, and then remained fairly constant at nearly present-day levels (Fig. 1C). Superimposed on the gradual trends at each site are Milankovitch cycles driven by variations in Earth's orbital parameters (*1*). On orbital time scales, these cycles can produce changes in the SST contrast between the two sites as large as the underlying long-term trends.

The temporal development of the zonal SST gradient along the equator (*7*) generally mirrors that of the meridional SST gradient in the eastern Pacific (Fig. 1D), suggesting a strong link between extratropical and tropical ocean conditions. The zonal SST gradient reaching its modern value later in the record indicates that meridional temperature changes precondition zonal changes along the equator.

To show that the strong reduction in the meridional temperature gradient in the early Pliocene is a robust result, we reconstructed the meridional SST distribution in the mid-Pacific roughly along the dateline (Fig. 2). The period of this reconstruction is ~4 to 4.2 Ma, sometimes called the Pliocene thermal optimum (*16*). This period coincides with an almost complete collapse of the east-west temperature gradient along the equator (*6*–*8*) (Fig. 1D); it also follows the closure of the Central America Seaway (*2*) but precedes climate cooling and the development of large Northern Hemisphere ice sheets (*1*).

The data in Fig. 2 are based on alkenone and Mg/Ca temperature proxies. Alkenone-derived records for ODP Sites 982, 1012, and 1090 and for Deep Sea Drilling Project Site 607 were produced specifically for this study; the original temperature records for other sites were published elsewhere (*6*–*10*, *17*–*21*). Adjustments were applied to some of the SST data to represent the mid-Pacific in the early Pliocene (*15*). For example, when using temperatures from the Atlantic to reconstruct Pacific SSTs, one must consider that temperatures in the North Atlantic are typically 2° to 7°C higher than in the North Pacific; when using SSTs from the eastern boundary of the basin to reconstruct temperatures in the mid-Pacific, one should correct for the effect of coastal upwelling. The overall temperature distribution in Fig. 2 is robust and does not depend on any individual data point.

Our analysis indicates a considerably warmer Pacific climate in the early Pliocene than that determined by the PRISM project in its mid-Pliocene SST reconstructions (*5*, *22*, *23*). Furthermore, a strong reduction in the SST gradient from the equator to the subtropics described in our study implies a vast poleward expansion of the ocean low-latitude warm pool (fig. S1), whereas the maximum tropical temperatures remained close to present-day values (28° to 29°C).

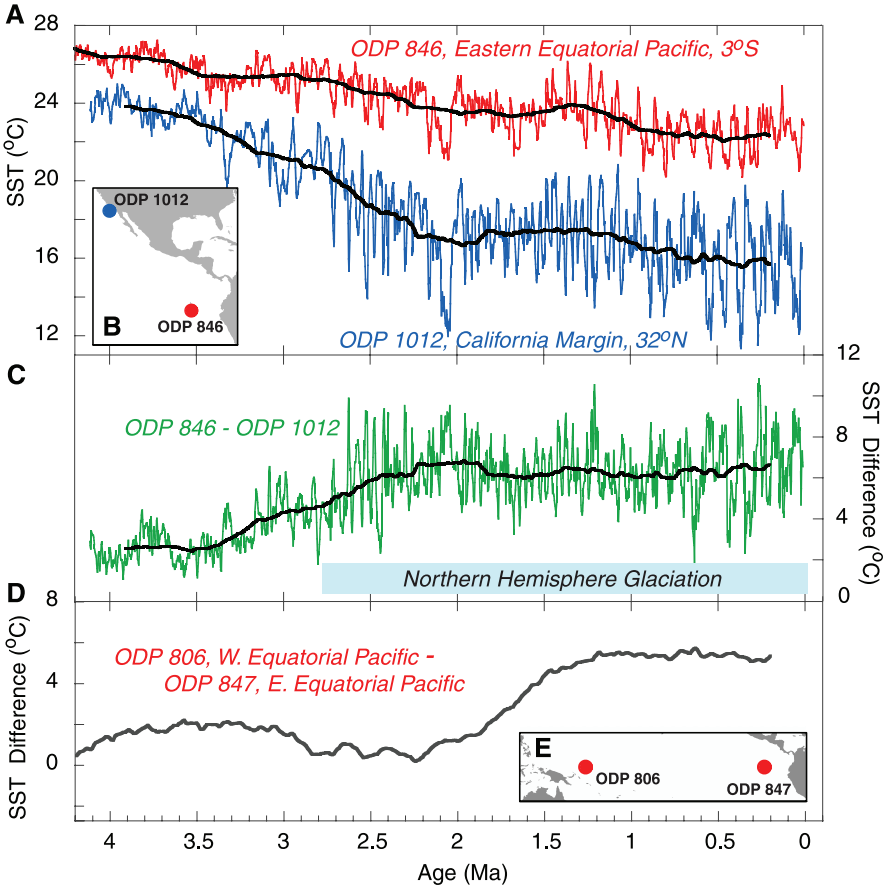

Fig. 1. (**A**) The evolution of SSTs, as derived from alkenones (*15*), in two locations: ODP Site 1012 (blue) off the coast of California (32°N, 118°W) and ODP Site 846 (red) in the eastern Pacific just south of the equator (3°S, 91°W). Note the cooling trends over the past 4 million years, shown here as 400,000-year running means (black lines). (**B**) Locations of the sites in (A). (**C**) SST difference between the two locations in (B). The meridional SST gradient is minimal at ~4 Ma (2°C) and then increases gradually to modern values (~7.5°C). (**D**) The zonal SST gradient along the equator (*7*) from Mg/Ca paleothermometry between ODP Site 806 in the western equatorial Pacific (0°N, 159°E) and ODP Site 847 in the eastern equatorial Pacific (0°N, 95°W). The strength of this temperature gradient varies from 0° to 2°C between 5 Ma and 2 Ma and then increases gradually to modern values (~5.5°C). (**E**) Locations of the sites in (D).

[1]Department of Geology and Geophysics, Yale University, New Haven, CT 06520, USA. [2]Department of Earth Sciences, University of Hong Kong, Hong Kong, PRC. [3]Department of Geological Sciences, Brown University, Providence, RI 02912, USA. [4]Geology and Environmental Geosciences, Lafayette College, Easton, PA 18042, USA. [5]Ocean Sciences, University of California, Santa Cruz, CA 95064, USA.

*These authors contributed equally to this work.
†To whom correspondence should be addressed. E-mail: alexey.fedorov@yale.edu

The ocean tropical warm pool (currently confined mainly to the western equatorial Pacific) is a critical component of the climate system (*24*), and changes in its meridional extent can have large implications for climate. In particular, meridional expansion of the warm pool provides a crucial mechanism for maintaining permanent El Niño conditions in the equatorial region, because cold water in the modern eastern equatorial Pacific is sourced from the subtropical subduction zones. Poleward expansion of the warm pool into the subduction regions would lead to warmer waters upwelling in the eastern equatorial Pacific, a deeper ocean thermocline, and consequently a substantial reduction of the SST gradient along the equator. Apparently, such a climate state prevailed at ~4 Ma (Fig. 1, C and D). Thus, to explain the permanent El Niño conditions during the early Pliocene, it is necessary to understand the meridional expansion of the ocean warm pool.

To quantify the atmospheric response to the expanded tropical warm pool and reduced meridional temperature gradient, we fit a hypothetical SST profile to the data in Fig. 2, which was then used as a boundary condition for an atmospheric general circulation model (GCM) (*15*). In the absence of reliable simulations of the Pliocene climate with coupled models, simulations with atmospheric GCMs forced with ocean surface boundary conditions arguably remain the best way to assess climate conditions. Previous studies of the Pliocene with atmospheric GCMs used either earlier PRISM SST reconstructions (*5*), which lacked adequate data for the tropics and subtropics, or the modern SST profile taken from the dateline and extended zonally (*25*).

Our numerical calculations confirm that the SST changes in Fig. 2 strongly affect the global climate and atmospheric circulation. As expected, the lack of an SST gradient along the equator acts to eliminate the atmospheric zonal circulation [the Walker cell (*13*)] (fig. S2). However, if the meridional SST gradient were kept at present-day values as in previous studies, the atmospheric meridional circulation [the Hadley cells (*26*)] would compensate by strengthening substantially (*25*). In contrast, in calculations using our Pliocene SST reconstruction, the Hadley circulation weakens (Fig. 3, A and B).

The Northern Hemisphere branch of the Hadley circulation weakens on average by roughly 30%. During boreal winter, the reduction reaches nearly 40%. The center of the Hadley cell moves northward by ~7°, whereas the cell's latitudinal extent (*26*) increases by 3° to 4°. These changes of the Northern Hemisphere circulation are a robust response to changes in meridional SST gradient as evinced by additional sensitivity calculations (table S2). The volume transport of the circulation's southern branch nearly halves, making the southern Hadley cell even weaker than the northern cell. Whether this is a genuine feature of the early Pliocene climate remains to be seen, because there are only a few SST data points currently available in the Southern Hemisphere. Note that coupled models simulating global warming also show a weakening and poleward expansion of the Hadley circulation. However, those effects are rather modest—roughly 4% and 1° of latitude, respectively, by the end of the 21st century (*26*).

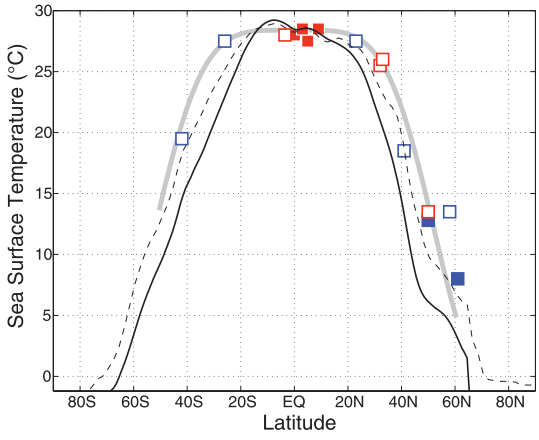

Fig. 2. Estimated distribution of SST with latitude in the middle of the Pacific (roughly along the dateline) at ~4 Ma. This temperature reconstruction uses data from the Pacific and Indian oceans (red boxes) and adjusted data from the Atlantic (blue boxes). Open boxes indicate alkenone-based data; solid boxes indicate Mg/Ca-based data. Thin solid line: SST from the dateline for the modern climate. Dashed line: latest estimates of the mid-Pliocene temperatures (~3 Ma) along the dateline from the PRISM project (*22*, *23*). Thick gray line: a portion of the hypothetical SST profile used as a boundary condition for numerical simulations. The original data and the temperature adjustments are given in table S1.

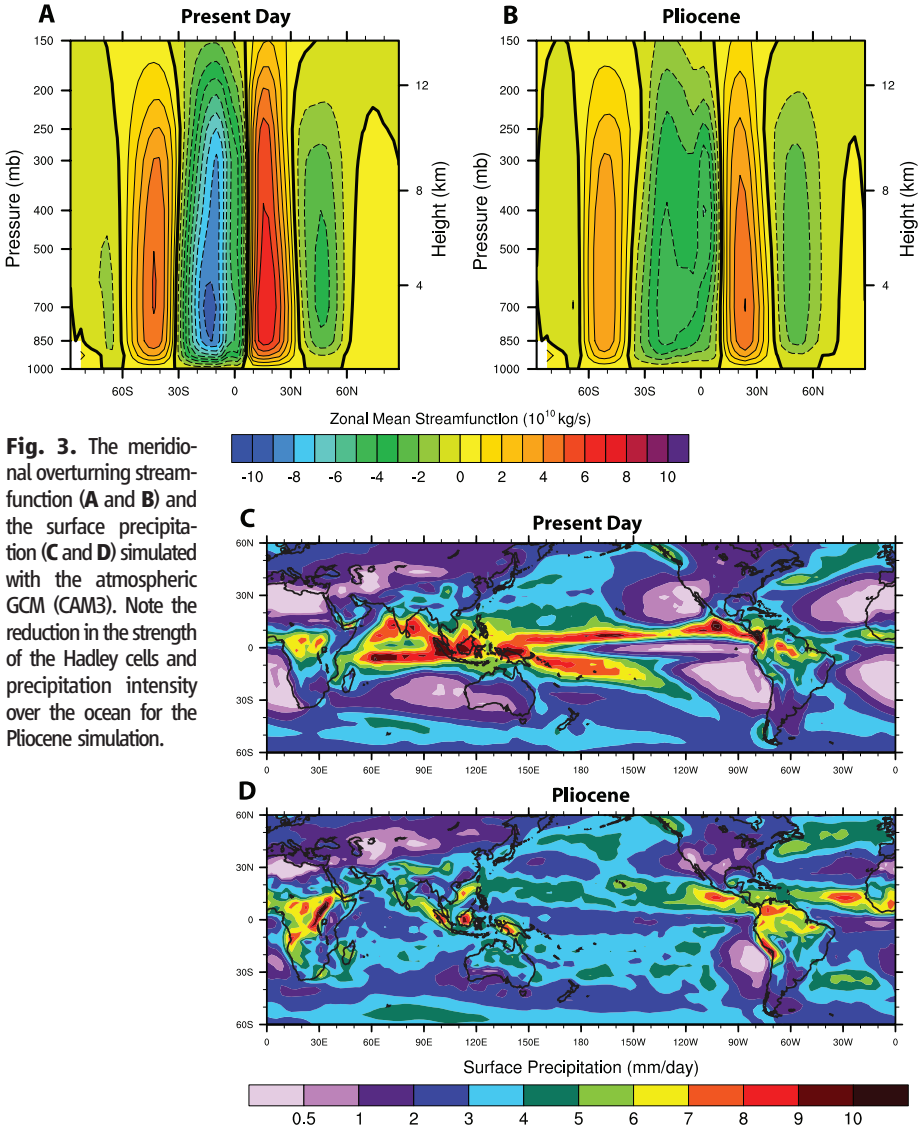

Fig. 3. The meridional overturning streamfunction (**A** and **B**) and the surface precipitation (**C** and **D**) simulated with the atmospheric GCM (CAM3). Note the reduction in the strength of the Hadley cells and precipitation intensity over the ocean for the Pliocene simulation.

In our calculations, the reduced meridional temperature gradient also widens the Intertropical Convergence Zone [ITCZ (*13*)] and decreases its precipitation intensity (Fig. 3, C and D). A second, weaker ITCZ develops in the Southern Hemisphere, caused by the use of a completely symmetrical SST profile. The spatial structure of Pliocene precipitation indicates that the strongest air uplift occurs over

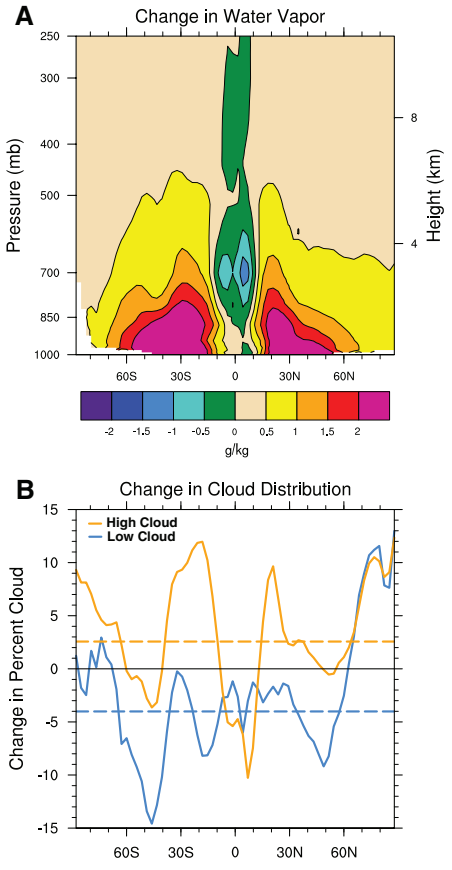

Fig. 4. Factors critical for maintaining a warm Pliocene climate. (**A**) The increase in zonal-mean specific humidity (or water vapor content) from the present day to the early Pliocene (in g/kg). The only reduction in water vapor occurs in a narrow region above the modern ITCZ location, which indicates a weakening of the deep convection in the tropics. (**B**) Changes in cloud distribution with latitude (solid lines) and their globally averaged values (dashed lines). There is a net increase in cloud fraction for "greenhouse" high clouds and a net decrease for highly reflective low clouds; both effects tend to warm Earth's surface.

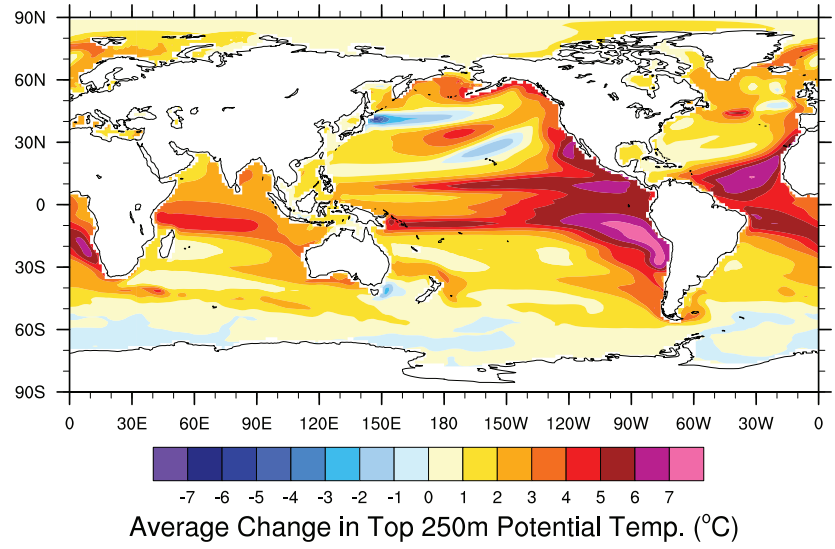

Fig. 5. Difference in ocean temperatures (averaged over the top 250 m) between two greenhouse-warming simulations: a simulation for which we increased the background vertical diffusivity in the upper 400 m of the ocean by an order of magnitude between 40°N and 40°S, and a control simulation. In each case, the CO_2 concentration was increased instantaneously from preindustrial levels to 355 ppm, and the coupled model (CCSM3) has been integrated for 180 years (the plot is obtained from a 30-year average at the end of the simulations). A gradual ocean adjustment will continue after 180 years, but we do not expect large qualitative changes in the warming pattern. The actual values of the ocean vertical diffusivity in the Pliocene are highly uncertain, so these experiments serve only to demonstrate the proposed mechanism.

orographic features (such as the East African Highlands) rather than over the ocean. Weak SST gradients, and hence a lack of localized wind convergence, over the ocean cause orographic air uplift and ocean-land temperature contrasts to become essential for triggering tropical precipitation.

Terrestrial paleodata provide verification of gross changes in precipitation anticipated over land by our calculations. For example, the model predicts stronger precipitation over southwest and east Africa, the Sahara desert, and Australia, consistent with pollen-based precipitation data (table S3). Comparison of changes over North America is inconclusive because of large error bars in the paleodata (*27*) and large natural variability in precipitation intensity in that region.

The water vapor content of the atmosphere increases significantly (Fig. 4A) as a consequence of the Clausius-Clapeyron relationship (*28*), despite the substantial reduction in the strength of atmospheric convection over the ITCZ in the Pacific. The increase in water vapor (a potent greenhouse gas) is a major factor in sustaining the warm Pliocene climate. It causes a reduction of 14.6 W m^{-2} in outgoing long-wave radiation at the top of the atmosphere (relative to the present); variations in cloud distribution (Fig. 4B) account for a further reduction of 5.6 W m^{-2}. Because the net increase in atmospheric water vapor (by roughly 30%) is largely a consequence of the expanded ocean warm pool, a climate model will not be able to capture the full extent of the Pliocene warmth unless it can simulate SST patterns in the tropics and subtropics correctly.

Further, our calculations show a slight increase in total poleward heat transport from low to high latitudes (fig. S3). However, the partitioning of the heat transport between the ocean and atmosphere poses the following problem: We find a significant decrease in the heat transport by the atmosphere and an implied increase in ocean heat transport (fig. S3). This result contradicts studies using ocean GCMs with low vertical diffusion, which suggest that a permanent El Niño should be associated with reduced heat transport by the ocean (*29*). According to those studies, the ocean typically gains a large amount of heat over the tropical Pacific cold tongue; warmer conditions in that region would entail a reduction in ocean heat uptake there, and hence a smaller ocean heat transport. Attempts to simulate the Pliocene climate with coupled atmosphere-ocean GCMs (*14*) have not yet succeeded in replicating the collapse of the SST gradient along the equator, presumably because of this issue.

One way to resolve the heat transport problem in such a climate state with weak SST gradients is to allow the ocean to gain heat over a much broader region of the tropics than just the equatorial cold tongue. This would necessitate a substantial increase in ocean vertical mixing rates (or vertical diffusion), which may result from weaker ocean stratification (*20*) and/or enhanced mixing of the upper ocean by hurricanes (*30*). Should such an increase in ocean mixing occur, it would lead to larger heat uptake and greater poleward heat transport by the ocean, even with a weak or absent equatorial cold tongue.

To test this hypothesis, we ran a coupled GCM with elevated atmospheric CO_2 concentrations and vertical diffusion uniformly increased in the upper tropical ocean. Preliminary results with enhanced mixing produce a mean state much closer to a permanent El Niño (Fig. 5). There is a much greater warming in the eastern equatorial Pacific than in the west, a warming of the upwelling regions, and a deeper ocean thermocline. At the same time, interannual variability becomes substantially weaker.

Thus, it may be necessary to incorporate additional mechanisms for increased ocean heat uptake when simulating the early Pliocene climate and, potentially, the response of the tropics to contemporary global warming. The enormous impacts of changes in the warm pool (such as shifts in global precipitation patterns and cloud cover), as well as tentative evidence that the tropical belt has been expanding poleward over the past few decades (*31*), make our findings especially relevant to current discussions about global warming.

References and Notes

1. J. Zachos, M. Pagani, L. Sloan, E. Thomas, K. Billups, *Science* **292**, 686 (2001).
2. G. H. Haug, R. Tiedemann, R. Zahn, A. C. Ravelo, *Geology* **29**, 207 (2001).

3. M. E. Raymo, B. Grant, M. Horowitz, G. H. Rau, *Mar. Micropaleontol.* **27**, 313 (1996).
4. H. Dowsett, J. Barron, R. Poore, *Mar. Micropaleontol.* **27**, 13 (1996).
5. A. M. Haywood, P. J. Valdes, B. W. Sellwood, *Global Planet. Change* **25**, 239 (2000).
6. A. V. Fedorov *et al.*, *Science* **312**, 1485 (2006).
7. M. W. Wara, A. C. Ravelo, M. L. Delaney, *Science* **309**, 758 (2005); published online 23 June 2005 (10.1126/science.1112596).
8. P. S. Dekens, A. C. Ravelo, M. D. McCarthy, *Paleoceanography* **22**, PA3211 (2007).
9. J. R. Marlow, C. B. Lange, G. Wefer, A. Rosell-Melé, *Science* **290**, 2288 (2000).
10. K. T. Lawrence, Z. Liu, T. D. Herbert, *Science* **312**, 79 (2006).
11. P. Molnar, M. A. Cane, *Paleoceanography* **17**, 1021 (2002).
12. A. V. Fedorov, S. G. Philander, *Science* **288**, 1997 (2000).
13. S. G. H. Philander, *El Niño, La Niño, and the Southern Oscillation* (Academic Press, New York, 1990).
14. A. M. Haywood, P. J. Valdes, V. L. Peck, *Paleoceanography* **22**, PA1213 (2007).
15. See supporting material on *Science* Online.
16. A. A. Velichko, I. Spasskaya, in *The Physical Geography of Northern Eurasia*, M. Shahgedanova, Ed. (Oxford Univ. Press, Oxford, 2002), pp. 36–69.
17. T. D. Herbert, J. D. Schuffert, *Proc. ODP Sci. Res.* **159T**, 17 (1998).
18. G. Bartoli *et al.*, *Earth Planet. Sci. Lett.* **237**, 33 (2005).
19. J. Tian, *Earth Planet. Sci. Lett.* **252**, 72 (2006).
20. G. H. Haug, D. M. Sigman, R. Tiedemann, T. F. Pedersen, M. Sarnthein, *Nature* **433**, 821 (2005).
21. J. Groeneveld *et al.*, *Proc. ODP Sci. Res.* **202**, 1 (2006).
22. H. J. Dowsett, M. M. Robinson, *Philos. Trans. R. Soc. London Ser. A* **367**, 109 (2009).
23. Data are available from http://geology.er.usgs.gov/eespteam/prism/prism_data.html.
24. A. C. Clement, R. Seager, G. Murtugudde, *J. Clim.* **18**, 5294 (2005).
25. M. Barreiro, G. Philander, R. Pacanowski, A. V. Fedorov, *Clim. Dyn.* **26**, 349 (2006).
26. J. Lu, G. A. Vecchi, T. Reichler, *Geophys. Res. Lett.* **34**, L06805 (2007).
27. U. Salzmann, A. M. Haywood, D. J. Lunt, P. J. Valdes, D. J. Hill, *Glob. Ecol. Biogeogr.* **17**, 432 (2008).
28. I. M. Held, B. J. Soden, *J. Clim.* **19**, 5686 (2006).
29. S. G. H. Philander, A. V. Fedorov, *Paleoceanography* **18**, 1045 (2003).
30. R. L. Sriver, M. Huber, *Nature* **447**, 577 (2007).
31. D. J. Seidel, Q. Fu, W. J. Randel, T. J. Reichler, *Nat. Geosci.* **1**, 21 (2008).

32. A.V.F. thanks G. Philander, M. Barreiro, R. Pacanowski, Y. Rosenthal, C. Ravelo, P. deMenocal, P. Dekens, A. Haywood, and C. Wunsch for numerous discussions of this topic. Supported by NSF grant OCE-0550439, U.S. Department of Energy Office of Science grants DE-FG02-06ER64238 and DE-FG02-08ER64590, and a David and Lucile Packard Foundation fellowship (A.V.F.), NSF grant OCE-0623487 (T.D.H.), and a Flint Fellowship at Yale University (Z.L.).

Supporting Online Material

www.sciencemag.org/cgi/content/full/1167625/DC1
SOM Text
Figs. S1 to S3
Tables S1 to S3
References

24 October 2008; accepted 9 February 2009
Published online 26 February 2009;
10.1126/science.1167625
Include this information when citing this paper.

Structure of P-Glycoprotein Reveals a Molecular Basis for Poly-Specific Drug Binding

Stephen G. Aller,[1] Jodie Yu,[1] Andrew Ward,[2] Yue Weng,[1,4] Srinivas Chittaboina,[1] Rupeng Zhuo,[3] Patina M. Harrell,[3] Yenphuong T. Trinh,[3] Qinghai Zhang,[1] Ina L. Urbatsch,[3] Geoffrey Chang[1]†

P-glycoprotein (P-gp) detoxifies cells by exporting hundreds of chemically unrelated toxins but has been implicated in multidrug resistance (MDR) in the treatment of cancers. Substrate promiscuity is a hallmark of P-gp activity, thus a structural description of poly-specific drug-binding is important for the rational design of anticancer drugs and MDR inhibitors. The x-ray structure of apo P-gp at 3.8 angstroms reveals an internal cavity of ~6000 angstroms cubed with a 30 angstrom separation of the two nucleotide-binding domains. Two additional P-gp structures with cyclic peptide inhibitors demonstrate distinct drug-binding sites in the internal cavity capable of stereoselectivity that is based on hydrophobic and aromatic interactions. Apo and drug-bound P-gp structures have portals open to the cytoplasm and the inner leaflet of the lipid bilayer for drug entry. The inward-facing conformation represents an initial stage of the transport cycle that is competent for drug binding.

The American Cancer Society reported over 12 million new cancer cases and 7.6 million cancer deaths worldwide in 2007 (*1*). Many cancers fail to respond to chemotherapy by acquiring MDR, to which has been attributed the failure of treatment in over 90% of patients with metastatic cancer (*2*). Although MDR can have several causes, one major form of resistance to chemotherapy has been correlated with the presence of at least three molecular "pumps" that actively transport drugs out of the cell (*3*). The most prevalent of these MDR transporters is P-gp, a member of the adenosine triphosphate (ATP)–binding cassette (ABC) superfamily (*4*). P-gp has unusually broad poly-specificity, recognizing hundreds of compounds as small as 330 daltons up to 4000 daltons (*5*, *6*). Most P-gp substrates are hydrophobic and partition into the lipid bilayer (*7*, *8*). Thus, P-gp has been likened to a molecular "hydrophobic vacuum cleaner" (*9*), pulling substrates from the membrane and expelling them to promote MDR.

Although the structures of bacterial ABC importers and exporters have been established (*10*–*15*) and P-gp has been characterized at low resolution by electron microscopy (*16*, *17*), obtaining an x-ray structure of P-gp is of particular interest because of its clinical relevance. We describe the structure of mouse P-gp (ABCB1), which has 87% sequence identity to human P-gp (fig. S1), in a drug-binding–competent state (*18*, *19*). We also determined cocrystal structures of P-gp in complex with two stereoisomers of cyclic hexapeptide inhibitors, cyclic-*tris*-(*R*)-valineselenazole (QZ59-RRR) and cyclic-*tris*-(*S*)-valineselenazole (QZ59-SSS), revealing a molecular basis for poly-specificity.

Mouse P-gp protein exhibited typical basal adenosine triphosphatase (ATPase) activity that was stimulated by drugs like verapamil and colchicine (fig. S2A) (*20*). P-gp recovered from washed crystals retained near-full ATPase activity (fig. S3). Both QZ59 compounds inhibited the verapamil-stimulated ATPase activity in a concentration-dependent manner (fig. S2B). Both stereoisomers inhibited calcein-AM export with median inhibitory concentration (IC_{50}) values in the low micromolar range (fig. S4) and increasing doses of QZ59 compounds resulted in greater colchicine sensitivity in P-gp–overexpressing cells (fig. S5).

The structure of P-gp (Fig. 1) represents a nucleotide-free inward-facing conformation arranged as two "halves" with pseudo two-fold molecular symmetry spanning ~136 Å perpendicular to and ~70 Å in the plane of the bilayer. The nucleotide-binding domains (NBDs) are separated by ~30 Å. The inward-facing conformation, formed from two bundles of six transmembrane helices (TMs 1 to 3, 6, 10, 11 and TMs 4, 5, 7 to 9, 12), results in a large internal cavity open to both the cytoplasm and the inner leaflet. The model was obtained as described in (*18*) by using experimental electron density maps (figs. S6 and S7 and table S1), verified by multiple $F_{obs} - F_{calc}$ maps (figs. S8 to S10), with the topology confirmed by (2-hydroxy-5-nitrophenyl)mercury(II) chloride (CMNP)–labeled cysteines (figs. S6, B to D; S7C, and S11, and table S2). Two portals (fig. S12) allow access for entry of hydrophobic molecules directly from the membrane. The portals are formed by TMs 4 and 6 and TMs 10 and 12, each of which have smaller side chains that could allow tight packing during NBD dimeriza-

[1]Department of Molecular Biology, The Scripps Research Institute, 10550 North Torrey Pines Road, CB105, La Jolla, CA 92037, USA. [2]Department of Cell Biology, The Scripps Research Institute, 10550 North Torrey Pines Road, CB105, La Jolla, CA 92037, USA. [3]Cell Biology and Biochemistry, Texas Tech University Health Sciences Center, 3601 4th Street, Lubbock, TX 79430, USA. [4]College of Chemistry and Molecular Sciences, Wuhan University, Wuhan, 430072 P. R. China.

†To whom correspondence should be addressed. E-mail: gchang@scripps.edu

tion (table S3). At the widest point within the bilayer, the portals are ~9 Å wide, and each is formed by an intertwined interface in which TMs 4 and 5 (and 10 and 11) crossover to make extensive contacts with the opposite α-helical bundle (Fig. 1). Each intertwined interface buries ~6900 $Å^2$ to stabilize the dimer interface and is a conserved motif in bacterial exporters (*13*, *14*). The structure is consistent with previous cross-linking studies that identified residue pairs in the intertwined interface (fig. S13). The volume of the internal cavity within the lipid bilayer is substantial (~6000 $Å^3$) and could accommodate at least two compounds simultaneously (*21*). The presumptive drug-binding pocket is made up of mostly hydrophobic and aromatic residues (table S3). Of the 73 solvent accessible residues in the internal cavity, 15 are polar and only two (His^{60} and Glu^{871}), located in the N-terminal half of the TMD, are charged or potentially charged. In this crystal form, two P-gp molecules (PGP1 and PGP2) are in the asymmetric unit and are structurally similar, with the only appreciable differences localized in the NBDs and the four short intracellular helices (IHs 1 to 4) that directly contact the NBDs (fig. S14).

P-gp can distinguish between the stereoisomers of cyclic peptides (Fig. 2, A and B), which result in different binding locations, orientation, and stoichiometry. QZ59-RRR (Fig. 2A) binds one site per transporter located at the center of the molecule between TM6 and TM12 (Fig. 2, C and E). The binding of QZ59-RRR to the "middle" site is mediated by mostly hydrophobic residues on TMs 1, 5, 6, 7, 11, and 12 (table S3). QZ59-SSS (Fig. 2B) binds two sites per P-gp molecule (Fig. 2, D and F). The QZ59-SSS molecule occupying the "upper" site is surrounded by hydrophobic aromatic residues on TMs 1, 2, 6, 7, 11, and 12 (table S3) and a portion of this ligand is disordered in both PGP1 and PGP2 (fig. S15). The ligand in the "lower" site that binds to the C-terminal half of the TMD is in close proximity to TMs 1, 5, 6, 7, 8, 9, 11, and 12 and surrounded by three polar residues (Gln^{721}, Gln^{986}, and Ser^{989}).

The cocrystal structures of P-gp with QZ59 compounds demonstrate that the inward-facing conformation is competent to bind drugs. Previ-

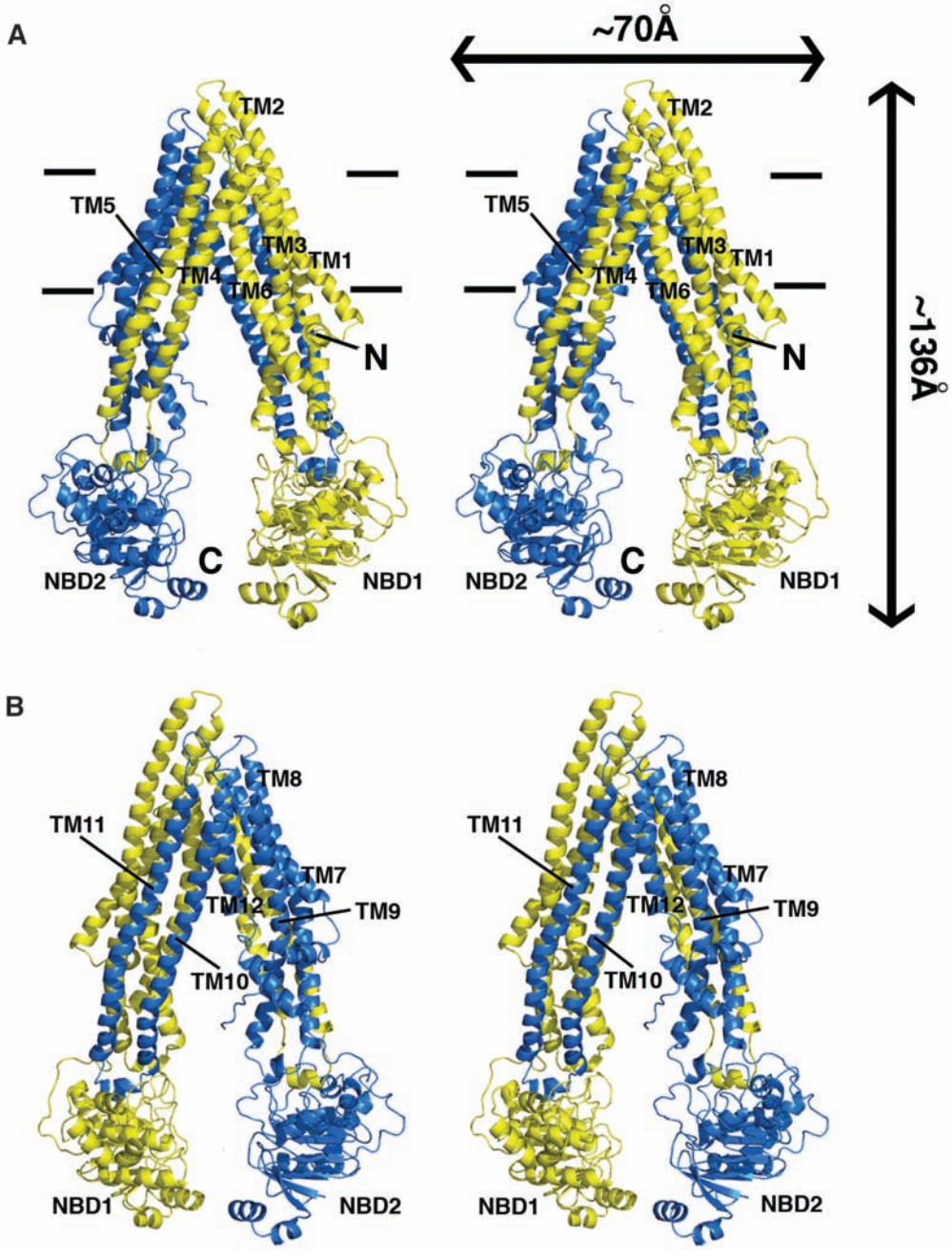

Fig. 1. Structure of P-gp. (**A**) Front and (**B**) back stereo views of PGP. TMs 1 to 12 are labeled. The N- and C-terminal half of the molecule is colored yellow and blue, respectively. TMs 4 and 5 and TMs 10 and 11 crossover to form intertwined interfaces that stabilize the inward-facing conformation. Horizontal bars represent the approximate positioning of the lipid bilayer. The N- and C-termini are labeled in (A). TM domains and NBDs are also labeled.

ous studies have identified residues that interact with verapamil (fig. S1) (*22*, *23*). Many of these residues face the drug-binding pocket (Fig. 3A and figs. S15 and S16, and table S3) and are highly conserved (fig. S1), which suggests a common mechanism of poly-specific drug recognition. For QZ59-RRR and both QZ59-SSS molecules, the isopropyl groups point in the same direction, toward TMs 9 to 12 (Fig. 3A). Although certain residues in P-gp contact both QZ59 compounds, the specific functional roles of the residues binding each inhibitor are different (fig. S17). For example, F332 contacts the molecules in the upper but not lower sites of QZ59-SSS but does contact the inhibitor in the middle (QZ59-RRR) site (fig. S17, C and J). F724 is near both the middle (fig. S17E) and lower (fig. S17M) sites, but is much closer to a selenium atom in QZ59-SSS. V978 plays an important role having close proximity to all three QZ59 sites (fig. S17, H and N). Note that both F724 (human F728) and V978 (human V982) are protected from methanethiosulfonate-verapamil (MTS-verapamil) labeling by verapamil (*22*, *23*) (Fig. 3B and figs. S1 and S18), which indicates that both are important for drug binding. Although the upper half of the drug-binding pocket contains predominantly hydrophobic and aromatic residues, the lower half of the chamber has more polar and charged residues (fig. S19). Hydrophobic substrates that are positively charged may bind using these residues similarly to the poly-specific drug-binding pockets of QacR and EmrE that use residues like glutamate to neutralize different drugs (*24*, *25*).

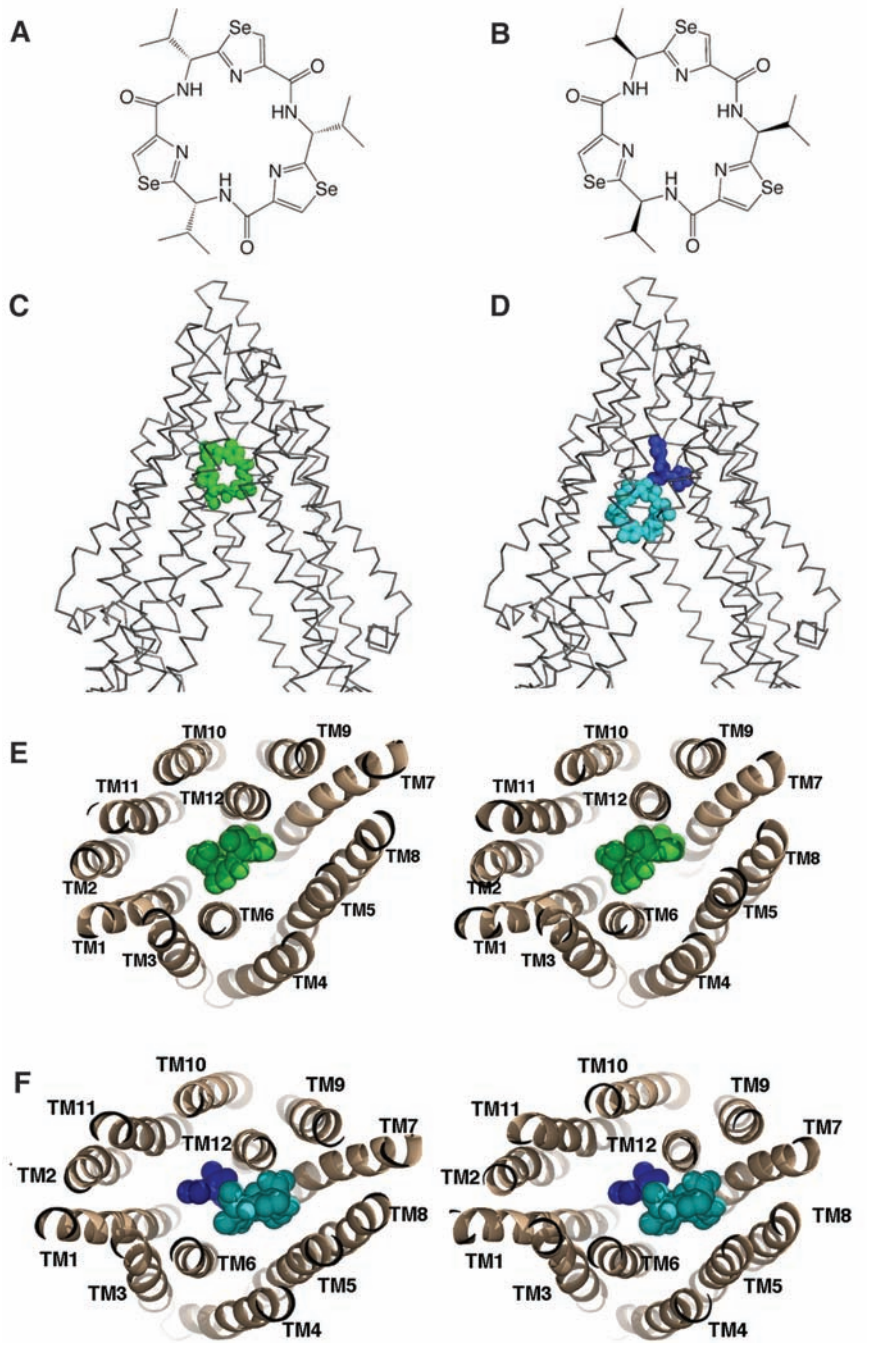

Fig. 2. Binding of novel cyclic peptide P-gp inhibitors. Chemical structures of (**A**) QZ59-RRR and (**B**) QZ59-SSS. (**C**) Location of one QZ59-RRR (green spheres) and (**D**) two QZ59-SSS (blue and cyan spheres) molecules in the P-gp internal cavity. (**E** and **F**) Stereo images showing interaction of transmembrane helices with QZ59 compounds viewed from the intracellular side of the protein looking into the internal chamber. In both cases, the compound(s) are sandwiched between previously identified drug-binding TMs 6 and 12. The location of the QZ59 compounds was verified by anomalous Fourier (fig. S15, B and C) and $F_{obs} - F_{calc}$ maps (figs. S15, D and E; S16; and S17).

The drug-binding pocket of P-gp is nearly six times as large as that of BmrR (YvcC) and hPXR and differs significantly from AcrB, wherein drug binding is mediated by residues from β sheets on the extracellular side of the inner cell membrane (*26*–*28*). For P-gp, along with the permeases from the three H^+ drug antiporter families (MATE, SMR, and MFS), the drug–binding site resides in the cell membrane and is formed by TM helices. Extraction of drug directly from the cytoplasm–lipid bilayer is a common theme (*29*). In fact, most P-gp substrates readily partition into the plasma membrane, and lipids are required for drug-stimulated ATPase activity (*30*). P-gp is a unidirectional lipid flippase (*4*), transporting phospholipids from the inner to outer leaflets of the bilayer (*31*). The inward-facing conformation of P-gp (Fig. 1) provides access to an internal chamber through two portals (fig. S12) that are open wide enough to accommodate hydrophobic molecules and phospholipids. The portals form a contiguous space spanning the width of the molecule that allow P-gp to "scan" the inner leaflet to select and bind specific lipids and hydrophobic drugs before transport (Fig. 4). Lipids and substrates may remain together during initial entry into the internal cavity and could explain their requirement in promoting ATPase activity.

To accommodate its largest substrates, P-gp may sample even wider conformations in the cell membrane than observed in this crystal form. We were able to soak small hydrophobic heavy-metal compounds [ethyl-mercury(II) chloride, 255 daltons, and tetramethyl-lead, 267 daltons] directly into preformed native P-gp crystals, but not QZ59 compounds (660 daltons) (fig. S20). Cocrystals of P-gp with QZ59-RRR and -SSS were only obtained by preincubating these compounds with detergent-solubilized P-gp before crystallization. Taken together, we propose that P-gp samples widely open conformations both in detergent-solution and within the membrane to bind larger molecules. Consistent with this hypothesis, a very wide open inward-facing crystal structure of the bacterial homolog of P-gp, MsbA, was previously determined and could accommodate its large substrate, Kdo_2-lipid A (M_r 2.3 kD)

(*14*). This large degree of flexibility is also supported by data from electron paramagnetic resonance spectroscopy of MsbA in the lipid membrane (*32*), as well as the inward-facing conformation of other ABC transporters that also have NBDs far apart (*33*, *34*).

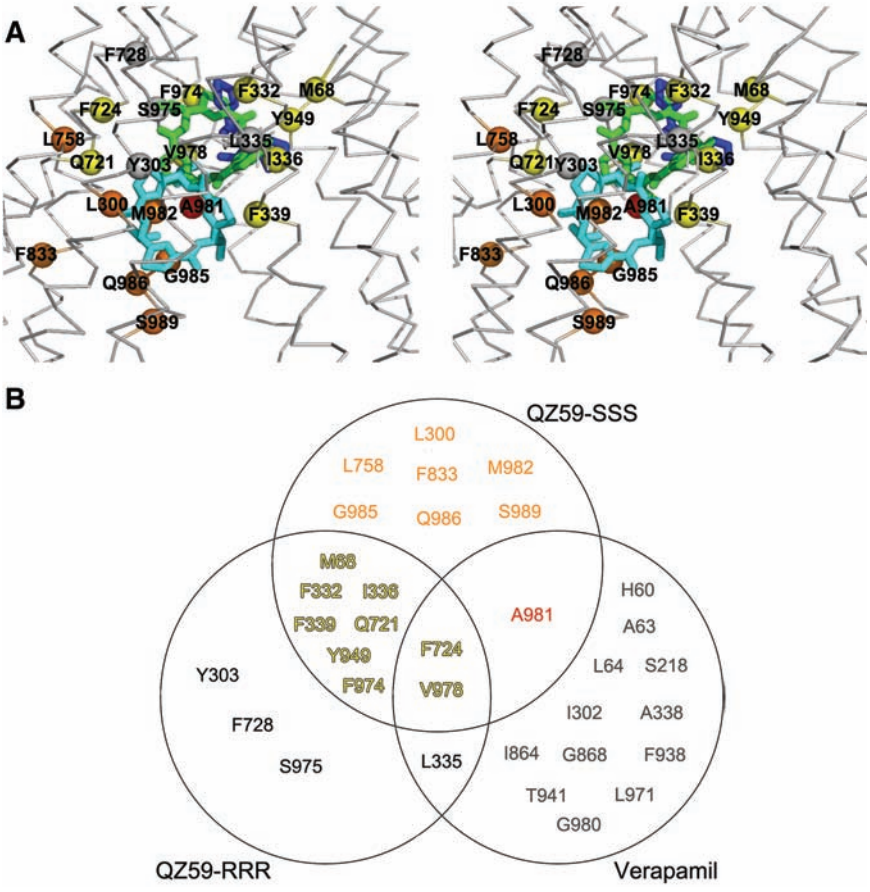

Fig. 3. Drug-binding residues of P-gp. (**A**) Stereo view of the drug-binding cavity. Cα trace shown in gray. The QZ59-SSS in the lower (cyan) and upper (blue), as well as QZ59-RRR occupying the middle site (green) are superimposed. Residues within ~4 to 5 Å of QZ59 compounds are shown as spheres. Spheres colored orange and red represent residues that only contact QZ59-SSS in the lower and upper site, respectively. Residues in common between QZ59-RRR and QZ59-SSS sites are yellow. Four residues (gray spheres) are close to QZ59-RRR but neither QZ59-SSS molecules. (**B**) Venn diagram of residues in close proximity to QZ59 molecules and residues that are protected from MTS labeling by verapamil binding (fig. S1) (*22*, *23*). Only residues in contact with the model for QZ59-SSS are displayed. Residues that interact only with verapamil are omitted from (A) for clarity and are shown in fig. S16.

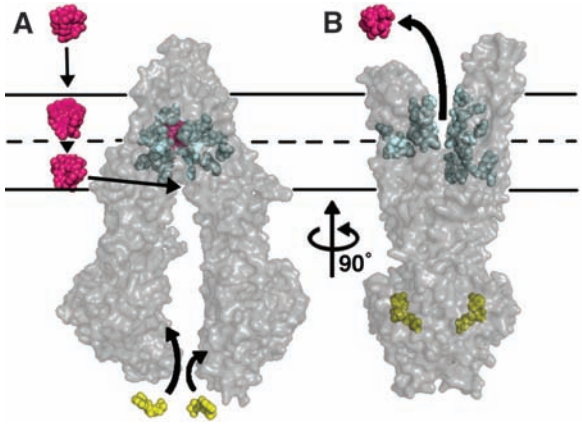

Fig. 4. Model of substrate transport by P-gp. (**A**) Substrate (magenta) partitions into the bilayer from outside of the cell to the inner leaflet and enters the internal drug-binding pocket through an open portal. The residues in the drug-binding pocket (cyan spheres) interact with QZ59 compounds and verapamil in the inward-facing conformation. (**B**) ATP (yellow) binds to the NBDs causing a large conformational change presenting the substrate and drug-binding site(s) to the outer leaflet and/or extracellular space. In this model of P-gp, which is based on the outward-facing conformation of MsbA and Sav1866 (*13*, *14*), exit of the substrate to the inner leaflet is sterically occluded, which provides unidirectional transport to the outside.

The inward-facing structure does not allow substrate access from the outer membrane leaflet nor the extracellular space (Fig. 4A). We propose that this conformation represents the molecule in a pretransport state, because we demonstrate drug binding to an internal cavity open to the inner leaflet and cytoplasm. This conformation likely represents an active state of P-gp because protein recovered from crystals had significant drug-stimulated ATPase activity. During the catalytic cycle, binding of ATP, stimulated by substrate, likely causes a dimerization in the NBDs, which produces large structural changes resulting in an outward-facing conformation similar to the nucleotide-bound structures of MsbA or Sav1866 (Fig. 4B). Depending on the specific compound, substrates could either be released as a consequence of decreased binding affinity caused by changes in specific residue contacts between the protein and drug going from the inward- to outward-facing conformation or, alternatively, facilitated by ATP hydrolysis. In either case, ATP hydrolysis likely disrupts NBD dimerization and resets the system back to inward facing and reinitiates the transport cycle (*35*) (Fig. 4).

References and Notes

1. Global Cancer Facts and Figures (The American Cancer Society Homepage, 2007); www.cancer.org/downloads/STT/Global_Cancer_Facts_and_Figures_2007_rev.pdf.
2. D. B. Longley, P. G. Johnston, *J. Pathol.* **205**, 275 (2005).
3. G. Szakacs, J. K. Paterson, J. A. Ludwig, C. Booth-Genthe, M. M. Gottesman, *Nat. Rev. Drug Discov.* **5**, 219 (2006).
4. F. J. Sharom, *Pharmacogenomics* **9**, 105 (2008).
5. M. Ramachandra *et al.*, *Biochemistry* **37**, 5010 (1998).
6. F. C. Lam *et al.*, *J. Neurochem.* **76**, 1121 (2001).
7. M. M. Gottesman, I. Pastan, *Annu. Rev. Biochem.* **62**, 385 (1993).
8. E. Gatlik-Landwojtowicz, P. Aanismaa, A. Seelig, *Biochemistry* **45**, 3020 (2006).
9. Y. Raviv, H. B. Pollard, E. P. Bruggemann, I. Pastan, M. M. Gottesman, *J. Biol. Chem.* **265**, 3975 (1990).
10. K. P. Locher, A. T. Lee, D. C. Rees, *Science* **296**, 1091 (2002).
11. K. Hollenstein, D. C. Frei, K. P. Locher, *Nature* **446**, 213 (2007).
12. H. W. Pinkett, A. T. Lee, P. Lum, K. P. Locher, D. C. Rees, *Science* **315**, 373 (2007).
13. R. J. P. Dawson, K. P. Locher, *Nature* **443**, 180 (2006).
14. A. Ward, C. L. Reyes, J. Yu, C. B. Roth, G. Chang, *Proc. Natl. Acad. Sci. U.S.A.* **104**, 19005 (2007).
15. M. L. Oldham, D. Khare, F. A. Quiocho, A. L. Davidson, J. Chen, *Nature* **450**, 515 (2007).
16. M. F. Rosenberg, A. B. Kamis, R. Callaghan, C. F. Higgins, R. C. Ford, *J. Biol. Chem.* **278**, 8294 (2003).
17. J.-Y. Lee, I. L. Urbatsch, A. E. Senior, S. Wilkens, *J. Biol. Chem.* **283**, 5769 (2008).
18. Materials and methods are available as supporting material on *Science* Online.
19. Single-letter abbreviations for the amino acid residues are as follows: A, Ala; C, Cys; D, Asp; E, Glu; F, Phe; G, Gly; H, His; I, Ile; K, Lys; L, Leu; M, Met; N, Asn; P, Pro; Q, Gln; R, Arg; S, Ser; T, Thr; V, Val; W, Trp; and Y, Tyr.
20. N. Lerner-Marmarosh, K. Gimi, I. L. Urbatsch, P. Gros, A. E. Senior, *J. Biol. Chem.* **274**, 34711 (1999).
21. T. W. Loo, M. C. Bartlett, D. M. Clarke, *J. Biol. Chem.* **278**, 39706 (2003).
22. T. W. Loo, D. M. Clarke, *J. Biol. Chem.* **272**, 31945 (1997).
23. T. W. Loo, M. C. Bartlett, D. M. Clarke, *Biochem. J.* **399**, 351 (2006).

24. M. A. Schumacher, R. G. Brennan, *Mol. Microbiol.* **45**, 885 (2002).
25. Y.-J. Chen *et al.*, *Proc. Natl. Acad. Sci. U.S.A.* **104**, 18999 (2007).
26. E. E. Zheleznova, P. N. Markham, A. A. Neyfakh, R. G. Brennan, *Cell* **96**, 353 (1999).
27. R. E. Watkins *et al.*, *Science* **292**, 2329 (2001).
28. S. Murakami, R. Nakashima, E. Yamashita, A. Yamaguchi, *Nature* **419**, 587 (2002).
29. A. B. Shapiro, V. Ling, *Eur. J. Biochem.* **250**, 122 (1997).
30. R. Callaghan, G. Berridge, D. R. Ferry, C. F. Higgins, *Biochim. Biophys. Acta* **1328**, 109 (1997).
31. I. Bosch, K. Dunussi-Joannopoulos, R. L. Wu, S. T. Furlong, J. Croop, *Biochemistry* **36**, 5685 (1997).
32. J. Dong, G. Yang, H. S. McHaourab, *Science* **308**, 1023 (2005).
33. M. Chami *et al.*, *J. Mol. Biol.* **315**, 1075 (2002).
34. M. Hofacker *et al.*, *J. Biol. Chem.* **282**, 3951 (2007).
35. G. Tombline, A. Muharemagi, L. B. White, A. E. Senior, *Biochemistry* **44**, 12879 (2005).
36. We thank D. C. Rees, I. Wilson, R. H. Spencer, M. B. Stowell, A. Senior, A. Frost, V. M. Unger, C. D. Stout, and P. Wright. Y. Weng was supported by a scholarship from P. R. China. We thank Stanford Synchrotron Radiation Lightsource, Advanced Light Source, and Advanced Photon Source. This work was supported by grants from the Army (W81XWH-05-1-0316), NIH (GM61905, GM078914, and GM073197), the Beckman Foundation, the Skaggs Chemical Biology Foundation, Jasper L. and Jack Denton Wilson Foundation, the Southwest Cancer and Treatment Center, and the Norton B. Gilula Fellowship. Coordinates and structure factors deposited to the Protein DataBank (PDB accession codes 3G5U, 3G60, and 3G61).

Supporting Online Material

www.sciencemag.org/cgi/content/full/323/5922/1718/DC1
Materials and Methods
Figs. S1 to S20
Tables S1 to S3
References

19 November 2008; accepted 17 February 2009
10.1126/science.1168750

CD24 and Siglec-10 Selectively Repress Tissue Damage–Induced Immune Responses

Guo-Yun Chen,[1] Jie Tang,[4] Pan Zheng,[1,2]* Yang Liu[1,3]*

Patten recognition receptors, which recognize pathogens or components of injured cells (danger), trigger activation of the innate immune system. Whether and how the host distinguishes between danger- versus pathogen-associated molecular patterns remains unresolved. We report that CD24-deficient mice exhibit increased susceptibility to danger- but not pathogen-associated molecular patterns. CD24 associates with high mobility group box 1, heat shock protein 70, and heat shock protein 90; negatively regulates their stimulatory activity; and inhibits nuclear factor κB (NF-κB) activation. This occurs at least in part through CD24 association with Siglec-10 in humans or Siglec-G in mice. Our results reveal that the CD24–Siglec G pathway protects the host against a lethal response to pathological cell death and discriminates danger- versus pathogen-associated molecular patterns.

Pathogen-associated molecular patterns (PAMPs) interact with Toll-like receptors (TLRs) on innate immune cells to initiate protective immune responses (*1*–*3*). Danger-associated molecular patterns (DAMPs) (*4*), which are intracellular components such as high mobility group box 1 (HMGB1), heat shock protein 70 (HSP70), heat shock protein 90 (HSP90), and cellular RNA released during cellular injury, also induce TLR-dependent inflammatory responses (*5*–*8*). Whether the host is able to discriminate between DAMPs and PAMPs is not clear.

We used an acetaminophen (AAP)-induced liver necrosis model (*9*) to identify genes that regulate the innate immune response resulting from tissue injury. A sublethal dose of AAP (10 mg/mouse), which is tolerated by wild-type (WT) mice, caused rapid death of *CD24*-deficient ($CD24^{-/-}$) mice within 20 hours (Fig. 1A). We then tested whether CD24 regulated the inflammatory response to AAP-induced liver injury because CD24 is expressed on liver oval cells and hematopoeitic cells, but not on hepatocytes (*10*). Indeed, we detected a massive increase in the inflammatory cytokines interleukin-6 (IL-6), monocyte chemotactic protein–1 (MCP-1), and tumor necrosis factor–α (TNF-α) after AAP treatment (Fig. 1B). This was accompanied by increased amounts of serum alanine transaminase (ALT), which is indicative of liver damage (Fig. 1C), and liver hemorrhage and necrosis (Fig. 1D). These observations revealed that CD24 protects against AAP-induced hepatoxicity, most likely by regulating the inflammatory response.

CD24 is a small glycosylphosphoinositol-anchored protein that is able to provide costimulatory signals to T cells and has been implicated in the development of autoimmune disease (*11*–*15*). We set out to identify proteins that associate with CD24 because none of the known CD24 ligands provided insight into its protective effect in our liver injury model. We focused on proteins whose interactions can be disrupted by the cation chelator EDTA, because more than 90% of the mass of CD24 is estimated to be derived from glycosylation (*12*) and because protein-polysaccharide interactions largely depend on cations. Briefly, we immunoprecipitated CD24 and its associated proteins from lysates of mouse splenocytes. The proteins eluted by EDTA were subjected to high-throughput mass spectrometry analysis and SDS–polyacrylamide gel electrophoresis (PAGE). HMGB1, a prototypical DAMP molecule that activates the immune response following tissue damage (*16*), was among the most prominent proteins that we identified (Fig. 2A and table S1). HMGB1 coimmunoprecipitated with CD24 and this interaction was specific (Fig. 2B and C). A recombinant CD24-Fc fusion protein specifically coimmunoprecipitated recombinant HMGB1, demonstrating that the interaction between CD24 and HMGB1 was direct (Fig. 2D).

To determine whether the hypersensitivity to AAP observed in $CD24^{-/-}$ mice was the result of an enhanced immune response to HMGB1, we injected AAP-treated mice with antibodies to HMGB1 (fig. S1). In one representative experiment, blockade of HMGB1 rescued 87.5% of the mice that received AAP (Fig. 2E). Treated mice exhibited decreased ALT abundance, indicating reduced hepatocyte destruction (Fig. 2F). The production of IL-6, MCP-1, and TNF-α was also greatly reduced (Fig. 2G). Thus, CD24 protects against AAP-induced lethal hepatoxicity by dampening the immune response against HMGB1.

HMGB1 can be divided into two domains: an inhibitory A box and a stimulatory B box (*17*). To determine whether CD24 inhibits HMGB1 by binding to the inhibitory A box, we produced deletion mutants lacking either the A box or the B box. CD24-Fc immunoprecipitated full-length HMGB1 and the box B–containing mutant, but not the box A–containing mutant (fig. S2). Thus, inhibition of HMGB1 by CD24 does not require direct interaction with box A.

CD24 has no known mechanism for signal transduction. To understand how CD24 negatively regulates HMGB1, we searched for a potential CD24 receptor that may transduce signals downstream of CD24. We were particularly interested in sialic acid–binding immunoglobulin (Ig)-like lectins (Siglecs), which are cell surface receptors of the immunoglobulin superfamily that recognize sialic acid–containing proteins (*18*). Siglecs are primarily expressed by cells of hematopoietic origin (*18*). Most Siglecs are considered to be negative regulators of the immune system because they contain one or more cytosolic immune receptor tyrosine-based inhibitory motifs (ITIMs) (*18*). To determine whether CD24 interacts with Siglecs, we incubated splenocytes on plates coated with the recombinant extracellular domains of ITIM-containing Siglec-5, -7, -10 or -11. Siglec-10, but not Siglecs -5, -7, or -11, bound to CD24 (Fig. 3A). Flow cytometric analysis indicated that

[1]Division of Immunotherapy, Department of Surgery, University of Michigan School of Medicine, Ann Arbor, MI 48109, USA. [2]Department of Pathology, University of Michigan School of Medicine, Ann Arbor, MI 48109, USA. [3]Department of Internal Medicine, University of Michigan School of Medicine, Ann Arbor, MI 48109, USA. [4]Institute of Biophysics, Chinese Academy of Science, Beijing, China.

*To whom correspondence should be addressed. E-mail: yangl@umich.edu (Y.L.), panz@umich.edu (P.Z.)

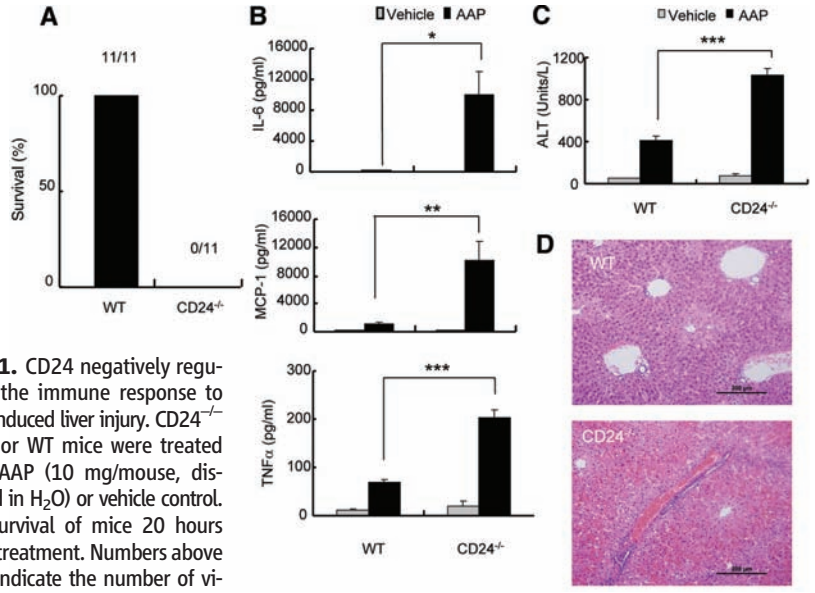

Fig. 1. CD24 negatively regulates the immune response to AAP-induced liver injury. $CD24^{-/-}$ mice or WT mice were treated with AAP (10 mg/mouse, dissolved in H_2O) or vehicle control. (**A**) Survival of mice 20 hours after treatment. Numbers above bars indicate the number of viable mice out of the total number of mice used per group. All WT mice remained healthy. (**B**) Serum concentrations of IL-6, MCP-1, and TNF-α at 6 hours after AAP injection (mean ± SD, $n = 5$; $^{*}P < 0.02$, $^{**}P < 0.009$; $^{***}P < 0.002$, Student's t test) . (**C**) ALT concentrations measured at 6 hours after treatment (mean ± SD, $n = 5$; $^{***}P < 0.00004$, Student's t test). Data shown in (B) and (C) were repeated two times. (**D**) Livers were isolated at 9 hours after treatment. Representative images (magnification, ×20) of hematoxylin and eosin (H&E) staining are shown ($n = 3$).

CD24 is the primary receptor for Siglec-10 because WT but not $CD24^{-/-}$ splenocytes showed detectable binding to soluble Siglec-10-Fc (Fig. 3B). Furthermore, in COS cells, FLAG-tagged Siglec-10 coimmunoprecipitated with CD24-Fc, whereas the inactivating R119A mutation (in which Arg^{119} is replaced with Ala) of Siglec-10 (analogous to the R97A in sialoadhesin (*19*)) abrogated the interaction (Fig. 3C).

We hypothesized that CD24, Siglec-10, and HMGB1 might form a trimolecular complex because CD24 can interact with both HMGB1 and Siglec-10. Indeed, Siglec-10-Fc was able to immunoprecipitate HMGB1 from lysates of WT but not $CD24^{-/-}$ splenocytes (Fig. 3D), indicating that their interaction was strictly dependent on CD24 expression.

The likely murine homolog of Siglec-10 is Siglec-G (*18*). We prepared antibodies to Siglec-G by immunizing $Siglecg^{-/-}$ mice (*20*) with WT spleen cells (fig. S3). With the use of this antisera, Siglec-G coimmunoprecipitated CD24 (Fig. 3E). CD24-Fc showed stronger binding to WT splenocytes in comparison to $Siglecg^{-/-}$ splenocytes, indicating that Siglec-G contributed to CD24-Fc binding; however, consistent with previous reports of multiple CD24 receptors (*12*), Siglec-G deficiency did not abrogate CD24-Fc splenocyte binding (fig. S4). We next determined if the absence of Siglec-G would also convey hypersensitivity to AAP. Indeed, only 25% of $Siglecg^{-/-}$ mice

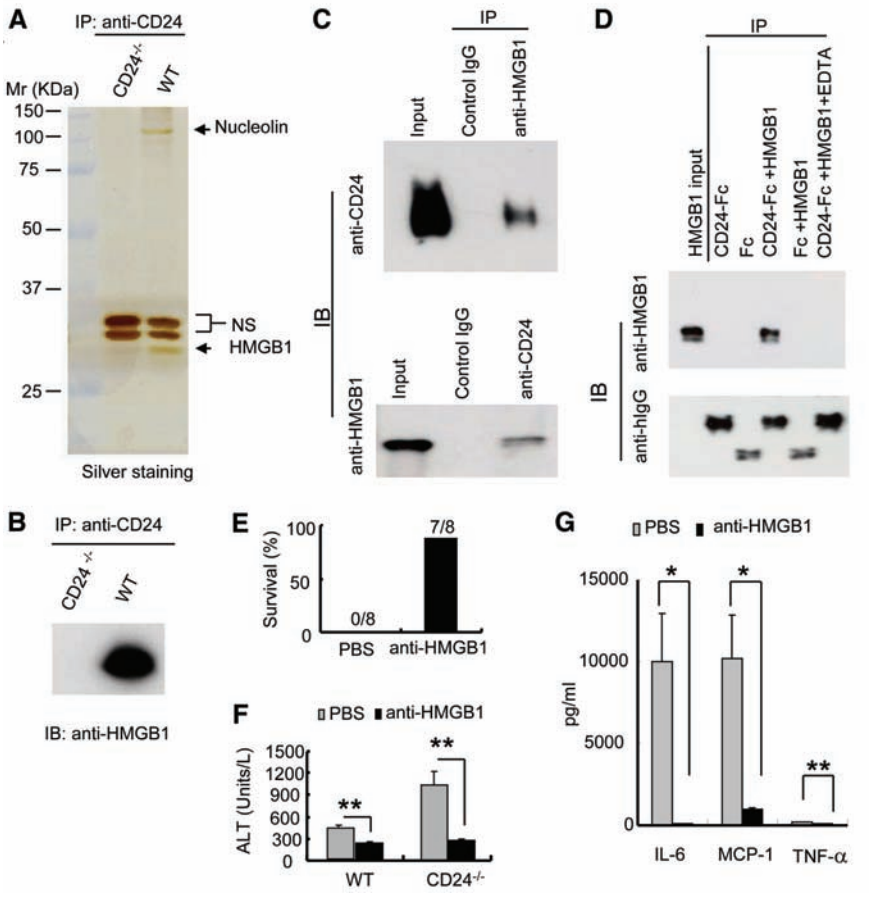

Fig. 2. CD24 associates with, and negatively regulates, the immune response to HMGB1. (**A**) Identification of CD24-associated proteins by coimmunoprecipitation. Silver staining of the SDS-PAGE gel is shown. Arrows indicate the positions of HMGB1 and nucleolin, two abundant CD24-associated DAMP molecules. NS: proteins that coimmunoprecipitated with anti-CD24 nonspecifically. (**B**) Confirmation of CD24-HMGB1 association by Western blot of EDTA-disassociated proteins. (**C**) Reciprocal immunoprecipitations of CD24 and HMGB1 were performed with splenocyte lysates isolated from WT mice. (**D**) Direct, cation-dependent interaction between CD24 and HMGB1. Coimmunoprecipitation of recombinant HMGB1 protein with CD24-Fc fusion protein or control IgG-Fc. The requirement for cations was confirmed by disruption of the complex with EDTA. This experiment was repeated three times. (**E**) Mice received intravenous injections with either vehicle (phosphate-buffered saline) or mouse HMGB1 monoclonal antibody (mAb) (clone 3B1, 150 μg/mouse) 30 min before intraperitoneal (ip) injection of AAP. Composite data from two independent experiments are shown ($n = 8$). (**F**) Serum ALT at 6 hours after treatment with AAP- and HMGB1-specific antibodies (mean ± SD, $n = 5$, $^{**}P < 0.005$). (**G**) Serum cytokine concentrations at 6 hours after treatment with AAP- and HMGB1-specific antibodies (mean ± SD, $n = 5$, $^{*}P$, 0.03, $^{**}P < 0.004$). Samples in (F) and (G) represent two independent experiments; the statistical significance was determined by Student's t test.

survived a sublethal dose of AAP (Fig. 3F). The enhanced susceptibility was accompanied by increased release of ALT (Fig. 3G), liver necrosis, and hemorrhage (Fig. 3H), as well as increased amounts of inflammatory cytokines in the blood (Fig. 3I). To test whether the enhanced liver toxicity was mediated by HMGB1, we treated *Siglecg*$^{-/-}$ mice with antibodies to HMGB1. Inhibition of HMGB1 prevented mortality in 90% of AAP-treated *Siglecg*$^{-/-}$ mice (Fig. 3J). Serum ALT and inflammatory cytokines were also largely diminished (Fig. 3, K and L).

CD24 and Siglec-10 are unlikely to function by acting directly on hepatocytes because they are not expressed by these cells (*10*, *18*). Dendritic cells (DCs), however, respond to HMGB1 (*21*) and express both CD24 (*22*) and Siglec-G (*20*). To test whether DCs can respond to HMGB1, we cultured bone marrow–derived DCs isolated from WT, *CD24*$^{-/-}$, or *Siglecg*$^{-/-}$ mice and stimulated them with HMGB1 or the TLR ligands lipopolysaccharide (LPS) or poly(I:C). HMGB1 stimulation resulted in significantly greater production of IL-6 and TNF-α by *CD24*$^{-/-}$ or *Siglecg*$^{-/-}$ DCs than by WT DCs (Fig. 4A). In contrast, CD24 or Siglec-G deficiency did not affect the production of inflammatory cytokines by DCs in response to LPS or poly(I:C) (Fig. 4A).

Siglec-10 associates with the tyrosine phosphatase SHP-1, a known negative regulator of nuclear factor κB (NF-κB) activation (*23*). In a subpopulation of B cells that reside in the peritoneum (*20*), the absence of Siglec-G results in the constitutive activation of NF-κB. To test whether activation of NF-κB by HMGB1 or LPS is affected by the absence of CD24 or Siglec-G, we assayed the nuclear translocation of the NF-κB subunit p65 in WT, *CD24*$^{-/-}$, and *Siglecg*$^{-/-}$ DCs. Both LPS and, to a much lesser extent, HMGB1, induced nuclear translocation of p65 in WT DCs; however, in *CD24* or *Siglecg*-deficient DCs, HMGB1 caused even greater increases in nuclear translocation of p65 than did LPS (Fig. 4B). These data suggest that the CD24-Siglec-G pathway may serve to decrease the host response to DAMPs, such as HMGB1, but not to TLR ligands of microbial origin (PAMPs), by selective repression of NF-κB.

To substantiate this hypothesis, we administered a lethal dose of LPS to WT, *CD24*$^{-/-}$, or *Siglecg*$^{-/-}$ mice. Neither the absence of Siglec-G nor the absence of CD24 affected the kinetics of LPS-induced lethality (Fig. 4C) or production of inflammatory cytokines (Fig. 4D). Despite an established contribution of HMGB1 to the late stage of sepsis (*24*), potential amplification of HMGB1 signaling by mutation of *CD24* or *Siglecg* did not affect host survival in response to LPS. Therefore, CD24 and Siglec-G are selective modulators of the host response to HMGB1, but not to TLR ligands such as LPS, despite their potential to induce release of HMGB1 (*24*, *25*).

In addition to nuclear DAMPs, such as HMGB1, DCs also respond to cytoplasmic DAMPs such as

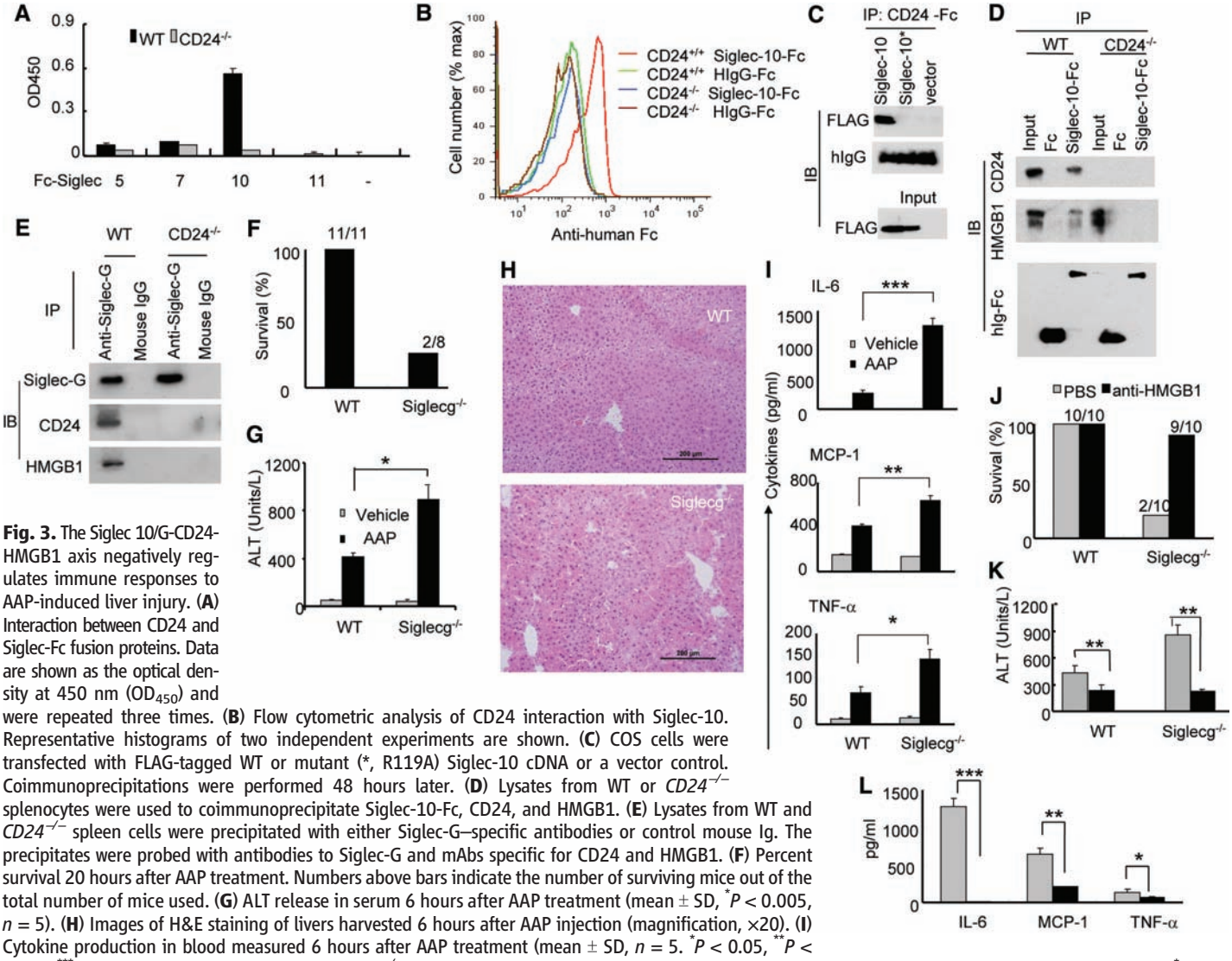

Fig. 3. The Siglec 10/G-CD24-HMGB1 axis negatively regulates immune responses to AAP-induced liver injury. (**A**) Interaction between CD24 and Siglec-Fc fusion proteins. Data are shown as the optical density at 450 nm (OD_{450}) and were repeated three times. (**B**) Flow cytometric analysis of CD24 interaction with Siglec-10. Representative histograms of two independent experiments are shown. (**C**) COS cells were transfected with FLAG-tagged WT or mutant (*, R119A) Siglec-10 cDNA or a vector control. Coimmunoprecipitations were performed 48 hours later. (**D**) Lysates from WT or *CD24*$^{-/-}$ splenocytes were used to coimmunoprecipitate Siglec-10-Fc, CD24, and HMGB1. (**E**) Lysates from WT and *CD24*$^{-/-}$ spleen cells were precipitated with either Siglec-G–specific antibodies or control mouse Ig. The precipitates were probed with antibodies to Siglec-G and mAbs specific for CD24 and HMGB1. (**F**) Percent survival 20 hours after AAP treatment. Numbers above bars indicate the number of surviving mice out of the total number of mice used. (**G**) ALT release in serum 6 hours after AAP treatment (mean ± SD, $^{*}P < 0.005$, $n = 5$). (**H**) Images of H&E staining of livers harvested 6 hours after AAP injection (magnification, ×20). (**I**) Cytokine production in blood measured 6 hours after AAP treatment (mean ± SD, $n = 5$. $^{*}P < 0.05$, $^{**}P < 0.009$, $^{***}P < 0.002$). (**J**) Survival of WT and *Siglecg*$^{-/-}$ mice 20 hours after treatment. (**K**) ALT release in the blood 6 hours after treatment (mean ± SD, $n = 5$, $^{*}P < 0.006$). (**L**) Cytokine release in the blood 6 hours after treatment (mean ± SD, $n = 5$, $^{*}P < 0.03$, $^{**}P < 0.0006$, $^{***}P < 0.0004$). (K) and (L) are representative of two independent experiments. Statistical significance was determined by the Student's *t* test.

HSP70 and HSP90 by TLR-dependent mechanisms (*6*). To determine if the CD24-Siglec-G pathway also regulates host responses to HSP70 and HSP90, we first evaluated whether HSP70 and HSP90 associate with CD24 and Siglec-G. Coimmunoprecipitations revealed that CD24 associates with both HSP70 and HSP90 (Fig. 4E). Similar to HMGB1, Siglec-G association with HSP70 and HSP90 was CD24 dependent (Fig. 4F), and *CD24*$^{-/-}$ and *Siglecg*$^{-/-}$ DCs produced significantly more IL-6 and TNF-α in response to recombinant HSP70 and HSP90 (Fig. 4G) compared to WT DCs. These data reveal a critical role for CD24 and Siglec-G in the negative regulation of DC response to multiple DAMPs.

Our results suggest that CD24 partners with Siglec-10 in humans or Siglec-G in mice to negatively regulate the immune response to proteins released by damaged cells, but not to ligands of microbial origin. Pattern recognition receptors such as TLRs and the receptor of advanced glycation end products (RAGE) mediate activation induced by DAMP (*7*, *8*). Our data indicate that repression of response to HMGB1 may be achieved by inhibition of NF-κB activation. Inhibition may be mediated by SHP-1. SHP-1 associates with Siglec-10 via its ITIM motif (*26*), and deficiency of either Siglec-G or SHP-1 enhances NF-κB activation (*20*, *23*). Given the role of HMGB1 in the pathogenesis of a number of diseases, including drug toxicity (*9*) and liver and cardiac ischemia and reperfusion (*27*, *28*), this pathway may uncover new targets for disease intervention.

Although it is well established that the host can recognize "danger" induced by damaged tissue (*4*), it is unclear whether or how an immune responses triggered by tissue damage is regulated. By identifying the CD24-Siglec-G pathway that selectively suppresses the immune response to DAMPs, our data demonstrate a mechanism by which tissue injury and infection are distinguished, even though they both use the evolutionarily conserved TLRs (*5*–*8*).

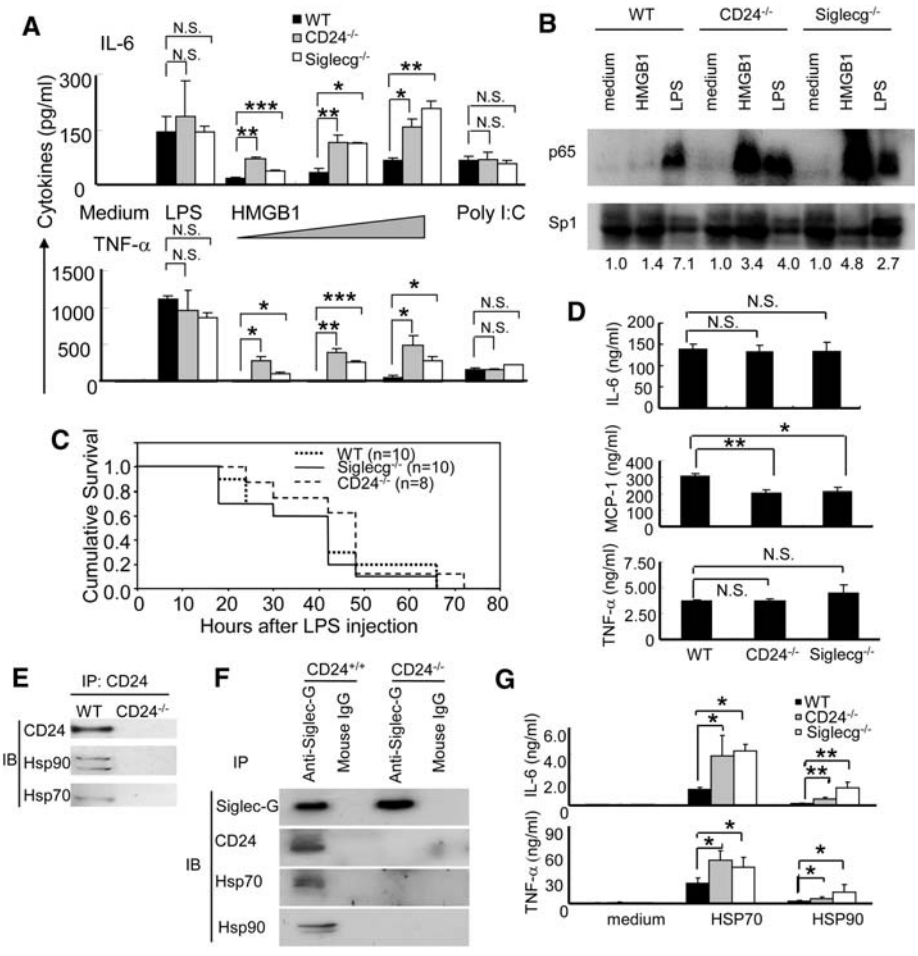

Fig. 4. CD24 and Siglec-G negatively regulate immune responses to HMGB1, HSP70, and HSP90, but not to LPS and poly(I:C). (**A**) Production of cytokines by DCs. DCs cultured from WT, *CD24*$^{-/-}$, or *Siglecg*$^{-/-}$ bone marrow were stimulated with LPS (100 ng/ml), poly(I:C) (10 μg/ml), or increasing doses (5, 10, and 20 μg/ml) of HMGB1 for 6 hours, and then the supernatants were analyzed for the presence of inflammatory cytokines with cytokine beads array. Data represent the mean ± SD for three independent cultures of DCs in each genotype and were repeated at least three times. (**B**) Bone marrow DCs isolated from WT, *CD24*$^{-/-}$, or *Siglecg*$^{-/-}$ mice were stimulated under the indicated conditions for 6 hours. The nuclear lysates were prepared and the activation of NF-κB was assessed by blotting for the p65 subunit of NF-κB. The loading of nuclear protein was determined by amounts of Sp1 protein. Fold induction over medium control is shown below the immunoblots. Data are representative of two independent experiments. (**C**) Age-matched male mice received ip injections of LPS (450 μg/mouse). Kaplan Meier survival plots are shown. No statistical significance was found by log-rank tests. (**D**) Cytokine production in the serum 4 hours after LPS injection (mean ± SD; the statistical significance of the differences between the control and one of the treated groups was determined by Student's *t* test. $^{*}P < 0.03$, $^{**}P < 0.002$). The numbers of mice used were the same as in (C). (**E**) Coimmunoprecipitation of CD24 and Hsp70 and Hsp90. (**F**) Siglec-G associates with Hsp70 and Hsp90 through CD24. The same precipitates used in Fig. 3E were analyzed for Hsp70 and Hsp90 by immunoblot. (**G**) Deficiencies in CD24 and Siglec-G enhanced production of IL-6 and TNF-α at 6 hours after stimulation with HSP70 and HSP90. Data shown represent the mean ± SD of cytokines from four independent isolates of DCs from each genotype and were repeated twice.

References and Notes

1. C. A. Janeway, *Cold Spring Harb. Symp. Quant. Biol.* **54**, 1 (1989).
2. Y. Liu, C. A. Janeway Jr., *Int. Immunol.* **3**, 323 (1991).
3. R. Medzhitov, P. Preston-Hurlburt, C. A. Janeway Jr., *Nature* **388**, 394 (1997).
4. P. Matzinger, *Annu. Rev. Immunol.* **12**, 991 (1994).
5. K. A. Cavassani *et al.*, *J. Exp. Med.* **205**, 2609 (2008).
6. D. G. Millar *et al.*, *Nat. Med.* **9**, 1469 (2003).
7. J. S. Park *et al.*, *J. Biol. Chem.* **279**, 7370 (2004).
8. J. Tian *et al.*, *Nat. Immunol.* **8**, 487 (2007).
9. P. Scaffidi, T. Misteli, M. E. Bianchi, *Nature* **418**, 191 (2002).
10. S. A. Ochsner *et al.*, *Stem Cells* **25**, 2476 (2007).
11. Y. Liu *et al.*, *J. Exp. Med.* **175**, 437 (1992).
12. Y. Liu, P. Zheng, *Trends Immunol.* **28**, 315 (2007).
13. X. F. Bai *et al.*, *J. Clin. Invest.* **105**, 1227 (2000).
14. L. Wang *et al.*, *PLoS Genet.* **3**, e49 (2007).
15. Q. Zhou *et al.*, *Proc. Natl. Acad. Sci. U.S.A.* **100**, 15041 (2003).
16. H. E. Harris, A. Raucci, *EMBO Rep.* **7**, 774 (2006).
17. H. Yang *et al.*, *Proc. Natl. Acad. Sci. U.S.A.* **101**, 296 (2004).
18. P. R. Crocker, J. C. Paulson, A. Varki, *Nat. Rev. Immunol.* **7**, 255 (2007).
19. M. Vinson *et al.*, *J. Biol. Chem.* **271**, 9267 (1996).
20. C. Ding *et al.*, *PLoS One* **2**, e997 (2007).
21. L. Apetoh *et al.*, *Nat. Med.* **13**, 1050 (2007).
22. O. Li *et al.*, *J. Exp. Med.* **203**, 1713 (2006).
23. L. I. Pao *et al.*, *Immunity* **27**, 35 (2007).
24. H. Wang *et al.*, *Science* **285**, 248 (1999).
25. E. Abraham, J. Arcaroli, A. Carmody, H. Wang, K. J. Tracey, *J. Immunol.* **165**, 2950 (2000).
26. G. Whitney *et al.*, *Eur. J. Biochem.* **268**, 6083 (2001).
27. M. Andrassy *et al.*, *Circulation* **117**, 3216 (2008).
28. A. Tsung *et al.*, *J. Exp. Med.* **201**, 1135 (2005).

29. This study was supported by grants from the NIH (AI064350, CA58033, and CA112001), U.S. department of Defense (W81XWH-08-1-0036), and Natural Science Foundation of China (30640420558) and Ministry of Science and Technology of China (2006CB910901). The authors have no conflicts of interest. We dedicate this study to Dr. Charles A. Janeway Jr.

Supporting Online Material

www.sciencemag.org/cgi/content/full/1168988/DC1
Materials and Methods
Figs. S1 to S4
Table S1
References

25 November 2008; accepted 26 February 2009
Published online 5 March 2009;
10.1126/science.1168988
Include this information when citing this paper.

Visualizing Antigen-Specific and Infected Cells in Situ Predicts Outcomes in Early Viral Infection

Qingsheng Li,[1] Pamela J. Skinner,[2] Sang-Jun Ha,[3] Lijie Duan,[1] Teresa L. Mattila,[2] Aaron Hage,[2] Cara White,[2] Daniel L. Barber,[4] Leigh O'Mara,[3] Peter J. Southern,[1] Cavan S. Reilly,[5] John V. Carlis,[6] Christopher J. Miller,[7] Rafi Ahmed,[3] Ashley T. Haase[1]*

In the early stages of viral infection, outcomes depend on a race between expansion of infection and the immune response generated to contain it. We combined in situ tetramer staining with in situ hybridization to visualize, map, and quantify relationships between immune effector cells and their targets in tissues. In simian immunodeficiency virus infections in macaques and lymphocytic choriomeningitis virus infections in mice, the magnitude and timing of the establishment of an excess of effector cells versus targets were found to correlate with the extent of control and the infection outcome (i.e., control and clearance versus partial or poor control and persistent infection). This method highlights the importance of the location, timing, and magnitude of the immune response needed for a vaccine to be effective against agents of persistent infection, such as HIV-1.

The outcome of viral infections in the acute stage of infection can be thought of as a numbers game and race, with the magnitude and speed of mounting host defenses competing against virus propagation and spread (*1*). Generally, in self-limited and fully controlled infections, the host wins by quickly generating large numbers of virus-specific cytotoxic T lymphocytes (CTLs) that terminate infection by clearing infected cells. However, a virus can win, and can establish a persistent infection, when the cellular immune response is delayed and is of insufficient magnitude to clear infection. The outcome then depends on the extent to which the CTL response can control infection and prevent progression to disease.

We studied correlates of these different outcomes of infection in simian immunodeficiency virus (SIV) and lymphocytic choriomeningitis virus (LCMV) infections. SIV (and HIV-1) cause persistent infections in which the CTL response in the early stages of infection (*2*, *3*) is too little and too late (*4*–*7*) to prevent systemic infection and massive depletion of $CD4^+$ T cells in the gut (*8*–*10*), but is usually sufficient to partially control virus production (*2*, *3*). LCMV strains cause infections in which the outcome may be clearance or persistence, depending on the strain: Infection with LCMV-Armstrong is cleared from adult C57B1/6 mice by 8 days post-inoculation (dpi), whereas animals infected with LCMV–clone 13 remain persistently viremic for months (*11*, *12*).

To identify correlates of clearance and the extent of control in persistent infections, we investigated the relationship between increasing numbers of infected cells and virus-specific CTLs in the early stages of SIV and LCMV infections. We hypothesized that the outcomes of infection would be determined by the timing, ratio, and spatial colocalization of virus-specific CTLs to infected cells. We tested this hypothesis with a method (*13*) called ISTH, as it combines in situ tetramer (IST) staining (*14*) and in situ hybridization (ISH) to locate and enumerate virus-specific $tetramer^+$ T cells and viral RNA^+ cells in tissues, using these as measures, respectively, of virus-specific CTLs and infected cells.

After intravaginal inoculation of SIV into adult female rhesus macaques, virus replicates in the first week in cervical vaginal tissues and then spreads throughout the lymphatic tissues to reach a peak in numbers of infected cells at 10 to 14 dpi (*8*, *15*). The peak in viral replication precedes the cellular immune response to immunodominant epitopes in SIV Gag and Tat that together constitute 70% of the cellular immune response in acute infection (*16*). This response is not detected until 14 dpi (*7*), which is too late to prevent a robust systemic infection. However, numbers of SIV RNA^+ cells do decline between 14 and 28 dpi, at a time coinciding with the detection of increasing numbers of Gag- and Tat-$tetramer^+$ cells by fluorescence-activated cell sorting (FACS) analysis and IST staining (*7*).

This decline in SIV RNA^+ cells was greater in cervical vaginal tissues than in lymphatic tissues (*15*), consistent with the hypothesis that the extent of control in each tissue compartment was related to the spatial proximity and numbers of $tetramer^+$ cells relative to the numbers of SIV RNA^+ cells. We used ISTH to test this hypothesis by visualizing, in the same section, effector (E) $tetramer^+$ cells and target (T) SIV RNA^+ cells, and then determining E:T cell ratios and the spatial proximity of $tetramer^+$ cells to their targets in cervical vaginal and lymphatic tissues (*13*).

We indeed found that the decline in numbers of infected cells in the cervix between the peak and 21 dpi (fig. S1, A and B) was correlated with detection by ISTH (Fig. 1A) of Gag-$tetramer^+$ cell–SIV RNA^+ cell conjugates. The decline in SIV RNA^+ cells in lymphatic tissues was also correlated with increasing numbers of $tetramer^+$ cells in close proximity to infected cells, illustrated for a lymph node at 21 dpi in Fig. 1B. We captured the spatial relationships between $tetramer^+$ and SIV RNA^+ cells in this lymph node by independently plotting their positions on a two-dimensional plane (*13*). In the montage of the whole lymph node section shown in Fig. 1B, arrows in the enlarged inset from the encircled area of the montage point to a red Gag-$tetramer^+$ cell and a blue SIV RNA^+ cell. The positions of these Gag-$tetramer^+$ cells are outlined against a gray-white mask of the section in Fig. 2A, and the positions of the Gag-$tetramer^+$ cell centers (centroids) are plotted in the upper panel of Fig. 2B. The positions of SIV RNA^+ cells in this section are plotted in the middle panel of Fig. 2B. The lower panel shows, in the superimposition of the upper and middle panels, Gag-$tetramer^+$ cells and SIV RNA^+ cells in close spatial proximity to one another throughout the lymph node. We thus conclude that effectors and targets are in close spatial proximity in these two tissue compartments.

By using ISTH to determine E:T ratios, we could further show that these ratios correlated with the extent of virus control in each tissue compartment. Defining extent of control as the reduction from peak numbers of copies of SIV RNA per microgram of tissue RNA to copy numbers at 20, 21, and 28 dpi, when the animals had mounted a tetramer response and viral load data were available from previously reported studies (*15*), we found a statistically significant relationship between the E:T ratio and relative reduction ($P = 0.001$). Reductions in viral loads by a factor of 80 to 160 were correlated with E:T ratios of ≥100. These ratios, with one exception, were achieved only in the female reproductive tract tissues where initial exposure and virus replication had elicited the most robust response.

We next investigated the relationship between the timing and magnitude of the effector response to infection outcome in LCMV-Armstrong and LCMV–clone 13 infections. LCMV-Armstrong infections are rapidly cleared by the second week of infection, whereas LCMV–clone 13 infections continue at high levels for months, with debilitating effects on virus-specific CTL proliferation and function mediated by programmed cell death–1 (PD-1) and its ligands (*11*, *12*, *15*, *17*). Because the two amino acid differences between LCMV-Armstrong and LCMV–clone 13 do not alter dominant or subdominant epitopes (*18*, *19*), it is not yet clear

[1]Department of Microbiology, Medical School, University of Minnesota, Minneapolis, MN 55455, USA. [2]Department of Veterinary and Biomedical Sciences, University of Minnesota, St. Paul, MN 55108, USA. [3]Emory Vaccine Center, Department of Microbiology and Immunology, Emory University School of Medicine, Atlanta, GA 30322, USA. [4]Immunobiology Section, National Institute of Allergy and Infectious Diseases, Bethesda, MD 20892, USA. [5]Division of Biostatistics, School of Public Health, University of Minnesota, Minneapolis, MN 55455, USA. [6]Department of Computer Science and Engineering, Institute of Technology, University of Minnesota, Minneapolis, MN 55455, USA. [7]Center for Comparative Medicine, California National Primate Research Center, University of California, Davis, CA 95616, USA.

*To whom correspondence should be addressed. E-mail: haase001@umn.edu

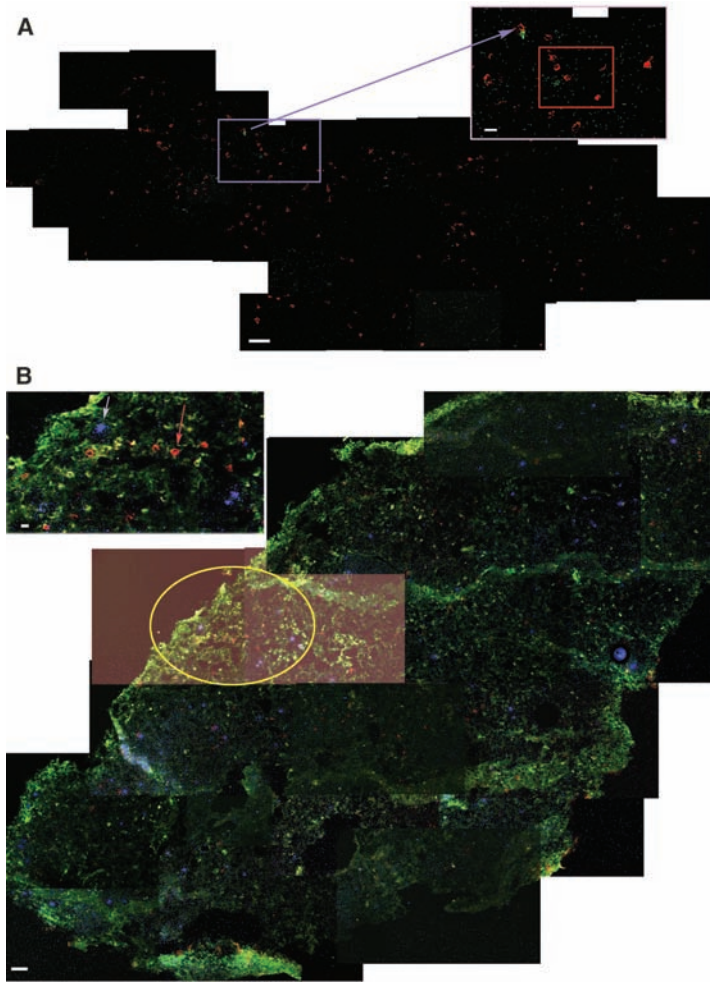

Fig. 1. ISTH analysis. (**A**) Cervical tissues, 21 dpi. The image of a whole section of cervix was reconstructed as a montage in Photoshop from separate confocal images, using the red channel for the Gag-tetramer$^+$ cells and green for the SIV RNA$^+$ cells. The blue arrow from the region enclosed by the blue rectangle points to a red Gag-tetramer$^+$ cell–green SIV RNA$^+$ cell conjugate in the enlarged inset. The excess of Gag-tetramer$^+$ cells is shown in the inset in a region enclosed by the red rectangle. (**B**) Lymphatic tissues, 21 dpi. Montage of a whole lymph node section reconstructed in Photoshop from separate images, using the red channel for the Gag-tetramer$^+$ cells, blue for the SIV RNA$^+$ cells, and green for CD8$^+$ T cells. The red arrow in the enlarged inset (upper left) points to a red Gag-tetramer$^+$ cell; the light blue arrow points to a blue SIV RNA$^+$ cell. The two lightened separate images with an encircled distinctive V-shaped constellation of Gag-tetramer$^+$ cells provide a frame of reference for Fig. 2. Scale bars for whole sections, 50 μm; insets, 10 μm.

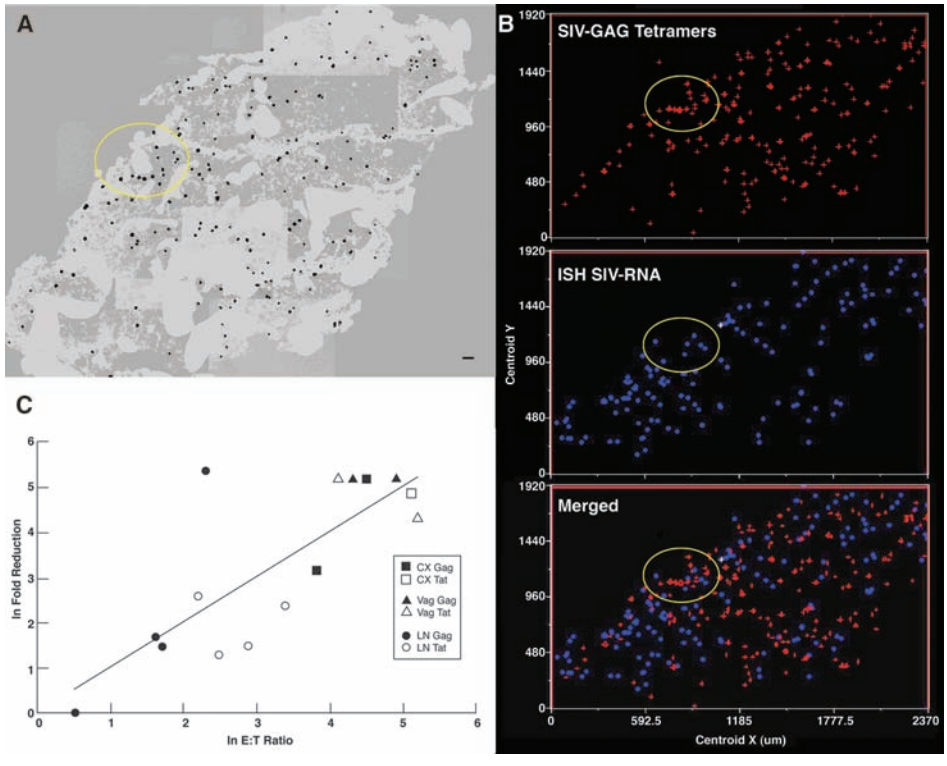

Fig. 2. Spatial relationships between SIV-tetramer$^+$ and SIV RNA$^+$ cells in the lymph node shown in Fig. 1B, and relationship between E:T ratios and reduction in viral replication. (**A**) Gag-tetramer$^+$ cells are shown against a gray-white mask of the section, with the V-shaped encircled constellation shown in Fig. 1B. Scale bar, 50 μm. (**B**) SIV RNA$^+$ and tetramer$^+$ cells were mapped by plotting the *x* and *y* coordinates of their centers (centroids) onto a two-dimensional grid measured from a fixed starting position (0,0). Upper panel, Gag-tetramer$^+$ cells; middle panel, SIV RNA$^+$ cells; lower panel, superimposition of upper and middle panels revealing the close spatial proximity of the virus-specific tetramer$^+$ cells with SIV RNA$^+$ throughout the lymph node. The white crosses and encircled areas in the panels are included as points of reference. (**C**) E:T ratio correlates with reduction in viral load in cervical vaginal and lymphatic tissues. Natural log–transformed viral load fold reductions are plotted against E:T ratios for Gag- and Tat-tetramer$^+$ cells in cervical (CX) and vaginal (Vag) tissues and lymph nodes (LN) from five animals at 20 to 28 dpi. E:T ratios were determined by ISH as described (*13*).

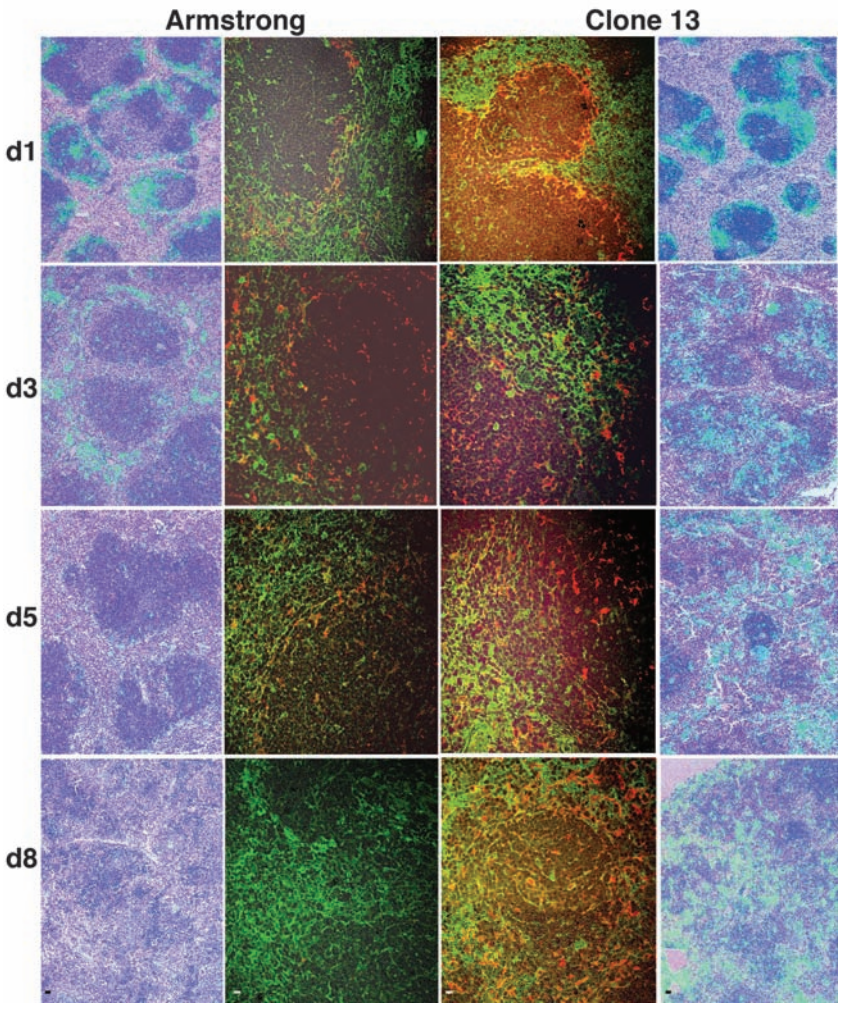

Fig. 3. Time course comparison of cells infected by LCMV-Armstrong or LCMV–clone 13. Outer columns: LCMV RNA$^+$ cells detected by ISH with LCMV-specific probes have a greenish appearance in developed radioautographs viewed in reflected light. Spleen white pulp is counterstained dark blue. Inner columns: LCMV-antigen$^+$ cells are stained red with polyclonal antibody to LCMV; FRCs in white pulp are stained green with the FRC marker ER-TR7. Both viral strains at 1 dpi (d1) infect macrophages in the marginal zone and FRCs in the white pulp, but LCMV–clone 13 infects larger numbers of both cell types. LCMV–clone 13 continues to infect large numbers of both cell types over the 8-day time course of the experiment, whereas the numbers of infected cells rapidly decline in LCMV-Armstrong infections. Scale bars (bottom row), 10 μm.

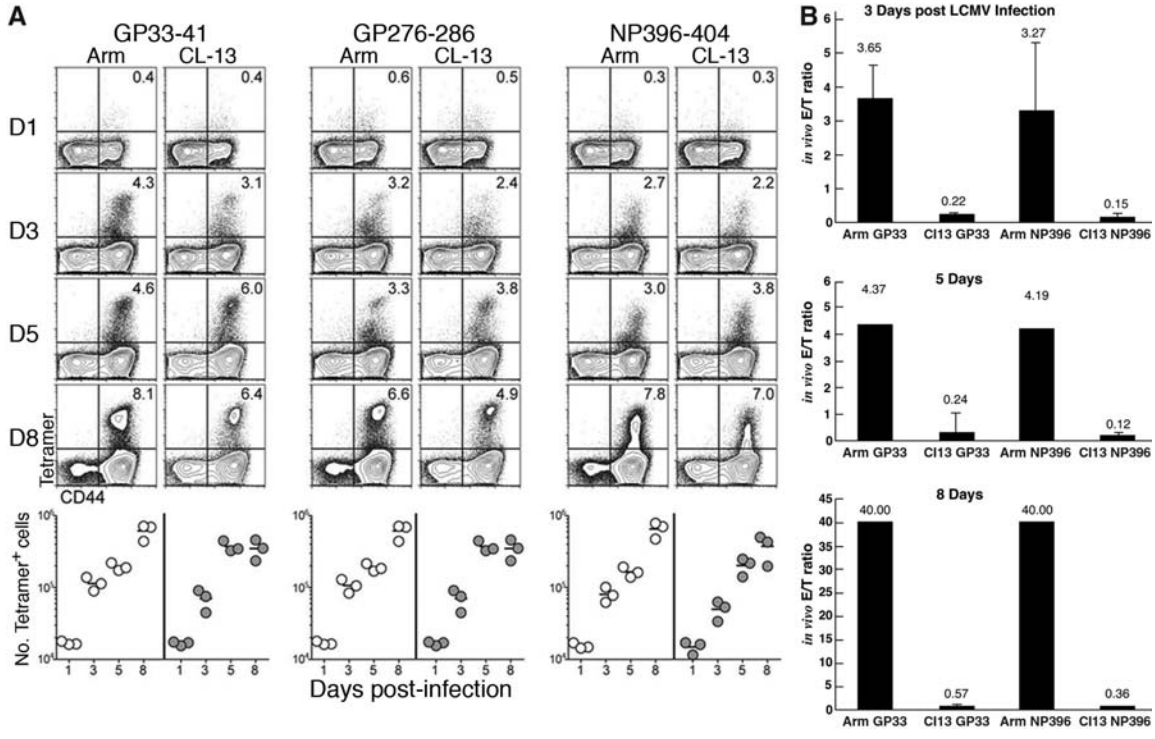

Fig. 4. (**A**) FACS analysis of the immunodominant epitope response to acute LCMV-Armstrong and LCMV–clone 13 infections in spleen. Flow cytometric quantification is presented as proportions and numbers of stained tetramer$^+$ cells from disaggregated spleens from groups of three mice per time point after LCMV-Armstrong or LCMV–clone 13 infection. Representative plots gated on CD8$^+$ T cells are shown by MHC class I tetramer (*y* axis) for each immunodominant epitope (GP33-41, GP276-286, and NP396-404) and CD44 (*x* axis). (**B**) E:T ratios in acute LCMV-Armstrong and LCMV–clone 13 infections in spleen. E:T ratios at the times shown were determined by ISTH as described (*13*).

why the initial CD8 T cell response should result in such divergent outcomes.

We determined by ISTH that strain LCMV-Armstrong is cleared because the number of immune effectors rapidly exceeds the number of infected cells. LCMV–clone 13, on the other hand, immediately infects larger numbers of macrophages (*18*) and fibroreticular cells (FRCs) (*20*) than does LCMV-Armstrong, thereby exceeding the capacity of the initial immune response to reduce the basic reproductive rate below 1 and thereby contain infection.

The divergent outcome and larger number of cells infected by LCMV–clone 13 in the spleen are illustrated in Fig. 3, which tracks LCMV RNA$^+$ cells and LCMV-antigen$^+$ FRCs (*13*) in the spleen from 1 to 8 dpi for the respective strains. As previously described, both strains of LCMV infect splenic marginal zone macrophages and FRCs in the white pulp, but LCMV–clone 13 infects larger numbers of both cell types (*18*, *20*). This difference, particularly the infection of FRCs, is already evident at 1 dpi, as judged by the diffuse ISH signal emanating from LCMV RNA$^+$ cells in the white pulp. LCMV–clone 13 infection of both cell types is sustained at high levels at 3, 5, and 8 dpi, whereas the numbers of LCMV-Armstrong–infected cells are barely detectable by 8 dpi.

The different infection outcomes produced by these two strains of LCMV cannot be explained by differences in the immune response seen in FACS analysis, but can be explained by ISTH, which provides the critical relevant measure of relative rates of increase in effectors and targets. By FACS analysis, the rapidly expanding populations of virus-specific tetramer$^+$ T cells were comparable for both strains from 3 to 8 dpi (Fig. 4A). However, E:T ratios determined by ISH reflect the increase of infected cells (relative to LCMV-GP and NP-tetramer$^+$ cells) in LCMV–clone 13 infection versus LCMV-Armstrong infection (Fig. 4B). Because of the faster increase of infected cells relative to LCMV-tetramer$^+$ cells, the E:T ratio for LCMV–clone 13 never approached 1. By contrast, the E:T ratio for LCMV-Armstrong was already ~4 at 3 dpi, higher than the ratio for LCMV–clone 13 at 3 dpi by a factor of 20.

Together, the ISTH analyses of SIV and LCMV infection tell us that location, timing, and numbers of effectors and targets all count in determining outcome. We have speculated elsewhere (*5*) that if the "too little, too late" response to SIV infection (*7*) had occurred earlier, when there were only small founder populations of infected cells confined to the portal of entry, vaginal transmission and systemic infection might be prevented with relatively few effector cells. Thus, in SIV (and, by extension, HIV-1) infections, a vaccine that elicited an immune response at the portal of entry "enough and soon enough" could prevent vaginal transmission.

References and Notes

1. P. C. Doherty, *Science* **280**, 227 (1998).
2. R. A. Koup *et al.*, *J. Virol.* **68**, 4650 (1994).
3. M. J. Kuroda *et al.*, *J. Immunol.* **162**, 5127 (1999).
4. M. P. Davenport, R. M. Ribeiro, A. S. Perelson, *J. Virol.* **78**, 10096 (2004).
5. A. T. Haase, *Nat. Rev. Immunol.* **5**, 783 (2005).
6. M. Pope, A. T. Haase, *Nat. Med.* **9**, 847 (2003).
7. M. R. Reynolds *et al.*, *J. Virol.* **79**, 9228 (2005).
8. Q. Li *et al.*, *Nature* **434**, 1148 (2005).
9. J. J. Mattapallil *et al.*, *Nature* **434**, 1093 (2005).
10. R. S. Veazey *et al.*, *Science* **280**, 427 (1998).
11. R. Ahmed, A. Salmi, L. D. Butler, J. M. Chiller, M. B. Oldstone, *J. Exp. Med.* **160**, 521 (1984).
12. E. J. Wherry, J. N. Blattman, K. Murali-Krishna, R. van der Most, R. Ahmed, *J. Virol.* **77**, 4911 (2003).
13. See supporting material on *Science* Online.
14. P. J. Skinner, M. A. Daniels, C. S. Schmidt, S. C. Jameson, A. T. Haase, *J. Immunol.* **165**, 613 (2000).
15. C. J. Miller *et al.*, *J. Virol.* **79**, 9217 (2005).
16. B. R. Mothe *et al.*, *J. Virol.* **76**, 875 (2002).
17. D. L. Barber *et al.*, *Nature* **439**, 682 (2006).
18. M. Matloubian, S. R. Kolhekar, T. Somasundaram, R. Ahmed, *J. Virol.* **67**, 7340 (1993).
19. M. Matloubian, T. Somasundaram, S. R. Kolhekar, R. Selvakumar, R. Ahmed, *J. Exp. Med.* **172**, 1043 (1990).
20. S. N. Mueller *et al.*, *Proc. Natl. Acad. Sci. U.S.A.* **104**, 15430 (2007).

21. We thank the Immunology Core Laboratory and Primate Services Unit of the California National Primate Research Center (CNPRC); D. Lu, T. Rourke, R. Dizon, and B. Vang for technical assistance; J. Sedgewick for assistance in setting up the confocal microscope to capture images of silver grains; D. Masopust for helpful discussion; and C. O'Neill and T. Leonard for help in preparing the manuscript and figures. Supported in part by NIH research grants AI48484 (A.T.H.), AI20048 (R.A.), and AI066314 (C.J.M.); National Center for Research Resources grant RR00169 (CNPRC, University of California, Davis); and a gift from the James B. Pendleton Charitable Trust (C.J.M.).

Supporting Online Material

www.sciencemag.org/cgi/content/full/323/5922/1726/DC1
Materials and Methods
Fig. S1
References

18 November 2008; accepted 9 February 2009
10.1126/science.1168676

Infection by Tubercular Mycobacteria Is Spread by Nonlytic Ejection from Their Amoeba Hosts

Monica Hagedorn,[1] Kyle H. Rohde,[2] David G. Russell,[2] Thierry Soldati[1]*

To generate efficient vaccines and cures for *Mycobacterium tuberculosis*, we need a far better understanding of its modes of infection, persistence, and spreading. Host cell entry and the establishment of a replication niche are well understood, but little is known about how tubercular mycobacteria exit host cells and disseminate the infection. Using the social amoeba *Dictyostelium* as a genetically tractable host for pathogenic mycobacteria, we discovered that *M. tuberculosis* and *M. marinum*, but not *M. avium*, are ejected from the cell through an actin-based structure, the ejectosome. This conserved nonlytic spreading mechanism requires a cytoskeleton regulator from the host and an intact mycobacterial ESX-1 secretion system. This insight offers new directions for research into the spreading of tubercular mycobacteria infections in mammalian cells.

Intracellular bacterial pathogens have evolved strategies to exploit host cell resources and replicate inside a variety of cell types, staying out of reach of the host's immune system. The concept is emerging that pathogenic bacteria evolved from environmental species by adapting to an intracellular lifestyle within free-living bacteria-eating protozoans. Consequently, cellular defense mechanisms that are active in animal immune phagocytes may have originated in amoebas (*1*, *2*). For example, during differentiation of the social amoeba *Dictyostelium* to form a multicellular structure, sentinel cells are deployed to combat pathogens (*1*).

Generally, infection follows the entry of a bacterium into a host cell, giving rise to a pathogen-containing vacuole usually called a phagosome. From this common starting point, pathogens subvert or resist the mechanisms that usually transform the phagosome into a bactericidal environment. Understanding of the passive or triggered uptake mechanisms and of the subsequent hijacking of host cell processes is increasing steadily, but little is known about how the pathogens exit their primary host cells and spread the infection.

Mycobacterium tuberculosis causes tuberculosis and other granulomatous lesions and is a major threat to human health. *M. marinum* is a close relative (*3*) responsible for fish and amphibian tuberculosis, in which it causes almost indistinguishable pathologies and lesions [reviewed in (*4*)]. Several elegant cross-species complementation studies between these two pathogens highlight their common mechanisms of pathogenicity [reviewed in (*4*)].

After passive uptake by immune phagocytes, *M. tuberculosis* and *M. marinum* arrest or bypass phago-lysosome maturation and replicate inside a compartment of endosomal nature (*5*–*7*).

[1]Département de Biochimie, Faculté des Sciences, Université de Genève, Sciences II, 30 quai Ernest Ansermet, CH-1211 Genève-4, Switzerland. [2]Department of Microbiology and Immunology, College of Veterinary Medicine, Cornell University, Ithaca, NY 14853, USA.

*To whom correspondence should be addressed. E-mail: thierry.soldati@unige.ch

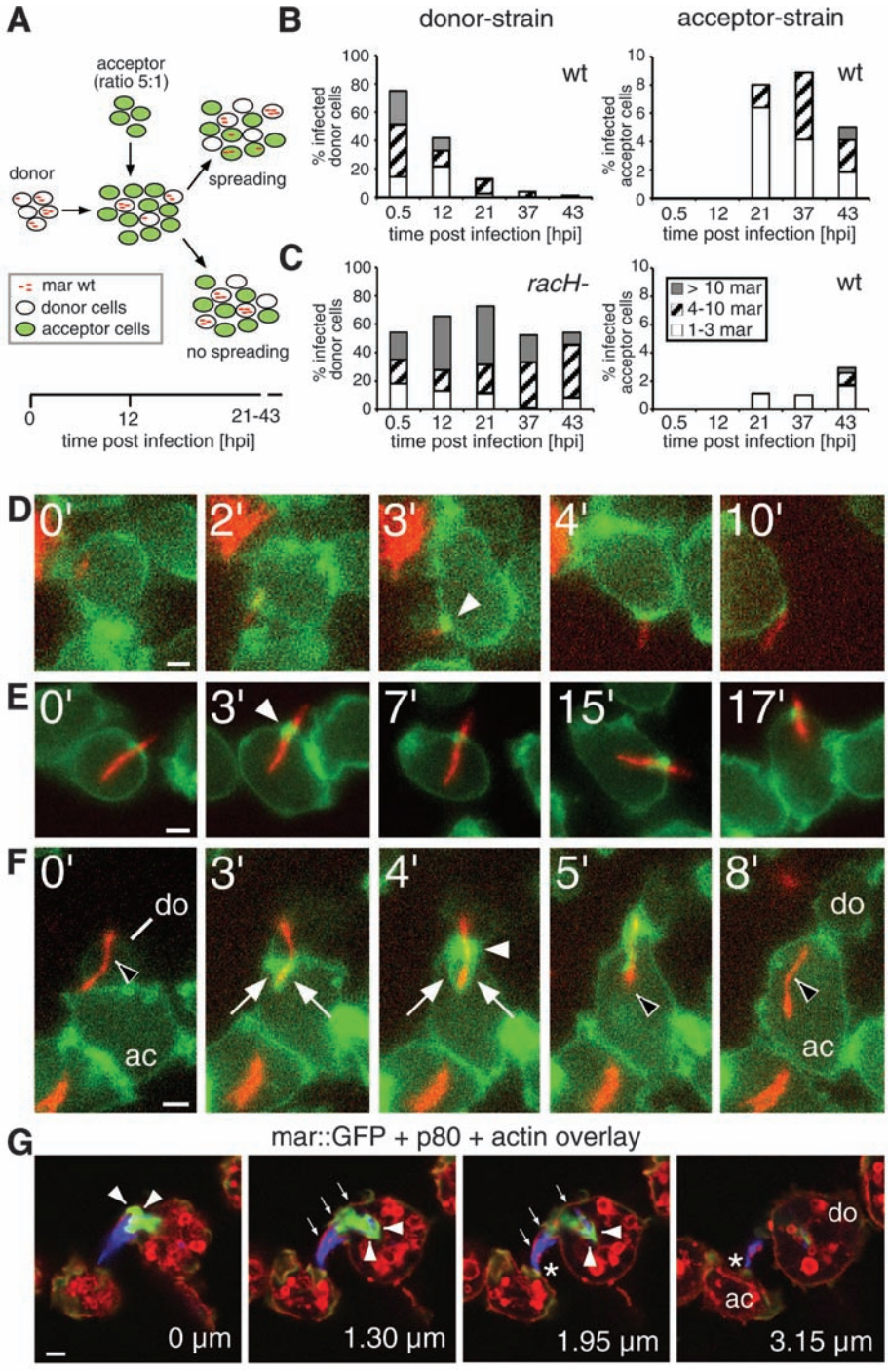

Fig. 1. Direct cell-to-cell transmission of *M. marinum* occurs via ejectosomes and is RacH-dependent. (**A**) Quantitative dissemination assay. A donor strain [wild-type (wt) or *racH*$^{-}$ cells] was infected with DsRed-expressing *M. marinum* (mar) and, at 12 hpi, mixed with a green fluorescent acceptor strain. The presence of bacteria in donor and acceptor cells was scored. Dissemination efficiency for wild-type (**B**) and *racH*$^{-}$ (**C**) donor cells is shown. The number of bacteria per cell (classified into groups of 1 to 3, 4 to 10, and >10 bacteria per cell) is indicated. [(D) to (F)] Live GFP–actin-binding domain (ABD)–expressing *Dictyostelium* cells (green) infected with DsRed-expressing *M. marinum* (red) were imaged at 35 hpi for the indicated times (upper left corners). (**D**) Nonlytic ejection of mycobacteria occurs through actin-dense ejectosomes (white arrowhead). (**E**) Cells with mycobacteria spanning the plasma membrane retain normal motility. (**F**) Cell-to-cell transmission of a cytosolic bacterium (black arrowhead) from a donor cell (do) to an acceptor cell (ac) through an ejectosome (white arrowhead) into a phagocytic cup (white arrows). (**G**) A bundle of bacteria is ejected from a donor cell (do). The plasma membrane bulge (small arrows) is ruptured at the tip (asterisk), where it contacts an acceptor cell (ac). Actin tails stained by phalloidin (green, arrowheads) were polarized at the posterior of bacteria (blue). The vertical distance from the first section is indicated in micrometers. Scale bars, 1 µm.

Both species can escape from this vacuole into the host cytosol (*8*–*11*), although at varying frequencies. Efficient translocation into the cytosol depends on an intact region of difference (RD) 1 locus (*10*, *11*), which encodes components of a type seven secretion system and essential secreted effectors (*12*). This ESX-1 secretion system has been implicated in the arrest of phagosome maturation (*13*), granuloma formation, and the spread of infection (*14*, *15*); however, it is not essential for replication inside macrophages (*14*). It has also been directly associated with the secretion of a membranolytic activity (*15*). Specifically, the secreted effector ESAT-6 has recently been linked to niche breakage and pore-forming activity in macrophages (*11*).

M. marinum and *M. tuberculosis* can disseminate through the release of bacilli after host cell lysis via necrotic or apoptotic cell death (*16*–*18*), but studies also document cell-to-cell, antibiotic-insensitive spreading inside an epithelial monolayer (*19*, *20*). *M. marinum* induces plasma membrane protrusions (*2*, *9*) suggested to participate in dissemination between macrophages in culture (*21*) and inside zebrafish embryos (*22*). Hence, escape into the cytosol may be a necessary precursor for cell-to-cell spread and may involve a direct nonlytic transmission process occurring within the granuloma (*5*, *6*).

We adopted the genetically tractable *Dictyostelium*–*M. marinum* model system to unravel basic mechanisms of intercellular dissemination. The course of *M. marinum* infection in *Dictyostelium* amoebas is very similar to that in macrophages (*8*). The mycobacteria replication vacuole accumulates a flotillin-like raft protein, then ruptures and releases *M. marinum* into the cytosol (fig. S1). A *Dictyostelium* mutant lacking the RacH guanosine triphosphatase (GTPase), which is involved in regulation of the actin cytoskeleton and endosomal membrane trafficking and acidification, was more permissive for *M. marinum* proliferation (*8*). Detailed fluorescence-activated cell sorting (FACS) analysis (fig. S2) of these infected cells suggested an interference with intercellular dissemination (fig. S3).

To test this hypothesis, we designed a quantitative dissemination assay (Fig. 1A). Briefly, an infected *Dictyostelium* donor strain (either wild-type or *racH*$^{-}$) was mixed with a green fluorescent wild-type acceptor strain at a donor:acceptor ratio of 1:5. Over the course of infection, the number of bacteria per donor cell and acceptor cell was determined by visual inspection. The proportion of wild-type infected donor cells decreased concomitantly with a sharp increase in infected acceptor cells at 21 hours post infection (hpi), and the number of bacteria per acceptor cell increased over time (Fig. 1B). This indicated successful transmission of bacteria and replication in acceptor cells. In contrast, the proportion of infected *racH*$^{-}$ donor cells remained relatively constant (above 50%). The infection of acceptor cells from *racH*$^{-}$ donor cells was about eight times less than from wild-type donor cells (Fig. 1C). The *racH*$^{-}$

cells were deficient in intercellular spreading of mycobacteria, and it appears that a RacH-dependent release mechanism is required for cell-to-cell transmission under these conditions.

Cytosolic pathogens such as *Listeria* and *Shigella* use actin-based tails and filopodia for intercellular spreading. During *M. marinum* infection of macrophages, unidentified mycobacterial proteins induce actin tails in a Wiskott-Aldrich syndrome protein–dependent manner (*23*), as well as structures reminiscent of *Shigella*-induced filopodia (*9*) that can be captured by neighboring cells (*9*) (fig S4). Hence, we monitored F-actin dynamics in infected cells expressing a green fluorescent protein (GFP) fusion with the actin-binding domain (ABD) of filamin (*24*) by live microscopy (movies S1 to S7; Fig. 1, D to F; and fig. S5, A and B). At late stages of infection, despite the presence of many cytosolic bacteria, cells exhibited apparently normal amoeboid motility (movie S1) and cell division (movie S2). In contrast to the observation in macrophages (*9*) (fig. S4), no persistent actin tails were visible on cytosolic bacteria, possibly due to the high rate of actin depolymerization in *Dictyostelium* (*25*). However, transient actin flashes were produced when bacteria contacted the cell cortex (fig. S5A and movie S3).

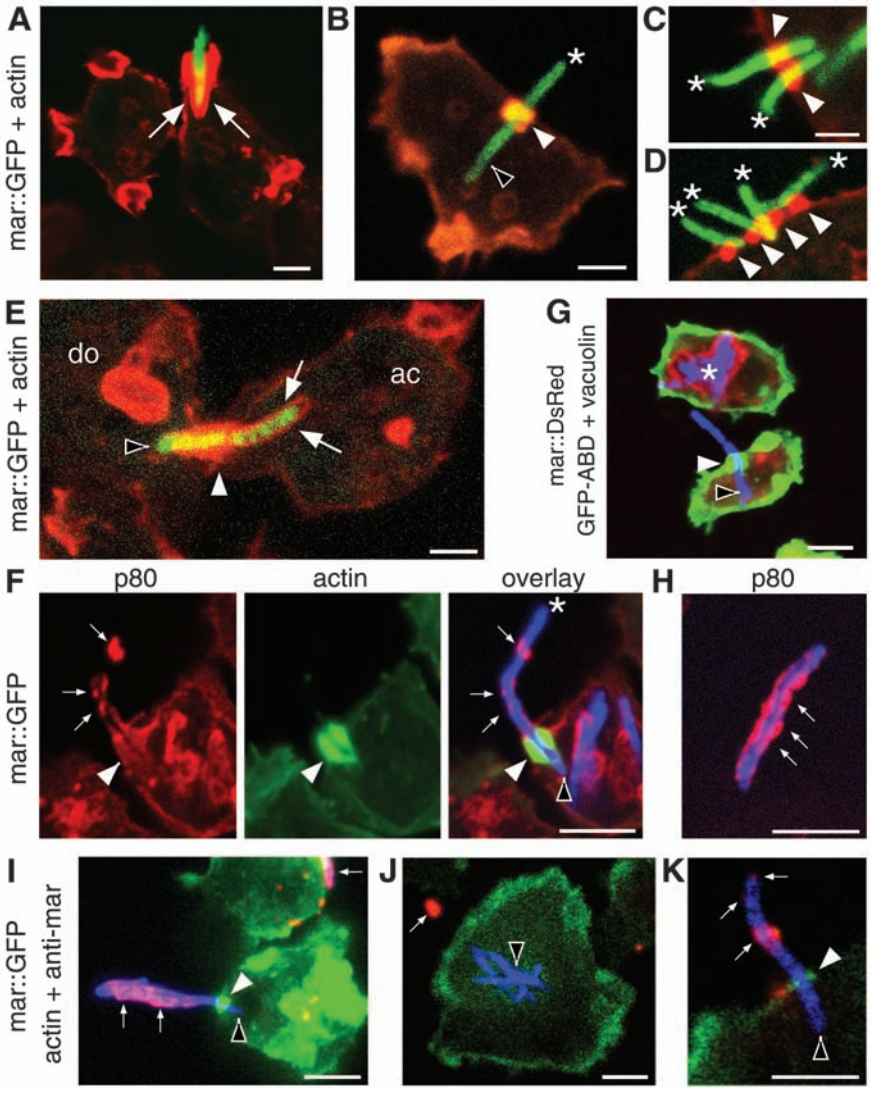

Fig. 2. Biogenesis, structure, and topology of ejectosomes. Paraformaldehyde-fixed cells infected with GFP-expressing *M. marinum* (green), stained for F-actin (red), are shown. (**A**) A phagocytic cup lined with F-actin (arrows). A single bacterium (**B**) or multiple bacteria (**C** and **D**) spanning the host cell plasma membrane (asterisks) through ejectosomes (white arrowheads), with the intracellular part of the bacterium devoid of actin labeling [black arrowhead in (B)]. (**E**) Cell-to-cell transmission of bacteria from a donor (do) to an acceptor (ac) cell through an ejectosome into a phagocytic cup (arrows). (**F**) The movement of cytosolic bacteria (blue) through ejectosomes (F-actin, green) induces a plasma membrane bulge (small arrows) that ruptures at the tip (asterisk). The intracellular part of the ejecting bacterium is devoid of p80, a plasma membrane marker (F), and vacuolin, a niche marker (asterisk in **G**). Some extracellular bacteria were positive for p80 (small arrows in **H**). (**I** to **K**) Live infected cells (*M. marinum*, blue; actin, green) were incubated in the presence of an anti–*M. marinum* serum. The extracellular parts of ejecting [small arrows in (I) and (K)] or outside [small arrow in (J)] bacteria were accessible to the antiserum and labeled red, in contrast to intracellular bacteria [black arrowhead in (J)], confirming partial loss of plasma membrane integrity. Scale bars, 1 μm.

Bacteria were ejected through an F-actin–dense structure we called an ejectosome (Fig. 1D and movie S4). Mycobacteria were also seen spanning the plasma membrane without inducing host cell lysis, a situation stable for the duration of the observation (17 min, Fig. 1E and movie S5). A substantial proportion of cells harbored multiple similar structures (fig. S5B and movie S6). Ejectosomes can apparently exert a contractile force, forming a tight septum around the bacteria as they are towed behind motile host cells (Fig. 1D and movie S4). We also captured images of synchronized ejection from a donor cell and phagocytosis by an acceptor cell (Fig. 1F and movie S7). Hence, an actin-based mechanism appeared to be responsible for nonlytic ejection of cytosolic mycobacteria, which, concomitantly with capture by neighboring cells, ensured efficient and antibiotic-insensitive intercellular spreading.

The live observations were confirmed by staining fixed infected cells with fluorescent phalloidin. During phagocytosis, the cell deforms toward the bacteria and extends lamellipodia that surround it along most of its length (Figs. 2A and 3E). In contrast, ejectosomes are short barrel-shaped structures usually found in flat membrane regions (Fig. 2B). Multiple ejectosomes were often observed to cluster at the surface of a cell (Fig. 2, C and D). Cell fixation preserved the structure of ejectosomes coupled to phagocytic cups, suggesting direct donor-to-acceptor transmission (Fig. 2E).

What propels bacteria during ejection is unclear, because we rarely observed bacteria with typical F-actin tails (Fig. 1G). Ejection may be powered by a mechanical process resulting from a combination of cortical tension, cytoplasmic pressure, and a reaction of the actin cortex to bacteria-induced deformation. The ejectosome was strongly enriched in myosin IB and coronin (fig. S5, G and H), whereas the F-actin barrel was weakly or not at all enriched in myosin II and the Arp2/3 complex (fig. S5, I and J). Thus, the ejectosome may either assemble de novo or result from a rearrangement of preexisting cortical structures.

In all cases of ejection, the part of the bacterium inside the cell was devoid of membrane markers from endosomes (Fig. 2F and fig. S5C) or the replication compartment (Fig. 2, F and G), which means that the phenomenon is not an exocytic event. The protruding part of the bacterium induced a bulge in the plasma membrane (Fig. 2F and fig. S5C), demonstrating that the bacterium is on an outward journey through the cell surface. The membrane labeling often appeared

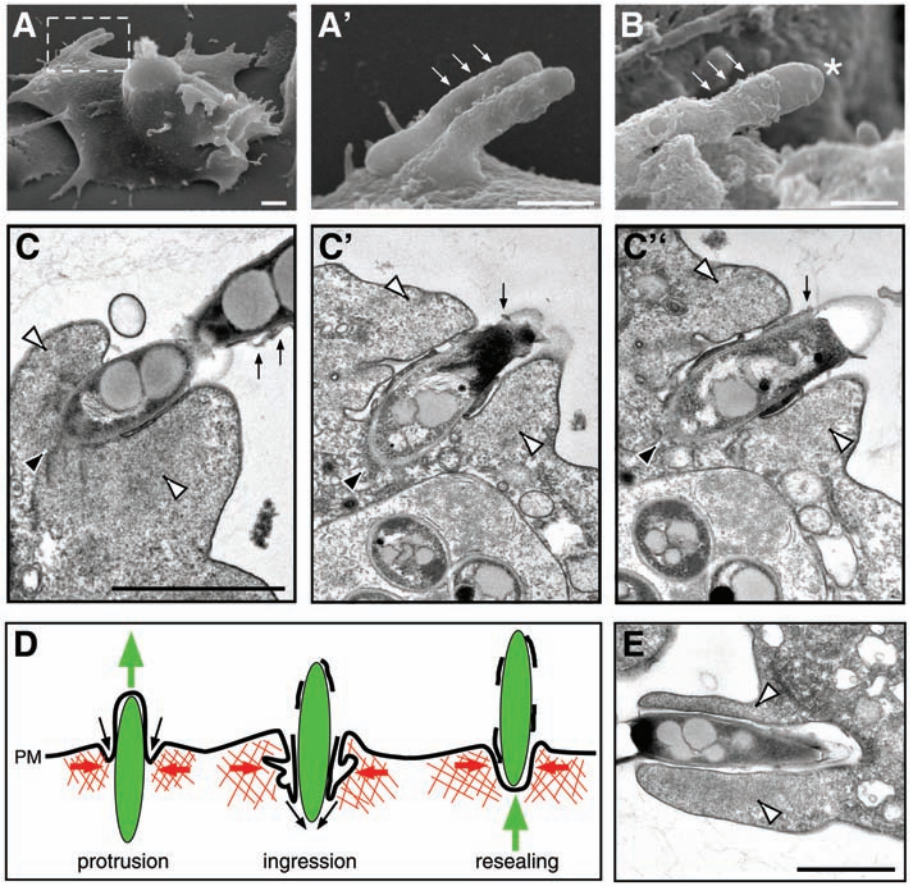

Fig. 3. Electron microscopy of ejecting bacteria and schematic representation of an ejection event. Scanning electron microscopy [**A** and **B**; **A'** is the magnified inset of (A)] showed bulges of the plasma membrane (small arrows), some ruptured at the tip of the ejecting bacterium [(B), asterisk]. Scale bars, 0.5 μm. (**C** to **C''**) Serial sections through an ejectosome revealed the organization of the F-actin (white arrowheads) and the plasma membrane. The posterior of the ejecting bacterium (black arrowhead) was in the cytosol. The bacterium was separated from the F-actin by the invaginated plasma membrane, which was tightly apposed to its surface. Membrane fragments were scattered along the extracellular part of the bacterium (small arrows). (**D**) Schematic representation of an ejection. During outward movement of a bacterium (green), the F-actin barrel exerts contraction (red arrows), and the invaginating plasma membrane (PM) reseals at the posterior of the bacterium (black arrows), maintaining a tight septum despite partial membrane rupture. (**E**) Micrograph of a phagocytic cup. The actin-filled lamellipodia (white arrowheads) extend and engulf a bacterium. Scale bars, 1 μm.

patchy at the tip of the bulge (Fig. 2F and fig. S5C), suggesting local loss of integrity. Sometimes, extracellular mycobacteria were wrapped in plasma membrane remnants (Fig. 2H and fig. S5D). Outward plasma membrane deformation (Fig. 3, A and C) and partial membrane rupture (Fig. 3, B and C) were also observed by scanning and transmission electron microscopy.

Labeling of the protruding part of ejected *M. marinum* with an anti–*M. marinum* serum in nonpermeabilized cells indicated the accessibility of the bacterium surface and hence local loss of plasma membrane integrity (Fig. 2, I and K). However, infected cells do not lyse, as judged by live imaging (Fig. 1E and movies S1 to S7), and they are also not leaky, as demonstrated by the exclusion of a membrane-impermeant DNA-binding dye during a 2-hour-long incubation (fig. S5E). Serial sections through an ejectosome (Fig. 3C) showed a cytosolic bacterium protruding from a cell, with the plasma membrane ruptured toward the tip of the bacterium but at the same time invaginated between the bacterium and a zone of dense actin meshwork. We propose that, during ejection, the ingressing plasma membrane stays tightly apposed to the bacterium surface and finally reseals at the posterior of the bacterium, resulting in a dynamic but tight seal that prevents host cell lysis or leakage (schematically depicted in Fig. 3D).

During *Dictyostelium* infections, *M. tuberculosis* was first found in spacious vacuoles (fig. S7) that accumulated vacuolin, the *Dictyostelium* flotillin homolog (fig. S6A). Then, with an efficiency lower than that of *M. marinum*, the bacilli translocated into the cytosol (Fig. 4A and figs. S6A and S7), where they induced ejectosomes (Fig. 4A and fig. S6, B and C). In *Dictyostelium*, *M. avium* also accumulated in spacious compartments decorated with vacuolin, but, in contrast to *M. tuberculosis* and *M. marinum*, no vacuole breakage was detected (Fig. 4A) and no ejectosome was observed. Vacuole escape and nonlytic ejection from the host cell may be conserved strategies among tubercular mycobacteria that could play a prominent role in the dissemination of infection, rather than intracellular survival per se.

We expected a direct correlation between the observed number of ejectosomes and the spreading of infection. Indeed, in wild-type cells, there were about 15 ejectosomes per 100 cells at 37 hpi, whereas no ejectosome was ever observed in *racH*$^{-}$ cells (Fig. 4B and fig. S8B). This is not due to deficient vacuole escape, because at 37 hpi, over 90% of *M. marinum* were cytosolic and free of vacuolin staining, as compared to 75% in wild-type cells (Fig. 4B and fig. S9). Complementation of *racH*$^{-}$ cells with GFP-RacH partially restored the capacity to form ejectosomes (fig. S8C). In accordance with this observation, membrane fragments carrying GFP-RacH polymerize actin around them upon the addition of guanosine 5′-*O*-(3′-thiotriphosphate) in a cell-free assay (*26*).

In correlation with the capacity to induce ejectosomes, the RD1 locus is present in *M. tuberculosis* and *M. marinum* (*13*–*15*) but absent from *M. avium* (*12*). A *M. marinum* mutant deleted of its RD1 locus (ΔRD1) replicated inefficiently in *Dictyostelium* (Fig. 4D), and the population of infected cells steadily decreased with time (Fig. 4E and fig. S8D). Vacuole escape was readily detectable (Fig. 4B and fig. S9) but was about four to five times less efficient than for wild-type *M. marinum*, as measured by colocalization with vacuolin or p80. This corroborates recent findings in macrophages when a collection of ESX-1 mutants was used (*11*). But the most striking observation was the complete absence of ejectosomes (Fig. 4B). If the ESX-1 locus secretes vacuole escape factors (*11*), it may also secrete factors that coordinate the egress of the resulting cytosolic bacteria. It is possible that ESAT-6, one of the major secreted effectors, plays a role in both processes. We designed a trans-complementation strategy in which *M. marinum* ESAT-6 was conditionally expressed directly inside the cytosol of *Dictyostelium* (Fig. 4C). *M. marinum* ΔRD1 apparently replicated better in ESAT-6–expressing cells than in wild-type cells (Fig. 4D) and showed a 1.5- to 2-fold increased frequency of niche escape. Most important, it induced ejectosome formation (Fig. 4B). Our data demonstrated that the nonlytic ejection of tubercular mycobacteria from *Dictyostelium* is a concerted process

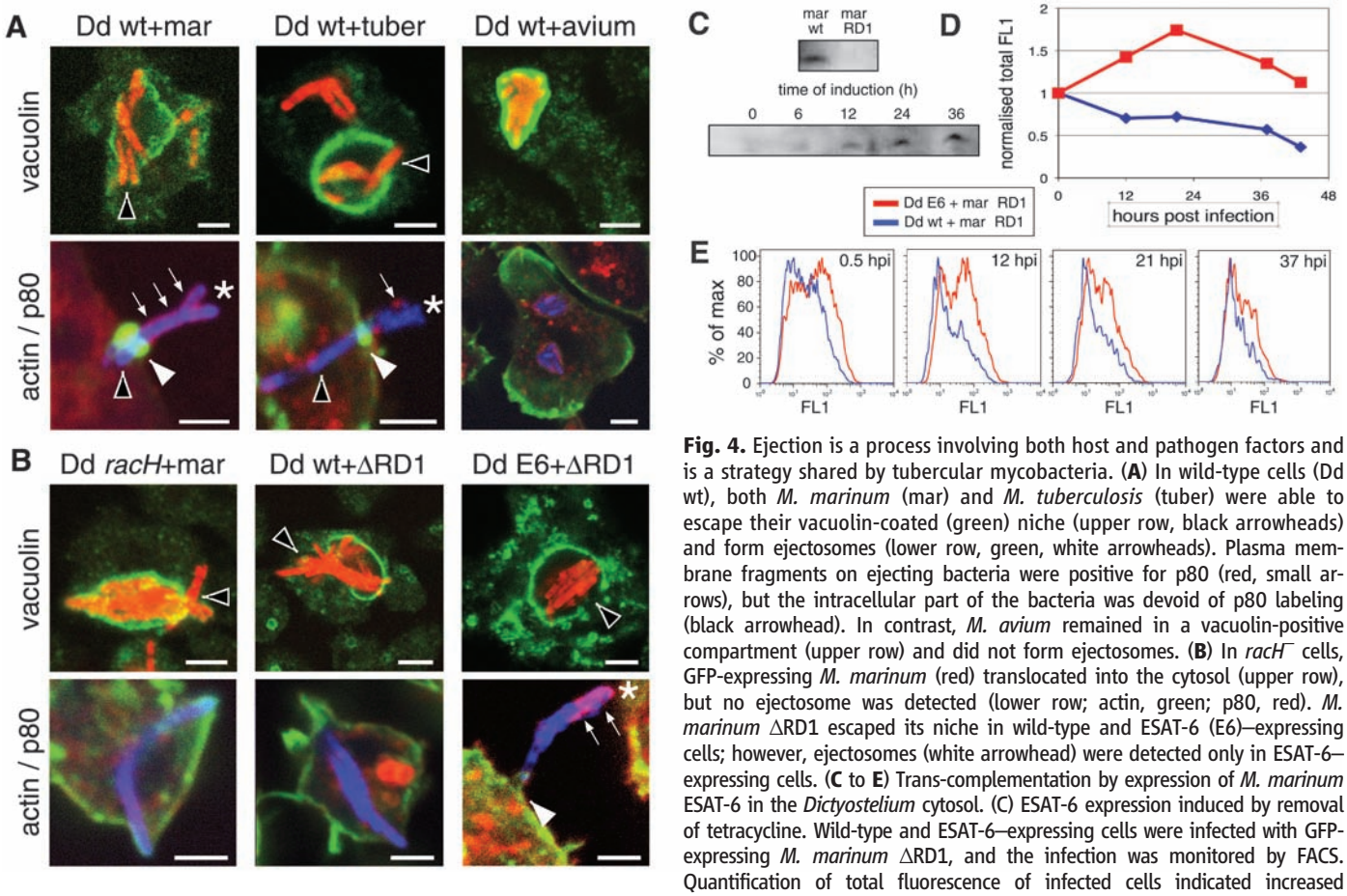

Fig. 4. Ejection is a process involving both host and pathogen factors and is a strategy shared by tubercular mycobacteria. (**A**) In wild-type cells (Dd wt), both *M. marinum* (mar) and *M. tuberculosis* (tuber) were able to escape their vacuolin-coated (green) niche (upper row, black arrowheads) and form ejectosomes (lower row, green, white arrowheads). Plasma membrane fragments on ejecting bacteria were positive for p80 (red, small arrows), but the intracellular part of the bacteria was devoid of p80 labeling (black arrowhead). In contrast, *M. avium* remained in a vacuolin-positive compartment (upper row) and did not form ejectosomes. (**B**) In *racH*$^{-}$ cells, GFP-expressing *M. marinum* (red) translocated into the cytosol (upper row), but no ejectosome was detected (lower row; actin, green; p80, red). *M. marinum* ΔRD1 escaped its niche in wild-type and ESAT-6 (E6)–expressing cells; however, ejectosomes (white arrowhead) were detected only in ESAT-6–expressing cells. (**C** to **E**) Trans-complementation by expression of *M. marinum* ESAT-6 in the *Dictyostelium* cytosol. (C) ESAT-6 expression induced by removal of tetracycline. Wild-type and ESAT-6–expressing cells were infected with GFP-expressing *M. marinum* ΔRD1, and the infection was monitored by FACS. Quantification of total fluorescence of infected cells indicated increased replication of *M. marinum* ΔRD1 in ESAT-6 expressers [(D), red curve, normalized to the total fluorescence values at time 0.5 hpi]. Infected ESAT-6 expressers with high fluorescence (FL1) persisted longer [(E), red curve] than did infected wild-type *Dictyostelium* [(D) and (E), blue curve].

that necessitates host and pathogen factor(s) and is crucial for the maintenance of an infection in a cell population.

Conceptually, the ejectosome bears intriguing analogies with the contracting actin ring formed during purse-string closure of membrane wounds in *Xenopus* oocytes (*27*) and during the repair of toxin-induced macroapertures in endothelial cells (*28*). Because lytic release from a single-celled amoeba would be lethal, the ejectosome may have first evolved as a plasma membrane repair mechanism. This concerted and mutually beneficial strategy might have been conserved during evolution to ensure the dissemination of mycobacteria between the immune phagocytes of their metazoan host.

Dictyostelium can be thought of as a rudimentary innate immune phagocyte, and this model has allowed us to identify a conserved strategy for egress and cell-to-cell spread that is shared by *M. marinum* and *M. tuberculosis*.

References and Notes

1. G. Chen, O. Zhuchenko, A. Kuspa, *Science* **317**, 678 (2007).
2. L. M. Stamm, E. J. Brown, *Microbes Infect.* **6**, 1418 (2004).
3. T. P. Stinear *et al.*, *Genome Res.* **18**, 729 (2008).
4. D. M. Tobin, L. Ramakrishnan, *Cell. Microbiol.* **10**, 1027 (2008).
5. D. G. Russell, *Nat. Rev. Microbiol.* **5**, 39 (2007).
6. C. L. Cosma, D. R. Sherman, L. Ramakrishnan, *Annu. Rev. Microbiol.* **57**, 641 (2003).
7. K. H. Rohde, R. B. Abramovitch, D. G. Russell, *Cell Host Microbe* **2**, 352 (2007).
8. M. Hagedorn, T. Soldati, *Cell. Microbiol.* **9**, 2716 (2007).
9. L. M. Stamm *et al.*, *J. Exp. Med.* **198**, 1361 (2003).
10. N. van der Wel *et al.*, *Cell* **129**, 1287 (2007).
11. J. Smith *et al.*, *Infect. Immun.* **12**, 5478 (2008).
12. A. M. Abdallah *et al.*, *Nat. Rev. Microbiol.* **5**, 883 (2007).
13. T. Tan, W. L. Lee, D. C. Alexander, S. Grinstein, J. Liu, *Cell. Microbiol.* **8**, 1417 (2006).
14. H. E. Volkman *et al.*, *PLoS Biol.* **2**, e367 (2004).
15. L. Y. Gao *et al.*, *Mol. Microbiol.* **53**, 1677 (2004).
16. S. C. Derrick, S. L. Morris, *Cell. Microbiol.* **9**, 1547 (2007).
17. M. Chen, H. Gan, H. G. Remold, *J. Immunol.* **176**, 3707 (2006).
18. J. M. Davis, L. Ramakrishnan, *Cell* **136**, 37 (2009).
19. T. F. Byrd, G. M. Green, S. E. Fowlston, C. R. Lyons, *Infect. Immun.* **66**, 5132 (1998).
20. J. Castro-Garza, C. H. King, W. E. Swords, F. D. Quinn, *FEMS Microbiol. Lett.* **212**, 145 (2002).
21. F. Carlsson, E. J. Brown, *J. Cell. Physiol.* **209**, 288 (2006).
22. J. M. Davis *et al.*, *Immunity* **17**, 693 (2002).
23. L. M. Stamm *et al.*, *Proc. Natl. Acad. Sci. U.S.A.* **102**, 14837 (2005).
24. E. Lee, D. A. Knecht, *Traffic* **3**, 186 (2002).
25. S. H. Zigmond, *Cell Motil. Cytoskeleton* **25**, 309 (1993).
26. B. P. Somesh, C. Neffgen, M. Iijima, P. Devreotes, F. Rivero, *Traffic* **7**, 1194 (2006).
27. C. A. Mandato, W. M. Bement, *J. Cell Biol.* **154**, 785 (2001).
28. L. Boyer *et al.*, *J. Cell Biol.* **173**, 809 (2006).

29. We gratefully acknowledge L. Ramakrishnan and C. Cosma for providing strains of *M. marinum,* various GFP expression vectors, and advice; G. Griffiths for GFP-expressing *M. avium*; B. C. VanderVen for providing GFP-expressing *M. tuberculosis*; F. Rivero and M. Maniak for providing *Dictyostelium* mutant strains; C. Bauer of the National Center of Competence in Research imaging platform for his help with microscopy; P. Walther and E. Schmid for their expert help with the SEM; and D. Soldati for critical reading of the manuscript. The work was supported by the Swiss National Science Foundation in the form of a grant to T.S. and an individual short-term fellowship to M.H. The T.S. group participates in the NEMO (nonmammalian experimental models for the study of bacterial infections) network supported by the Swiss 3R Foundation. D.G.R. and K.H.R. are supported by grants AI 067027 and HL 055936 from the U.S. NIH.

Supporting Online Material

www.sciencemag.org/cgi/content/full/323/5922/1729/DC1
Materials and Methods
Figs. S1 to S9
References
Movies S1 to S7

5 December 2008; accepted 6 February 2009
10.1126/science.1169381

Critical Population Density Triggers Rapid Formation of Vast Oceanic Fish Shoals

Nicholas C. Makris,[1]* Purnima Ratilal,[2] Srinivasan Jagannathan,[1] Zheng Gong,[2] Mark Andrews,[2] Ioannis Bertsatos,[1] Olav Rune Godø,[3] Redwood W. Nero,[4] J. Michael Jech[5]

Similarities in the behavior of diverse animal species that form large groups have motivated attempts to establish general principles governing animal group behavior. It has been difficult, however, to make quantitative measurements of the temporal and spatial behavior of extensive animal groups in the wild, such as bird flocks, fish shoals, and locust swarms. By quantifying the formation processes of vast oceanic fish shoals during spawning, we show that (i) a rapid transition from disordered to highly synchronized behavior occurs as population density reaches a critical value; (ii) organized group migration occurs after this transition; and (iii) small sets of leaders significantly influence the actions of much larger groups. Each of these findings confirms general theoretical predictions believed to apply in nature irrespective of animal species.

Many species of oceanic fish band together in large shoals (*1*, *2*) that can span tens of kilometers and involve hundreds of millions of individuals. Grouping leads to survival advantages through enhanced spawning, predator avoidance, and feeding mechanisms (*3*–*6*). Little information has been available about the formation process and behavior of large oceanic fish shoals. Traditional methods rely on local measurements from slow-moving research vessels that enable sampling of only a small fraction of a shoal during an entire survey, typically by vertical profiling, and cannot distinguish between temporal and spatial changes (*7*–*9*). Here, we describe fundamental temporal and spatial processes by which vast oceanic shoals form by observation of entire shoals in space and time over their full horizontal extent and relate these processes to likely governing mechanisms. We do this using Ocean Acoustic Waveguide Remote Sensing (OAWRS) (*10*), which enables instantaneous imaging and continuous monitoring of oceanic fish populations over tens of thousands of square kilometers.

We studied *Clupea harengus* (Atlantic herring), because they are known to regularly mass in large shoals for spawning at specific times and locations like other clupeid fish. Clupeids are keystone species in many of the world's major marine ecosystems, from the coastal upwelling regions of South America and Africa to the temperate areas of the Nordic Sea, Baltic Sea, and Gulf of Maine (*11*). They provide trophic links between plankton, such as krill, and larger predators, such as humans, birds, whales, dolphins, seals, sharks, cod, pollock, and haddock (*12*). Georges Bank is one of the primary spawning grounds for herring in the Gulf of Maine, which was once one of the world's most productive fisheries before its collapse in the 1970s (*8*, *13*). Herring migrate to Georges Bank to spawn in early autumn, typically September and October, from offshore regions of the Gulf of Maine and beyond (*8*, *14*).

We used OAWRS to monitor herring behavior continuously on Georges Bank during the autumn 2006 spawning season, in conjunction with traditional conventional fish-finding sonar (CFFS) (*9*) and trawl (*8*) line transects. The OAWRS system instantaneously imaged areas spanning 100 km in diameter every 75 s and so enabled continuous time-space monitoring of shoaling behavior over an ecosystem scale. We focused our experiment on regions where herring shoals were most likely to form. We determined these regions by analysis of a decade of National Marine Fisheries Services (NMFS) annual surveys made with conventional line-transect methods. These historic data showed that the herring traditionally first mass in dense layers near the seafloor along the northern flank of Georges Bank in deeper water (150 to 200 m) before spawning just to the south in shallow waters on the bank (<50 m).

We found shoal formation to depend on initial conditions and to ensue rapidly when these conditions were satisfied. First, we found that the preexisting population density of diffusely scattered individuals had to reach a critical threshold of 0.2 fish per square meter (fish/m^2). Given this, we found shoal formation to consistently commence in a highly organized fashion near sunset, apparently triggered by reduction in light level. The process depended on orderly and coherent horizontal convergences of leading individuals to produce denser and thicker vertical layers at a few discrete horizontal locations. This process occurred within favored bathymetric contours (Fig. 1). From preexisting diffuse background levels consistent with scattered individuals displaying no coherent interaction (Fig. 1A), small catalyzing clusters of much higher areal population density emerge in OAWRS imagery within the favored bathymetric contours (160 to 190 m) just before sunset (Fig. 1B), introducing bursts of coherent horizontal structure. Simultaneous vertical profiles from CFFS line transects show that, before the leading clusters form, the fish are widely distributed in a diffuse low-density layer within 5 m of the seafloor (Fig. 2A). The leading clusters (100-m horizontal scale) form as thick (10 to 30 m in the vertical) and dense groups within 20 to 40 m of the seafloor (Fig. 2A), when the fish rise slightly and converge in the horizontal as seen in both OAWRS (Fig. 1, A and B) and CFFS data (Fig. 2A). Formation of these denser clusters requires horizontal convergence by conservation of mass from the original thin, low-density layers.

The emergence of leading clusters of high population density set off chain reactions that caused rapid growth into vast shoals. We found the growth to propagate horizontally outward as convergence waves emanating from the cluster initiation points, which appeared to act as sources of the wave action. The waves propagated over tens of kilometers in tens of minutes, as can be seen for example in Fig. 1, A to F, and Fig. 3. The 3.0 to 6.0 m/s propagation speed of these waves (Fig. 3A) is an order of magnitude faster than the typical 0.2 m/s speed at which herring swim (*15*) and so is likely the apparent speed (*10*) of sequences of local synchronous convergence actions and reactions (*16*, *17*) by members of the shoal. Such local actions define a propagating compressional wave in a medium of variable density (*18*). Our observations provide experimental evidence for the existence of compressional waves in vast fish shoals, which have been predicted in physical theories (*19*). We found these shoal-forming waves to be highly directional and to propagate most rapidly along the direction of favored bathymetric contours (Fig. 1, A to F). Before the waves appeared, areal population density slowly increased at a rate of 0.06 to 0.1 fish/m^2 per hour (Fig. 3, B and C). As soon as the critical density of 0.2 fish/m^2 was reached (Fig. 3, B and C), coherent shoal-forming waves appeared (Fig. 3A), and the population density rapidly increased at a rate of roughly 5 fish/m^2 per hour (Fig. 3, B and C).

After formation, we observed growth in shoal width and population as light levels remained low in the evening. Growth normal to the favored bathymetric contours appeared to be from movement of surrounding diffusely scattered fish populations to the shoal, which acted as an attractor (Fig. 1, G to L). These vast shoals, sometimes extending continuously for 40 km (Fig. 1I), would remain stable throughout the evening and dissipate as light levels increased with sunrise. When viewed vertically with CFFS transects, the shoals evolved from small, isolated, catalyzing clusters (Fig. 2A) to extensive, dense layers within 20 to 40 m of the sea floor, but typically disconnected from it by a few meters (Fig. 2B). The layer growth required horizontal convergence by conservation of fish mass.

Once vast shoals formed, they migrated at speeds consistent with the synchronous swimming of hundreds of millions of individual fish, in accord with the predictions of general behavioral models. The migrations, however, were not in a random direction, as in some theoretical models (*19*–*21*), but toward southern spawning grounds on Georges Bank, apparently for synchronized reproductive activities. Such a migration of the 3 October shoal's southern edge, from near the alpha-to-omega CFFS

[1]Massachusetts Institute of Technology, 77 Massachusetts Avenue, Cambridge, MA 02139, USA. [2]Northeastern University, 360 Huntington Avenue, Boston, MA 02115, USA. [3]Institute of Marine Research, Post Office Box 1870, Nordnes, N-5817 Bergen, Norway. [4]Southeast Fisheries Science Center, 3209 Frederic Street, Pascagoula, MS 39568, USA. [5]Northeast Fisheries Science Center, 166 Water Street, Woods Hole, MA 02543, USA.

*To whom correspondence should be addressed. E-mail: makris@mit.edu

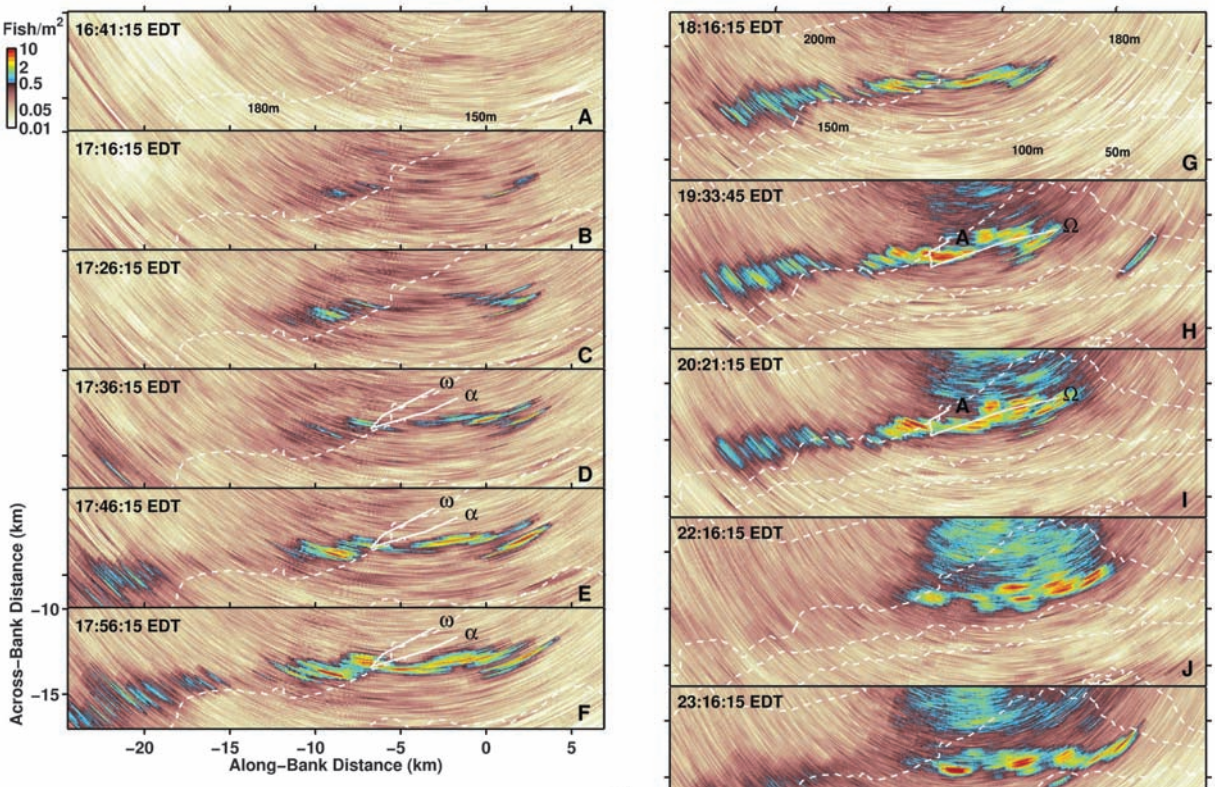

Fig. 1. Millions of Atlantic herring abruptly form vast shoals on 3 October 2006 just before sunset, which was at 18:08 EDT, on the northern flank of Georges Bank. (**A** to **F**) Sequence of instantaneous OAWRS areal density (fish/m^2) images illustrating initiation and along-bank shoal growth over tens of kilometers in tens of minutes. (**G** to **L**) Spatial and temporal evolution of massive herring shoals during the evening of 3 October 2006. Instantaneous OAWRS images taken over 6 hours illustrate shoal thickening in the across-bank direction and gradual migration of its southern edge. Roughly 250 million herring (50,000 tons) are imaged in (L), or 5 to 20% of the entire Georges Bank stock based on NMFS CFFS line-transect surveys (Fig. 4E) and combined CFFS, bottom trawls, and catch landings (*12*). Our simultaneous capture trawl surveys show that over 99% of the fish imaged by OAWRS within the dense shoals are Atlantic herring, combined with a small fraction of Acadian redfish (*Sebastes fasciatus*) and haddock (*Melanogrammus aeglefinus*). The moored OAWRS source is the coordinate origin in all OAWRS images, at 42.2089°N, 67.6892°W on 3 October. The positive vertical axis in all OAWRS images points 16° counter-clockwise of true north. The dashed lines indicate water depth contours.

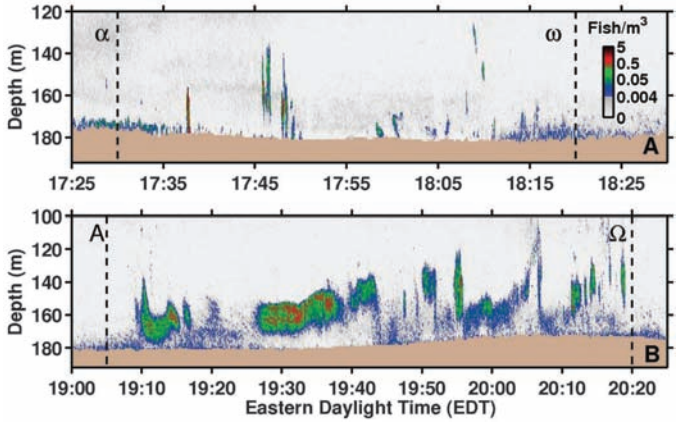

Fig. 2. Time-depth profile of fish volumetric density (fish/m^3) measured by CFFS along: (**A**) the V-shaped line transect shown in Fig. 1, D to F, and (**B**) the J-shaped line transect through the shoal shown in Fig. 1, H and I. Black dashed vertical lines correspond to transect start (alpha) and end (omega) points.

transect of Fig. 1H to the 150-m contour 2 to 4 km to the south in Fig. 1L, is evident in the most populous region and quantified in Fig. 3A. The migration is slow, roughly 0.2 m/s (Fig. 3A), which is consistent with the average swimming speed of herring in a school (*15*). Another example of a southern migration appears in Fig. 4 for 29 September. Shoals first form as usual by sunset (Fig. 4, A and B). Massive portions of their southern edges then migrate upslope from depths greater than 50 m (Fig. 4B) to spawning grounds 2 to 3 km to the south where depths are less than 50 m (Fig. 4D). The migration speed is similar to that observed on 3 October, following that expected for the material displacement of millions of swimming herring. Dense evening shoals sometimes developed a diffuse northern component (Fig. 1, H to L), which could indicate a north-south migration route for spawning herring from offshore regions of the Gulf of Maine to Georges Bank. The southern edge of the shoals, in contrast, was typically sharp (Fig. 1, G to L), following the general bathymetric contour of the spawning grounds of Georges Bank, indicating the leading edge of a synchronous mass migration.

We found the overall process of rapid shoal formation, triggered by attainment of a critical density of 0.2 fish/m^2 near sunset, and subsequent migration toward spawning grounds to define a regular diurnal behavioral pattern that was consistently observed (*22*) during our roughly 1-week measurement period as shown in Figs. 1 to 4 and Figs. S1 to S4. The

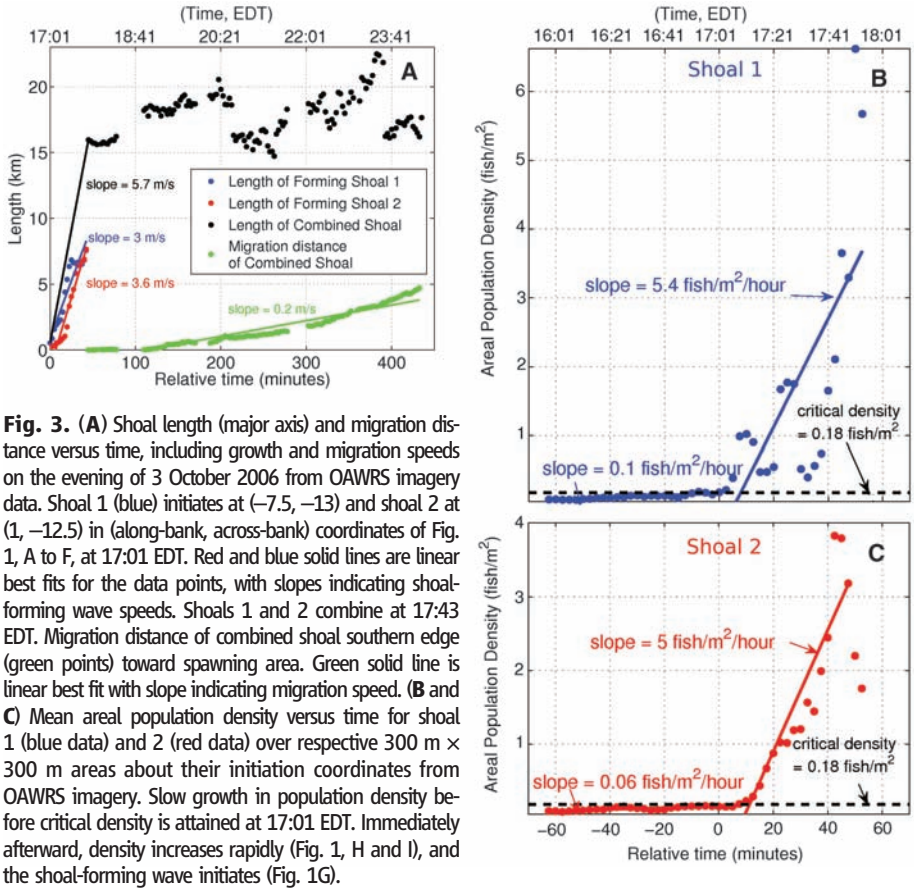

Fig. 3. (**A**) Shoal length (major axis) and migration distance versus time, including growth and migration speeds on the evening of 3 October 2006 from OAWRS imagery data. Shoal 1 (blue) initiates at (–7.5, –13) and shoal 2 at (1, –12.5) in (along-bank, across-bank) coordinates of Fig. 1, A to F, at 17:01 EDT. Red and blue solid lines are linear best fits for the data points, with slopes indicating shoal-forming wave speeds. Shoals 1 and 2 combine at 17:43 EDT. Migration distance of combined shoal southern edge (green points) toward spawning area. Green solid line is linear best fit with slope indicating migration speed. (**B** and **C**) Mean areal population density versus time for shoal 1 (blue data) and 2 (red data) over respective 300 m × 300 m areas about their initiation coordinates from OAWRS imagery. Slow growth in population density before critical density is attained at 17:01 EDT. Immediately afterward, density increases rapidly (Fig. 1, H and I), and the shoal-forming wave initiates (Fig. 1G).

evidence suggests the primary biological function of the shoals is a prelude to synchronized spawning. Close proximity of individuals can induce synchronous reproductive development through visual and olfactory stimulus (*17*). Synchronous development is often critical because each female must typically produce a large number of eggs within very tight time constraints to enable group spawning (*17*, *23*). Shoal formation at greater depths allows these activities to proceed with reduced risk of attack from predators (*24*), such as pilot whales, porpoise, and tuna, that prefer to hunt in the shallower spawning grounds (*4*, *25*). Evening formation allows matching and subsequent migration to spawning grounds to occur under cover of darkness, with more safety from predator attack. The shoaling behavior we observed is evidently unrelated to diurnal feeding (*4*) activities, because trawl samples obtained during our survey show 99% of the herring have empty stomachs and have not yet spawned. This is consistent with historic observations showing that herring do not feed during the spawning period (*26*).

More generally, our observations during the spawning period show the formation processes of large oceanic fish shoals (i) require initial conditions on population density and external stimuli, such as light level; (ii) follow the actions of a small number of leaders; (iii) rely upon extremely rapid and efficient time-space convergence events that propagate as coherent waves over great distances by chain reaction; and (iv) involve extensive horizontal structures that evolve in a highly organized and predictable

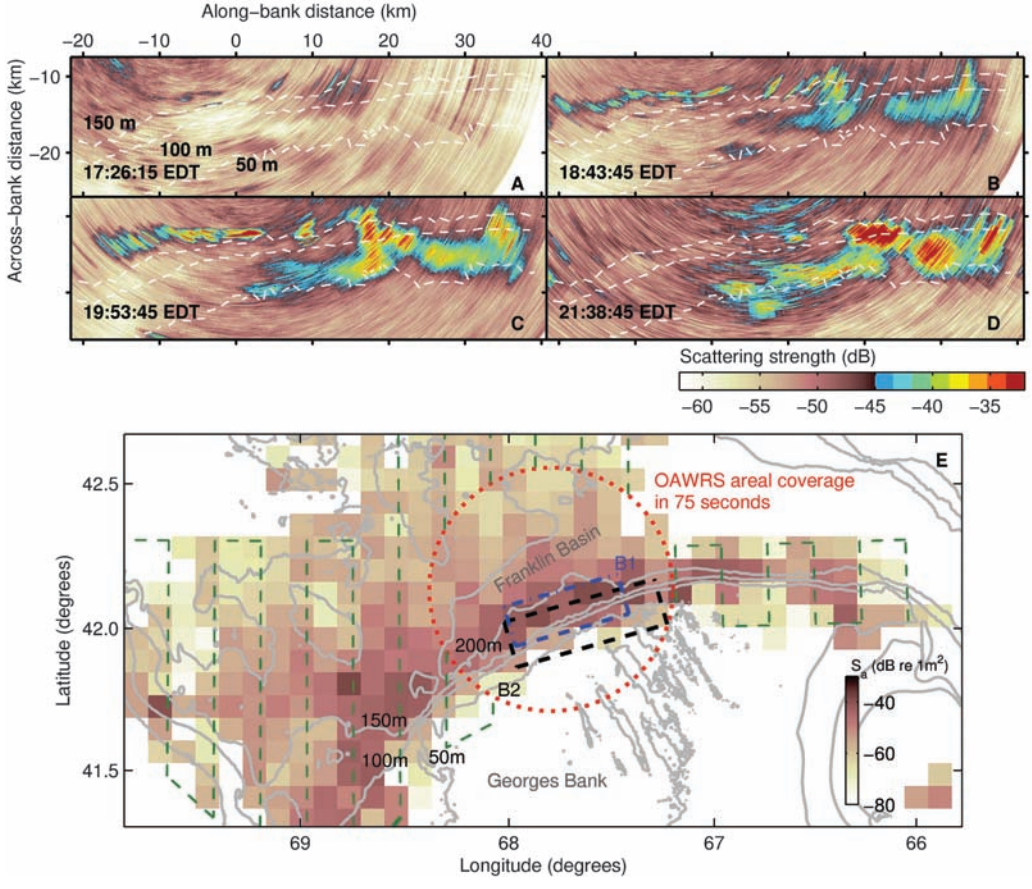

Fig. 4. (**A** to **D**) Sequence of OAWRS scattering strength (*32*) images illustrates formation, growth, and subsequent southern migration of herring shoals toward the Georges Bank spawning grounds on the evening of 29 September 2006. Sunset was at 18:15 EDT. Same region as Fig. 1, G to L. (**E**) Backscattering strength s_a (*33*) at 5 by 5 nautical miles (1 nmi = 1852 m) grid obtained by averaging CFFS line-transect data from 1999 through 2005 NMFS Annual Fall Herring Surveys (*34*). Boxes B1 and B2 are regions shown in Fig. 1, G to L, and Fig. 4, A to D, respectively. Regions of maximum herring concentration are consistent between OAWRS 2006 imagery (Fig. 1) and NMFS 6-year average (Fig. 4E). Red circle indicates OAWRS areal coverage in 75 s. Green dashed line indicates the line transect of a typical 2-week NMFS survey, not shown within red circle.

manner. The rapidity with which these shoal-forming waves spread once the initial conditions are satisfied is indicative of the advantage the group has over the isolated individual in transferring information over great distances. Our observations also provide ecosystem-scale evidence that a critical population density triggers rapid transition from disordered to highly synchronized behavior, and small groups of leaders often play crucial roles in affecting the actions of much larger groups, as has recently been predicted in general theoretical investigations (*19*, *21*, *27*–*29*), simulations, and laboratory experiments (*26*, *27*) about animal group behavior (*20*, *30*, *31*). These findings provide information essential to the conservation of marine ecosystems that vast oceanic fish shoals inhabit.

References and Notes

1. J. H. S. Blaxter, J. R. Hunter, *Adv. Mar. Biol.* **20**, 1 (1982).
2. D. J. Hoare, G. D. Ruxton, J.-G. J. Godin, J. Krause, *Oikos* **89**, 546 (2000).
3. T. J. Pitcher, J. K. Parrish, in *The Behaviour of Teleost Fishes*, T. J. Pitcher, Ed. (Chapman & Hall, London, 1993), pp. 363–439.
4. M. Milinski, in *Predation Risk and Feeding Behaviour*, T. J. Pitcher, Ed. (Chapman & Hall, London, 1993), pp. 285–305.
5. D. P. Croft, J. Krause, I. D. Couzin, T. J. Pitcher, *Fish Fish.* **4**, 138 (2003).
6. T. J. Pitcher, in *Encyclopedia of Ocean Sciences*, J. H. Steele, K. K. Turekian, S. A. Thorpe, Eds. (Academic Press, London, 2001), pp. 978–987.
7. O. R. Godø *et al.*, *ICES J. Mar. Sci.* **61**, 1093 (2004).
8. W. J. Overholtz, J. M. Jech, L. Michaels, L. D. Jacobson, P. J. Sullivan, *J. Northwest Atl. Fish. Sci.* **36**, 127 (2006).
9. D. N. MacLennan, E. J. Simmonds, *Fisheries Acoustics* (Chapman & Hall, London, 1992).
10. N. C. Makris *et al.*, *Science* **311**, 660 (2006).
11. C. Ray, C. R. Robins, J. Douglass, R. T. Peterson, *Peterson Field Guide: Atlantic Coast Fishes* (Houghton Mifflin, New York, 1999).
12. W. J. Overholtz, J. S. Link, *ICES J. Mar. Sci.* **64**, 83 (2007).
13. W. J. Overholtz, *Fish. Res.* **57**, 237 (2002).
14. V. N. Zinkevich, *ICNAF Bull.* **4**, 101 (1967).
15. I. Huse, E. Ona, *ICES J. Mar. Sci.* **53**, 863 (1996).
16. L. Nottestad *et al.*, *Sarsia* **80**, 277 (1996).
17. G. Skaret, L. Nottestad, A. Ferno, A. Johannessen, B. E. Axelsen, *Aquat. Living Resour.* **16**, 299 (2003).
18. J. W. S. Rayleigh, in *The Theory of Sound*, J. W. S. Rayleigh, R. B. Lindsay, Eds. (Dover, New York, 1976), vol. 2, pp. 1–48.
19. J. Toner, Y. Tu, *Phys. Rev. E* **58**, 4828 (1998).
20. G. Gregoire, H. Chate, *Phys. Rev. Lett.* **92**, 025702 (2004).
21. T. Vicsek, A. Czirok, E. Ben-Jacob, I. Cohen, O. Schochet, *Phys. Rev. Lett.* **75**, 1226 (1995).
22. Materials and methods are available as supporting material on *Science* Online.
23. R. Vabo, G. Skaret, *Ecol. Modell.* **214**, 125 (2008).
24. S. Mackinson, *J. Fish Biol.* **55**, 972 (1999).
25. R. Toresen, *ICES J. Mar. Sci.* **48**, 15 (1991).
26. J. S. Link, J. Brunett, *J. Fish Biol.* **59**, 783 (2001).
27. J. Buhl *et al.*, *Science* **312**, 1402 (2006).
28. S. G. Reebs, *Anim. Behav.* **59**, 403 (2000).
29. I. D. Couzin, J. Krause, N. R. Franks, S. Levin, *Nature* **433**, 513 (2005).
30. D. J. T. Sumpter, *Philos. Trans. R. Soc. London Ser B* **361**, 5 (2006).
31. S. V. Viscido, J. K. Parrish, D. Grunbaum, *Ecol. Modell.* **183**, 347 (2005).
32. R. J. Urick, *Principles of Underwater Sound* (McGraw-Hill, New York, 3rd ed., 1983).
33. D. N. MacLennan, P. G. Fernandes, J. Dalen, *ICES J. Mar. Sci.* **59**, 365 (2002).
34. J. M. Jech, W. L. Michaels, *Can. J. Fish. Aquat. Sci.* **63**, 2225 (2006).

35. This research was supported by the National Oceanographic Partnership Program, the Office of Naval Research, and the Alfred P. Sloan Foundation and is a contribution to the Census of Marine Life. We would like to thank the science parties, officers, and crew of the research vessels *Oceanus*, *Endeavor*, *Delaware II*, and *Hugh Sharp*.

Supporting Online Material

www.sciencemag.org/cgi/content/full/323/5922/1734/DC1
Materials and methods
Figs. S1 to S6
References
Movie S1

8 December 2008; accepted 19 February 2009
10.1126/science.1169441

Genetic Contribution to Variation in Cognitive Function: An fMRI Study in Twins

Jan Willem Koten Jr.,[1,2]* Guilherme Wood,[3] Peter Hagoort,[4,7] Rainer Goebel,[5,8] Peter Propping,[6] Klaus Willmes,[1] Dorret I. Boomsma[2]

Little is known about the genetic contribution to individual differences in neural networks subserving cognition function. In this functional magnetic resonance imaging (fMRI) twin study, we found a significant genetic influence on brain activation in neural networks supporting digit working memory tasks. Participants activating frontal-parietal networks responded faster than individuals relying more on language-related brain networks. There were genetic influences on brain activation in language-relevant brain circuits that were atypical for numerical working memory tasks as such. This suggests that differences in cognition might be related to brain activation patterns that differ qualitatively among individuals.

The direct link between genes, brain, and behavior can be difficult to establish (*1*). Structural and functional investigations in the human and mouse brain suggest that some genes are expressed in highly specific brain regions, whereas other genes have more global effects (*1*–*4*). The total heritability of individual differences can be examined with twin studies (*5*–*8*). Functional magnetic resonance imaging (fMRI) studies investigating specific brain regions assumed to subserve some cognitive function did not demonstrate high heritability of brain activity (*9*–*14*). Genetic influences on brain activation in areas that typically subserve a cognitive function might be modest because these areas will be activated similarly among humans. By contrast, brain regions activated in some individuals only might be better candidates for genetic analysis. Thus, genetic effects should be tested cortex-wide.

Structural and functional brain investigations suggest that brain areas that are similarly activated among humans may be embedded in larger brain networks that vary among individuals (*1*, *4*), possibly causing individual differences in cognition. An attractive candidate for the study of genetic influences on brain networks is working memory for digits under arithmetic distraction. Heritability estimates for behavioral measures in this task are high (*15*), and stable individual differences in the spatial organization of function-carrying areas were shown (*16*). A distractor task causes an interruption of verbal rehearsal, leading to rapid forgetting (*17*). The decay model of working memory (*18*, *19*) states that numbers can be retained without explicit verbal rehearsal, but it does not specify neural correlates of these memory processes. The triple-code model (*20*) claims that number processing and arithmetic require both magnitude and language-related number representations in inferior parietal cortex, angular gyrus, and perisylvian cortex. Individuals holding numbers in memory in a language-related or magnitude code suffer from code interference when executing arithmetic tasks. Employing early motor coding routes protects memory traces from distraction (*21*), which corresponds to the importance of finger representations for number processing also in adulthood (*22*).

For genetic fMRI studies, appropriate brain alignment, sufficient individual differences, reliability, and statistical power are of core importance (*6*, *23*–*25*). We used an extended twin design consisting of male monozygotic (MZ) twins with an additional nontwin brother, where every brother is related to both twins. We examined reaction times (RT) as a measure of proficiency and blood oxygen level–dependent (BOLD) response as a measure of relative brain (de)activation (*26*) during two identical scanning sessions in all participants. These two observations of the phenotypes of interest were entered into a genetic structural equation model (SEM) that estimates additive genetic effects corrected for measurement error (*23*). Heritability h^2 was expressed as the percentage of reliable variance accounted for

[1]Section Neuropsychology, RWTH Aachen University, Germany. [2]Biological Psychology, Vrije Universiteit, Amsterdam, Netherlands. [3]Institute of Psychology, Paris-Lodron University Salzburg, Austria. [4]Donders Institute for Brain, Cognition, and Behaviour, Radboud University Nijmegen, Netherlands. [5]Department of Cognitive Neuroscience, Faculty of Psychology, Maastricht University, Netherlands. [6]Institute of Human Genetics, University of Bonn, Germany. [7]Max Planck Institute for Psycholinguistics, Nijmegen, Netherlands. [8]Netherlands Institute for Neuroscience, an institute of the Royal Netherlands Academy of Arts and Sciences (KNAW), Amsterdam, Netherlands.

*To whom correspondence should be addressed. E-mail: jan.koten@gmx.de

by additive genetic factors. With 10 families, sufficient power (0.82) is provided to detect ($\alpha = 0.05$) a heritability of 80% or more after correction for measurement error (accounting for one-sixth of the variance) in a bivariate design (*23*–*25*).

In the digit memory tasks (*15*), participants had to verify (recognition phase) whether a single digit was contained in a previously memorized digit set (encoding phase) that consisted of either two (DTM2) or four (DTM4) digits. The tasks differed in the distraction phase, which consisted of either simple arithmetic interference (additions and subtractions) or of object categorization (fruits, vegetables, kitchen utensils, and tools). The latter was employed with a memory load of four digits (DTC4), because two digits did not provoke sufficient individual differences (*25*).

Heritability of brain activity at the vertex level was estimated for BOLD contrasts (*23*–*27*) separately for the encoding, distraction, and recognition phase of the working memory tasks. A substantial part of response time (tables S2 and S3) and brain activity (Fig. 1) proved to be under genetic influence (red-blue color scale) (*25*) (more detailed images in fig. S10, A to I). Genetic effects were found bilaterally and included visual cortex, angular gyrus, intraparietal sulcus (IPS), temporo-parietal junction, motor and premotor cortex, frontal eye field, inferior frontal gyrus, cuneus, and anterior cingulate cortex (ACC), regions related to working memory functions (*28*). Both number interference tasks show genetic influences on larger parts of the brain. Genetic influences were smaller for the DTC4 task that includes less resource competition. Genetic influences were modulated by memory load; they were high for DTM2 during encoding and high for DTM4 during recognition.

Next, we looked for brain areas that were significantly (de)activated among most participants. Brain areas with consistent BOLD responses (transparent yellow in Fig. 1) are considered to be typically supporting a cognitive function. We found fronto-parietal activations regularly encountered in studies of working memory (*28*); in line with the triple-code model, there were activations in perisylvian language-related areas and in inferior parietal number magnitude estimation areas. This activation pattern was found only for the encoding and the distraction phase. Absence of consistent left hemisphere activation during recognition with previous arithmetic distraction indicates number interference, but no interference effect was found for object categorization as a distracting activity.

We focused on individual differences in brain activation patterns because heritability and brain activation maps revealed only partial overlap (Fig. 1). Relative frequency of brain activation (RFBA) maps reflect the percentage of participants with significant brain activation, and standard deviation maps illustrate variation in brain activation contrasts. Figure 2 reports these maps for DTM4 recognition (*25*). Genetic influences on left fronto-parietal, perisylvian and visual cortices go along with higher standard deviations and more individualized brain activation. The partial overlap between heritability and brain activation maps suggests two mechanisms for genetic influences on brain activity: Genes can influence brain activation patterns that reflect systematic quantitative differences in regions characterized by between-subject consistency in a significant BOLD contrast (red-blue, overlaid with transparent yellow in Fig. 1), but genes can also affect qualitative differences in cognition through the employment of qualitatively different neural processes. The latter case might lead to absence of a significant BOLD contrast at the group level (red-blue only), but it is in line with characteristics of genetics: Regions with more intersubject variability are more likely to show genetic effects (*25*). If genes affect typical as well as atypical areas of brain activation subserving cognition, this raises three questions: (i) Are brain activations under genetic influence interpretable in terms of cognition? (ii) Are the two mechanisms for genetic influences on brain activity related to behavior? (iii) May genes affect neural networks that are highly individualized in nature?

Question (i): Digits that suffered from arithmetic interference are retrieved from memory via a right-hemispheric network comprising inferior parietal and temporal areas with low memory load and inferior parietal and inferior frontal areas with high memory load. These brain regions are reminiscent of an evolutionary old memory system found in primates (*29*). The absence of activation in left hemispheric language and number magnitude related cortices suggests that the arithmetic interference tasks impair the number semantic and verbal aspects of digit memory, whereas the object categorization interference task does not (Fig. 1). In the distractor phase, there is a genetic influence on

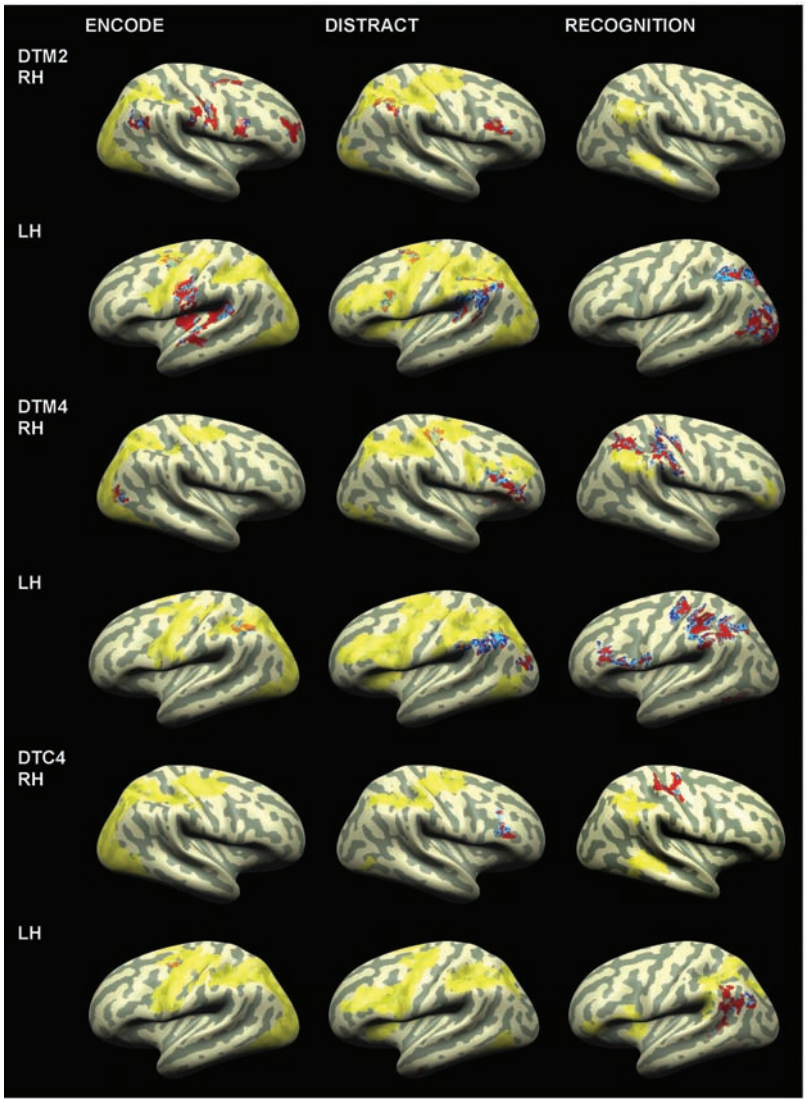

Fig. 1. Error-corrected heritability estimates (red-blue scale, based on data from two identical scanning sessions) of functional brain activations for three working memory tasks, and significant group-level brain activation contrasts against resting baseline (transparent yellow), visualized on an inflated, cortically aligned average brain, separately for left (LH) and right (RH) hemispheres with encoding, distraction, and recognition phase from left to right: DTM2 resp.; DMT4: two resp., four digits memorized with arithmetic distraction; DTC4: four digits memorized with object categorization as distraction. Red: heritability > 80% detectable with statistical power > 0.82; light blue: heritability 60 to 80% (power > 0.44); dark blue: heritability < 60% (power < 0.44).

executive functions subserved by right prefrontal areas for all three tasks (Fig. 1). It is most extended in the high load plus arithmetic distractor condition, exerting the highest load on the executive processor (*18*). In the left hemisphere, there is substantial heritability of activation in the angular gyrus, but only for number interference tasks. The latter finding suggests number-specific retrieval mechanisms from long-term storage (*18*, *20*). In the recognition phase, there is a genetic influence on arithmetic distraction in the left parietal cortex, extending into the frontal cortex for high working memory load. This suggests that retrieval from the working storage (*18*) is under substantial genetic influence, but without significant group activation effect. This implies that conventional brain activation analyses at the group level might be less informative for genetic differences research.

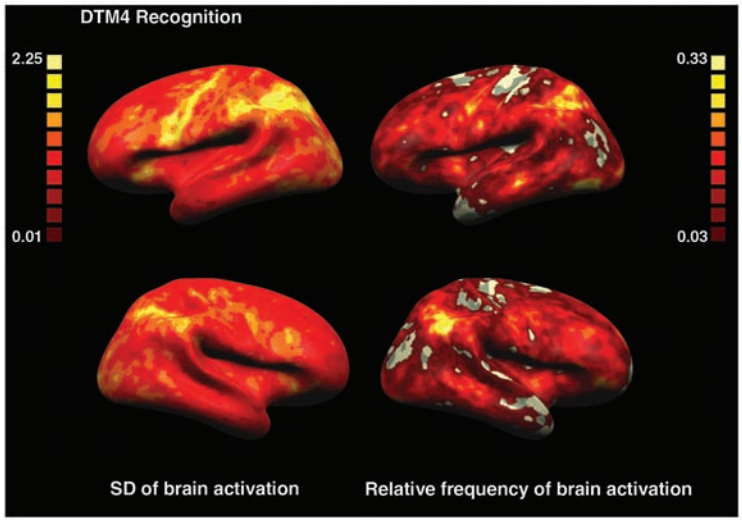

Fig. 2. Standard deviation of averaged (test and retest-run) brain activation *t*-contrast (cognitive activation minus resting baseline) maps (left) as well as relative frequency of brain activation maps (right) for the DTM4 recognition phase.

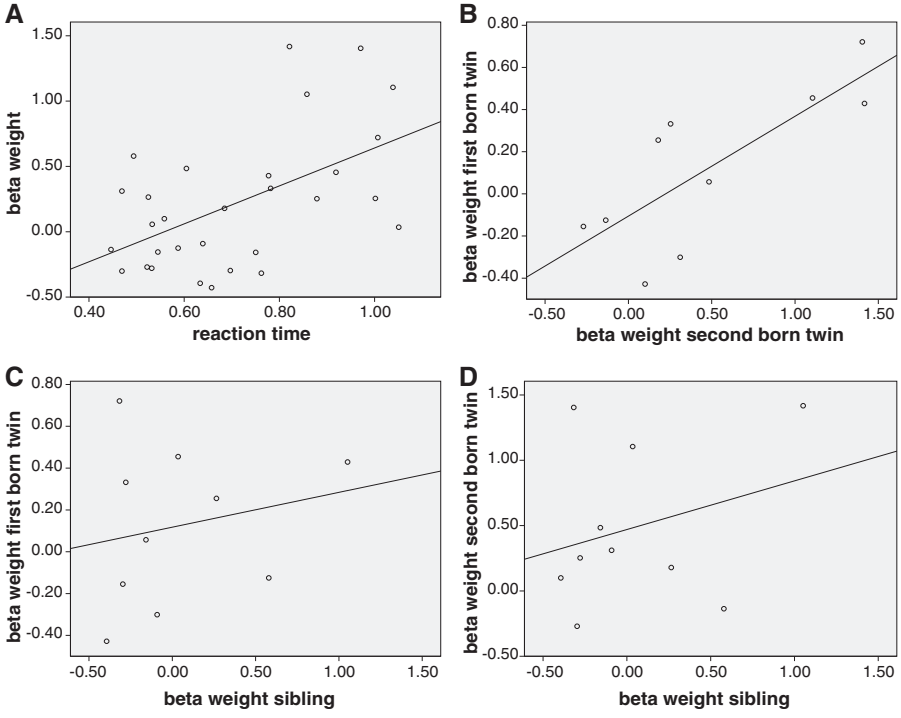

Fig. 3. Relation between observable behavior (RT) in the recognition phase and brain activation in the encoding phase of the DTM2 task in a region of interest located in Broca's area (fig. S3). (**A**) Relation between averaged (test and retest run) RT and brain activation contrast beta values (r = 0.54, P = 0.001, one-sided); (**B** to **D**) Twin and twin-sib correlations of brain activation contrast beta values with some participants showing deactivation and average activation about zero. This region showed a genetic influence on brain activation with h^2 = 0.895 (table S6A), and there was a genetic influence on RT (table S3).

Some participants showed strong activation effects outside the confines of average brain activation, indicating that this does not necessarily represent the relation between brain anatomy and working memory function (*16*).

Question (ii): In particular for the number interference tasks, we showed that memorizing numbers with the involvement of cortices supporting a number magnitude code (IPS) and/or a language-related code (Broca's area) suffered from code interference. This code conflict may be inferred from increased activation in anterior cingulate cortex, which was a good predictor of both response times in the distracting arithmetic and the recognition memory phase (figs. S5 and S6). In contrast, participants activating a finger representation system in anterior IPS monitored by prefrontal cortex showed no conflict and were faster for both response measures.

Broca's area and the angular gyrus were not significantly activated at the group level due to a mixed pattern of activation and deactivation. Nevertheless, for Broca's area there were genetic influences on brain activity (Fig. 3, B to D) that were related to reaction time (Fig. 3A), which in turn was genetically influenced (table S3). In conclusion, encoding processes act like a switch that affects participants' processing for the whole working memory experiment (figs. S4, S7, and S8). Atypical, but genetically influenced, brain activation topology shows its impact through neural networks that directly affect genetically influenced behavior (*1*, *25*).

We found the most extended brain area with significant genetic influences on brain activation outside the confines of the average brain activity maps in the DTM4 recognition phase in the left hemisphere (Fig. 2). One way to demonstrate that this brain activation is not due to regional noise is to show that activations among regions covary.

Question (iii): Activation data for the DTM4 recognition phase from the left brain areas showing genetic influences on brain activation in atypical areas were subjected to SEM. Results suggested the presence of a hippocampus-guided, visual recognition network that is partly under genetic influence. Moreover, an extended network—including areas for language-related number processing as postulated in the triple-code model—was under genetic influence (fig. S9). A similar network has been identified at the anatomical level (*4*).

Our findings demonstrate that genetically influenced differences in brain activation patterns exist, causing qualitative differences in neurocognitive processing routes.

References and Notes

1. A. E. Green *et al.*, *Nat. Rev. Neurosci.* **9**, 710 (2008).
2. A. R. Hariri *et al.*, *Science* **297**, 400 (2002).
3. Allen Institute for Brain Science; http://mouse.brain-map.org/welcome.do.
4. J. E. Schmitt *et al.*, *Cereb. Cortex* **18**, 1737 (2008).
5. A. J. Bartley, D. W. Jones, D. R. Weinberger, *Brain* **120**, 257 (1997).
6. P. M. Thompson *et al.*, *Nat. Neurosci.* **4**, 1253 (2001).
7. C. E. van Beijsterveldt, G. C. van Baal, *Biol. Psychol.* **61**, 111 (2002).
8. D. Boomsma, A. Busjahn, L. Peltonen, *Nat. Rev. Genet.* **3**, 872 (2002).

9. I. E. Sommer, N. F. Ramsey, R. C. Mandl, R. S. Kahn, *Brain* **125**, 2710 (2002).
10. K. L. Sakai, K. Miura, N. Narafu, Y. Muraishi, *Cereb. Cortex* **14**, 1233 (2004).
11. C. Côté *et al*., *Hum. Brain Mapp.* **28**, 482 (2007).
12. S. C. Matthews *et al*., *Neuroimage* **38**, 223 (2007).
13. T. A. Polk, J. Park, M. R. Smith, D. C. Park, *J. Neurosci.* **27**, 13921 (2007).
14. G. A. Blokland *et al*., *Biol. Psychol.* **79**, 70 (2008).
15. P. A. Vernon, *Pers. Individ. Diff.* **10**, 573 (1989).
16. E. Feredoes, G. Tononi, B. R. Postle, *J. Neurosci.* **27**, 11003 (2007).
17. L. R. Peterson, M. J. Peterson, *J. Exp. Psychol.* **58**, 193 (1959).
18. G. J. Hitch, *Cogn. Psychol.* **10**, 302 (1978).
19. A. D. Baddeley, G. J. Hitch, *The Psychology of Learning and Motivation: Advances in Research and Theory* (Academic Press, New York, 1974).
20. S. Dehaene, M. Piazza, P. Pinel, L. Cohen, *Cogn. Neuropsychol.* **20**, 487 (2003).
21. B. R. Postle, *Neuroscience* **139**, 23 (2006).
22. B. Butterworth, *What Counts: How Every Brain Is Hardwired for Math* (Free Press, New York, 1999).
23. M. C. Neale, S. M. Boker, G. Xie, H. M. Maes, (2004). Mx Manual (available at www.vipbg.vcu.edu/~vipbg/software/mxmanual.pdf).
24. D. Posthuma, D. I. Boomsma, *Behav. Genet.* **30**, 147 (2000).
25. Materials and methods are available as supporting material on *Science* Online.
26. A. Shmuel, M. Augath, A. Oeltermann, N. K. Logothetis, *Nat. Neurosci.* **9**, 569 (2006).
27. R. Goebel, F. Esposito, E. Formisano, *Hum. Brain Mapp.* **27**, 392 (2006).
28. T. D. Wager, E. E. Smith, *Cogn. Affect. Behav. Neurosci.* **3**, 255 (2003).
29. O. Gruber, T. Goschke, *Acta Psychol. (Amst.)* **115**, 105 (2004).

30. We thank C. van Baal, K. Amunts, and J. Weber. Grants from the Netherlands Organisation for Scientific Research (NWO) (DN-58-103) and the German Research Foundation (DFG) (WI 1804/3-1&2; PR131/20-1&2) are gratefully acknowledged.

Supporting Online Material

www.sciencemag.org/cgi/content/full/323/5922/1737/DC1
Materials and Methods
Figs. S1 to S10
Tables S1 to S9
References

20 October 2008; accepted 10 February 2009
10.1126/science.1167371

Changes in Temperature Preferences and Energy Homeostasis in Dystroglycan Mutants

Ken-ichi Takeuchi,[1,2] Yoshiro Nakano,[3] Utako Kato,[1] Mizuho Kaneda,[2] Masako Aizu,[2] Wakae Awano,[4] Shigenobu Yonemura,[5] Shigeki Kiyonaka,[6] Yasuo Mori,[6] Daisuke Yamamoto,[7] Masato Umeda[1,2]*

Temperature affects the physiology, behavior, and evolution of organisms. We conducted mutagenesis and screens for mutants with altered temperature preference in *Drosophila melanogaster* and identified a cryophilic (cold-seeking) mutant, named *atsugari* (*atu*). Reduced expression of the *Drosophila* ortholog of dystroglycan (DmDG) induced tolerance to cold as well as preference for the low temperature. A sustained increase in mitochondrial oxidative metabolism caused by the reduced expression of DmDG accounted for the cryophilic phenotype of the *atu* mutant. Although most ectothermic animals do not use metabolically produced heat to regulate body temperature, our results indicate that their thermoregulatory behavior is closely linked to rates of mitochondrial oxidative metabolism and that a mutation in a single gene can induce a sustained change in energy homeostasis and the thermal responses.

Earth has experienced cooling and warming cycles, and organisms exposed to these climate changes either were exterminated or adapted to survive (*1*, *2*). Animals have thermoregulatory systems to adapt their physiological functions, such as energy utilization, growth, reproduction, and locomotion, in response to the wide range of changes in ambient temperature (*3*–*5*). Although mobile animals commonly select a preferred temperature, the biochemical and metabolic processes that underlie the temperature preference remain poorly understood (*5*–*7*).

We isolated several mutants with aberrant temperature preferences; these included warm-seeking mutants, temperature-insensitive mutants, and the cryophilic mutant, designated as *atsugari* (*atu*), described here. On a linear thermal gradient ranging from 12° to 35°C, the third-instar larvae of wild-type *Drosophila* (Canton S) that had grown at 25°C showed a strong temperature preference that peaked at 22°C (Fig. 1, A and C). The *atu* mutant larvae had a preference peak at 18°C (Fig. 1, B and D). The behavioral traits of the *atu* mutant, including assays of olfactory, visual, and locomotory functions, were normal (fig. S1). To exclude the potential effects of the genetic background on the *atu* mutation, we outcrossed the *atu* mutant with the isogenic line w^{1118} and generated P-element excision strains. The *atu* mutant larvae again exhibited low-temperature preference after outcrossing, and a revertant line with precise P-element excision had a normal temperature preference that peaked at 22°C (Fig. 1E).

We cloned the genomic DNA that flanked the P element in the *atu* mutant. A P element had been inserted 251 base pairs (bp) downstream of the transcription initiation site in the first exon of the *Drosophila* ortholog of the mammalian gene for dystroglycan (*DmDG*) (*8*) (fig. S2, A and B). The inserted P element reduced the expression of the DmDG transcript to 15% of that in wild-type larvae (Fig. 1H). The reduced expression of DmDG in the *atu* mutant was confirmed with polyclonal antibodies to DmDG (Fig. 1I). Immunohistolog-

Table 1. Reversal of the *atu* cryophilic phenotype by the transgenic expression of DmDG and phenocopying by an RNA interference–mediated suppression of DmDG in the wild-type larvae. Comparisons among multiple groups were evaluated by two-way analyses of variance (ANOVAs) followed by the Tukey-Kramer post hoc tests. In each group, values not sharing the same superscript letter are significantly different ($P < 0.05$). Effects of the cell-specific transgenic expression in the neurons of the antennomaxillary complex (*19*) (figs. S4 and S5) were also examined. The numerical analyses of data are shown in table S1. μ and σ^2 denote population mean and population variance, respectively.

Flies	Preferred temperature μ (°C), σ^2	
DmDG-overexpression experiment		
atu	$\mu = 18.8^a$	$\sigma^2 = 3.5^2$
Control *atu:UAS-DmDG* line	$\mu = 18.5^a$	$\sigma^2 = 3.5^2$
Control *atu:actin5C-GAL4* line	$\mu = 18.4^a$	$\sigma^2 = 4.5^2$
Ubiquitous-DmDG transgenic *atu* line	$\mu = 21.1^b$	$\sigma^2 = 3.8^2$
Accessory cell–DmDG transgenic *atu* line	$\mu = 18.2^a$	$\sigma^2 = 3.0^2$
Soma sheath cell–DmDG transgenic *atu* line	$\mu = 18.2^a$	$\sigma^2 = 3.0^2$
DmDG-depletion experiment		
w^{1118}	$\mu = 22.3^a$	$\sigma^2 = 2.8^2$
Control *actin5C-GAL4* line	$\mu = 22.0^a$	$\sigma^2 = 3.3^2$
Control *UAS-dsRNA* line	$\mu = 21.0^b$	$\sigma^2 = 3.5^2$
DmDG-depleted line	$\mu = 19.9^c$	$\sigma^2 = 3.7^2$

[1]Institute for Chemical Research, Kyoto University, Uji, Kyoto 611-0011, Japan. [2]The Tokyo Metropolitan Institute of Medical Science, 3-18-22 Honkomagome, Bunkyo-ku, Tokyo 113-8613, Japan. [3]Department of Genetics, Hyogo College of Medicine, 1-1 Mukogawa-cho, Nishinomiya 663-8501, Japan. [4]Mitsubishi Kasei Institute of Life Sciences, Machida, Tokyo 194-8511, Japan. [5]RIKEN Center for Developmental Biology, Chuo-ku, Kobe 650-0047, Japan. [6]Department of Synthetic Chemistry and Biological Chemistry, Graduate School of Engineering, Kyoto University, Kyoto 606-8501, Japan. [7]Graduate School of Life Sciences, Tohoku University, Sendai 980-8578, Japan.

*To whom correspondence should be addressed. E-mail: umeda@scl.kyoto-u.ac.jp

ical analysis showed that DmDG was expressed predominantly in glial cells of the peripheral and central nervous system, epidermis, digestive tract, neuromuscular junction, and ring gland, and the expression of DmDG was severely reduced in all of these tissues of the *atu* mutant (fig. S3). In the *EP2241* mutant fly line that harbors the P-element insertion 330 bp downstream of the transcription initiation site of the *DmDG* gene (*9*), the DmDG expression was reduced in a manner similar to that in the *atu* mutant (Fig. 1I), and the *EP2241* mutant exhibited a significant low-temperature preference (Fig. 1F). The heteroallelic combination of *atu* and *EP2241* also induced a low-temperature preference (Fig. 1G). These results indicate that the *atu* mutation is a hypomorphic allele of the *DmDG* gene and that the reduced expression of DmDG results in the cryophilic phenotype of the *atu* mutant.

The preferred temperature of the DmDG transgenic *atu* line (*actin5C-DmDG* transgenic *atu* line), in which the expression of DmDG was driven by the *actin5C* promotor (fig. S4) in the *atu* background, was significantly higher than that of the control *atu* mutant carrying either *UAS-DmDG* or *actin5C-GAL4* (Table 1). To suppress the expression of DmDG in wild-type larvae, we used double-stranded RNA (dsRNA) interference. We constructed a transgenic line carrying *UAS-dsRNA* and crossed it with the *actin5C-GAL4* driver to induce ubiquitous expression of dsRNA specific for DmDG. Immunoblotting with DmDG-specific antibodies showed that the expression of DmDG was reduced to an amount similar to that in the *atu* mutant (fig. S6). The preferred temperature of the "DmDG-depleted" line was significantly lower than those of the control lines (Table 1). These results confirm that the reduced expression of DmDG induced low-temperature preference in *Drosophila*.

The tolerance of the *atu* mutant larvae to cold was greater than that of the wild type (Fig. 2A), though susceptibility to high temperatures was similar in both strains (Fig. 2B). The cold-tolerant phenotype was completely reversed by the transgenic expression of the DmDG transcript (Fig. 2C) and was reproduced in the "DmDG-depleted" line (Fig. 2D). Thus, reduced expression of DmDG causes cold-tolerance as well as preference for low temperatures. Many ectothermic animals compensate for thermal changes by altering their metabolic rate, and the acclimation to low temperature is frequently associated with an increased metabolic rate (*3*). Indeed, the metabolic rate of the *atu* mutant, measured in terms of the production of CO_2, was almost twice (1.9 times) as high as that of the wild type (Fig. 2E). Concentrations of adenosine 5′-triphosphate (ATP) were significantly increased in the *atu* mutant (Fig. 2F). The activity of

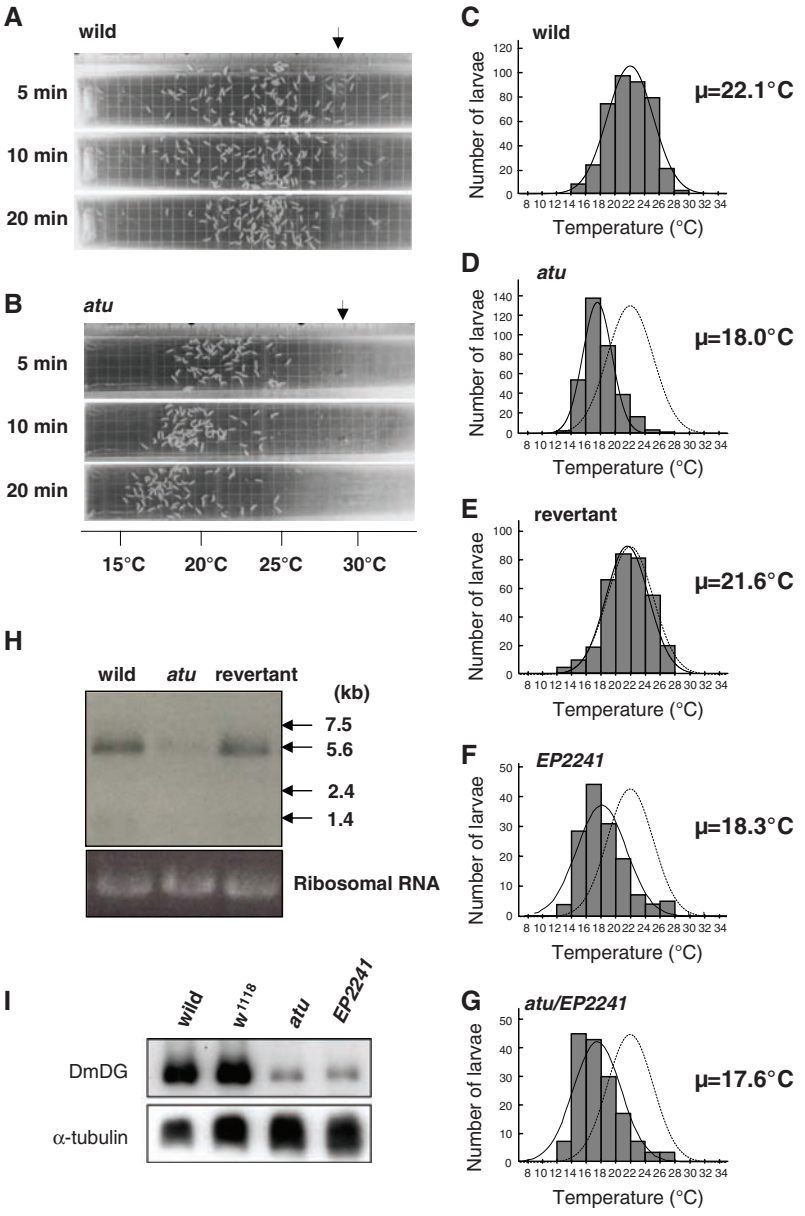

Fig. 1. Identification and characterization of the *atu* mutant. Representative results of temperature-preference assays. (**A**) Wild type; and (**B**) the *atu* mutant. Arrowheads indicate the region, at 28°C, where the larvae were placed initially. The summed histograms of the larval distributions after 20-min wandering for the wild type (Canton S) (**C**), the *atu* mutant (**D**), revertant line R1 (**E**), *EP2241* line (**F**), and *atu/EP2241* heteroallelic mutant (**G**). The dotted lines in (D) to (G) represent the Gaussian distribution of the wild type. The numerical analyses of data are shown in table S1. (**H**) Northern blot of total RNA extracted from third-instar larvae after probing with DmDG cDNA. (**I**) Expression of DmDG in the *atu* mutant and the *EP2241* line. Western blots of total homogenates prepared from third-instar larvae after incubation with antibodies to DmDG (anti-DmDG) or anti-tubulin are shown.

Table 2. Reversal of the cryophilic phenotype of the *atu* mutant by the *PDP* mutation, a pharmacological inhibitor of oxidative phosphorylation, and hyperoxic treatment. Comparisons among multiple groups were evaluated by ANOVAs followed by the Tukey-Kramer post hoc tests. In each group, values not sharing the same superscript letter are significantly different ($P < 0.05$). The numerical analyses of data are shown in table S1.

Flies	Preferred temperature μ (°C), σ^2	
w^{1118}	$\mu = 21.5^a$	$\sigma^2 = 2.8^2$
atu	$\mu = 17.9^b$	$\sigma^2 = 2.4^2$
atu with *PDP* mutation	$\mu = 22.2^c$	$\sigma^2 = 2.4^2$
PDP mutant	$\mu = 23.1^d$	$\sigma^2 = 2.6^2$
Pharmacological manipulation experiment of the atu *mutant*		
–	$\mu = 16.8^a$	$\sigma^2 = 2.2^2$
Rotenone	$\mu = 19.2^b$	$\sigma^2 = 3.0^2$
Tolbutamide	$\mu = 17.1^a$	$\sigma^2 = 3.2^2$
60% O_2	$\mu = 18.9^b$	$\sigma^2 = 2.7^2$
80% O_2	$\mu = 19.4^c$	$\sigma^2 = 3.4^2$
100% O_2	$\mu = 22.6^d$	$\sigma^2 = 3.9^2$
Wild + ambient air	$\mu = 21.8$	$\sigma^2 = 3.4^2$
Wild + 100% O_2	$\mu = 22.6$	$\sigma^2 = 3.9^2$

pyruvate dehydrogenase (PDH), a rate-limiting enzyme of the tricarboxylic acid cycle that catalyzes the conversion of pyruvate to acetyl–coenzyme A, was also increased in the *atu* mutant (2.0 times as high as that of the wild type) (Fig. 2G). The increased metabolic rate, concentrations of ATP, and enzymatic activity of PDH returned toward wild-type levels upon the transgenic expression of DmDG (Fig. 2, E to G), indicating that the reduced expression of DmDG was responsible for the increased energy metabolism. These results raise the possibility that the sustained increase in energy metabolism caused by the reduced expression of DmDG affected the thermoregulatory behavior of *Drosophila*.

To examine whether the increased energy metabolism contributed to the cryophilic phenotype of the *atu* mutant, we genetically manipulated the activity of PDH using a mutant line with reduced expression of pyruvate dehydrogenase phosphatase (PDP), an activator of PDH (*10*). The PDP mutant line exhibited a preference for higher temperature than did control lines, and the mutation of the *PDP* gene completely reversed the *atu* cryophilic phenotype (Table 2). The cryophilic phenotype of the *atu* mutant was alleviated to some extent by administering rotenone, a pharmacological inhibitor of oxidative phosphorylation, but not tolbutamide, a sulphonylurea that stimulates metabolic rate by raising the lymphatic concentration of glucose (*11*) (Table 2). These results indicated that the increased energy metabolism was responsible for the low-temperature preference of the *atu* mutant. Furthermore, brief exposure of the *atu* mutant to hyperoxic conditions for 45 min under humid conditions increased preferred temperature of the *atu* mutant, and the cryophilic phenotype was no longer discernible after the hyperoxic (100% O_2) treatment (Table 2). The metabolic rates of the *atu* mutant were significantly decreased at low temperatures (1.5 ± 0.05 μl CO_2 mg^{-1} $hour^{-1}$, $n = 5$ at 18°C; 1.2 ± 0.13 μl CO_2 mg^{-1} $hour^{-1}$, $n = 3$ at 14°C), becoming comparable to those observed in the wild type (1.4 ± 0.09 μl CO_2 mg^{-1} $hour^{-1}$, $n = 5$ at 18°C; 1.2 ± 0.10 μl CO_2 mg^{-1} $hour^{-1}$, $n = 3$ at 14°C). Together, these results indicate that the cryophilic phenotype of the *atu* mutant is a homeostatic response that depresses the increased oxidative metabolism to establish a steady state in which the increased consumption of oxygen and the supply of oxygen are balanced. Hypoxia elicits a regulated decrease in body temperature in organisms from protozoans to mammals (*12*). This behavioral thermoregulation is believed to be an adaptation to hypoxia because it lowers the metabolic rate when the supply of O_2 is limited, thereby facilitating survival. It seems unlikely that the cryophilic phenotype of the *atu* mutant is caused by hypoxia, because the expression of the gene for lactate dehydrogenase (LDH), a hypoxia-inducible gene in both *Drosophila* and mammals, was not increased in the *atu* mutant (fig. S7). Also, the metabolic rate and the concentrations of ATP generally decrease during hypoxia, whereas both increased in the *atu* mutant (Fig. 2, E and F).

An increase in the intracellular Ca^{2+} concentration ($[Ca^{2+}]_i$) in response to a decrease in the environmental temperature has been widely observed in mammals, ectotherms, and plants, suggesting that $[Ca^{2+}]_i$ is a key sign of low temperature (*13*, *14*). An increase in $[Ca^{2+}]_i$, which causes a subsequent uptake of Ca^{2+} by mitochondria, activates mitochondrial matrix dehydrogenases including PDH, resulting in the acceleration of mitochondrial ATP synthesis (*15*, *16*). In human patients suffering from inherited myopathies, disruption of the dystrophin-dystroglycan complex is suggested to impair the stability of the plasma membrane, resulting in a greater fragility toward mechanical stress and increased permeability to Ca^{2+}, which may lead to the degeneration of muscle fibers (*16*, *17*). To test whether the decreased expression of DmDG might cause an increase in $[Ca^{2+}]_i$, leading to the activation of PDH and the acceleration of the mitochondrial oxidative metabolism, we examined whether $[Ca^{2+}]_i$ was affected in the *atu* mutant. The basal $[Ca^{2+}]_i$ of fat body cells from the *atu* mutant was significantly higher than that of the wild type (Fig. 2H). The increased basal $[Ca^{2+}]_i$ in the *atu* mutant returned to the wild-type value upon the transgenic expression of DmDG, indicating that the reduced expression of DmDG causes a sustained increase in the basal $[Ca^{2+}]_i$ in fat body cells. In midgut epithelial cells, the basal $[Ca^{2+}]_i$ of the *atu* mutant was also higher than that of the wild type (Fig. 2I), and the increased basal $[Ca^{2+}]_i$ in the epithelial cells of the *atu* mutant was significantly decreased

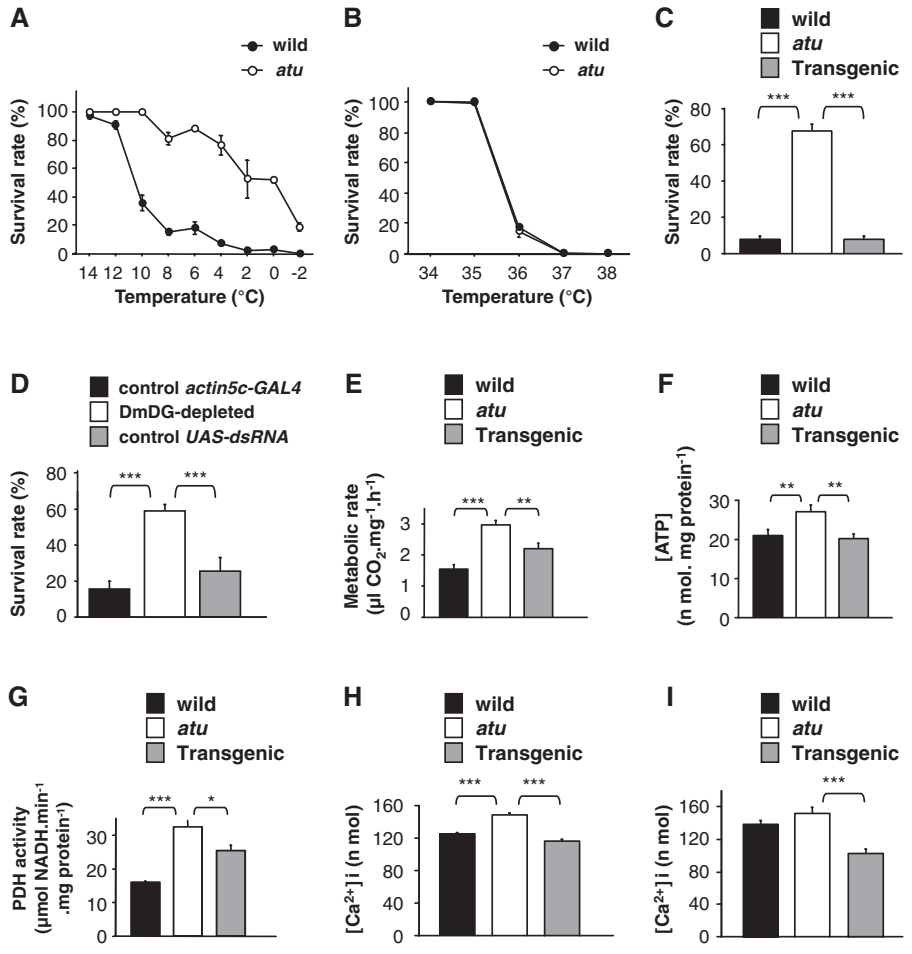

Fig. 2. Cold tolerance and increased energy metabolism induced by the decreased expression of DmDG. Tolerance of the wild type and the *atu* mutant to low (**A**) or high (**B**) temperatures. Results represent the average of three independent experiments and error bars indicate the SEM. (**C** to **I**) The statistical significance of differences between each group was assessed by ANOVA followed by Fisher's protected least significant difference post hoc test (*$P < 0.05$; **$P < 0.01$; ***$P < 0.001$). (C) Cold tolerance of the wild type, the *atu* mutant, and the *atu* mutant with transgenic expression of DmDG. The numerical data are shown in (*20*). (D) Cold tolerance of "DmDG-knockdown" larvae. The numerical data are shown in (*21*). (E) Metabolic rates as measured by CO_2 production. The numerical data are shown in (*22*). (F) ATP concentrations of the third-instar larvae. The numerical data are shown in (*23*). (G) PDH activities assessed by NADH (nicotinamide adenine dinucleotide, reduced) production in the mitochondrial fraction. The numerical data are shown in (*24*). (H) The basal $[Ca^{2+}]_i$ in fat body cells. The numerical data are shown in (*25*). (**I**) The basal $[Ca^{2+}]_i$ in the epithelial cells of the midgut. The numerical data are shown in (*26*).

upon the transgenic expression of DmDG (Fig. 2I). Among mitochondrial dehydrogenases in insects, PDH is the only enzyme that is reported to show Ca^{2+}-dependent activation (*18*), and therefore, it is possible that the reduced expression of DmDG causes the sustained increase in the $[Ca^{2+}]_i$, which, in turn, induces the activation of PDH, resulting in increased mitochondrial oxidative metabolism. Based on these observations, we propose that a reduction in the DmDG content initiates a chain of sequential reactions, i.e., increased membrane fluidity, activation of Ca^{2+} influx, elevated mitochondrial metabolism, and eventually, altered thermoregulatory behavior (fig. S9). It remains an enigma, however, how the metabolic changes in a cell are translated into neural code that induces behavioral change at the level of the whole animal (see also supporting online text).

References and Notes

1. T. J. Crowley, G. R. North, *Science* **240**, 996 (1988).
2. P. J. Mayhew, G. B. Jenkins, T. G. Benton, *Proc. Biol. Sci.* **275**, 47 (2008).
3. T. H. Bullock, *Biol. Rev. Camb. Philos. Soc.* **30**, 311 (1955).
4. M. J. Angilletta Jr., P. H. Niewiarowski, C. A. Navas, *J. Therm. Biol.* **27**, 249 (2002).
5. I. A. Johnston, A. F. Bennett, Eds., *Animals and Temperature: Phenotypic and Evolutionary Adaptation* (Cambridge Univ. Press, Cambridge, 1996).
6. C. V. Gisolfi, M. Francisco, *The Hot Brain: Survival, Temperature and the Human Body* (MIT Press, Cambridge, MA, 2000).
7. B. Heinrich, *The Hot-Blooded Insects: Strategies and Mechanisms of Thermoregulation* (Harvard Univ. Press, Cambridge, MA, 1993).
8. M. J. Greener, R. G. Roberts, *FEBS Lett.* **482**, 13 (2000).
9. W. M. Deng *et al.*, *Development* **130**, 173 (2003).
10. M. S. Patel, L. G. Korotchkina, *Biochem. Soc. Trans.* **34**, 217 (2006).
11. S. K. Kim, E. J. Rulifson, *Nature* **431**, 316 (2004).
12. A. A. Steiner, L. G. Branco, *Annu. Rev. Physiol.* **64**, 263 (2002).
13. S. Mahajan, N. Tuteja, *Arch. Biochem. Biophys.* **444**, 139 (2005).
14. J. E. Kammenga *et al.*, *PLoS Genet.* **3**, e34 (2007).
15. J. G. McCormack, A. P. Halestrap, R. M. Denton, *Physiol. Rev.* **70**, 391 (1990).
16. P. Gailly, *Biochim. Biophys. Acta* **1600**, 38 (2002).
17. R. Barresi, K. P. Campbell, *J. Cell Sci.* **119**, 199 (2006).
18. J. G. McCormack, R. M. Denton, *Biochem. J.* **196**, 619 (1981).
19. L. Liu, O. Yermolaieva, W. A. Johnson, F. M. Abboud, M. J. Welsh, *Nat. Neurosci.* **6**, 267 (2003).
20. Wild type, 7.3 ± 1.8% (mean ± SEM); *atu* mutant, 67.3 ± 3.7%; and DmDG transgenic *atu* mutant (*atu/atu*; *actin5C-GAL4/UAS-DmDG*), 7.3 ± 1.8%. Error bars represent SEM (n = 3).
21. Control *actin5C-GAL4* line (*actin5C-GAL4/+*), 15.7 ± 4.2% (mean ± SEM); "DmDG-knockdown" line (*actin5C-GAL4/UAS-dsRNA*), 59.0 ± 3.6%; and control *UAS-dsRNA* line (*+/UAS-dsRNA*), 25.4 ± 7.7%. Error bars represent SEM (n = 7).
22. Wild type, 1.6 ± 0.1 (mean ± SEM); *atu* mutant, 3.0 ± 0.1; and DmDG-transgenic *atu* mutant (*atu/atu*; *actin5C-GAL4/UAS-DmDG*), 2.2 ± 0.2. Error bars represent SEM (n = 6).
23. Wild type, 20.9 ± 1.5 (mean ± SEM; n = 9); *atu* mutant, 27.0 ± 1.8 (n = 8); and DmDG-transgenic *atu* mutant (*atu/atu*; *actin5C-GAL4/UAS-DmDG*), 20.2 ± 1.2 (n = 8).
24. Wild type, 15.7 ± 0.4 (mean ± SEM); *atu* mutant, 32.3 ± 1.8; and DmDG-transgenic *atu* mutant (*atu/atu*; *actin5C-GAL4/UAS-DmDG*), 25.2 ± 1.6 (n = 3).
25. Wild type, 124.9 ± 1.9 (mean ± SEM; n = 202); *atu* mutant, 148.5 ± 2.3 (n = 194); and DmDG-transgenic *atu* mutant (*atu/atu*; *actin5C-GAL4/UAS-DmDG*), 115.5 ± 2.9 (n = 119).
26. Wild type, 139.0 ± 4.7 (mean ± SEM; n = 98); *atu* mutant, 151.8 ± 7.4 (n = 88); and DmDG-transgenic *atu* mutant (*atu/atu*; *actin5C-GAL4/UAS-DmDG*), 101.9 ± 6.3 (n = 79).

27. We thank Y. Nakano for statistical analysis; H. Suzuki and J. Ikenouchi for assistance with electron microscopy; R. Niwa, M. O'Connor, A. P. Gould, and M. Kamakura for providing GAL4 flies; N. Juni for helpful discussions; A. Yamaguchi, Y. Yamaguchi, and M. Nishikawa for technical assistance; and R. Matsuda, H. Takeshima, Y. Nagai, and M. Ui for valuable advice and encouragement. This work was supported in part by Special Coordination Funds for Promoting Science and Technology from MEXT (Ministry of Education, Culture, Sports, Science and Technology), Japan, and by a research grant from The Novartis Foundation (Japan) for the Promotion of Science. D.Y. was supported by Specially Promoted Research grant 1802012 from MEXT and The Tohoku Neuroscience Global Centers of Excellence program.

Supporting Online Material

www.sciencemag.org/cgi/content/full/323/5922/1740/DC1
Materials and Methods
SOM Text
Figs. S1 to S11
Tables S1
References

9 September 2008; accepted 27 January 2009
10.1126/science.1165712

Quantitative 3D Video Microscopy of HIV Transfer Across T Cell Virological Synapses

Wolfgang Hübner,[1] Gregory P. McNerney,[3] Ping Chen,[1] Benjamin M. Dale,[1] Ronald E. Gordon,[2] Frank Y. S. Chuang,[3] Xiao-Dong Li,[4] David M. Asmuth,[4] Thomas Huser,[3,4] Benjamin K. Chen[1]*

The spread of HIV between immune cells is greatly enhanced by cell-cell adhesions called virological synapses, although the underlying mechanisms have been unclear. With use of an infectious, fluorescent clone of HIV, we tracked the movement of Gag in live CD4 T cells and captured the direct translocation of HIV across the virological synapse. Quantitative, high-speed three-dimensional (3D) video microscopy revealed the rapid formation of micrometer-sized "buttons" containing oligomerized viral Gag protein. Electron microscopy showed that these buttons were packed with budding viral crescents. Viral transfer events were observed to form virus-laden internal compartments within target cells. Continuous time-lapse monitoring showed preferential infection through synapses. Thus, HIV dissemination may be enhanced by virological synapse-mediated cell adhesion coupled to viral endocytosis.

Human immunodeficiency virus (HIV) infection leads to depletion of CD4 T cells throughout the lymphoid system. Both cell-free and cell-associated infection routes contribute to viral dissemination in vivo (*1*). In vitro, infection with cell-associated HIV can be thousands fold more efficient than infection with cell-free virus (*2*), and inhibition of cell-cell contacts severely limits replication (*3*). Infection through synapses between virus-carrying dendritic cells and CD4 T cells is highly efficient (*4*, *5*). For human T cell lymphotropic virus type I, viral synapses between T cells are essential for dissemination (*6*). For HIV, infected and uninfected CD4 T cells form virological synapses that organize viral receptors CD4, CXCR4, and Env (*7*). These infectious contacts are regulated by cell adhesion through integrins and intercellular adhesion molecules (*8*), dynamic actin and tubulin (*9*), cell signaling (*10*), and lipid raft recruitment (*11*). T cell virological synapses transfer virus with high efficiency (*12*), yet how this route fundamentally differs from cell-free infection remains unclear.

To examine the spatial and temporal organization of synapse formation, we used an infectious, fluorescent HIV clone, carrying a Gag-internal, interdomain insertion of the green fluorescent protein (GFP), called HIV Gag-iGFP (*13*). This virus faithfully reveals Gag localization, allowing infected cells and viral particles to be tracked with high sensitivity (*12*). Time-lapse fluorescence microscopy of virological synapse formation showed that 24% of HIV Gag-iGFP–expressing Jurkat cells formed stable adhesions to primary CD4 T cells within 4 hours (Fig. 1 and table S1A). After adhesion, 80% formed focal Gag accumulations at the contact site with an average 82-min interval (Fig. 1, A and B). In contrast, an Env-deficient clone was unable to induce cell-cell conjugates or Gag accumulation (table S1B), illustrating that adhesion precedes Gag redistribution.

[1]Division of Infectious Diseases, Department of Medicine, Immunology Institute, Mount Sinai School of Medicine, New York, NY 10029, USA. [2]Department of Pathology, Mount Sinai School of Medicine, New York, NY 10029, USA. [3]NSF Center for Biophotonics Science and Technology, University of California Davis (UCD), Sacramento, CA 95817, USA. [4]Department of Internal Medicine, University of California Davis Medical Center, Sacramento, CA 95817, USA.

*To whom correspondence should be addressed. E-mail: ben.chen@mssm.edu

In fixed samples, high-resolution confocal imaging revealed prominent Gag accumulations at the synapse (Fig. 1C). In three-dimensional (3D) reconstructions, these appeared as button-shaped discs, 1 to 3 μm in diameter (Fig. 1D and movie S1). Synaptic buttons were also observed in HIV Gag-iGFP–expressing primary CD4 T cells cocultured with homologous primary CD4 cells (fig. S1). We assessed viral assembly at the synapse by measuring Gag oligomerization with fluorescence resonance energy transfer (FRET) (*13*–*15*) between Cerulean and Venus variants of HIV Gag-iGFP, which form a donor-acceptor FRET pair (*16*). Excitation of the Cerulean donor in cotransfected Jurkat cells generated a robust Venus-shifted FRET signal at synaptic buttons that is indicative of Gag homo-oligomerization (Fig. 1E). Photobleaching the Venus acceptor at a synapse lead to increased donor emission, providing additional evidence for FRET (Fig. 1, F to H, and fig. S2). Three-dimensional reconstruction of FRET images revealed concentrated Gag oligomerization at synapses (movie S2).

With transmission electron microscopy, we observed that 100-nm budding viral crescents at the virological synapse protruded from the donor cell with bud tips directly abutting the target cell membrane (Fig. 1I). Viral buds were also observed far from the synapse, although at lower densities (fig. S3). Native, non–GFP-expressing HIV induced similar budding crescents, ruling out that GFP induced these accumulations (fig. S4). In thick 150-nm sections, near-complete viral buds and a virus-containing invagination in the synapsed target cell were observed (fig. S4, A and B).

To capture the dynamics of Gag trafficking, reorganization, and viral transfer with higher temporal and spatial resolution, we recorded high-speed, spinning disc confocal fluorescence images. Forty-three putative synaptic events encompassing 1187 min revealed dynamic Gag movements during virological synapse formation (table S2). New synaptic button formation (n = 4) was captured where patches of membrane-associated Gag moved toward the cell adhesion site within minutes (Fig. 2A and movie S3). At existing buttons, a ring-shaped zone of Gag depletion often surrounded the synaptic button (Fig. 2B), indicative of a synapse-proximal region from which Gag was recruited.

HIV Gag-iGFP–labeled structures (n = 8) close to existing buttons moved rapidly and directionally into the button (Fig. 2C, fig. S5, and movies S4 to S6). The structures moved into the synapse with average velocities of 0.10 to 0.25 μm/s and peaks up to 0.8 μm/s (Fig. 2C and fig. S5). Other small, mobile Gag puncta emerged from and then moved back into the synaptic button (Fig. 2D and movie S7). The fast, directional movement of Gag was seen predominantly from nearby puncta.

During cell-to-cell viral transfer (n = 10, table S2), fluorescent Gag signal protruded from buttons, penetrated the attached target cell, was released into the target cell, and then migrated distally with a mean velocity of 0.12 μm/s (Fig. 2E and movie S8). Notably, puncta 1.5 μm in diameter were observed (fig. S6A), and on occasion an entire synaptic button was transferred (movie S9). Large vesicular structures were also observed to fractionate into smaller vesicles while moving toward the distal pole of the cell (movies S4 and S8). The size of these translocated puncta exceeds individual clathrin- or caveolin-associated structures, which are uniformly small (100 to 200 nm) (*17*). By using quantitative confocal microscopy, we found that the accumulation and maintenance of Gag puncta in target cells was remarkably stable over time (fig. S6, B to D, and movie S10).

The GFP signal in flow-sorted HIV+ CD4 target cells was uniformly punctate, without evidence

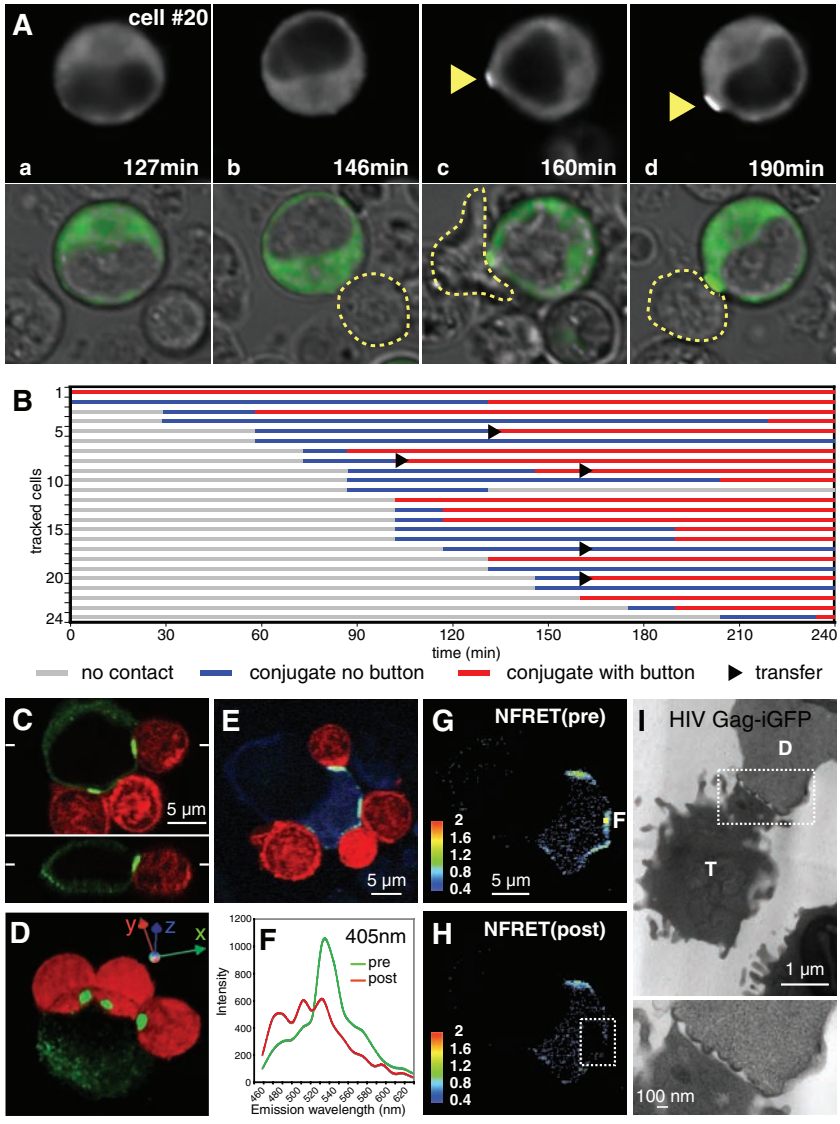

Fig. 1. Gag accumulates at synaptic buttons after T cell adhesion. (**A**) Time-lapse fluorescence imaging of synapse formation between an HIV Gag-iGFP–expressing Jurkat cell and a CD4 T cell. GFP image (top) and GFP/phase contrast overlay (bottom). Cells (a) before stable contact, (b) in stable adhesion (outlined), and (c and d) showing synaptic buttons (arrowheads). (**B**) Timing of synapse formation following 24 HIV+ Jurkat cells; each line represents an interactive cell. (**C**) Confocal fluorescence image of an HIV Gag-iGFP-expressing Jurkat T cell (green) synapsed with three primary CD4 T cells [red, labeled with CellTracker Orange CMRA (Invitrogen, Carlsbad, CA)]. Positioning of perpendicular planes marked at edges. (**D**) Reconstructed 3D view of (C). (**E** to **H**) FRET analysis of Gag-iCerulean (donor) and Gag-iVenus (acceptor) fluorophores at the synaptic button. (E) Three-color overlay donor Cerulean (blue, 405-nm excitation), FRET channel (green, 405-nm excitation), and target cells [red, 543-nm excitation stained with CellTracker Orange CMTMR (Invitrogen)]. (F) Emission spectra at synaptic button, point F, pre- and postacceptor photobleaching. (G and H) Normalized FRET (NFRET) signal (*13*) before and after acceptor photobleaching in boxed area. (**I**) Transmission electron micrographs of the synaptic junction between HIV Gag-iGFP–expressing donor, D, and target, T, cells. Low (top) and high (bottom) magnification of 70-nm sections.

of syncitia, and confocal imaging suggested that puncta were not surface-associated (fig. S7). Anti-Env staining of the Gag-iGFP puncta required cell permeabilization, indicating that Env was present in an internal Gag+ compartment (Fig. 2, F and G). Transmission electron microscopy of the target cells revealed multivesicular structures, which were not seen in control, unexposed cells, that contained viruslike densities inside 1- to 2-μm compartments (Fig. 2H). We conclude that synapses target HIV into vesicular compartments within recipient cells.

To track the fate of cells after synapse formation, we performed continuous, long-duration imaging. Jurkat donor cells were cotransfected with HIV Gag-iGFP and HIV NL-GI, an HIV molecular clone that expresses GFP in place of the viral early gene nef (*18*). This approach can visualize viral transfer (as puncta), as well as productive infection (as diffuse GFP) in the target cell. In example one, the infected cell synapsed with the target cell for 18 hours, the cells separated, and at 32 hours a diffuse, bright GFP signal indicated productive infection (Fig. 3, A C, and movie S11). Bystander target cells remained negative. Over 67 hours, 112 conjugates tracked resulted in seven productively infected MT4 target cells (table S3). In five cases, synapses were observed, and in four cases virus transfer was recorded (Fig. 3, A to C, and movie S12). Under culture conditions that limited new cell-cell interactions, productively infected cells arose preferentially after observed virological synapse events.

Because synapse-mediated viral transfer is coreceptor-independent (*12*, *19*), we tested whether infection through T cell synapses requires coreceptor expression. Infection of MT4 cells by cell-associated HIV was inhibited when cells were separated by a 0.4-μm transwell barrier (Fig. 4A). Under these contact-dependent infection conditions, productive infection by cell-associated HIV NL-GI was inhibited by CXCR4-antagonist, AMD3100 (Fig. 4B). Furthermore, productive infection by cell-associated R5-tropic virus HIV NL-GI (JRFL) was dependent on expression of the chemokine receptor, CCR5 (Fig. 4C). The results suggest that infection through T cell synapses does not bypass the coreceptor requirement.

Synapse-mediated viral transfer is potently inhibited by actin inhibitors such as cytochalasin D (*9*, *12*). We find that cytochalasin D had little effect on cell-free HIV infection yet effectively inhibited productive infection by cell-associated HIV (Fig. 4D). Additionally, a well-characterized patient antisera, which can potently block cell-free infection but not transfer of virus through virological synapses (*12*), did not efficiently block infection of the homologous cell-associated

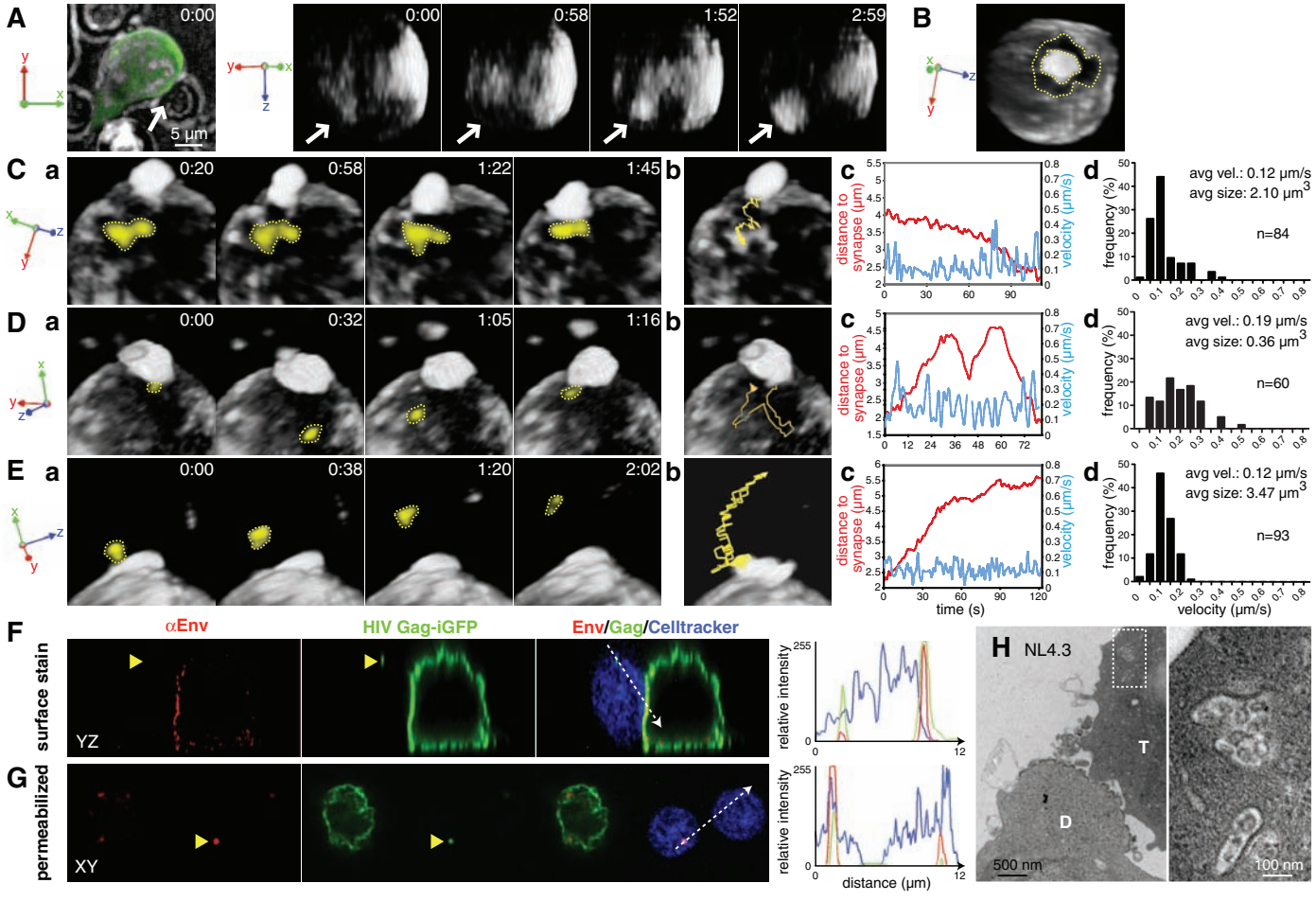

Fig. 2. Dynamic recruitment of Gag puncta to the synapse and viral transfer into a target cell compartment revealed with rapid spinning-disc 3D confocal fluorescence microscopy. (**A**) Formation of a buttonlike accumulation of Gag at the site of adhesion, *z* projection at time = 0 (left), selected 3D reconstructions of contact site (arrows) over time (right four images). (**B**) A zone of Gag depletion, 2 to 3 μm wide, surrounds the synaptic button (dotted yellow line). (**C**) Patches of synapse-proximal Gag merge into the synapse. (**D**) A Gag-iGFP puncta moves out of and into the synapse. (**E**) During a transfer event, Gag puncta emerge from the synapse, separate, and then move to the distal pole. In (C) to (E), (a) selected frames highlight movement of Gag-iGFP puncta (yellow). (b) Object path is overlayed on the initial image. (c) Object distance to the synapse center and relative velocity are graphed over time. (d) Histogram distribution of the tracked objects velocities. (**F** and **G**) Immunostaining of Gag puncta requires membrane permeabilization. (F) Nonpermeabilized, anti-Env immunostain (red) does not stain the Gag-iGFP+ puncta (green) within the CD4 target cell (CellTracker Blue CMF2HC, Invitrogen), whereas surface Env-staining at synapse is observed. Three-color intensity profile along the 12-μm line (right). (G) Permeabilization of fixed cells reveals anti-Env immunostain (red) at the GFP puncta (green) within the CD4 target cell (blue). (**H**) Transmission electron micrograph of vesicles containing corelike structures in a CD4 cell engaged in synapse with an HIV-infected Jurkat cell. Low (left) and high (right) magnification of 70-nm sections.

virus (Fig. 4E). Thus, inhibitor studies clearly distinguish the mechanisms of cell-free from those of cell-associated infection.

The live imaging of HIV cell-to-cell transfer reveals that dynamic Gag movements in infected cells organize Gag puncta into synaptic buttons from which HIV is directly transferred into adjacent target cells. Although endocytic entry of cell-free HIV contributes only modestly to productive

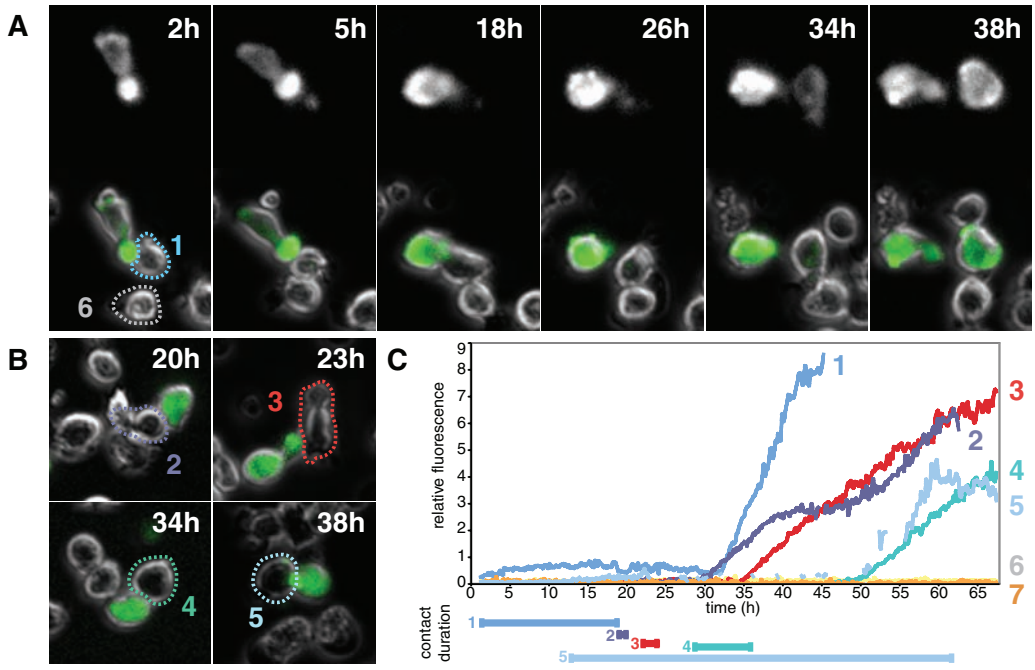

Fig. 3. Productive infection of synapsed cells is visualized by 72-hour imaging of immobilized cells engaged in virological synapse. (**A**) Donor cells cotransfected with HIV Gag-iGFP to track viral transfer and HIV NL-GI to visualize new early gene expression in target cells. Images show a synapsed pair where the target cell (number 1) separates from donor at 18 hours and expresses increasing levels of diffuse GFP at 32 hours. Top row shows GFP images; bottom, GFP/phase overlays. (**B**) Four examples of synapsed MT4 target cells that subsequently expressed HIV (numbers 2 to 5). (**C**) Fluorescence intensity of the target cells 1 to 7. Numbers 6 and 7 are control bystander cells. Duration of cell contact indicated on bottom.

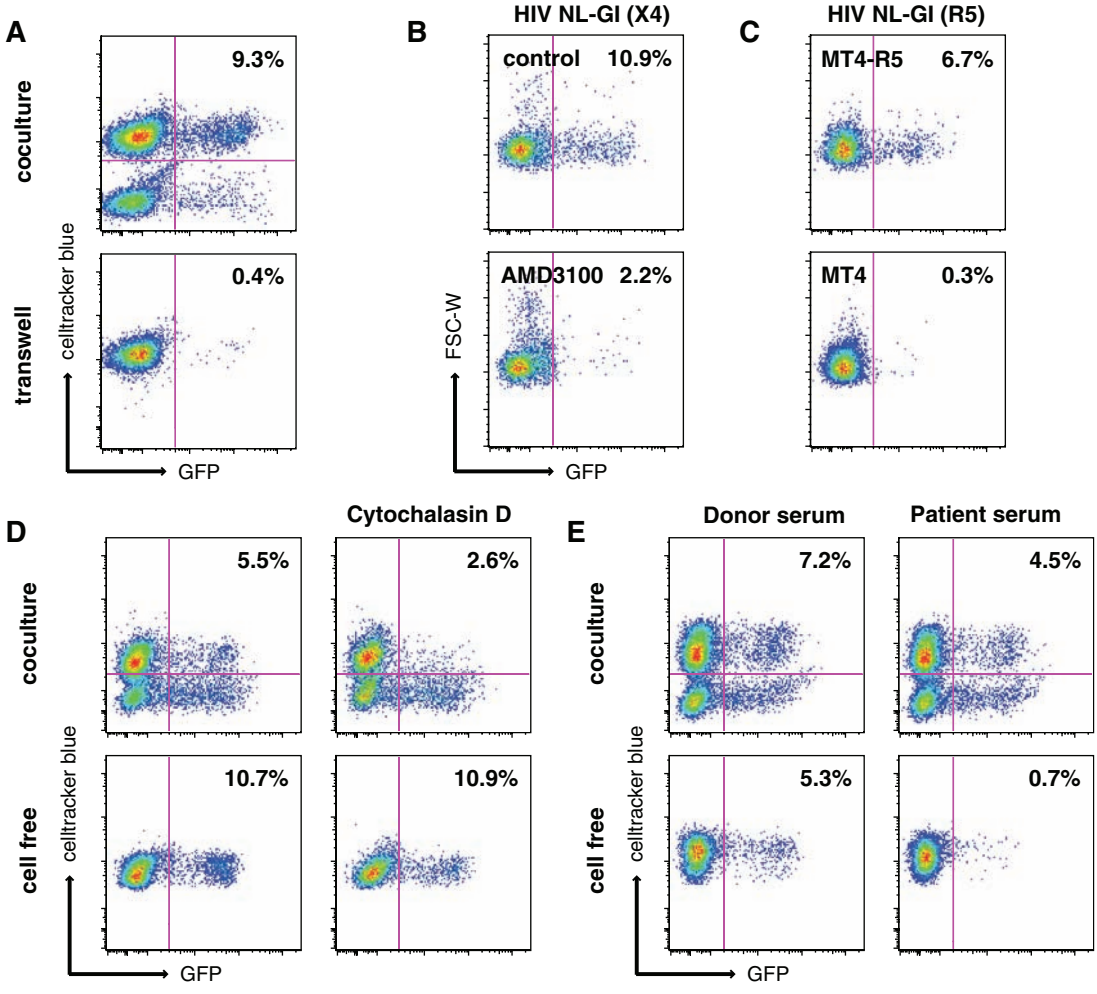

Fig. 4. Cell-associated infection is coreceptor-dependent and actin-dependent and can resist a neutralizing antiserum. (**A**) HIV NL-GI–expressing Jurkat cells were cocultured with CellTracker Blue CMF2HC–labeled MT4 cells in the absence or the presence of a 0.4-μm transwell barrier between cells. Productive infection (GFP expression) in CellTracker-labeled target cells was measured by flow cytometry at 48 hours. (**B**) Coreceptor antagonist AMD3100 (10 μg/ml) inhibits infection of target cells by cell-associated X4-tropic virus, HIV NL-GI, at 48 hours. Productive infection in gated target cells indicated by GFP expression and is plotted against forward scatter width (FSC-W). (**C**) Cell-associated R5-tropic virus infects CCR5-expressing MT4 cells but not CCR5-negative MT4 cells. Jurkat cells expressing R5-tropic HIV NL-GI(JRFL) were donor cells. (**D**) Cytochalasin D (2.5 μM) inhibits cell-associated infection (top) but fails to block infection with cell-free virus (bottom). (**E**) A neutralizing antiserum that blocks cell-free infection (bottom) is less effective at blocking homologous cell-associated infection (top). Results representative of at least three independent experiments.

infection (*20*–*22*), our results suggest that the cell-to-cell transmission could favor endocytic routes. Thus when spreading via synapses, it is possible that HIV resembles a majority of viruses that enter preferentially through endocytosis (e.g., influenza, adenoviruses, picornaviruses, alphaviruses) (*23*). Given this scenario, the tight coupling of Env fusogenicity with particle maturation (*24*, *25*) may activate viral fusion within a target cell compartment that is cloistered from neutralizing antibodies (*12*). Alternatively, the prominent endocytic process that accompanies synapse formation may create viral reservoirs in intracellular compartments.

Future vaccine strategies may be focused against unique cell-surface Env epitopes that block cell-associated infection, and future antiviral drugs may target factors required for synapse formation. Ultimately the dynamics of virological synapse formation must be understood within lymphoid tissues, where high density and lymphocyte mobility (*26*) are likely to promote synaptic viral spread.

References and Notes

1. A. T. Haase, *Nat. Rev. Immunol.* **5**, 783 (2005).
2. D. S. Dimitrov *et al.*, *J. Virol.* **67**, 2182 (1993).
3. M. Sourisseau, N. Sol-Foulon, F. Porrot, F. Blanchet, O. Schwartz, *J. Virol.* **81**, 1000 (2007).
4. P. U. Cameron *et al.*, *Science* **257**, 383 (1992).
5. D. McDonald *et al.*, *Science* **300**, 1295 (2003); published online 1 May 2003 (10.1126/science.1084238).
6. T. Igakura *et al.*, *Science* **299**, 1713 (2003); published online 13 February 2003 (10.1126/science.1080115).
7. C. Jolly, K. Kashefi, M. Hollinshead, Q. J. Sattentau, *J. Exp. Med.* **199**, 283 (2004).
8. C. Jolly, I. Mitar, Q. J. Sattentau, *J. Virol.* **81**, 13916 (2007).
9. C. Jolly, I. Mitar, Q. J. Sattentau, *J. Virol.* **81**, 5547 (2007).
10. N. Sol-Foulon *et al.*, *EMBO J.* **26**, 516 (2007).
11. C. Jolly, Q. J. Sattentau, *J. Virol.* **79**, 12088 (2005).
12. P. Chen, W. Hubner, M. A. Spinelli, B. K. Chen, *J. Virol.* **81**, 12582 (2007).
13. W. Hubner *et al.*, *J. Virol.* **81**, 12596 (2007).
14. A. Derdowski, L. Ding, P. Spearman, *J. Virol.* **78**, 1230 (2004).
15. D. R. Larson, Y. M. Ma, V. M. Vogt, W. W. Webb, *J. Cell Biol.* **162**, 1233 (2003).
16. M. A. Rizzo, G. H. Springer, B. Granada, D. W. Piston, *Nat. Biotechnol.* **22**, 445 (2004).
17. M. Lakadamyali, M. J. Rust, X. Zhuang, *Cell* **124**, 997 (2006).
18. G. B. Cohen *et al.*, *Immunity* **10**, 661 (1999).
19. J. Blanco *et al.*, *J. Biol. Chem.* **279**, 51305 (2004).
20. O. T. Fackler, B. M. Peterlin, *Curr. Biol.* **10**, 1005 (2000).
21. V. Marechal *et al.*, *J. Virol.* **75**, 11166 (2001).
22. E. Schaeffer, V. B. Soros, W. C. Greene, *J. Virol.* **78**, 1375 (2004).
23. M. Marsh, A. Helenius, *Cell* **124**, 729 (2006).
24. D. J. Wyma *et al.*, *J. Virol.* **78**, 3429 (2004).
25. S. Wyss *et al.*, *J. Virol.* **79**, 12231 (2005).
26. R. N. Germain, M. J. Miller, M. L. Dustin, M. C. Nussenzweig, *Nat. Rev. Immunol.* **6**, 497 (2006).

27. We thank R. H. Cheng, V. Simon, M. Klotman, R. Iyengar, and A. Del Portillo for critiques and discussions; R. Huq for microscopy support; S. Izadmehr for image analysis; M. Grisotto and V. Sahi for cell sorting; H. Bell for electron microscopy support; and S. Lira for imaging support. Work was supported by NIH grant AI074420-02, Burroughs Wellcome Fund Investigator Award, and Hirschl Weill-Caulier Career Scientist Award to B.K.C. Imaging was supported by Mount Sinai School of Medicine–Microscopy Shared Resource Facility grants NIH-NCI 5R24 CA095823-04, NSF-DBI-9724504, and NIH-S10RR09145-01; by the NSF Center for Biophotonics Science and Technology (cooperative agreement PHY012099); a UCD Health System Research Award to T.H.; and the UCD Clinical and Translational Science Center grant NIH-NCRR ULRR024146 (T.H. and D.M.A.).

Supporting Online Material

www.sciencemag.org/cgi/content/full/323/5922/1743/DC1
Materials and Methods
Figs. S1 to S7
Tables S1 to S3
Movies S1 to S12

22 October 2008; accepted 30 January 2009
10.1126/science.1167525

A Transposon-Based Genetic Screen in Mice Identifies Genes Altered in Colorectal Cancer

Timothy K. Starr,[1]* Raha Allaei,[1] Kevin A. T. Silverstein,[2] Rodney A. Staggs,[2] Aaron L. Sarver,[2] Tracy L. Bergemann,[3] Mihir Gupta,[4] M. Gerard O'Sullivan,[5] Ilze Matise,[5] Adam J. Dupuy,[6] Lara S. Collier,[7] Scott Powers,[8] Ann L. Oberg,[9] Yan W. Asmann,[9] Stephen N. Thibodeau,[9] Lino Tessarollo,[10] Neal G. Copeland,[11] Nancy A. Jenkins,[11] Robert T. Cormier,[12] David A. Largaespada[1]*

Human colorectal cancers (CRCs) display a large number of genetic and epigenetic alterations, some of which are causally involved in tumorigenesis (drivers) and others that have little functional impact (passengers). To help distinguish between these two classes of alterations, we used a transposon-based genetic screen in mice to identify candidate genes for CRC. Mice harboring mutagenic Sleeping Beauty (SB) transposons were crossed with mice expressing SB transposase in gastrointestinal tract epithelium. Most of the offspring developed intestinal lesions, including intraepithelial neoplasia, adenomas, and adenocarcinomas. Analysis of over 16,000 transposon insertions identified 77 candidate CRC genes, 60 of which are mutated and/or dysregulated in human CRC and thus are most likely to drive tumorigenesis. These genes include *APC*, *PTEN*, and *SMAD4*. The screen also identified 17 candidate genes that had not previously been implicated in CRC, including *POLI*, *PTPRK*, and *RSPO2*.

Recent genomic studies have revealed that human colorectal cancers (CRCs) undergo numerous genetic and epigenetic alterations (*1*–*4*). These alterations probably derive from a mixture of "drivers" that play a causal role in tumor formation and progression and "passengers" that have little or no effect on tumor growth. The design of targeted therapeutics for CRCs is dependent on the ability to distinguish drivers from passengers.

To help identify potential driver genes in CRC, we developed a forward genetic screen in mice by using a Sleeping Beauty (SB) system to generate insertional mutations. To confine transposition to the gastrointestinal tract, SB11 transposase cDNA, preceded by a LoxP-flanked stop cassette, was knocked into the *Rosa26* locus (fig. S1) (*5*). These mice were then crossed with *Villin-Cre* transgenic mice to activate SB transposase in epithelial cells of the gastrointestinal tract (*6*). Once expressed, SB transposase catalyzed the transposition of *T2/Onc*, a mutagenic SB transposon (Fig. 1A) (*7*). *T2/Onc* contains a murine stem-cell virus long terminal repeat and splice donor site (MSCV-LTR-SD), which can deregulate the expression of a nearby proto-oncogene. *T2/Onc* also carries splice acceptor sites in both DNA strands and a bidirectional polyadenylate signal, which can inactivate the expression of a tumor suppressor gene. Because SB transposition is biased toward reintegration of the transposon into the same chromosome as the donor transposon (a phenomenon referred to as "local hopping"), we used two *T2/Onc* transgenic lines that each carried approximately 25 copies of the *T2/Onc* transposon in a concatamer on different donor chromosomes (chrs 1 and 15) (*7*).

A histochemical analysis of the triple transgenic mice (*Rosa26-LsL-SB11*, *T2/Onc*, and *Villin-Cre*) showed that SB transposase was strongly expressed in epithelial cells of the gut and pancreas but undetectable in other tissues (fig. S2). We created a cohort of 28 triple transgenic mice and 72 double transgenic control mice carrying all possible dual combinations of the three transgenes. Mice in this first cohort were monitored daily for 18 months. We generated a second cohort of 50 triple transgenic mice that were maintained in a separate facility for 12 months and also monitored daily.

Triple transgenic mice died at a faster rate than double transgenic controls, beginning around one year of age (Fig. 1B). Examination of the gastrointestinal tract of moribund animals revealed discrete raised lesions ranging from 2 mm to as large as 5 mm in diameter in the small and large intestine. In the first cohort, 100% (12 out of 12)

of the experimental mice that died before 18 months harbored intestinal lesions (table S1), whereas none of the control mice killed before 18 months had lesions. In the second cohort, 72% (36 out of 50) of triple transgenic mice had intestinal lesions, with an average of 1.9 intestinal lesions in the small intestines and 0.2 lesion in the large intestine.

We performed histopathologic analyses of tumor tissue sections from 11 mice. These analyses identified 39 and 16 intraepithelial neoplasias, 50 and 15 adenomas, and 3 and 0 adeocarcinomas in the small and large intestines, respectively (Fig. 1, C to E). An additional adenocarcinoma was identified whose site of origin was undetermined. We also selected six large tumors (≥5 mm) from six additional mice and found that three were adenocarcinomas and three were adenomas.

For use in DNA isolation and sequencing experiments, we harvested 135 tumors: 42 tumors from 11 of the triple transgenic mice from the first cohort (data set 1) and 93 tumors from 36 mice in the second cohort (data set 2). The majority of the tumors were small, and the entire tumor was used for DNA isolation. This precluded our ability to perform histological analysis and to link the molecular data to the histopathology of specific tumors. However, given the distribution of frank intestinal lesions from the histopathological analysis, the majority of tumors were likely to be adenomas. We then performed linker-mediated polymerase chain reaction (PCR) on DNA from these 135 harvested tumors in order to generate PCR products containing transposon-genomic junction fragments. We sequenced over 195,000 of these PCR products, of which 99,624 could be specifically mapped to thymine-adenine (TA) dinucleotides in the mouse genome, which is consistent with SB insertion-site requirements. After combining duplicate insertions within a given tumor, we found that 45% of the insertions mapped to the same chromosome as the donor concatamer (chr 1 or 15), which is consistent with the local hopping seen in previous SB screens. We removed these insertions from further analysis to eliminate statistical bias due to local hopping. We also eliminated insertions mapping to the precise TA dinucleotide in tumors from two or more different mice because these insertions could represent a PCR artifact. The consummate total of 16,690 mapped, nonredundant, genomic loci (table S2) equates to an average of 124 mapped insertions per tumor.

To define common insertion sites (CISs), we performed Monte Carlo simulations using randomly assigned insertions. Genomic window sizes were chosen on the basis of simulations that used the same number of insertions as the data sets so that one would not expect to find a single CIS after randomly distributing transposon insertions throughout the genome (expected value $E < 1$). For example, in a random assignment of 16,690 insertions we would not expect to find a single cluster of five insertions within 25 kb, six insertions within 50 kb, seven insertions within 80 kb, and so on. (*8*). Any cluster of insertions meeting or exceeding these parameters was defined as a CIS. We removed one CIS from this list because it was composed entirely of insertions from a single mouse, indicating that those tumors may be related.

As a final control, we amplified and sequenced 15,556 SB insertions present in tail DNA derived from 89 double transgenic weanling mice. These mice contained an ubiquitously expressed SB11 transposase transgene and the *T2/Onc* transposon concatamers (*7*, *9*). Because there was no selection pressure for tumor outgrowth in these mice and because SB integration does not have a strong bias for any individual TA dinucleotide (*10*), we expected the insertions to be distributed randomly throughout the genome, except for local hopping. From this control data set, we identified six CISs. This was more than expected but considerably less than was observed in the tumor DNA (table S3). These CISs could be previously unknown hotspots for transposon integration. Alternatively, they could reflect incipient clonal neoplastic growth because these genetically manipulated mice eventually develop lymphoma (*9*). Two of these six CISs were also identified in the tumor data sets; thus, they were eliminated from the list of tumor CISs, which left us with 77 CISs (table S4).

Candidate genes were assigned to the 77 CISs according to the percentage of insertions in or near a gene within the CIS boundaries. Insertions were mainly located within introns (51%), only 2% in an exon, and the remaining 47% either upstream or downstream of a coding region. The top 10 CISs, as ranked by the number of insertions found, are listed in Table 1.

The goal of this study was to identify genes that are drivers of tumorigenesis in order to identify new candidate genes whose mutational status in human CRC can then be tested. We compared our list of mouse CIS genes with the human genes

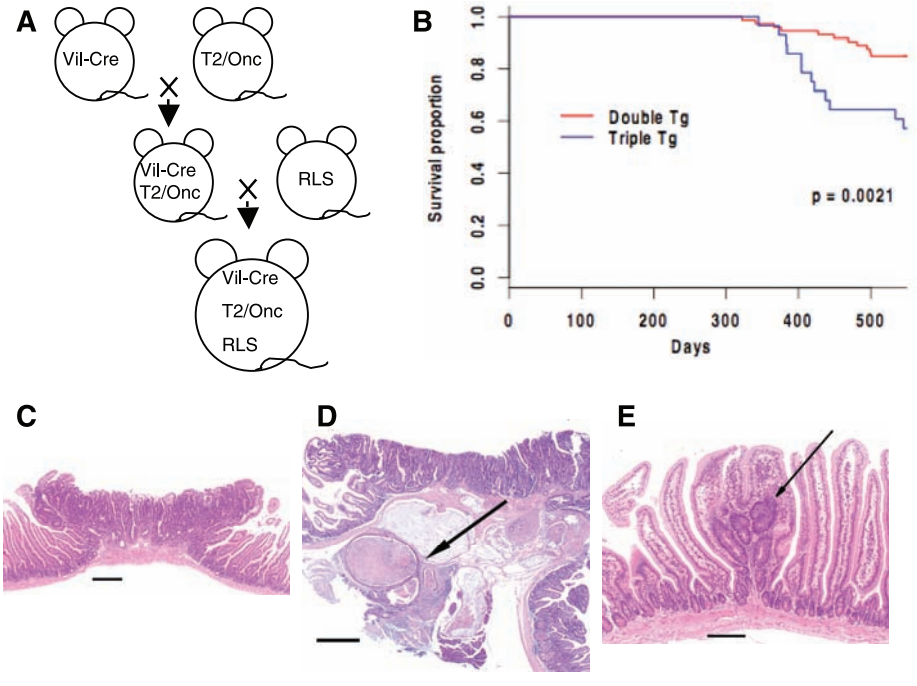

Fig. 1. Triple transgenic mice develop intestinal tumors and become moribund faster than double transgenic controls. (**A**) Breeding scheme for generating triple transgenics. Vil, *Villin* promoter; RLS, *Rosa26-Lox-stop-Lox-Sleeping Beauty* 11; Tg, transgenic. (**B**) Kaplan-Meier survival curve comparing triple transgenics with double transgenic controls. (**C** to **E**) Photomicrographs of hematoxylin- and eosin-stained representative tissue showing an adenoma (C); an adenocarcinoma (D), the arrow pointing to a cluster of glands that has invaded through the serosa, and gastrointestinal intraepithelial neoplasia (E), the arrow indicating a cluster of dysplastic glands accompanied by fusion of villi. Scale bars, 250 μm in (C), 500 μm in (D), and 100 μm in (E).

[1]Department of Genetics, Cell Biology and Development, Center for Genome Engineering, Masonic Cancer Center, University of Minnesota, Minneapolis, MN 55455, USA. [2]Department of Biostatistics and Informatics, Masonic Cancer Center, University of Minnesota, Minneapolis, MN 55455, USA. [3]Department of Biostatistics, School of Public Health, University of Minnesota, Minneapolis, MN 55455, USA. [4]Department of Physical and Chemical Biology, Harvard College, Cambridge, MA 02138, USA. [5]College of Veterinary Medicine, University of Minnesota, St. Paul, MN 55108, USA. [6]Department of Anatomy and Cell Biology, University of Iowa, Iowa City, IA 52242, USA. [7]School of Pharmacy, University of Wisconsin, Madison, WI 53705, USA. [8]Cold Spring Harbor Laboratory, Cold Spring Harbor, NY 11724, USA. [9]Mayo Clinic College of Medicine, Rochester, MN 55905, USA. [10]Neural Development Group, Mouse Cancer Genetics Program, Center for Cancer Research, National Cancer Institute (NCI), Frederick, MD 21702, USA. [11]Institute of Molecular and Cell Biology, 138673 Singapore. [12]University of Minnesota Medical School, Duluth, MN 55812, USA.

*To whom correspondence should be addressed. E-mail: star0044@umn.edu (T.K.S.); larga002@umn.edu (D.A.L.)

listed in the Catalog of Somatic Mutations in Cancer (COSMIC) database (*11*). Among our list of 77 CIS genes, 38 have human homologs present in the COSMIC database, and 18 (47%) of these 38 homologs have documented nonsilent mutations in human cancers (table S5), which would not be expected by chance ($P < 0.05$). Furthermore, if we limit our analysis of COSMIC to genes mutated in human CRC, the overlap has a lower probability of being due to chance ($P < 0.001$) (*8*).

Similarly, our CIS list overlaps with a recent large-scale exon-resequencing project that cataloged mutations in 18,191 human genes in 11 colorectal tumor samples (*1*). That project identified 848 human gene mutations, 140 of which were considered likely to be driver mutations for CRC. Of the 77 CIS mouse genes identified in our study, 74 have human homologs that were included in the exon-resequencing study. Among these 74 homologs, 10 had a mutation and four were identified as candidate driver mutations in human CRC (table S6), making these findings highly significant ($P < 0.005$) (*8*).

We then investigated whether the human homologs of the mouse CIS genes were amplified or deleted in human CRC. We examined a data set that identified 482 deletions and 224 amplifications in human CRCs (*8*). The human homologs of 10 CIS genes were located in deleted regions, and 23 were located in amplified regions (tables S7 and S8). This represents a significant overlap ($P < 0.05$) (*8*) and suggests that the candidates found in this screen are relevant to human CRC.

Finally, we analyzed cDNA microarray data to determine whether CIS genes were differentially expressed in human CRC versus normal colonic tissue. The Oncomine database (*12*) contains five microarray data sets that compare gene expression levels in 138 CRCs and 88 normal samples. Of the 77 CIS human homologs, 50 were identified as being differentially regulated ($P < 0.05$) in one or more of these studies (table S9).

By comparing our list of mouse CIS genes with human genes that are (i) mutated in CRC, (ii) listed in COSMIC, (iii) amplified or deleted in CRC, (iv) aberrantly expressed in CRC, or (v) known cancer genes identified by the Cancer Genome Project (CGP) (*13*), we identified 15 CIS genes that are the most likely to be driver mutations in human CRC (Table 2) by virtue of being present in at least three of the five categories listed above. Among these 15 genes is *adenomatous polyposis coli* (*Apc*), a member of the Wnt signaling pathway and the most commonly mutated gene in human CRC (70 to 80%) (*14*). Also included in this list are *bone morphogenetic protein receptor, type IA* (*Bmpr1a*), *Smad4*, and *phosphatase and tensin homolog* (*Pten*), which are responsible for juvenile polyposis syndrome, juvenile intestinal polyposis, and Cowden disease, respectively. Another gene on the list, *F-box and WD repeat domain–containing 7* (*Fbxw7*), is a component of the SKP1/cullin/F-box protein (SCF) ubiquitin ligase complex, which is mutated in 11.5% of human CRCs (*15*). Thus, of the 15 prioritized genes in our study, five are validated human CRC genes and together represent some of the most commonly mutated genes identified in human CRC.

Three other genes on the complete CIS list (table S4) are also implicated in human CRC: *cyclin-dependent kinase 8* (*CDK8*), *mutated in colorectal cancers* (*MCC*), and *Staphylococcal nuclease and tudor domain–containing 1* (*SND1*). *CDK8*, which encodes cell division protein kinase 8, is commonly amplified in human CRC and plays a direct role in β catenin–driven cell transformation (*16*). *MCC* encodes the colorectal mutant cancer protein and, in addition to finding somatic mutations in *MCC* (*17*), a recent study found that 50% of primary CRCs exhibited *MCC*-promoter methylation (*18*). Furthermore, MCC interacts with β-catenin and its reexpression in CRC cells inhibits Wnt signaling and proliferation, suggesting that MCC is a tumor suppressor (*19*). *SND1*, a component of the RNA-induced silencing complex, is highly expressed in CRC, and its overexpression in rat epithelial cells leads to a loss of contact inhibition and increased cell growth (*20*). *SND1* overexpression leads to a down-regulation of APC protein, even though mRNA levels are unchanged.

In addition to identifying genes whose human homologs are known to be altered in cancer, our screen identified a number of other candidate CRC genes that could, on the basis of their function, be drivers of CRC. These candidate CRC genes include *polymerase (DNA directed) iota* (*POLI*), *protein phosphatase 1 regulatory (inhibitor) subunit 13B* (*PPP1R13B*), and *R-spondin 2* (*RSPO2*), which affect DNA stability, p53-induced apoptosis, and Wnt signaling, respectively. POLI, the product of *POLI*, is an error-prone DNA polymerase responsible for the high frequency of ultraviolet-induced mutations in xeroderma pigmentosum variant cells (*21*). PPP1R13B, the product of *PPP1R13B*, enhances the ability of p53 to stimulate the expression of pro-apoptotic genes (*22*). RSPO2 is a member of a previously undiscovered family of Wnt-signaling regulators, the R-spondins (*23*). Finally, two microRNA genes not previously associated with CRC, *microRNA 181b-2* (*Mirn181b-2*) and *Mirn181a-2*, reside

Table 1. Top 10 CIS candidate genes, ranked according to the number of distinct insertions defining the CIS.

Candidate gene	Chromosome	Insertions (no.)	Function
Apc	18	61	Wnt signaling
Rspo2	15	17	Wnt signaling
Kcnq1	7	14	Potassium channels
Tcf12	9	13	Transcription factor
Wac	18	13	Adaptor
Fbxw7	3	11	Ubiquitination
Ptprk	10	11	Cell adhesion
Cugbp1	2	10	RNA binding
Nr6a1	2	10	Orphan nuclear receptor
Zcchc7	4	10	Zinc finger

Table 2. Candidate CIS genes likely to be drivers of human CRC.

Gene symbol	Mutated in human cancer*	Amplified or deleted in human CRC†	Aberrantly expressed in human CRC‡	Known human cancer gene§
ANKRD11	x	x	x	
APC	x		x	x
BMPR1A	x	x	x	x
DSTN	x	x	x	
EVI1	x		x	x
FBXW7	x			x
GPBP1	x	x	x	
NOTCH1	x	x	x	x
NSD1	x		x	x
PPP1R12A	x		x	
PTEN	x	x	x	x
RREB1	x	x	x	
SMAD4	x	x	x	x
TCF12	x	x	x	x
TNPO3	x	x	x	

*A somatic mutation was identified in COSMIC or by exon resequencing of human CRCs by (*1*, *2*). †Gene is located in a region known to be deleted or amplified in human CRC. ‡mRNA level was significantly different ($P < 0.05$) in human CRC as compared with normal colon tissue. §Gene is identified as a human cancer gene by the CGP (*13*).

within an intron of *nuclear receptor subfamily 6, group A, member 1* (*Nr6a1*), one of the CIS genes identified in our screen. Both of these microRNAs are aberrantly expressed in CRC (*24*, *25*) and inhibit glioma cell growth in vitro (*26*).

Our transposon-based forward genetic screen encountered some limitations. We believe the screen was unable to recapitulate the effect of certain activating point mutations, such as the $Kras^{G12V}$ mutation that is found in a large percentage of CRCs. In addition, random transposon insertions could potentially miss small genetic loci such as microRNAs. By design, the statistical method we used to determine CISs in order to identify likely candidate driver mutations ignores the majority of mapped transposon insertions that occurred in only one or two tumors. These non-CIS insertions may also have contributed to carcinogenesis by creating CRC driver or cooperating mutations or by causing some other level of genomic instability.

Our transposon-mediated forward genetic screen in mice identified genetic mutations that lead to the development of an epithelial cancer. The discovery of a significant overlap of mouse candidate genes and human genes that are altered in cancer indicates that this mouse model will be useful for distinguishing between driver and passenger mutations. In addition, the large number of CISs uncovered in this screen affirms the hypothesis that the growth of human CRC is driven by a few commonly mutated genes and a much larger number of genes that are rarely mutated (*1*).

References and Notes

1. L. D. Wood *et al.*, *Science* **318**, 1108 (2007).
2. D. L. Stoler *et al.*, *Proc. Natl. Acad. Sci. U.S.A.* **96**, 15121 (1999).
3. E. Staub *et al.*, *Mol. Cancer* **6**, 79 (2007).
4. H. Hayashi *et al.*, *Hum. Genet.* **120**, 701 (2007).
5. B. P. Zambrowicz *et al.*, *Proc. Natl. Acad. Sci. U.S.A.* **94**, 3789 (1997).
6. F. el Marjou *et al.*, *Genesis* **39**, 186 (2004).
7. L. S. Collier, C. M. Carlson, S. Ravimohan, A. J. Dupuy, D. A. Largaespada, *Nature* **436**, 272 (2005).
8. Materials and methods are available as supporting material on *Science* Online.
9. A. J. Dupuy, K. Akagi, D. A. Largaespada, N. G. Copeland, N. A. Jenkins, *Nature* **436**, 221 (2005).
10. S. R. Yant *et al.*, *Mol. Cell. Biol.* **25**, 2085 (2005).
11. S. Forbes *et al.*, *Br. J. Cancer* **94**, 318 (2006).
12. D. R. Rhodes *et al.*, *Neoplasia* **6**, 1 (2004).
13. P. A. Futreal *et al.*, *Nat. Rev. Cancer* **4**, 177 (2004).
14. S. Segditsas, I. Tomlinson, *Oncogene* **25**, 7531 (2006).
15. H. Rajagopalan *et al.*, *Nature* **428**, 77 (2004).
16. R. Firestein *et al.*, *Nature* **455**, 547 (2008).
17. K. W. Kinzler *et al.*, *Science* **251**, 1366 (1991).
18. M. R. Kohonen-Corish *et al.*, *Oncogene* **26**, 4435 (2007).
19. R. Fukuyama *et al.*, *Oncogene* **27**, 6044 (2008).
20. N. Tsuchiya *et al.*, *Cancer Res.* **67**, 9568 (2007).
21. Y. Wang *et al.*, *Cancer Res.* **67**, 3018 (2007).
22. A. Sullivan, X. Lu, *Br. J. Cancer* **96**, 196 (2007).
23. K. A. Kim *et al.*, *Cell Cycle* **5**, 23 (2006).
24. J. Lu *et al.*, *Nature* **435**, 834 (2005).
25. E. Bandres *et al.*, *Mol. Cancer* **5**, 29 (2006).
26. L. Shi *et al.*, *Brain Res.* **1236**, 185 (2008).

27. Insertion data are deposited in the Retrovirus Tagged Cancer Gene Database (RTCGD). We thank S. Singh for help with GSFlex 454 sequencing; K. Akagi for maintaining the RTCGD; A. Weber-Main and K. Stone for editing assistance; the Masonic Cancer Center shared resources including Biostatistics and Bioinformatics, Comparative Pathology, and the Mouse Genetics Laboratory; and the Minnesota Supercomputing Institute for providing computational resources. Research was funded by the American Cancer Society fellowship PF-06-282-01-MGO (to T.K.S.), NIH grant R01CA113636-01A1 (to D.A.L.), NCI grant K01CA122183-03 (to L.S.C.), the Biomedical Research Council of A*STAR (Agency for Science, Technology and Research) Singapore (N.A.J. and N.G.C.), and the NCI Intramural Research Program of NIH (L.T.). A University of Minnesota Academic Health Center Faculty Development Grant provided additional funding to D.A.L. and R.T.C. D.A.L. is a cofounder of, and has an equity interest in, Discovery Genomics, Inc., a biotechnology company that is pursuing SB technology for human gene therapy. The University of Minnesota has filed a patent related to the work described in this paper.

Supporting Online Material

www.sciencemag.org/cgi/content/full/1163040/DC1
Materials and Methods
Figs. S1 and S2
Tables S1 to S9
References

10 July 2008; accepted 6 February 2009
Published online 26 February 2009;
10.1126/science.1163040
Include this information when citing this paper.

Benchtop Cell Culture System

The BioLevitator 3-D Cell Culture System is designed to deliver productivity gains to researchers in drug discovery and development, therapeutics, and regenerative medicine. The BioLevitator eliminates traditional peripheral cell culture instruments, such as incubators and centrifuges, and minimizes manual handling. Each of the BioLevitator's four hydrophilic, PTFE-filtered, 50-ml cell culture tubes can produce cell growth equivalent to up to 10 T75 flasks, depending on the cell line. The system features a user-friendly touch-screen interface with real-time monitoring and control of environmental temperature and carbon dioxide levels.

Hamilton Company
For information 775-858-3000
www.hamiltoncompany.com

Stem Cell Picker

The CellCelector automated stem cell picker consists of an inverted Olympus microscope, robotic arm, and liquid handling station integrated with powerful image acquisition and analysis software. This walkaway system allows researchers to set parameters for the cell or colony types they want, including size, proximity to other colonies, or roundness. The picking tool on the robotic arm gently picks and dispenses cells into a microplate well in just 30 seconds, while assuring that the cells chosen are of consistent quality. The compact unit can fit under any standard laminar flow hood to keep the cells free of contamination. The system can also be fitted with an autoclavable metal tool for scraping adherent cells or a disposable glass capillary for picking single cells, both of which are designed to maintain cell integrity and viability.

The Automation Partnership
For information +44-(0)-1763-227200
www.automationpartnership.com

Temperature-Responsive Surface

The Nunc UpCell Surface for temperature-induced cell harvesting is designed to enable quick dissociation of cells from the culture surface at a simple change in temperature. This process negates the need for enzymatic treatment and cell scraping, while maintaining cell viability and the integrity of surface receptors and antigens. Even cell types that are difficult to detach by other methods and contiguous cell sheets can be harvested from the Nunc UpCell Surface. Harvested cell sheets can be stacked on top of each other to create three-dimensional models and cocultures. It is available as sterile MicroWell plates, dishes, and multidishes. The surface consists of a covalently immobilized polymer that forms a thin, even layer on the culture dish or plate. The surface is slightly hydrophobic at 37°C, allowing cells to attach and grow, but it turns hydrophilic at temperatures below 32°C, binding water and swelling, and releasing adherent cells with their underlying extracellular matrix.

ThermoFisher Scientific
For information 508-742-5254
www.thermo.com/UpCell

Cell-Based ECIS Instruments

The new Electric Cell-substrate Impedance Sensing (ECIS) models Z and ZΘ provide multiple frequency measurements, broad bandwidth, speed, high sensitivity, and comprehensive data analysis capabilities. In ECIS, cells are cultured on small gold electrodes whose impedance is measured with a weak AC signal. When cells attach and spread on these electrodes, their insulating membranes constrain the current. These impedance changes can be used to quantify real-time data on cell behavior without the use of fluorescence or radiolabeled materials. Cell behaviors that can be measured include cell attachment and spreading on extracellular matrix proteins, cell migration, extravision of endothelial cell layers, barrier function, signal transduction, cytopathic effects of viral infections, cytotoxicity, cell proliferation, and more. The ECIS ZΘ system adds the capability to measure complex impedance and report its constituent components of resistance and capacitance over a spectrum of frequencies.

Applied BioPhysics
For information 866-301-3247
www.biophysics.com

Cell Analyzer

The MACSQuant Analyzer is a benchtop cell analyzer for sensitive multicolor flow analysis. The analyzer features a compact design, multiparameter cell analysis, absolute cell counting, sensitive rare cell analysis using MACS technology, multisample processing, and autolabeling of samples.

Miltenyi Biotec
For information 800-367-6227
www.miltenyibiotec.com

Stem Cell Sorting and Analysis

The BD Human Pluripotent Stem Cell Sorting and Analysis Kit makes use of flow cytometry for reliable characterization and sorting. This ready-to-use kit includes pre-titrated fluorochrome conjugated antibodies, experiment setup beads, validated protocols, and software analysis templates. The kit is optimized for use on the widely used BD flow cytometry instruments. The system's integrated approach minimizes assay-to-assay variability to produce dependable, comparable results quickly. Its open design allows for the easy addition of supplementary antibodies to adapt the kit to meet specific research objectives.

BD Biosciences
For information 201-847-5533
www.bdbiosciences.com/stemcellsource

Electronically submit your new product description or product literature information! Go to **www.sciencemag.org/products/newproducts.dtl** for more information.

Newly offered instrumentation, apparatus, and laboratory materials of interest to researchers in all disciplines in academic, industrial, and governmental organizations are featured in this space. Emphasis is given to purpose, chief characteristics, and availabilty of products and materials. Endorsement by *Science* or AAAS of any products or materials mentioned is not implied. Additional information may be obtained from the manufacturer or supplier.

Science Careers
Classified Advertising

For full advertising details, go to **ScienceCareers.org** and click **For Advertisers**, or call one of our representatives.

UNITED STATES & CANADA
E-mail: advertise@sciencecareers.org
Fax: 202-289-6742

Joribah Able
Industry – US & Canada
Phone: 202-326-6572

Alexis Fleming
Northeast Academic
Phone: 202-326-6578

Tina Burks
Southeast Academic
Phone: 202-326-6577

Daryl Anderson
Midwest/Canada Academic
Phone: 202-326-6543

Nicholas Hintibidze
West Academic
Phone: 202-326-6533

EUROPE & INTERNATIONAL
E-mail: ads@science-int.co.uk
Fax: +44 (0) 1223 326532

Tracy Holmes
Associate Director, *Science* Careers
Phone: +44 (0) 1223 326525

Alex Palmer
Phone: +44 (0) 1223 326527

Dan Pennington
Phone: +44 (0) 1223 326517

Susanne Kharraz Tavakol
Phone: +44 (0) 1223 326529

Louise Moore
Phone: +44 (0) 1223 326528

JAPAN
Mashy Yoshikawa
Phone: +81 (0) 3 3235 5961
E-mail: myoshikawa@aaas.org

POSITIONS OPEN

NATIONAL LABORATORY OF GENOMICS FOR BIODIVERSITY
Langebio - Mexico
Call for Applications

FACULTY POSITIONS are available for outstanding young scientists at the National Laboratory of Genomics for Biodiversity (Langebio), a new research unit of the Centro de Investigación y de Estudios Avanzados del Instituto Politécnico Nacional (Cinvestav) in Mexico. We are particularly interested in hiring PIs with a quantitative background in the fields of computational biology, evolutionary biology, metabolic engineering, and cell biology, but will consider exceptional candidates in other fields. Access to Langebio's state-of-the-art genomic and metabolomic facilities will provide opportunities for collaborative and interdisciplinary research. Preference will be given to individuals with publications in high-impact journals and who have held a Ph.D. or equivalent for no more than six years.

Applications are due by April 15, 2009. Please submit curriculum vitae, a short outline of your scientific accomplishments and proposed research program (maximum of three pages), copies of three selected publications, and contact information of three colleagues who have agreed to write letters of recommendation for you. Recruitment is expected to initiate in May 2009, and selected applicants are expected to start joining the facilities in July 2009. Rank and salary are dependent upon qualifications. **Submit applications to: Alejandro Hernández (attention Dr. Luis Herrera-Estrella), Langebio-Cinvestav, Apartado Postal 629 C.P. 36821 Irapuato, Guanajuato, Mexico. Fax: 52-462-623-96-56; e-mail: ahernandez@ira.cinvestav.mx.**

POSTDOCTORAL FELLOW
Cleveland Clinic, Cleveland, Ohio, U.S.A.

Postdoctoral positions are available in the Angiogenesis Center and Taussig Cancer Center of the Cleveland Clinic. Highly motivated individuals are sought with a strong interest in vascular and angiogenesis research. Focus is on the mechanisms of blood vessel development, stem cell mobilization and recruitment into vasculature with emphasis on integrin and Akt kinase dependent signaling (**Chen** et al., *Nat. Med.* **11:**1295-1298, 2005; **Feng** et al., *JCB*, 2008; **Malinin** et al., *Nat. Med.*, **15:**313-315, 2009). Visit **website: http://www.lerner.ccf.org/moleccard/byzova/** for more information.

Successful applicants must have a Ph.D. degree in molecular/cellular biology, cancer biology, or a related biological science. We encourage and facilitate career development of postdoctoral researchers to independence. Interested individuals should send their curriculum vitae, a one-page statement of research interests, and at least three references to: **Lisa Plungas, Cleveland Clinic, 9500 Euclid Avenue, NB50, Cleveland, OH 44195. Fax: 216-445-8204; e-mail: plungal@ccf.org.**

Cleveland Clinic is an Equal Opportunity, Affirmative Action Employer. Members of underrepresented groups are strongly encouraged to apply.

RESEARCH ASSOCIATE, cellular signaling experience required. Send resume to: **Dr. J. Letterio, Case Western Reserve University, Department of Pediatrics, 2103 Cornell Road, Wolstein Research Building, Room 3501, Cleveland, OH 44106.** Must reference **job code FF2009.**

POSITIONS OPEN

VCU

TENURE -TRACK FACULTY POSITIONS
Department of Biochemistry and Molecular Biology
Virginia Commonwealth University
School of Medicine

As part of an ongoing major expansion in biomedical research at Virginia Commonwealth University Medical Center, we invite applications from outstanding individuals with expertise in any area of biochemistry and biomolecular sciences, particularly cellular and molecular signaling, cancer biology, lipidomics, gene regulation, genetics, and epigenetics. Candidates with Ph.D. or M.D.-Ph.D. will be considered at all ranks based upon qualifications and experience. Substantial start-up and salary packages are available for outstanding investigators.

VCU has a very active community of investigators and is committed to providing an outstanding research environment. More information about the School of Medicine and departments and this open position can be found at **websites: http://www.vcu.edu/biochem/department/pos.shtml** and **http://www.pubinfo.vcu.edu/facjobs/.** Applicants should submit their curriculum vitae, names and e-mail addresses of three references, and a summary of research interests electronically to: **Dr. Sarah Spiegel and Dr. Paul Dent at e-mail: biocrecruit@vcu.edu, Department of Biochemistry and Molecular Biology, Virginia Commonwealth University School of Medicine.**

Virginia Commonwealth University is an Equal Opportunity/Affirmative Action Employer. Women, Persons with Disabilities, and Minorities are encouraged to apply.

DIRECTOR OF BIOLOGY TEACHING AND LEARNING
University of Tennessee

The Division of Biology at the University of Tennessee seeks applicants for a tenure-track position to direct the freshman and sophomore core biology program and to lead the development and implementation of innovative teaching approaches in biology, beginning August 2009. Responsibilities of the Director include: (1) implementing ongoing curriculum evaluation and assessment, (2) research publications in biology teaching practices at the college level, (3) course design and administration in coordination with faculty, (4) training and supervision of instructional staff including development of teaching workshops, and (5) teaching in the biology core. The Director is expected to play a leadership role in obtaining outside funds for improved biology teaching. The successful candidate will have: (1) a Ph.D. in the biological sciences, (2) published scholarship in the area of biology education, (3) a demonstrated record of teaching excellence in biology courses, (4) success in procuring external grants (preferably federal grants) to support activities in biology education, and (5) experience with administration of biology courses (e.g., curriculum revision). Experience with graduate teaching, including the mentoring of graduate students, is highly desirable. Please see **website: http://www.bio.utk.edu/division** to find information about the Biology Division at the University of Tennessee. Review of applicants will begin immediately and continue until the position is filled. Please submit curriculum vitae, statement of teaching philosophy, interests, and experience, teaching evaluation summaries if available, and names with contact information of three references to **e-mail: jcall1@utk.edu.**

The University of Tennessee is an Equal Employment Opportunity/Affirmative Action/Title VI/Title IX/Section 504/ADA/ADEA institution in the provision of its education and employment programs and services. All qualified applicants will receive equal consideration for employment without regard to race, color, national origin, religion, sex, pregnancy, marital status, sexual orientation, gender identity, age, physical or mental disability, or covered veteran status.

WWW.NIH.GOV
Positions @ NIH
THE NATIONAL INSTITUTES OF HEALTH

DEPARTMENT OF HEALTH AND HUMAN SERVICES (DHHS)
NATIONAL INSTITUTES OF HEALTH (NIH)
National Institute of Arthritis and Musculoskeletal and Skin Diseases (NIAMS)
Director, Division of Extramural Research Activities (DERA)

The Department of Health and Human Services (DHHS) and the National Institutes of Health (NIH) are seeking exceptional candidates for the position of Director, Division of Extramural Research Activities (DERA), National Institute of Arthritis and Musculoskeletal and Skin Diseases (NIAMS) to support research into the causes, treatment, and prevention of arthritis and musculoskeletal and skin diseases, the training of basic and clinical scientists to carry out this research, and the dissemination of information on research progress in these diseases, while promoting public health and addressing issues of health disparities. This position offers a unique opportunity to direct, manage, and provide oversight to the Grants Management Branch (GMB) and the Scientific Review Branch (SRB), as well as, to oversee human subject protection and clinical trial activities under the extramural programs of NIAMS.

The DERA Director manages and directs all DERA program activities, which includes developing and justifying the yearly budget request. The DERA Director provides guidance and leadership to the GMB and SRB Chiefs on the development of new programs and projects, directs collaboration with Federal organizations, grantees, contractors, and private industry to develop models for DERA programs, and best practice models for providing DERA services, and provide leadership and advice to the Director, NIAMS, on developing, implementing, and coordinating extramural research contract, grant, and training program policies. The DERA Director maintains ongoing analysis and evaluation of the review of applications and the management of grants and contracts to support overall policy research, development and reporting for the extramural activities of the Institute. In addition, the DERA Director will collaborate with leading figures in the scientific community at NIH and other government organizations, representatives of academic institutions, and members of foreign governments and scientific organizations to exchange information on scientific research and coordinate projects of mutual interest. Te DERA Director is a full partner in the executive leadership of the NIAMS.

Applicants may browse the NIAMS Home Page at **http://www.niams.nih.gov/** for additional information on the Institute. Applicants must possess an M.D., Ph.D., or equivalent degree in a biomedical field related to the mission of NIAMS and have professional experience with a broad national programmatic or scientific background; be able to interact with the Scientific Program Division with equal authority; have the demonstrated capability to plan and direct programs of national and international importance; and have the ability to communicate with and obtain the cooperation of public, private and national and international organizations and individuals. Salary is commensurate with his/her qualifications and experience. Full Federal benefits including leave, health and life insurance, long-term care insurance, retirement, and a savings plan (401k equivalent). A detailed vacancy announcement that includes application procedures is available at: **http://www.jobs.nih.gov (under vacancy announcement NIAMS-09-327761). Questions may be addressed to Ms. Ruth Fritz, 301-496-6051 e-mail: fritzr@mail.nih.gov**. A CV and bibliography, including a statement addressing the qualifications and interest in the position, should be received by **April 30, 2009**. *Applications received after this date will be considered until the position is filled.*

Department of Health and Human Services
National Institutes of Health, National Cancer Institute
Center for Cancer Research

BIOINFORMATICIAN / BIOINFORMATICS SCIENTIST

The Laboratory of Biochemistry and Molecular Biology (LBMB), Center for Cancer Research (CCR), National Cancer Institute (NCI), National Institutes of Health (NIH), Department of Health and Human Services (DHHS), Bethesda, Maryland is seeking a mid-level or senior bioinformatics scientist. The candidate should have a B.S., M.S. or Ph.D. degree in Bioinformatics, Computer Science, or the equivalent. Previous experience with biological research and working knowledge of the statistical tools appropriate to task is preferred.

The successful candidate will have experience analyzing high-throughput genomic datasets derived from ChIP-chip and ChIP-Seq technologies, familiarity with available software tools for analyzing these data, and the ability to develop tools where none are available. Candidate should be proficient in performing basic quality control and analysis such as data set normalization, significance testing, clustering, identification of gene regulatory themes, and mapping of binding events; be able to provide support in custom microarray design and in the visualization and quantification of large datasets; and be able to communicate effectively with and feel comfortable working closely with a group of biochemists and molecular biologists with diverse research interests. Salary will be commensurate with experience and accomplishments, and a full Civil Service package of benefits (including retirement, health, life and long term care insurance, Thrift Savings Plan participation, etc.) Hiring will occur under the Title 42 appointing mechanism, which is a time-limited appointment.

Interested applicants should send a cover letter, curriculum vitae, and three letters of reference to: **Ms. Azalia Zandieh, National Cancer Institute, National Institutes of Health, 9000 Rockville Pike, Building 37, Room 6106C, Bethesda, MD 20892-4260, Email: zandieha@mail.nih.gov**.

The NIH Director's Wednesday Afternoon Lecture Series

Biomedical scientists around the world are invited to join us online to hear leading investigators present their latest results to the NIH Intramural Research community. Lectures may be viewed live at 3:00 p.m., EST (20:00 GMT) on Wednesdays, from September through June. Live webcasts can be viewed under "Today's Events" at: <http://videocast.nih.gov/>

The current schedule of lectures is available at: <http://www1.od.nih.gov/wals/schedule.htm

Upcoming Lectures:

- **April 1:** A. James Hudspeth, Rockefeller University, *"Making an Effort to Listen: Mechanical Amplification by Myosin Molecules and Ion Channels in Hair Cells of the Inner Ear"*
- **April 8:** S. Ananth Karumanchi, Beth Israel Deaconess Medical Center, "Pathogenesis of Preeclampsia"
- **April 15:** Lois Smith, Children's Hospital Boston, "Understanding Angiogenesis through Retinopathy"
- **April 22:** Ruslan Medzhitov, Yale School of Medicine, *"Innate Host Defense: Mechanisms and Pathways*
- **April 29:** Eric Nestler, *University of Texas Southwestern Medical Center, "Transcriptional Mechanisms of Drug Addition"*

University of Colorado Denver

School of Medicine

The University of Colorado Denver School of Medicine seeks applicants for the position of Chair of the Department of Pharmacology. The Department consists of 24 faculty members whose interests span neurosciences, cell biology, drugs of abuse, genomics and bioinformatics, signal transduction, lipid mediators, and structural biology. The Department occupies dramatic new laboratories and offices in twin towers of the Research Complex at the new University of Colorado Denver Anschutz Medical Campus.

The Department of Pharmacology has a large basic science research program with more than $19 million in annual research funding. The Department has won numerous awards for the teaching of medical students. Details are available at the departmental web site: **http://pharmacology.ucdenver.edu/index.shtm**.

The Chair of the Department of Pharmacology reports to the Vice-Chancellor for Health Affairs/Dean of the School of Medicine and participates with other department chairs and faculty to develop School and Department programs, curriculum, administration, and budgetary planning and implementation. The position requires excellence in teaching, demonstrated administrative ability/leadership and leadership in research and scholarly activity.

Review of applications will continue until the position is filled. Applicants should apply online at the **https://www.jobsatcu.com** website using posting number **806418**. Questions about the application process may be directed to **Jan.Bodin@ucdenver.edu**.

The University of Colorado Denver is committed to the recruitment and employment of a diverse faculty. We encourage applications from women and minorities.

CIFAR

Junior Fellowship in Experience-based Brain and Biological Development

The **Experience-based Brain and Biological Development Program** of the Canadian Institute for Advanced Research (CIFAR) invites applications for a **CIFAR Junior Fellowship**, a two-year postdoctoral appointment to begin by the fall of 2009. CIFAR is a catalyst for discovery, incubating ideas that revolutionize the international research community. The EBBD Program explores the core question of how genes and socially partitioned early environments interact to bias the epigenetic and neurobiologic processes shaping child health and development. It includes scientists employing insights and techniques from modern developmental, behavioural, neural and molecular biological, genetic, immunological, epidemiological, and population health sciences.

The successful candidate will have an outstanding record of accomplishment in an area of interest to the program, excellent communication skills, and strong potential to collaborate with program members. During his or her tenure, the Junior Fellow will be integrated as a member of the EBBD Program and will also participate in CIFAR's elite Junior Fellow Academy, interacting with peers in the Institute's other programs. The position is tenable at any of the Canadian or U.S. institutions where program members are based. More information, including the list of eligible supervisors, is available in the full advertisement posted at **http://www.cifar.ca/JFA**.

Candidates should apply directly to the program member(s) they wish to work with. The application should include a full CV and an imaginative, 3-5 page research proposal related to ongoing projects by members of the program. Materials should be sent in PDF format to the member's e-mail address. Applicants should also arrange for 3-4 letters of reference to be sent to the same address (at least 3 must not be from CIFAR members). To receive full consideration, applications must be received by **May 1, 2009**.

USDA ars Agricultural Research Service

www.ars.usda.gov

The USDA, Agricultural Research Service (ARS), Animal and Natural Resources Institute in Beltsville, Maryland, is seeking an **Associate Institute Director** for a permanent full-time position. Salary is commensurate with experience and can range between $120,830 to $153,200 per annum, plus benefits. The mission of the institute is to conduct research and technology transfer programs that ensure high quality and safe food and other animal products while protecting the natural resource base and the environment. The mission is accomplished through fundamental and applied research in 8 laboratories, and a Veterinary Services Unit and Animal Care Compliance Office. The Associate Director participates with the Director in planning, coordinating, and evaluating the institute's programs, and provides leadership and operational accountability for the institute's research and technology transfer programs. The position requires thorough knowledge of animal, natural resources, and/or environmental sciences; knowledge of budgetary processes and procedures; and managerial skills in establishing goals and priorities and in the assessment and assignment of human resources to accomplish goals.

Refer to announcement **ARS-X9E-0098** at: **http://www.afm.ars.usda.gov/divisions/hrd/vacancy/VAC2.HTM** for detailed information regarding qualification requirements and for complete application information and instructions. Applications must be postmarked by **April 10, 2009**.

U.S. Citizenship is required.
USDA/ARS is an Equal Opportunity Employer and Provider.

BIG DREAMS. BOLD FUTURE.

Director (Associate/Full Professor)

Department: Florida Center of Excellence for Biomolecular Identification and Targeted Therapeutics (FCoE-BITT) - Office of Research and Innovation
Campus: University of South Florida, Tampa Campus
Position Number: 10685 - **Deadline to Apply:** Open until Filled
Annual Salary: Negotiable - **FTE:** 100 percent, 9 months; Tenure Earning

FCoE-BITT is a comprehensive center funded by the State of Florida and USF that enhances interactions between scientists and engineers to identify molecules of human health significance and develop novel methods for use in diagnosis, prevention and treatment of human disease. The Center consists of 100 research faculty associated with the Colleges of Arts and Sciences, Engineering, Medicine and Public Health, and oversees several shared core equipment facilities, including a 600 MHz and 800 MHz NMR Core Facility and a Proteomics Core Facility.

Duties: FCoE-BITT seeks a person with a Ph.D. or equivalent degree in a relevant field who is nationally recognized as a leader in Center-related research areas with demonstrated excellence in both research and administration who will be able to provide visionary leadership for all aspects of the Center, including research, finance, administration and education. The Director is responsible for building and maintaining partnerships with industry, government agencies and community organizations.

Minimum Qualifications: Ph.D. or equivalent degree in a scientific area related to FCoE-BITT research focus areas, record of external funding, and relevant publications.

Preferred Qualifications: Evidence of administrative experience and industry/university collaboration.

Applicants should send (as PDF files) a CV, a statement of research and three letters of recommendation to: **FCoE-BITT - Office of Research and Innovation, University of South Florida, Attn: Alma Julia, 30338 USF Holly Drive, Tampa, FL 33612; or ajulia@bitt.usf.edu , phone (813) 974-0274.**

USF is an Equal Opportunity/Equal Access University.

USF UNIVERSITY OF SOUTH FLORIDA

• TAMPA • ST. PETERSBURG • SARASOTA - MANATEE • POLYTECHNIC

The University of Stavanger (UiS) currently enrolls 8.300 students and employs 1200 academic and administrative staff. It offers a range of study and research programs and engages in dissemination of knowledge. The academic activity is organized into three faculties and the University Museum of Archeology. Many of the externally funded research activities are carried out in cooperation with our affiliated International Research Institute of Stavanger AS (IRIS).

The University is located in Norway's most attractive region with 300.000 inhabitants.
The region has a dynamic labor market and offers excellent opportunities for housing, cultural events and leisure.

University of Stavanger

The University of Stavanger invites applications for the following positions:

Post-doctorate position in Mass spectrometry

Faculty of Science and Technology, Department of Mathematics and Natural Sciences, Centre for Organelle Research

Research Fellow in Plant Biochemistry

Faculty of Science and Technology, Department of Mathematics and Natural Sciences, Centre for Organelle Research

Research Fellow in Plant Molecular, Cell and Computational Biology

Faculty of Science and Technology, Department of Mathematics and Natural Sciences, Centre for Organelle Research

Explore the job opportunities at www.uis.no

CICERO tt

SCHOOL OF MEDICINE
INDIANA UNIVERSITY

ENDOWED CHAIR, GASTROINTESTINAL CANCER

The Division of Gastroenterology and Hepatology at Indiana University School of Medicine, in conjunction with the IU Simon Cancer Center, is seeking applications from qualified individuals for a senior level, tenured/tenure-track position to expand basic and translational research to complement existing excellent clinical research and clinical practice in the area of GI cancer. The institution is particularly strong in colon, pancreatic, biliary, and liver cancers. Qualified applicants will also be considered for an Endowed Professorship in the School of Medicine. The position requires a strong record of productive independent research and a record of peer-reviewed extramural funding.

Interested individuals should send their curriculum vitae, a brief overview of research plans, and three (3) letters of reference (NOTE: full professors must submit six (6) letters of reference) to: **Naga Chalasani, MD, Chief, Division of Gastroenterology and Hepatology, Indiana University School of Medicine, RG 4100, 1050 Wishard Blvd., Indianapolis, IN 46202**. Or email application materials to **bjcraig@iupui.edu**; reference "Faculty Position" in the subject line. To ensure full consideration, applications should be received by **June 1, 2009**.

Indiana University is an Affirmative Action, Equal Opportunity Employer. Applications from women and minorities are encouraged.

Technical University of Denmark

DTU

H.C. ØRSTED POSTDOC

DTU invites highly talented young researchers who have already obtained outstanding results during their PhD studies and have demonstrated excellence and potential in their field of study to apply for one the stipends under the H.C. Oersted Postdoc Programme. The programme is named after the founder of the university, H. C. Oersted, who discovered Electromagnetism.

Two of the scholarships are allocated research at the European Graduate School in Sustainable Energy www.dtu.dk/EGSSE of the European University Alliance which includes the Technical University of Munich and Eindhoven University of Technology.

Applications must be based on the details of the full text announcement. Application deadline: 16 May 2009

The Technical University of Denmark (DTU) is a modern, specialized technical university with considerable international influence and a high international standard. DTU develops and creates value using the natural sciences and technical sciences to benefit society. Our 6000 students are educating themselves for the future, and DTU's 4500 employees focus intensely on education, research, public-sector consultancy and innovation, which contribute to enhancing the economy and improving social welfare. DTU places high demands on and provides unique opportunities for all University employees. We strive for academic excellence, collegial respect and freedom tempered by responsibility.

Further details: dtu.dk/vacancy

THE UNIVERSITY OF KANSAS
CANCER CENTER

Faculty Positions: Basic, Translational, and Clinical Cancer Research

The University of Kansas Cancer Center is seeking laboratory-based faculty members with a Ph.D., M.D. or DVM and an interest in cancer research. Based on qualifications, the successful candidates will be appointed on the University tenure track at the assistant, associate or full professor. The candidates will be expected to establish and maintain an independently funded research program concentrating on basic, translational and/or clinical cancer research.

An excellent start-up package including space and equipment is available, as well as a competitive salary. Additional attractions are emphasis on cancer research within the university, the consolidation of cancer researchers with similar interests, and the chance to collaborate with an outstanding drug discovery, development and delivery team associated with the top ranked NIH funded School of Pharmacy. The University of Kansas Cancer Center is experiencing significant growth in basic, translational, and clinical research with an increase in the number of faculty and basic and clinical research facilities.

To view the complete position description and apply on-line only, go to **http://jobs.kumc.edu** and search for position **J0084013**.

The University of Kansas Medical Center is an Affirmative Action/Equal Opportunity Employer.

Director Position

Institute of BioMedical Sciences
Academia Sinica, Taiwan

Academia Sinica, Taiwan, invites applications and nominations for the position of Director of Institute of BioMedical Sciences (IBMS). The initial appointment is for a period of three years (renewable for a second term), and will also carry the title of Research Fellow.

Academia Sinica is the pre-eminent academic institution in Taiwan. It is devoted to basic and applied research in mathematics and physical sciences, life sciences, and humanities and social sciences. IBMS engages in carrying out research into mechanisms leading to human diseases, especially those which are common in Taiwan. Current research efforts of IBMS cover the following six areas: cancer research, cardiovascular research, infectious diseases, neuroscience research, epidemiology and public health research and structural biology. IBMS is well funded and equipped with modern research facilities. For details about Academia Sinica and IBMS, please consult the website: **http://www.sinica.edu.tw**

Interested candidates should have a PhD or MD/PhD degree, a distinguished record of academic scholarship, and diverse experience in university and professional service. He/she is expected to pursue a vigorous research program. The successful candidate will be expected to build on the existing strengths of the institution, develop new research thrusts, promote basic biomedical sciences and provide intellectual leadership in relevant basic and applied life sciences in Taiwan.

Applications and nominations, including complete curriculum vitae, a publication list, and three letters of recommendation, should be submitted to **Dr. Andrew H.-J. Wang, Vice President, Academia Sinica, 128 Academia Road Section 2, Nankang, Taipei, 115, Taiwan**. Screening of applications/nominations will begin immediately, and will continue until the position is filled.

UNIVERSITY OF CAMBRIDGE
A world of opportunities
www.cam.ac.uk/jobs/

University Lecturer: Physical Chemistry

Department of Chemistry
£36,532 - £46,278 pa

Candidates should have a strong research background in physical chemistry or chemical physics and be capable of forging strong links to other cognate scientific disciplines. Applications would be particularly welcome from candidates with research experience in cutting-edge applications of any form of spectroscopy. The successful candidate must also be able to teach physical chemistry at undergraduate level. Appointment to a Lectureship will be for an initial probationary period of five years, with reappointment to the retiring age subject to satisfactory performance.

Prospective candidates may make informal enquiries to Professor Elliott (sre1@cam.ac.uk) or Professor Pyle (physical-sec@ch.cam.ac.uk).

This post is available from October 2009.

Applications can be electronic or single-sided hard copy, and should include a CV, publications list, contact details for three professional referees, and a statement (up to eight pages) covering your research experience to date and research plans for the future. This should be accompanied by a completed PD18 Parts I and III (downloadable from http://admin.cam.ac.uk/offices/hr/forms/pd18/), and should be sent to Dr Howard Jones, Academic Secretary, Department of Chemistry, Lensfield Road, Cambridge CB2 1EW (email: hrnj1@cam.ac.uk).

Information about all the Department's research and teaching activities is available from the Chemistry Department's website (http://www.ch.cam.ac.uk).

Please quote reference: MA04867. Closing date: 23 April 2009.

The University is committed to Equality of Opportunity.

UNIVERSITY OF CAMBRIDGE
A world of opportunities
www.cam.ac.uk/jobs/

Readership in Inorganic Chemistry

Department of Chemistry
£52,628 pa

Applicants should have a strong research background in any area of core inorganic chemistry that embraces reactivity, synthesis and structural chemistry. Subject areas in which applications would be especially welcome include: molecular catalysis (identified as a priority area by EPSRC); solution phase co-ordination chemistry, for example in regard to highly functionalized small molecules for such applications as electrochemical hydrogen production, photochemical energy production, luminescence and imaging; solid state chemistry, including synthesis and characterisation of materials relevant to gas storage and separation, magnetochemistry and other device applications. Applicants must also be able to make a significant contribution to the Department's undergraduate and graduate teaching programmes.

Informal enquiries about the post may be addressed to Professor Richard Lambert (rml1@cam.ac.uk).

Applications can be electronic or single-sided hard copy, and should include a CV, publications list, contact details for three professional referees, and a statement (up to eight pages) covering your research experience to date and research plans for the future. This should be accompanied by a completed PD18 Parts I and III (downloadable from http://admin.cam.ac.uk/offices/hr/forms/pd18/), and should be sent to Dr Howard Jones, Academic Secretary, Department of Chemistry, Lensfield Road, Cambridge CB2 1EW (email: hrnj1@cam.ac.uk).

Please quote reference: MA04868. Closing date: 30 April 2009.

This post is available from October 2009.

Information about all the Department's research and teaching activities is available from the Chemistry Department's website (http://www.ch.cam.ac.uk).

The University is committed to Equality of Opportunity.

VTC Virginia Tech Carilion RESEARCH INSTITUTE

FOUNDING DIRECTOR

The Virginia Tech Carilion Research Institute (VTCRI) invites applications for its founding Director. With the benefit of a robust research university collaborating with a transformational, integrated health system, the Director will have the rare opportunity to help lead, create, and transform health-related research. The VTC Research Institute is a result of the partnership of Carilion Clinic, the newly formed Virginia Tech Carilion School of Medicine, and the solid biomedical and life science research programs at Virginia Tech. VTCRI has the strong support of senior leadership across VT and Carilion, and their partnership is committed to excellence in all aspects of health sciences.

The mission of VTCRI is to be a premier institute of interdisciplinary and translational research within the health sciences. The Director will provide leadership for VTCRI, with responsibility for development of research strategy, the recruitment of up to 40 research teams, development of collaborative programs of translational research, and integration of VTCRI with the VTC School of Medicine, Carilion Clinic, and existing programs at Virginia Tech.

VTCRI will be part of an emerging biomedical complex that includes the Carilion Clinic and VTC School of Medicine. The VTC facility is currently under construction in Roanoke, Virginia, with an anticipated Fall 2010 completion date.

The successful candidate will be an MD or PhD scientist of national distinction having a track record of discovery and publication who will continue his or her research activities. Applicants should have exceptional communication and strategic planning skills, an established record of leading and fostering large research programs, a commitment to translational research, and the ability to work with VT, VTCSOM, and CC leaders, faculty, and clinicians to develop a common vision and purpose. Area of expertise and specialization are open.

Candidates should submit a cover letter, curriculum vitae, and contact information for three references to **www.jobs.vt.edu** posting **#090048**. After a preliminary review, references will be contacted and asked to submit letters of recommendation for selected candidates. The review of candidates will begin on June 1, 2009 and will continue until a candidate is selected. The anticipated start date for the successful candidate is on or before January 1, 2010.

Virginia Tech is the recipient of the National Science Foundation ADVANCE Institutional Transformation Award to increase the participation of women in academic science and engineering careers.

Southwestern Virginia is a wonderful location with strong communities, plentiful recreation and arts, and never-ending vistas across beautiful mountains. It provides a diversity of lifestyles with remarkably easy access to Washington DC, Richmond, North Carolina, mountains and beaches. A more complete description of VTCRI can be found at the VTCRI website **www.vtc.vt.edu.**

Virginia Tech does not discriminate against employees, students, or applicants on the basis of race, color, sex, sexual orientation, disability, age, veteran status, national origin, religion or political affiliation. Anyone having questions concerning discrimination should contact the Office for Equal Opportunity.

a partnership of CARILION CLINIC and VirginiaTech

University at Buffalo The State University of New York

TENURE TRACK FACULTY POSITIONS IN ORAL BIOLOGY

The Department of Oral Biology invites applications for two full-time, tenure-track faculty positions at the Professor/Associate Professor/Assistant Professor level. We are seeking outstanding individuals capable of establishing and maintaining an independent research program, with an emphasis on molecular, cellular, genetic and/or computational biology approaches to:

- Host/immune response against oral pathogens
- Tissue engineering/mineralized tissue (bone) biology
- Craniofacial developmental biology
- Oral cancer

Candidates with research interests in bioinformatics, functional genomics, proteomics, or computational biology will have the opportunity to work as a member of the NYS Center of Excellence in Bioinformatics and Life Sciences. Additional collaborative opportunities are available through the UB School of Medicine and Biomedical Sciences, the UB School of Dental Medicine, Roswell Park Cancer Institute, and other affiliated organizations.

The successful candidate will be expected to contribute to the teaching mission of the department, including supervision of graduate students in Oral Biology and instruction in the undergraduate and graduate Dental School curricula. Candidates should hold DDS, DMD, MD, PhD or equivalent. Applications from individuals with dual degrees (e.g., DDS/PhD, DMD/PhD) are especially encouraged. Successful candidates will be expected to have or achieve significant grant funding, appropriate teaching experience, and for appointments at a higher rank, a national/international research reputation. Please apply through the UBJobs website at **www.ubjobs.buffalo.edu/applicants/Central?quickFind=52523** (all applications MUST be submitted through this site).

The University at Buffalo is committed to increasing diversity within its faculty by seeking women and minority candidates.

CONFERENCE

Deadline for Early Registration April 15, 2009

34th FEBS Congress

July 4 - 9, 2009
Prague, Czech Republic

Life's Molecular Interactions

- Cells' Modular Components
- Social Life of the Cell
- Organism, the Network of Interactions

Czech Society for Biochemistry and Molecular Biology

Federation of European Biochemical Societies

www.febs2009.org

POSITIONS OPEN

SCRIPPS FLORIDA

FACULTY POSITIONS
Departments of Cancer Biology, Chemistry, Infectology, Metabolism and Aging, Molecular Therapeutics, and Neuroscience

The Scripps Florida campus of The Scripps Research Institute (TSRI) is seeking outstanding applicants for tenure track faculty positions in the Departments of Cancer Biology, Chemistry, Infectology, Metabolism and Aging, Molecular Therapeutics, and Neuroscience at its newly opened, state-of-the-art campus in Jupiter, Florida. TSRI applies integrative molecular genetic, biochemical, biophysical and chemical biology approaches to elucidate the cellular, molecular and physiological mechanisms that control learning and memory, addiction and behavior, cognitive and neurodegenerative disorders, cancer, infectious diseases, metabolic and autoimmune syndromes, and aging. Through collaborations with TSRI's Translational Research Institute, these arenas are exploited for the development and testing of novel therapeutics.

The six Departments are seeking highly qualified, interactive and extramurally funded investigators who will bring and initiate creative research programs that will take advantage of the unique cores of Scripps Florida, including high throughput genomic screening, proteomics, crystallography, pharmacokinetics, medicinal chemistry and the ultra high throughput small molecule facility that greatly facilitate lead optimization for developing unique research tools and novel drugs.

Appointments are available at all levels in the six Departments. TSRI offers very attractive startup packages and an outstanding intellectual environment for fostering top-tier basic and translational research. In addition, the Max Planck Florida Institute, the first Max Planck Institute in the United States, is under construction adjacent to Scripps Florida, and will offer state-of-the-art bioimaging capabilities.

Interested candidates should submit their Curriculum Vitae, a synopsis of their past research accomplishments, and of their current and proposed research programs, along with complete contact information for at least four professional references, to:

Dr. John L. Cleveland, Chairman,
Department of Cancer Biology
c/o Marika Kernick
E-mail: mkernick@scripps.edu

Dr. Charles Weissmann, Chairman,
Department of Infectology
c/o Marilena Fernandez
E-mail: marilena@scripps.edu

Dr. Patrick R. Griffin, Chairman,
Department of Molecular Therapeutics
c/o Mary Krosky
E-mail: krosky@scripps.edu

Dr. William R. Roush, Executive Director of Medicinal Chemistry, Professor,
Department of Chemistry
c/o Carol Mills
E-mail: cmills@scripps.edu

Dr. Roy G. Smith, Chairman,
Department of Metabolism and Aging
c/o Beth Perconte
E-mail: bpercont@scripps.edu

Dr. Ronald L. Davis, Chairman,
Department of Neuroscience
c/o Hollie Alkema
E-mail: hollie@scripps.edu

The Scripps Research Institute, Scripps Florida
130 Scripps Way, Jupiter, Florida, 33458

International Society for Stem Cell Research

ISSCR

7th ANNUAL MEETING

The world's premier stem cell research event

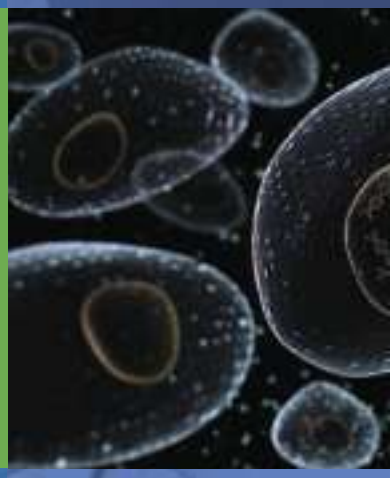

July 8–11, 2009

Centre Convencions Internacional Barcelona
Barcelona, Spain

Featured Speakers

Keynote Speaker
Wednesday, July 8

Nancy Wexler, PhD
Columbia University, Hereditary Disease Foundation
New York, NY USA

Anne McLaren Memorial Lecture
Saturday, July 11

Janet Rossant, PhD
Hospital for Sick Children
Toronto, Ontario, Canada

Early registration discount offers ends May 14.
Register online: www.isscr.org/meetings

BOSTON UNIVERSITY

Boston University School of Medicine
Continuing Medical Education

Joint Sponsor for Continuing Medical Education

This activity has been planned and implemented in accordance with the Essential Areas and policies of the Accreditation Council for Continuing Medical Education through the joint sponsorship of the Boston University School of Medicine and the International Society for Stem Cell Research.

Co-sponsored by

CRG

CMR[B]

POSITIONS OPEN

POSTDOCTORAL POSITIONS IN MOLECULAR AND CELLULAR BIOLOGY
The Wine Research Centre, University of British Columbia, Vancouver, B.C., Canada

Two Postdoctoral positions are available immediately in the Wine Research Centre **(website: http://www.landfood.ubc.ca/wine/index.html)** for a 24-month appointment with potential for extending employment. These positions are funded by large-scale Genome British Columbia wine genomics grants to characterize fermentation stress response genes in *S. cerevisiae*. Successful candidates will be responsible for establishing function of each of these 62 genes induced during wine fermentation using a systems biology approach. Outstanding research facilities are available. Salary approximately $50,000 annually, including benefits.

A Ph.D. in molecular and cellular biology is required. Experience in transcriptomics/proteomics/metabolomics will be an asset. Interested candidates should apply with curriculum vitae and names of three references to: **Dr. Hennie J. J. van Vuuren, Director, e-mail: hjjvv@interchange.ubc.ca.**

NEUROSCIENCE POSITION
at Georgia State University

Georgia State University (GSU) (**website: http://www.gsu.edu**) invites applications for a senior neuroscience faculty position at the associate or full professor level. In exceptional cases, applicants at the assistant professor level will be considered. This position is part of a major initiative to enhance existing strengths in neuroscience at GSU over the next three years coordinated by the Center for Behavioral Neuroscience (**website: http://www.cbn-atl.org**) and the GSU Brains and Behavior Program (**website: http://brainsbehavior.gsu.edu**) working with GSU's newly formed Neuroscience Institute (**website: http://www.neuroscience.gsu.edu**). Preference will be given to applicants working in behavioral or systems neuroscience. We are particularly interested in research that complements the CBN's focus on the mechanisms of social behavior, neuroendocrinology, and the neuroscience of emotion. We are open both to applicants using standard laboratory animal models and to applicants with a neuroethological perspective using vertebrate or invertebrate species. Successful applicants will be individuals who will take advantage of the interdisciplinary collaborative research opportunities available within the Center for Behavioral Neuroscience and the Brains and Behavior Program.

Applicants must have a Ph.D. degree with relevant postdoctoral experience and demonstrated ability to conduct an independent research program using modern techniques. They must also have skills and interest in teaching. Submit curriculum vitae, bibliography, statements of research and teaching interests, and the names of three references, either electronically to: **Ms. Veronica Williamson at website: http://biowfw@langate.gsu.edu,** with the subject line "Neuroscience Search," or by mail to: **Neuroscience Institute, Attn: Ms. Tara Alexander, Georgia State University, P.O. Box 5030, Atlanta, GA 30302-5030, U.S.A.** The review of applications will begin immediately and will continue until position is filled.

Georgia State University is an Affirmative Action/Equal Opportunity Employer.

POSTDOCTORAL POSITIONS are available immediately for studying the enzymology of B12 trafficking and H2S biogenesis. A Ph.D. in chemistry or biochemistry and relevant experience are required. To apply, please contact: **Dr. Ruma Banerjee, University of Michigan, e-mail: rbanerje@umich.edu.**

POSITIONS OPEN

GENPATH

JOB ROLE: DIRECTOR OF MICROARRAY SERVICES

Basic Purpose: Develop and implement microarray based testing in an oncology diagnostics setting.

Duties and Responsibilities: The successful candidate will collaborate with scientific thought leaders in academia and clinical research to develop and validate clinically relevant platforms. Responsibilities will include facilitating experimental design, data interpretation and large-scale analyses of various datasets from microarrays. Candidate should be able to take initiative and hire and train laboratory personnel on various microarray platforms and maintain the workflow in a high throughput diagnostic setting.

Requirements: The position requires an M.S. or a Ph.D. in a relevant field of biology preferably with a background in bioinformatics. Peer-reviewed publications in the field are highly desirable. Experience with Agilent or Nimbelgen microarray platforms is required.

Please send your resume to **e-mail: genpath@genpathdiagnostics.com.** For more information, please visit us at **website: http://www.genpathdiagnostics.com.**

POSTDOCTORAL FELLOW
HIV Virological Synapse
Mount Sinai School of Medicine

VIROLOGIST/CELL BIOLOGIST to study the mechanisms of cell-to-cell infection of HIV through virological synapses (27-Mar 09 issue *Science*). Applicants with Ph.D. or M.D. with expertise in virology, live/intravital microscopy, immunology, molecular/cell biology should send a curriculum vitae, cover letter and letters of reference to: **Ben Chen, M.D., Ph.D., e-mail: ben.chen@mssm.edu.**

POSITIONS OPEN

Texas A&M Health Science Center College of Medicine

POSTDOCTORAL POSITIONS
in Cardiovascular Molecular Signaling Networks

Two NIH-funded positions are immediately available to study intracrine mechanisms of renin-angiotensin system actions in cardiac cells and animal models. Recent Ph.D. graduates in the biological sciences, with a background in immunohistochemistry, confocal imaging, intracellular trafficking, culture of neonatal and adult heart cells, RT-polymerase chain reaction, cell transfection, and small animal surgical techniques are encouraged to apply.

Please forward a cover letter, curriculum vitae, and three reference letters to **e-mail: kbaker@medicine.tamhsc.edu** or to: **Kenneth M. Baker, M.D., Division of Molecular Cardiology, Mayborn Chair in Cardiovascular Research, Texas A&M Health Science Center, College of Medicine, 1901 South First Street, Building 205, Temple, Texas 76504.**

MARKETPLACE